ÉVOLUTION MORPHOLOGIQUE DU CERVEAU CHEZ LES SALAMANDRES

Thèse présentée

dans le cadre du programme de doctorat en biologie

en vue de l'obtention du grade de philosophiæ doctor (Ph.D.)

PAR

© LAURENT HOULE

Mai 2026

Composition du jury :

Robert Schneider, président du jury, Université du Québec à Rimouski

Richard Cloutier, directeur de recherche, Université du Québec à Rimouski

Alice Clement, examinateur externe, Flinders University

France Dufresne, examinateur interne, Université du Québec à Rimouski

Dépôt initial le 9 janvier 2026 Dépôt final le 13 mai 2026

« Before I do anything, I ask myself: Would an idiot do that? And if they would, I do not do that thing. »

Dwight K. Schrute (played by Rainn Wilson)

REMERCIEMENTS

Je tiens à exprimer ma reconnaissance envers ma famille et mes amis qui m'ont soutenu durant mon parcours académique. Je remercie spécialement ma conjointe Marie pour son appui, sa patience et son soutien sans faille au cours de ces nombreuses années. Je tiens aussi à remercier tous les membres du Laboratoire de Paléontologie et de Biologie évolutive de l'UQAR qui ont contribué, de près ou de loin, au succès de ce projet. Je souligne particulièrement les contributions d'Olivia Vanhaesebroucke et d'Olivier Larouche. Je remercie aussi tout spécialement mon directeur de recherche, Richard Cloutier, non seulement pour son encadrement et son support tout au long de ce projet, mais aussi pour les innombrables discussions enrichissantes qui m'ont fait évoluer en tant que biologiste au cours des cinq dernières années. Je tiens à remercier Robert Schneider, France Dufresne et Alice Clement pour avoir accepté de faire partie du comité d'évaluation lors de ma soutenance de thèse doctorale. Leurs commentaires et leurs suggestions m'ont ouvert de nouvelles pistes de réflexion. Je remercie Hillary Maddin pour le don de spécimens d'axolotl ainsi que Jade Atkins, Alanna Cantelon et Bassel Arnaout pour m'avoir aidé dans la préparation du protocole de laboratoire pour le premier chapitre de ma thèse. Je remercie les équipes des collections du musée Canadien de la Nature (CMN), du Royal Ontario Museum (ROM), du American Museum of Natural History (AMNH), du Kansas University Biodiversity Institute (KUBI), du Field Museum of Natural History (FMNH) et du Museum of Vertebrate Zoology (MVZ) pour leur collaboration pour les prêts de spécimens. Je remercie également les contributeurs du site web de partage d'images Morphosource.org ainsi que Jason Pardo pour avoir partagé des images de scans de salamandre. Ce projet n'aurait pu être mené à terme sans la contribution financière du Conseil de Recherches en Sciences naturelles et en Génie du Canada. Finalement, je remercie l'ensemble de l'équipe de la série télé The Office (US), qui m'a permis de rester sain d'esprit durant d'incalculables heures de segmentation d'images.

RÉSUMÉ

Comprendre les mécanismes qui façonnent l'évolution morphologique du cerveau représente un enjeu important pour mieux saisir l'origine de la disparité neuroanatomique chez les vertébrés. Deux modèles principaux ont été proposés pour expliquer l'évolution morphologique du cerveau chez les vertébrés : les modèles concerté et mosaïque. Le modèle concerté repose sur l'idée que des contraintes développementales limitent les variations possibles entre les différentes régions cérébrales, de sorte que la taille des régions tend à être proportionnelle à la taille globale du cerveau. À l'inverse, le modèle mosaïque met l'accent sur les contraintes fonctionnelles, qui peuvent permettre à certaines régions du cerveau de suivre des trajectoires évolutives distinctes en fonction de leur rôle spécifique. L'influence relative de ces deux types de contraintes peut varier d'un groupe de vertébrés à l'autre, ainsi qu'entre les différentes échelles d'organisation étudiées. Les travaux portant sur ces modèles se sont surtout concentrés sur les amniotes, tandis que les vertébrés non amniotes ont longtemps reçu moins d'attention. Parmi ces derniers, les amphibiens constituent un groupe intéressant à l'histoire évolutive riche et dynamique. Les salamandres, en particulier, offrent un système d'étude pertinent : elles présentent un Bauplan relativement conservé, notamment lorsqu'on les compare aux espèces fossiles d'amphibiens ou encore aux premiers tétrapodes. Elles représentent ainsi un groupe stratégique pour explorer l'évolution cérébrale et établir des comparaisons pertinentes avec des taxons fossiles occupant une position clé dans l'évolution des vertébrés. L'objectif général de cette thèse est donc d'examiner l'évolution morphologique du cerveau chez les salamandres, en intégrant des perspectives micro- et macro-évolutives, afin de mieux cerner l'importance relative des modèles concerté et mosaïque chez les vertébrés non amniotes.

Le premier objectif était d'investiguer quels types de contraintes affectent le développement du cerveau chez une espèce de salamandre modèle, l'axolotl mexicain. Les cerveaux de 77 larves d'axolotl, divisés en quatre stades de développement, ont été analysés à l'aide de la méthode de morphométrie géométrique et de mesures volumétriques. La présence de modularité forte et de différences des relations allométriques entre les régions du cerveau a suggéré la présence de contraintes fonctionnelles lors du développement de l'axolotl. Cependant, la relation générale entre le volume total du cerveau et celui des différentes régions, la stabilité relative de l'hypothalamus et le niveau intermédiaire d'intégration inter-module permettaient de supporter la présence de contraintes développementales. De plus, une hypothèse de modularité à six modules distincts au sein du cerveau a été détectée comme étant la mieux supportée.

Le deuxième objectif était d'étudier le patron de covariation morphologique des régions du cerveau au sein de plusieurs espèces de salamandres afin d'identifier des contraintes fonctionnelles et développementales. Les cerveaux de 76 espèces de salamandres, appartenant aux dix familles taxonomiques du groupe, ont été analysés à l'aide la méthode de morphométrie géométrique en considérant l'arbre phylogénétique du groupe. Les analyses ont démontré qu'une hypothèse de modularité à six modules était la plus pertinente pour

expliquer le patron de covariation des traits du cerveau et de l'endocaste. La forte relation entre la position de la suture coronale et le chiasme optique ainsi que le niveau intermédiaire d'intégration inter-module suggèrent la présence de contraintes développementales. Le fort signal de modularité global mis en lumière par cette étude représente une évidence d'indépendance entre certains modules, suggérant la présence de contraintes fonctionnelles.

Le troisième objectif était d'identifier des facteurs majeurs affectant l'évolution de la morphologie du cerveau chez les salamandres. Le même échantillon de 76 espèces a aussi été utilisé pour cet objectif et la morphologie du cerveau a été étudiée à l'aide de la méthode de morphométrie géométrique également. Les relations de parenté entre les espèces ont été considérées dans les analyses lorsqu'elles étaient nécessaires. Les analyses ont montré une importance majeure de l'allométrie et de la phylogénie sur l'évolution morphologique du cerveau des salamandres. Elles ont aussi montré une importance secondaire des cycles de vie et des microhabitats sur l'évolution du cerveau.

Globalement, ces travaux démontrent que le patron de covariation micro- et macro-évolutif du cerveau semble conservé chez les salamandres. Un mélange de contraintes développementales et fonctionnelles sont associées à l'évolution du cerveau chez ce groupe. De plus, les analyses ont permis de démontrées que la morphologie de l'endocaste représente assez fidèlement celle du cerveau dans des contextes de modularité, de disparité et de taux d'évolution, mais que cette correspondance est variable selon les régions cérébrales. De façon générale, cette thèse permet d'améliorer le niveau de connaissance sur le portait de variations morphologiques du cerveau ainsi que sur les mécanismes modelant l'évolution de cette structure chez un groupe de vertébrés non-amniote.

Mots clés : Modularité, Caudata, Disparité morphologique, Cerveau, Endocaste, Évolution mosaïque, Évolution concertée, Ontogénie, Morphométrie géométrique

ABSTRACT

Two main models have been proposed to explain the morphological evolution of the vertebrate brain: the concerted and mosaic models. The concerted model is based on the idea that developmental constraints limit the range of possible variation among brain regions, such that regional sizes tend to scale proportionally with overall brain size. In contrast, the mosaic model emphasizes functional constraints, that may allow certain regions to follow distinct evolutionary trajectories depending on their specific roles. The relative influence of these two types of constraints can vary across vertebrate groups and across organizational scales. Research on these models has focused predominantly on amniotes, whereas non-amniote vertebrates have long been comparatively understudied. Among the latter, amphibians represent an evolutionarily interesting group. Salamanders, in particular, provide a relevant study system: they exhibit a relatively conserved Bauplan, especially when compared with fossil amphibians and early tetrapods. They therefore represent a strategic group for investigating brain evolution and for establishing meaningful comparisons with fossil taxa that occupied key positions during major vertebrate evolutionary transitions. The primary goal of this thesis is to investigate the morphological evolution of the brain in salamanders by integrating both micro- and macroevolutionary perspectives, in order to better assess the relative importance of the concerted and mosaic models in non-amniote vertebrates.

The first objective was to investigate the types of constraints that influence brain development in a model salamander species, the Mexican axolotl. The brains of 77 axolotl larvae, divided into four developmental stages, were analysed using geometric morphometrics and volumetric measurements. The presence of strong modularity and differences in allometric relationships among brain regions suggested that functional constraints act during axolotl development. However, the general relationship between total brain volume and the volume of individual regions, the general stability of the hypothalamus area and the intermediate level of inter-modular integration supported the presence of developmental constraints as well. Moreover, a six-module modularity hypothesis was identified as the best-supported structure of the developing brain.

The second objective was to examine the pattern of morphological covariation among brain regions across multiple salamander species to identify functional and developmental constraints. The brains of 76 salamander species, associated with all ten taxonomic families of the group, were analysed using geometric morphometrics while accounting for the phylogeny. The analyses revealed that a six-module hypothesis was the most relevant to explain covariation patterns across species for the brain and endocast. The strong association between the position of the coronal suture and the optic chiasm, along with an intermediate level of integration among modules, suggested the influence of developmental constraints. On the other hand, the strong global modularity signal provided evidence for partial independence among certain modules, consistent with functional constraints.

The third objective was to identify major factors shaping the evolution of brain morphology in salamanders. The same dataset of 76 species was used, and brain morphology was

analyzed using geometric morphometrics while incorporating phylogenetic information when required. The analyses demonstrated a dominant influence of allometry and phylogeny on brain evolution in salamanders, as well as secondary effects of life-history strategies and microhabitats.

Overall, this thesis demonstrates that the micro- and macroevolutionary covariation patterns of salamander brain appear broadly conserved. A combination of developmental and functional constraints underlies brain evolution in this group. In addition, the analyses showed that endocast morphology represents the brain morphology with reasonable fidelity in terms of modularity, disparity, and evolutionary rates, but this correspondence varies depending on the brain region. This promotes the use of the endocast as a reasonable proxy of the brain in fossil amphibians and other lower tetrapods. More broadly, this work enhances our understanding of morphological variation in the brain and of the mechanisms shaping its evolution in a group of non-amniote vertebrates.

Keywords: Modularity, Caudata, Morphological disparity, Brain, Endocast, Mosaic evolution, Concerted evolution, Ontogeny, Geometric morphometrics

TABLE DES MATIÈRES

LISTE DES TABLEAUX

LISTE DES FIGURES

INTRODUCTION GÉNÉRALE

Le cerveau des vertébrés est un organe hautement complexe, au cœur du système nerveux central, dont les fonctions sont essentielles à la perception de l'environnement, au traitement de l'information et à la coordination des réponses comportementales et physiologiques (Butler et Hodos, 2005). Son étude permet non seulement de mieux comprendre les capacités sensorielles et cognitives propres à chaque espèce, mais aussi de reconstituer les grandes transitions évolutives survenues au cours de l'histoire des vertébrés. Sur le plan morphologique et fonctionnel, le cerveau est organisé en régions distinctes, mais interconnectées, issues de processus développementaux conservés, et dont la différenciation relative reflète souvent des adaptations écologiques et comportementales (Nieuwenhuys *et al.*, 2014). Les comparaisons interspécifiques révèlent que, malgré une architecture générale conservée, la taille relative et la spécialisation des différentes régions cérébrales ont évolué de manière répétée et indépendante en réponse à des contraintes fonctionnelles, développementales et phylogénétiques au cours des 540 millions d'années de l'évolution des vertébrés (Finlay et Darlington, 1995; Gonzalez-Voyer *et al.*, 2009; Montgomery *et al.*, 2016; Smith *et al.*, 2001; Yopak *et al.*, 2010). Cependant, plusieurs défis sont associés à l'étude de l'évolution du cerveau, l'un d'eux venant du fait que les tissus mous sont rarement préservés lors de la fossilisation, ce qui cause une faible représentation de la morphologie du cerveau chez des espèces fossiles (de Sousa *et al.*, 2023). De plus, les recherches sur l'évolution du cerveau utilisant des représentants actuels se sont longtemps concentrées sur les mammifères et les oiseaux (Baron et Jolicoeur, 1980; Esteve-Altava, 2017; Jerison, 2012; Jerison, 1985; Jolicoeur *et al.*, 1984; Kappers *et al.*, 1936; Stephan *et al.*, 1981; Stephan et Pirlot, 1970). Depuis les vingt dernières années, un effort croissant a été déployé pour étudier les vertébrés dits « basaux », défini ici comme les vertébrés non-amniotes, afin de mieux retracer l'origine et la diversification du cerveau (Clement *et al.*, 2021; Gonzalez-Voyer *et al.*, 2009; Lamanna *et al.*, 2023; Ollonen *et al.*, 2024). Une utilité d'étudier des vertébrés non-amniotes est de

pouvoir faire des parallèles plus adéquats entre ces groupes et des espèces fossiles associées à certains moments clés de l'évolution des vertébrés. Un de ces moments clés est la terrestrialisation des vertébrés, qui représente un tournant majeur dans l'histoire évolutive du cerveau, marqué par l'adaptation à la vie terrestre et la réorganisation de nombreuses structures sensorielles et motrices (Challands *et al.*, 2020; Clement *et al.*, 2021; MacIver et Finlay, 2022; MacIver *et al.*, 2017). L'histoire évolutive de la morphologie du cerveau chez les vertébrés demeure donc un sujet important en biologie évolutive. De plus, l'étude comparative du cerveau chez des vertébrés non-amniotes actuels offre un cadre intéressant pour explorer la diversification morphologique et les principes évolutifs qui sous-tendent la complexification du système nerveux au sein des vertébrés.

Cette thèse doctorale s'intéresse aux mécanismes qui affectent l'évolution du cerveau chez des vertébrés basaux en utilisant les salamandres comme organismes modèles. Dans cette introduction générale, les fondements théoriques constituant le cadre conceptuel des analyses effectuées dans cette thèse seront abordés. La définition de plusieurs concepts évolutifs importants, tels que la modularité, l'intégration morphologique et la disparité, sera fournie. Le choix des salamandres comme groupe modèle sera justifié principalement dans l'optique de mieux comprendre l'origine de l'évolution du cerveau des vertébrés basaux. Enfin, les principaux concepts seront synthétisés à la lumière de la problématique, des objectifs et de la méthodologie présentés dans les chapitres de cette thèse.

1. LE CERVEAU DES VERTEBRES

1.1 Origines développementales

Chez les vertébrés, le cerveau trouve son origine développementale dans l'ectoderme, l'un des trois feuillets embryonnaires (Hodos, 1988). Très tôt au cours du développement des chordés, une portion de l'ectoderme se différencie pour former la plaque neurale, laquelle s'invagine afin de constituer le tube neural, à l'origine du système nerveux central (Senovilla-Ganzo et García-Moreno, 2024). Rapidement, le cerveau embryonnaire se subdivise en trois

régions principales : le prosencéphale (cerveau antérieur), le mésencéphale (cerveau moyen) et le rhombencéphale (cerveau postérieur; Hodos, 1988). Ces divisions de base sont hautement conservées chez tous les vertébrés, mais leur croissance relative et leur degré de différenciation varient considérablement selon les lignées évolutives (Northcutt, 2002). Chez les mammifères, le prosencéphale connaît une expansion marquée, notamment avec le développement du néocortex (Figure 0.1), une structure associée aux fonctions cognitives avancées, à la mémoire et au traitement sensorimoteur complexe (Lancaster, 2024). À l'inverse, d'autres groupes, tels que les poissons ou les amphibiens, présentent une organisation moins compacte et plus segmentée (Figure 0.1), dans laquelle certaines régions, comme le bulbe olfactif ou le cervelet, sont proportionnellement plus développées et reflètent des adaptations sensorielles et locomotrices spécifiques (Kotrschal et Kotrschal, 2020; Lisney *et al.*, 2018; Manzano *et al.*, 2017; Olivares et Schmachtenberg, 2019). Ces variations traduisent une flexibilité évolutive du plan d'organisation cérébral, où la mosaïque de changements régionaux est le résultat de pressions sélectives distinctes agissant sur des fonctions sensorielles, motrices ou comportementales (Napoli et Powers, 2020).

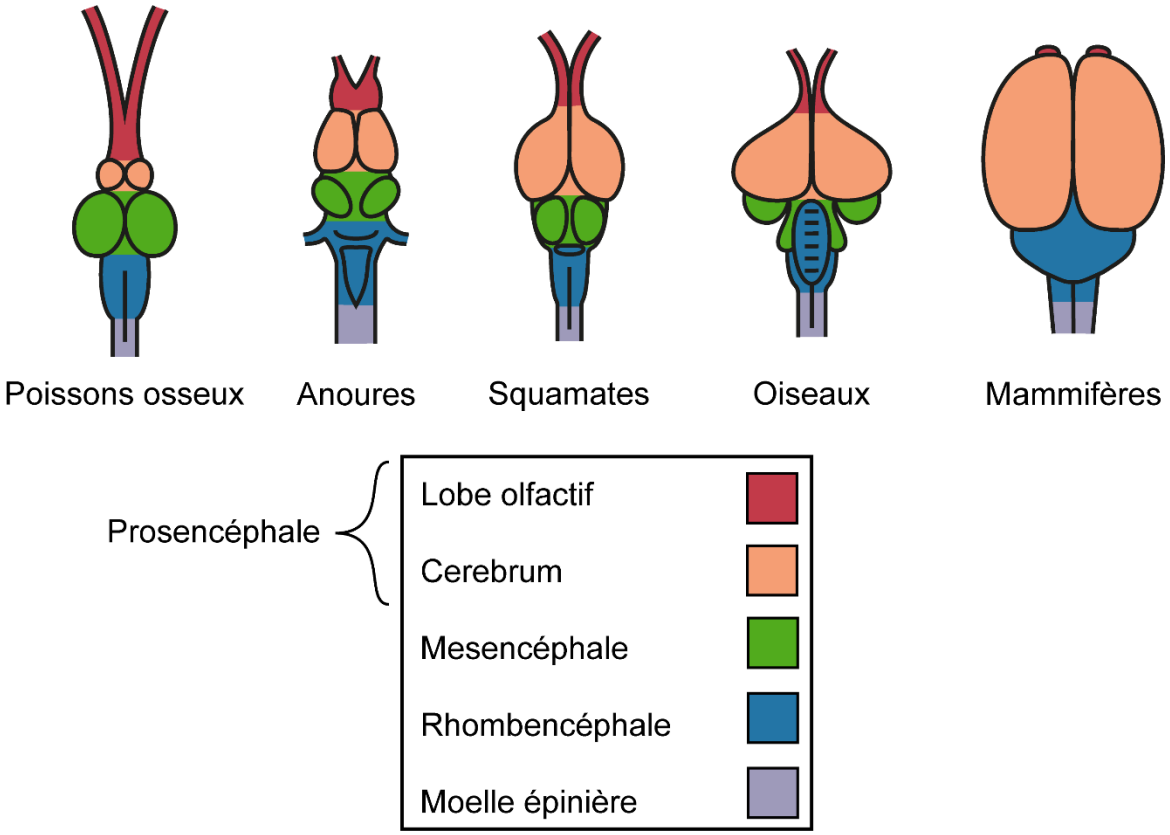

Figure 0.1 Représentation des trois régions principales du cerveau au sein de différents groupes de vertébrés. Image modifiée de Luisetto *et al.* (2018).

1.2 Régions majeures et leurs fonctions

Chaque région majeure du cerveau est associée à des fonctions spécifiques. La région la plus antérieure est le prosencéphale (Hodos, 1988). Cette zone comprend deux sous-régions, soit le télencéphale et le diencéphale (Hodos, 1988). Le prosencéphale (Figure 0.2) est impliqué dans les fonctions supérieures telles que la mémoire, l'apprentissage et la régulation hormonale (Hodos, 1988). Le télencéphale abrite notamment des réseaux neuronaux assurant une intégration multimodale complexe, c'est-à-dire la capacité à combiner simultanément des informations issues de plusieurs modalités sensorielles (p. ex., visuelle, auditive, olfactive, somatosensorielle) pour produire une réponse comportementale cohérente, une propriété particulièrement développée chez les mammifères (Karten, 2015). En outre, le

télencéphale joue un rôle clé dans la planification comportementale, la prise de décision et la modulation des circuits de récompense (Briscoe et Ragsdale, 2019). Le diencéphale, et en particulier l'hypothalamus, constitue un centre d'intégration neuroendocrinien qui contrôle les rythmes circadiens, l'équilibre énergétique, la reproduction et les réponses au stress (Croizier *et al.*, 2015; Sánchez-Vázquez *et al.*, 2019). D'un point de vue développemental, le prosencéphale présente une prolifération cellulaire tardive (Hodos, 1988; Nieuwenhuys *et al.*, 2014). La régionalisation du prosencéphale repose sur des gradients de facteurs de transcription, notamment Paired box gene 6 (*PAX6*) et Empty spiracles homeobox 2 (*EMX2*), ainsi que sur des signaux morphogénétiques tels que Sonic hedgehog (*Shh*) et les « fibroblast growth factors » (*FGF*), qui établissent de nombreuses subdivisions dans cette région (Leung *et al.*, 2022; Wilson et Houart, 2004).

Le mésencéphale (Figure 0.2) joue un rôle central dans l'intégration sensorielle et le contrôle moteur, servant de station relais pour les informations visuelles et auditives (Hodos, 1988). Il contient notamment le tectum optique, une structure impliquée dans l'orientation vers des stimuli visuels et auditifs, c'est-à-dire la capacité de diriger les mouvements de la tête, des yeux ou du corps en réponse à une source sensorielle dans l'espace (Croizier *et al.*, 2015; Deeg *et al.*, 2009). Cette région est essentielle pour coordonner les réponses rapides aux signaux environnementaux pertinents (Deeg *et al.*, 2009; Thompson *et al.*, 2016). Fonctionnellement, le tectum intègre les signaux rétiniens, auditifs et somatosensoriels dans une carte topographique de l'espace, permettant des mouvements d'orientation rapides et adaptatifs (Maximino, 2008). D'un point de vue développemental, l'identité et l'extension du mésencéphale sont contrôlées par l'organisateur isthmique situé à la frontière mésencéphale-rhombencéphale, où des signaux *FGF* et Wingless/Integrated (*Wnt*) orchestrent la prolifération et la différenciation des précurseurs neuronaux qui formeront les circuits tectaux et dopaminergiques (Leung *et al.*, 2022; Wilson et Houart, 2004).

Le rhombencéphale (Figure 0.2), quant à lui, comprend le cervelet et la moelle allongée (medulla oblongata), responsables de la coordination des mouvements et des fonctions

végétatives, c'est-à-dire les processus physiologiques automatiques assurant le maintien de la vie, tels que la respiration, la régulation du rythme cardiaque et la pression artérielle (Gilland et Baker, 2005; Hodos, 1988). Il renferme également les noyaux de nombreux nerfs crâniens et des relais sensoriels vestibulaires, auditifs et somatosensoriels qui assurent la posture, le contrôle du regard, les réflexes orofaciaux et la modulation des comportements respiratoires (Butler et Hodos, 2005). D'un point de vue embryologique, le rhombencéphale est segmenté en neuromères, des unités de développement répétées le long de l'axe antéro-postérieur du tube neural (Krumlauf et Wilkinson, 2021). Chacun de ces neuromères donne naissance à des structures distinctes du cerveau postérieur, selon des portions métamériques, c'est-à-dire des subdivisions en série du plan d'organisation (Butler et Hodos, 2005). Ces rhombomères se distinguent par des combinaisons spécifiques de gènes à homéoboîte (*Hox*) qui déterminent la position des noyaux moteurs et sensoriels associés à chaque nerf crânien, organisant ainsi la topologie des circuits sensorimoteurs de la moelle allongée (Krumlauf, 1994; Krumlauf et Wilkinson, 2021; Parker *et al.*, 2016).

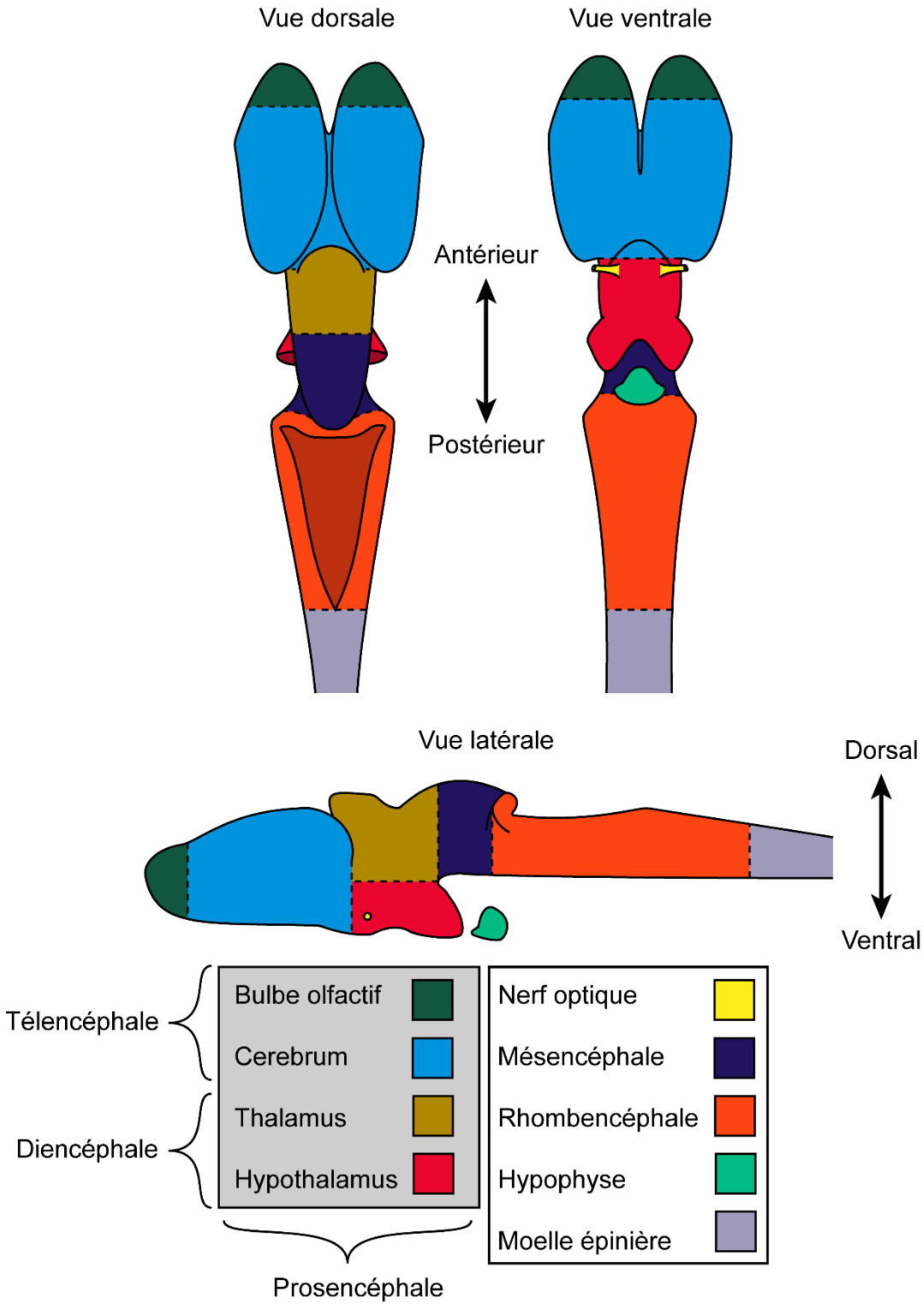

Figure 0.2 Représentation des régions majeures du cerveau chez les salamandres.

La diversité fonctionnelle de ces régions explique en partie les variations morphologiques observées au sein des vertébrés, en lien avec leurs modes de vie et leurs environnements (Corfield *et al.*, 2015; Murakami *et al.*, 2005; Schumacher et Carlson, 2022; Sukhum *et al.*, 2018). Par exemple, chez les espèces aquatiques fortement dépendantes de la vision, le mésencéphale peut être hypertrophié pour traiter efficacement les stimuli optiques, tandis que chez les espèces terrestres, le cervelet est souvent plus développé afin d'ajuster finement les mouvements complexes requis par la locomotion sur un substrat irrégulier (Murakami *et al.*, 2005). De même, chez plusieurs lignées de poissons électriques téléostéens, l'évolution d'un système électrosensoriel actif s'accompagne d'une augmentation marquée et localisée de la taille du cervelet et du rhombencéphale, en lien avec les exigences de traitement des signaux électriques produits et perçus par ces espèces (Schumacher et Carlson, 2022; Sukhum *et al.*, 2018). À l'inverse, chez certaines espèces d'oiseaux fortement dépendantes de l'olfaction, notamment celles vivant et s'alimentant en milieu semi-aquatique ou nocturne, les bulbes olfactifs sont proportionnellement plus volumineux, ce qui reflète l'importance accrue de cette modalité sensorielle dans leur écologie (Corfield *et al.*, 2015). Ces observations montrent que la variation interspécifique de la taille relative des régions cérébrales peut refléter l'adaptation des systèmes nerveux aux contraintes écologiques et aux exigences fonctionnelles propres à chaque environnement.

1.3 Modèles d'évolution morphologique du cerveau chez les vertébrés

L'évolution du cerveau chez les vertébrés est souvent expliquée par deux grands modèles évolutifs : l'hypothèse de l'évolution mosaïque et celle de l'évolution concertée (Barton et Harvey, 2000; Striedter, 2005). Ces deux perspectives reposent sur l'influence conjointe des contraintes développementales et fonctionnelles dans l'évolution cérébrale (Montgomery *et al.*, 2016; Striedter, 2005; Willemet, 2013). Selon Montgomery *et al.* (2016), certains aspects du développement du cerveau, comme les gènes qui interagissent entre eux, les liens entre plusieurs traits influencés par les mêmes gènes (pléiotropie), ou encore les gradients qui orientent la formation des tissus, peuvent empêcher les différentes régions cérébrales

d'évoluer complètement séparément les unes des autres. Willemet (2013) souligne aussi que les réseaux de connexions entre les régions du cerveau, ainsi que la nécessité pour ces régions de communiquer et de se synchroniser efficacement, limitent aussi leur capacité à évoluer de façon totalement indépendante. L'hypothèse de l'évolution concertée postule que la croissance des différentes régions cérébrales est étroitement corrélée à la taille totale du cerveau, du fait de contraintes développementales largement partagées (p. ex., timing de neurogenèse, durée des cycles cellulaires). Dans ce modèle, toute augmentation de taille d'une région impliquerait une expansion concomitante des autres zones pour maintenir les proportions et la connectivité globale (Finlay et Darlington, 1995). Ce modèle évolutif souligne ainsi l'importance d'une intégration structurelle et d'une interdépendance développée entre les régions (Finlay et Darlington, 1995; Finlay *et al.*, 2001).

À l'opposé, l'hypothèse mosaïque avance que les différentes régions cérébrales peuvent évoluer de façon relativement indépendante, sous l'effet de pressions sélectives ciblées sur des fonctions particulières (Barton et Harvey, 2000). Un exemple frappant est fourni par l'étude expérimentale de Fong *et al.* (2021), qui ont montré que la sélection artificielle pour un télencéphale plus volumineux chez le guppy (*Poecilia reticulata*) entraîne une augmentation ciblée de cette seule région, sans modification des autres structures cérébrales, ce qui constitue une démonstration claire d'évolution mosaïque. Par ailleurs, Yopak *et al.* (2015) ont montré que chez les requins et les raies, la taille relative du cervelet, des lobes optiques et du pallium varie indépendamment selon les modes de vie, qu'il s'agisse de prédation active, de navigation dans des environnements tridimensionnels ou d'une dépendance accrue à l'olfaction, révélant des trajectoires évolutives distinctes entre ces régions et illustrant une spécialisation adaptative propre à chaque espèce. Les contraintes fonctionnelles, liées aux exigences comportementales, écologiques ou sociales propres à chaque espèce, peuvent favoriser la spécialisation adaptative de certaines structures cérébrales indépendamment des autres, produisant ainsi une évolution mosaïque du cerveau (Schumacher et Carlson, 2022; Triki *et al.*, 2022).

Ces deux modèles ne doivent cependant pas être considérés comme mutuellement exclusifs, car de nombreuses études suggèrent qu'ils opèrent de manière conjointe dans l'évolution du cerveau des vertébrés (Gonzalez-Voyer *et al.*, 2009; Gutiérrez-Ibáñez *et al.*, 2014; Moore et DeVoogd, 2017). Chez plusieurs groupes de vertébrés, certaines régions cérébrales montrent une évolution fortement corrélée à la taille totale du cerveau, soutenant l'hypothèse d'une croissance concertée, tandis que d'autres régions varient plus librement en réponse à des pressions fonctionnelles ou écologiques spécifiques, selon un mode mosaïque (Gonzalez-Voyer *et al.*, 2009; Gutiérrez-Ibáñez *et al.*, 2014; Hoops *et al.*, 2017). Chez les oiseaux, Gutiérrez-Ibáñez *et al.* (2014) ont montré que certaines structures du système visuel, comme les noyaux isthmiques, augmentent de taille en suivant étroitement la croissance générale du cerveau, alors que d'autres centres sensoriels changent de taille plus librement. Cela indique que certaines régions sont fortement intégrées au développement global du cerveau, tandis que d'autres s'adaptent de façon plus ciblée aux besoins propres à chaque lignée (Gutiérrez-Ibáñez *et al.*, 2014). De même, chez les poissons cichlidés, les bulbes olfactifs et l'hypothalamus présentent une évolution disproportionnée par rapport au reste du cerveau, indiquant un effet mosaïque régional lié à la communication chimique et au comportement reproducteur (Gonzalez-Voyer *et al.*, 2009). Chez les lézards du genre *Ctenophorus*, certaines régions comme le tectum et le rhombencéphale suivent des tendances d'expansion spécifiques associées au type d'habitat et de locomotion, tandis que d'autres structures conservent une covariation plus globale avec la taille cérébrale, traduisant un équilibre entre intégration développementale et adaptations fonctionnelles (Hoops *et al.*, 2017). Ce compromis entre contraintes développementales et fonctionnelles se retrouve également dans le cadre d'études expérimentales, où la sélection artificielle sur des capacités cognitives entraîne des modifications régionales différenciées sans changement proportionnel de la taille du cerveau, révélant une plasticité mosaïque à l'intérieur d'un cadre concerté (Triki *et al.*, 2022). De plus, Watanabe *et al.* (2021) ont montré que, chez les oiseaux actuels, même les cerveaux présentant une forte intégration générale, comme ceux des Néognathes, se sont construits progressivement par l'ajout successif de groupes de traits morphologiques spécialisés. Leur organisation moderne résulte ainsi d'un mélange d'interdépendances

développementales et d'adaptations régionales qui se sont accumulées au fil de l'évolution (Watanabe *et al.*, 2021). Ensemble, ces observations appuient l'idée que l'évolution cérébrale procède souvent d'un mélange d'intégration concertée et de spécialisation mosaïque, résultant de l'interaction entre des contraintes développementales et fonctionnelles.

1.4 Modularité et intégration du cerveau chez les vertébrés

L'intégration morphologique se définit comme le degré d'interconnexions existant entre différents traits morphologiques (Olson et Miller, 1958). Ce concept, formalisé concrètement par Olson et Miller (1958), reconnaît que de nombreuses structures anatomiques ne varient pas de manière indépendante, mais de façon coordonnée au sein de réseaux intégrés. L'étude du degré d'intégration morphologique permet de comprendre comment la variation phénotypique est structurée et comment les contraintes internes peuvent orienter l'évolution de la morphologie. La modularité, concept intimement lié à celui d'intégration, se définit comme la tendance des organismes à être organisés en unités anatomiques partiellement indépendantes les unes des autres (Mitteroecker et Bookstein, 2007; Wagner, 1996). Wagner (1996) et Wagner et Altenberg (1996) ont proposé que la modularité constitue la contrepartie évolutive de l'intégration : les modules représentent des ensembles de traits fortement intégrés entre eux, mais faiblement liés aux autres parties de l'organisme ou de l'organe concerné. Dans cette perspective, l'étude conjointe de l'intégration et de la modularité permet de mieux comprendre le patron d'organisation des organismes et comment les interactions entre les contraintes internes et l'indépendance relative des modules influencent l'évolution des structures morphologiques.

Dans le contexte de l'évolution du cerveau, l'intégration morphologique et la modularité sont des concepts pertinents (Gómez-Robles *et al.*, 2014; Willemet, 2013). En effet, le cerveau étant confronté à des contraintes développementales et fonctionnelles diverses, ces deux concepts peuvent permettre de décrire la covariation phénotypique, ce qui peut favoriser la détection d'évidences de la prépondérance du modèle concerté ou mosaïque au sein d'un

groupe d'organismes (Gómez-Robles *et al.*, 2014; Gonzalez-Voyer *et al.*, 2009; Moore et DeVoogd, 2017). L'évolution tend à être concertée lorsque les régions cérébrales sont fortement intégrées par des liens génétiques ou épigénétiques, limitant ainsi leur réorganisation (Mitteroecker et Bookstein, 2008). À l'inverse, une indépendance phénotypique entre régions favorise la modularité, permettant à chaque module de suivre une trajectoire évolutive potentiellement distincte (Gómez-Robles *et al.*, 2014; Wagner, 1996).

1.5 Les relations entre le cerveau et le crâne

Le cerveau n'évolue pas de manière indépendante par rapport aux autres structures anatomiques de la tête. Le crâne est considéré comme une structure fortement intégrée au cerveau, tant du point de vue développemental qu'évolutif (Gómez-Robles *et al.*, 2014; Mitteroecker et Bookstein, 2008; Nie *et al.*, 2006). En effet, la croissance et la morphogenèse de plusieurs régions du crâne sont étroitement couplées à celles du cerveau, notamment à travers les interactions tissulaires entre le neurocrâne et le tissu neural durant l'embryogenèse (Mitteroecker et Bookstein, 2008; Piekarski *et al.*, 2014; Teng *et al.*, 2019). Le développement des méninges, du chondrocrâne et des os dermiques est directement influencé par la forme et l'expansion du cerveau, qui déterminent la position et l'orientation de certaines sutures, telles que la suture coronale (Conith *et al.*, 2023; Richtsmeier et Flaherty, 2013; Teng *et al.*, 2019). Réciproquement, la structure osseuse du crâne impose des contraintes mécaniques et spatiales sur le cerveau, influençant sa forme et son organisation régionale (Conith *et al.*, 2023; Kuratani, 2005). Ainsi, les changements évolutifs du cerveau peuvent se répercuter sur la morphologie crânienne, et inversement, soulignant l'importance des interactions développementales dans la diversification conjointe de ces deux systèmes.

Dans ce contexte, les endocastes, moulages de la cavité endocrânienne, constituent un outil central pour étudier l'évolution du cerveau, en particulier chez les taxons fossiles pour lesquelles la conservation des tissus mous lors de la fossilisation est généralement minimale ou inexistante (Challands *et al.*, 2020; de Sousa *et al.*, 2023). Ils fournissent une estimation

de la taille et de la forme globale du cerveau, et peuvent parfois conserver des informations sur la vascularisation et la position des nerfs crâniens, ce qui en fait l'une des rares sources d'information sur la morphologie du cerveau dans le registre fossile (Challands *et al.*, 2020; Clement *et al.*, 2015; de Sousa *et al.*, 2023; Watanabe, Gignac*, et al.*, 2019). Des études récentes montrent que, chez plusieurs groupes de vertébrés (p. ex., squamates, oiseaux), la forme de l'endocaste reproduit de manière étroite la variation de taille et de forme du cerveau, ce qui soutient son utilisation comme proxy pour des comparaisons macro-évolutives (Allemand *et al.*, 2023; Watanabe, Gignac*, et al.*, 2019). Cette correspondance n'est toutefois ni parfaite ni homogène au sein des vertébrés : elle varie selon les clades, les régions du cerveau et même les conditions de développement (Challands *et al.*, 2020; Clement *et al.*, 2021; Watanabe, Gignac*, et al.*, 2019). De plus, la fiabilité de l'identification de certaines frontières entre des régions cérébrales sur les endocastes demeure débattue (Allemand *et al.*, 2023; Bonfili *et al.*, 2022). L'utilisation des endocastes nécessite donc de prendre en compte ces limites, mais leur utilisation reste un outil majeur pour des questions de biologie évolutive sur une grande échelle de temps géologique.

2. LES SALAMANDRES

Les amphibiens constituent un groupe de vertébrés particulièrement informatif pour étudier l'évolution cérébrale chez les vertébrés basaux (Clement *et al.*, 2021). Leur double affiliation, à des milieux aquatiques et terrestres, offre un cadre de comparaison intéressant pour examiner comment le cerveau a pu s'ajuster à la transition eau-terre lors de la terrestrialisation des vertébrés. À cet égard, les salamandres (Caudata) sont particulièrement pertinentes. En effet, leur morphologie et leur mode de locomotion restent parmi les plus proches de ceux des premiers tétrapodes : un corps allongé, une alternance entre déplacements aquatiques par ondulation axiale et marche terrestre par appui des membres chez plusieurs espèces, ainsi qu'un squelette et une disposition des ceintures pectorale et pelvienne relativement conservés (Ashley-Ross, 1994; Pierce *et al.*, 2012). Par exemple, les salamandres ont été utilisées comme analogues modernes des premiers tétrapodes pour

étudier la génération et la coordination des circuits locomoteurs aquatiques et terrestres (Chevallier *et al.*, 2008; Kawano et Blob, 2022; Kawano *et al.*, 2024). Leur usage permet non seulement d'inférer comment les capacités motrices ont pu évoluer, mais aussi comment le système nerveux central a pu s'adapter à des contraintes mécaniques, posturales, physiologiques et sensorielles nouvelles. De plus, des études de neuroanatomie ont montré que le cerveau des salamandres présente certains traits partagés avec des amniotes (Piekarski *et al.*, 2014; Teng *et al.*, 2019), tout en conservant plusieurs caractéristiques plus plésiomorphes susceptibles de refléter des étapes évolutives antérieures du cerveau des vertébrés (Pan *et al.*, 2023). Enfin, comme clade actuel, les salamandres permettent également d'explorer les liens entre la morphologie crânienne et celle du cerveau, ouvrant ainsi des perspectives intéressantes pour la paléoneurologie.

Les salamandres sont caractérisées par une grande diversité spécifique (830 espèces) et une disparité marquée de forme et de taille corporelle (AmphibiaWeb, 2025; Bonett et Blair, 2017; Roth *et al.*, 1990). Ce clade se distingue également par l'une des plus grandes diversités de stratégies de cycle de vie parmi les vertébrés (Liedtke *et al.*, 2022). À l'échelle biogéographique, bien que la richesse spécifique de ce groupe soit maximale dans les régions équatoriales, les salamandres présentent une distribution assez élargie, étant présentes sur tous les continents à l'exception de l'Océanie et de l'Antarctique (Wake et Vredenburg, 2008). Elles occupent une large gamme de microhabitats, allant des environnements aquatiques et souterrains jusqu'aux milieux arboricoles (Blankers *et al.*, 2012). Sur le plan trophique, les salamandres sont majoritairement carnivores à l'état adulte, bien qu'il existe une diversité de type de capture de proie (Petranka, 1998; Wells, 2019). Enfin, plusieurs espèces de ce groupe constituent des modèles biologiques majeurs en raison de caractéristiques physiologiques ou développementales remarquables ; l'axolotl mexicain (*Ambystoma mexicanum*), notamment, est largement étudié pour ses capacités de régénération tissulaire (Voss *et al.*, 2009). Ces particularités traduisent une capacité exceptionnelle des salamandres à coloniser et exploiter une vaste diversité de niches écologiques, illustrant la complexité des interactions entre histoire évolutive, contraintes

physiologiques et facteurs environnementaux. Ainsi, la richesse de leur histoire évolutive et la diversité des formes qu'elles présentent font des salamandres un groupe particulièrement pertinent pour étudier les processus évolutifs à large échelle, y compris ceux qui sous-tendent l'évolution morphologique du cerveau.

Le clade des salamandres comprend dix familles taxonomiques (Jetz et Pyron, 2018). La famille la plus diversifiée est celle des Plethodontidae, avec 519 espèces décrites (AmphibiaWeb, 2025). Les représentants de ce groupe se caractérisent notamment par l'absence de poumons (AmphibiaWeb, 2025). Les Salamandridae et les Hynobiidae constituent les deux autres familles majeures en termes de richesse spécifique, regroupant un peu moins de 150 et près de 100 espèces respectivement, principalement distribuées en Europe (Salamandridae) et en Asie (Hynobiidae; AmphibiaWeb, 2025). Les sept autres familles totalisent ensemble environ 60 espèces, dont la moitié appartient aux Ambystomatidae, un groupe associé à une grande diversité de stratégies de cycle de vie (AmphibiaWeb, 2025). Les Cryptobranchidae, Amphiumidae, Proteidae et Sirenidae regroupent quant à elles des espèces exclusivement associées à des environnements aquatiques (AmphibiaWeb, 2025). Enfin, les Rhyacotritonidae et les Dicamptodontidae comprennent des taxons associés aux habitats terrestres (à l'âge adulte) et répartis principalement le long de la côte ouest de l'Amérique du Nord (AmphibiaWeb, 2025).

L'origine des lissamphibiens est généralement estimée entre ~330 et 250 millions d'années (MA), à partir d'ancêtres appartenant au groupe des temnospondyles (Marjanović et Laurin, 2007; Ruta et Coates, 2007; San Mauro, 2010). En ce qui concerne l'évolution spécifique des salamandres, les premiers fossiles identifiés comme appartenant à ce groupe ont été associés à la période du Trias supérieur (~230 MA; Jones *et al.*, 2022; Marjanović et Laurin, 2014; San Mauro *et al.*, 2005; Schoch *et al.*, 2020). Les salamandres auraient été affectées par l'extinction massive qui a eu lieu à transition entre le Crétacé et le Paléogène (il y a environ 66 millions d'année), qui aurait été suivi par une augmentation de leur diversification (Jetz et Pyron, 2018). Au cours de l'évolution des salamandres, elles auraient subi une

simplification secondaire quant à plusieurs de leurs structures anatomiques (Roth *et al.*, 1993; Roth *et al.*, 1997; Trueb et Cloutier, 1991; Wake, 1991). Une simplification secondaire consiste à présenter des structures anatomiques plus simples que le prédirait la tendance globale à la complexification de structures comme le cerveau au sein du groupe des vertébrés (O'Malley *et al.*, 2016; Roth *et al.*, 1997). Le cerveau et le crâne des amphibiens, spécialement les anoures et les salamandres, ont été identifiés comme ayant subi cette simplification (Hanken et Wake, 1993; Roth *et al.*, 1997). Dans l'ensemble, cette trajectoire évolutive à la fois riche, dynamique et marquée par des épisodes de diversification et de simplification fait des salamandres un groupe particulièrement pertinent pour explorer les processus qui ont façonné l'évolution morphologique du cerveau chez les vertébrés non-amniotes.

2.1 Les cycles de vie

Les salamandres présentent une grande diversité de types de cycle de vie (Duellman et Trueb, 1994). Les deux cycles de vie les plus courants chez les salamandres sont le cycle biphasique et le développement direct (Duellman et Trueb, 1994; Wake et Hanken, 1996). Le cycle de vie biphasique (Figure 0.3) comporte une phase de vie larvaire aquatique suivie d'une métamorphose vers un état adulte associé à des caractéristiques morphologiques et anatomiques typiques d'un tétrapode terrestre (Wilbur et Collins, 1973). Le développement direct (Figure 0.3), qui est commun à la majorité des espèces de la famille des Plethodontidae est caractérisé par une phase « larvaire » qui se déroule dans l'œuf (Wake et Hanken, 1996; Wake et Dickie, 1998). Chez les espèces à développement direct, les modifications développementales associées à la métamorphose chez des espèces biphasiques se produisent avant l'éclosion de l'œuf (Kerney, 2011; Marks et Collazo, 1998). Après l'éclosion, les individus de ces espèces possèdent la majorité des caractéristiques morphologiques et anatomiques similaires à ceux des individus adultes (Kerney, 2011). D'autres espèces, comme le necture tacheté (*Necturus maculosus*), par exemple, ont un mode de vie complètement aquatique associé au cycle de vie de paedomorphe obligatoire (Figure 0.3;

Petranka, 1998). Ces espèces sont caractérisées par une phase larvaire aquatique qui n'est pas suivie d'une métamorphose (Denoël *et al.*, 2005; Duellman et Trueb, 1994). Des changements morphologiques et anatomiques graduels peuvent survenir (telle que la maturation sexuelle), mais aucun changement drastique ne se produit (Duellman et Trueb, 1994; Whiteman, 1994). Les individus conservent ainsi plusieurs caractéristiques juvéniles à l'état adulte (Duellman et Trueb, 1994; Whiteman, 1994). Dans le cas des salamandres, ce patron évolutif a été associé au processus de néoténie, dans lequel le développement de certaines structures phénotypiques est retardé (Denoël et Joly, 2000; Iordansky, 2005). Chez certaines espèces, cependant, la paedomorphose peut être facultative au sein des populations et individus (Figure 0.3), ce qui constitue un autre type de cycle de vie (Denoël *et al.*, 2005; Whiteman, 1994). Chez l'espèce *Ambystoma talpoideum*, par exemple, certains individus peuvent présenter un cycle de vie paedomorphe, alors que d'autres présentent un cycle de vie biphasique (Semlitsch, 1987; Semlitsch *et al.*, 1990). Chez cette espèce, la détérioration des conditions aquatiques, notamment l'assèchement progressif de l'habitat ou la diminution de la disponibilité des ressources, peut induire la métamorphose chez des individus initialement paedomorphes (Semlitsch, 1987; Semlitsch *et al.*, 1990). Finalement, d'autres types de cycle de vie plus complexes existent également chez les salamandres, tels que le cycle de vie triphasique, la viviparité larvipare facultative et la viviparité puéripare (Bruce, 2003; Buckley *et al.*, 2007; Liedtke *et al.*, 2022). Bien que peu d'espèces présentent ces types de cycle de vie (Liedtke *et al.*, 2022), la présence d'une grande diversité de stratégies de cycle de vie illustre la complexité associée au développement de ce groupe. La métamorphose a été identifiée par plusieurs auteurs comme étant un facteur important qui a influencé l'évolution de certaines structures morphologiques (Fabre *et al.*, 2020; Mai et Liao, 2019). L'évolution du crâne des salamandres, par exemple, aurait été fortement affectée par les stratégies développementales associées aux cycles de vie (Fabre *et al.*, 2020).

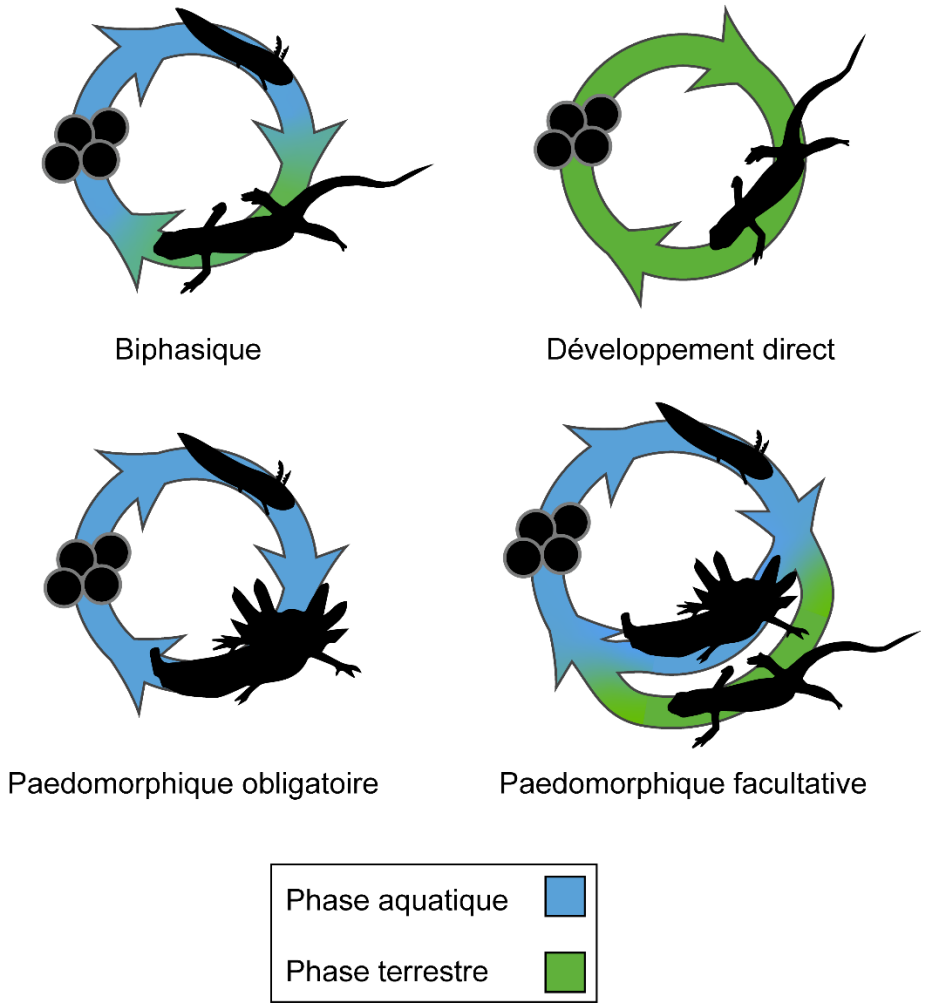

Figure 0.3 Représentation visuelle des quatre types de cycle de vie les plus communs chez les salamandres actuelles.

2.2 Les microhabitats

Les salamandres peuvent être retrouvées dans des types d'habitats contrastés (Petranka, 1998; Wells, 2019). En effet, certaines espèces sont associées à un mode de vie arboricole, alors que d'autres se retrouvent au sol, et d'autres sont plutôt associés au milieu aquatique (Baken et Adams, 2019; Blankers *et al.*, 2012). Certaines espèces (plus rares) sont uniquement retrouvées dans des grottes (Sket, 1997). Plusieurs caractéristiques

morphologiques et anatomiques diffèrent entre les salamandres qui vivent dans des habitats différents (Lauder et Shaffer, 1985; Lowe et Addis, 2019; Manenti *et al.*, 2009; Wake et Dresner, 1967). Certaines de ces différences sont associées à la locomotion (Deban et Marks, 2002; Lauder et Shaffer, 1988). Plusieurs espèces arboricoles, par exemple, présentent des adaptations au niveau des pattes afin de faciliter leurs déplacements dans la végétation (Hanna *et al.*, 2022; Huie *et al.*, 2025). Certaines espèces aquatiques à l'état adulte, comme le triton vert (*Notophthalmus viridescens*), sont associées à une queue élargie dorso-ventralement qui facilite la nage (Brossman *et al.*, 2013). D'autres différences morphologiques entre les espèces associées à des habitats différents sont quant à elles d'ordre plutôt sensoriel (Deban et Richardson, 2011; Durand, 1976; Hawes, 1945). Certaines salamandres vivant dans des grottes ont subi une réduction considérable de leurs capacités visuelles, comme le Protée anguillard (*Proteus anguinus*; Durand, 1976; Hawes, 1945). Chez d'autres vertébrés vivant de ce type d'habitat, ce genre de changement a été associé à une modification de la morphologie du tectum optique, zone du cerveau ayant un rôle important dans la vision (Jeffery, 2008; Yamamoto *et al.*, 2003). Chez les salamandres, d'autres types de différences morphologiques peuvent aussi être associées à l'alimentation, puisque le contraste entre certains types d'habitats peut impliquer des réseaux trophiques bien distincts (Wells, 2019).

2.3 La capture de proie

À l'âge adulte, les salamandres sont carnivores à l'exception de la sirène lacertine (*Siren lacertina*) qui a été documentée comme étant omnivore (Duellman et Trueb, 1994; Petranka, 1998; Pryor *et al.*, 2006; Wells, 2019). Malgré cette faible diversité de régimes alimentaires, il existe plusieurs types de préhension de proie au sein du groupe (Deban *et al.*, 1997; Reilly et Lauder, 1991; Wake *et al.*, 2000). Suivant les différents types de préhension de proie, il existe une variété intéressante de morphologie associée à l'appareil buccal (Lauder et Shaffer, 1985; Wake *et al.*, 2000). Les espèces qui s'alimentent en milieu aquatique vont habituellement procéder par succion en créant un courant d'eau vers l'intérieur de leur cavité

buccale (Lauder et Shaffer, 1985). Deux des modes de préhension les plus communs chez les espèces s'alimentant en milieu terrestre sont la protrusion linguale musculaire et la capture mandibulaire, dans lequel la salamandre se projette vers l'avant (avec ou sans la projection de la langue, respectivement) et capture la proie en refermant la bouche sur celle-ci (Wake *et al.*, 2000). Plusieurs espèces de la famille des Plethodontidae ont cependant développé un mode de préhension basé sur une projection balistique de la langue (Deban *et al.*, 2007; Deban et Richardson, 2011; Deban *et al.*, 2020; Deban *et al.*, 1997). Ces espèces possèdent des adaptions particulières associées à leur squelette hyoïdien, musculature faciale et leur langue elle-même (Deban *et al.*, 2007; Deban *et al.*, 2020), leur permettant une projection (parfois importante) de celle-ci. Ces espèces ont été rapportées comme utilisant de façon plus intensive leur vue durant la capture de leur proie (Deban *et al.*, 1997). Ainsi, il est possible que ces différences soient aussi associées à des modifications d'ordre cérébral.

2.4 L'allométrie

Les représentants actuels des amphibiens présentent une taille du corps bien inférieure (de manière générale) à celle des ancêtres de ce groupe de vertébrés (Gee, 2020; Schoch, 2013). Cela suggère que des changements allométriques importants ont eu lieu lors de l'évolution des amphibiens (Gee, 2020; Schoch, 2013). Chez les salamandres, la plus grande espèce vivante, la salamandre géante de Chine (*Andrias davidianus*), a une longueur moyenne d'environ 100 cm, avec des spécimens allant jusqu'à 180 cm, alors que les plus petites espèces (du genre *Thorius*) ont une taille adulte de seulement 2 cm (AmphibiaWeb, 2025). La miniaturisation de ces dernières a été associée à certaines particularités morphologiques et anatomiques : les espèces de petite taille de la famille des Plethodontidae sont connues pour avoir des yeux et un cerveau proportionnellement plus gros que la majorité des salamandres, ainsi qu'un crâne simplifié et un nombre réduit d'éléments squelettiques (Roth *et al.*, 1990; Roth et Schmidt, 1993). Elles sont aussi associées à une forme particulière de certaines régions du cerveau, influencées par les contraintes spatiales et développementales au sein du crâne (Roth *et al.*, 1990; Roth et Schmidt, 1993). Du côté opposé du gradient de

taille, le gigantisme des Cryptobranchidae s'accompagne d'un squelette crânien massif, d'os des membres particulièrement robustes et d'un schéma d'ossification et de croissance continu après la maturité sexuelle, caractéristiques mises en évidence par des études récentes de skeletogenèse crânienne et d'histologie osseuse chez les espèces du genre *Andrias* (Browne *et al.*, 2012; Fabre *et al.*, 2020; Fortuny *et al.*, 2015). Ces salamandres géantes occupent des rivières froides de montagne où elles agissent comme prédateurs de haut niveau trophique, avec une longévité pouvant dépasser plusieurs décennies, et un mode d'alimentation par succion (Fortuny *et al.*, 2015; Matsumoto *et al.*, 2024; Zhao, 1998). Dans l'ensemble, le contraste entre miniaturisation extrême et gigantisme au sein des salamandres offre un système modèle pour étudier comment les contraintes allométriques et développementales façonnent l'évolution conjointe de la taille du corps, du crâne et du cerveau.

3. LA DISPARITÉ MORPHOLOGIQUE

Dans l'étude de l'évolution morphologique, des outils quantitatifs comme la disparité morphologique permettent de caractériser et comparer la diversité des formes au sein d'un groupe taxonomique. Hopkins et Gerber (2017) ont montré que l'analyse de la disparité morphologique permet non seulement de mesurer l'étendue des formes explorées par un clade, mais aussi de mettre en lumière les trajectoires évolutives privilégiées ainsi que les zones du morpho-espace qui demeurent inoccupées. En caractérisant la dispersion des morphologies dans un espace de formes, la disparité constitue un outil puissant pour détecter des transitions évolutives majeures, telles que des épisodes d'innovation, de radiation adaptative ou encore des phases de simplification (Hopkins et Gerber, 2017). Cette approche peut permettre d'estimer l'influence relative des contraintes développementales et fonctionnelles, en mettant en évidence les structures anatomiques pour lesquelles l'évolution demeure canalisée par rapport à celles qui se diversifient plus rapidement (Hopkins et Gerber, 2017). Comparer la disparité entre clades ou entre ensembles anatomiques met en évidence des régimes évolutifs distincts, montrant que certaines régions du corps suivent des trajectoires fortement contraintes alors que d'autres présentent une grande plasticité. Dans le

cadre des salamandres, ces analyses ont offert un moyen d'identifier les traits les plus labiles, tels que la forme du crâne, la longueur des membres, la forme générale du corps ou l'architecture du cerveau, et de mieux comprendre comment les processus développementaux et écologiques ont façonné leur évolution (Bonett *et al.*, 2022; Fabre *et al.*, 2020; Roth et Walkowiak, 2015).

4. LES LIENS ENTRE LA MODULARITE ET LA DISPARITE MORPHOLOGIQUE

La modularité et la disparité morphologique entretiennent une relation étroite dans les processus évolutifs : la modularité favorise la diversification en permettant à certaines régions ou structures de varier indépendamment, tandis que l'intégration en canalise la variation vers des axes coordonnés (Claverie et Patek, 2013; Goswami et Polly, 2010). Dans le cas du cerveau et du crâne des salamandres, ces relations sont particulièrement pertinentes puisque les deux structures coévoluent sous l'influence de contraintes mécaniques et développementales (Roth *et al.*, 1997; Teng *et al.*, 2019). Différentes régions d'une même structure anatomique, comme les portions antérieure et postérieure du neurocrâne par exemple, peuvent réagir de manière distincte aux pressions sélectives associées à la locomotion, à la respiration ou aux perceptions sensorielles (Szostakiwskyj et Anderson, 2022; Watanabe *et al.*, 2021). Ces réponses différentielles peuvent générer une disparité morphologique propre à certaines zones, ce qui peut se refléter dans les patrons de covariation observés. L'étude conjointe de la modularité et de la disparité fournit un outil intéressant pour comprendre comment les processus développementaux et fonctionnels façonnent la trajectoire évolutive des structures morphologiques comme le cerveau.

5. PROBLEMATIQUE

La problématique de cette thèse s'inscrit dans un cadre théorique reliant deux modèles évolutifs de la morphologie du cerveau chez les vertébrés, soit le modèle concerté et mosaïque, à la lumière de propriétés fondamentales de l'organisation biologique que sont la modularité et l'intégration morphologique. Les modules correspondent à des groupes de traits

morphologiques quasi indépendants. Ces modules peuvent ainsi suivre des trajectoires développementales ou évolutives distinctes. Cette relative indépendance confère aux organismes une flexibilité évolutive accrue : la modularité représente ainsi une composante essentielle de l'évolvabilité, c'est-à-dire la capacité des systèmes biologiques à générer de la variation héréditaire et à s'adapter au fil du temps (Wagner et Altenberg, 1996). En somme, la combinaison de la modularité, de l'intégration morphologique et des modèles évolutifs du cerveau constitue une base essentielle pour explorer la remarquable disparification morphologique au sein des salamandres.

L'objectif principal de cette thèse est donc d'étudier l'influence des modèles d'évolution concertée et mosaïque du cerveau grâce au concept de modularité et d'intégration morphologique, et ce en utilisant les salamandres comme groupe modèle. Ce choix stratégique a été fait pour mieux comprendre les modalités de l'évolution du cerveau chez un groupe qui permet de faire certains parallèles avec des groupes éteints associés à un moment clé de l'évolution des vertébrés, soit la terrestrialisation.

Le modèle mosaïque de l'évolution du cerveau propose que les différentes régions cérébrales puissent suivre des trajectoires évolutives distinctes selon leurs fonctions, alors que le modèle concerté suggère que leur évolution est intégrée à celle du cerveau entier sous l'effet de contraintes développementales (Barton et Harvey, 2000 ; Finlay et Darlington, 1995). Chez plusieurs groupes de vertébrés, des études ont mis en évidence l'influence conjointe de ces deux modèles (Gutiérrez-Ibáñez et al., 2014; Hoops et al., 2017; Moore et DeVoogd, 2017). Ce travail vise à étudier ces concepts chez un groupe de vertébrés inférieurs afin de mieux comprendre l'influence des contraintes fonctionnelles et développementales sur l'évolution du cerveau chez un groupe non-amniote. Pour ce faire, la modularité et l'intégration morphologique seront utilisées afin de trouver des évidences de contraintes développementales et fonctionnelles, mais aussi d'évaluer si les patrons de covariation ontogénétique et interspécifique des régions du cerveau sont similaires ou non.

Les principales questions abordées dans cette thèse sont les suivantes. (1) Lors du développement, les régions du cerveau présentent-elles un patron de covariation

intraspécifique associé à des contraintes fonctionnelles et/ou développementales ? (2) Dans un contexte phylogénétique, les régions du cerveau présentent-elles un patron de covariation associé à des contraintes fonctionnelles et/ou développementales ? (3) Les patrons de covariation sont-ils similaires entre les échelles ontogénétiques et interspécifiques ? (4) Est-ce que des facteurs tels que l'allométrie, la phylogénie, les cycles de vie, les microhabitats et le mode de préhension de proie influencent l'évolution du cerveau chez les salamandres ? (5) Existe-t-il une relation entre la disparité et le taux d'évolution morphologique du cerveau chez les salamandres ?

6. OBJECTIFS DE RECHERCHE ET METHODOLOGIE

Cette thèse doctorale s'articulait autour de trois objectifs principaux. Le premier visait à décrire le patron de covariation au sein des régions du cerveau en développement d'une espèce de salamandre pour identifier l'importance des contraintes fonctionnelles et développementales. Le second avait pour but d'identifier la présence de contraintes fonctionnelles et développementales à partir du patron de covariation du cerveau chez plusieurs espèces de salamandres. Enfin, le troisième objectif visait à évaluer l'influence de facteurs allométriques, phylogénétiques, développementaux et écologiques sur l'évolution du cerveau des salamandres. Une présentation plus détaillée de ces objectifs, accompagnée d'une synthèse des approches méthodologiques employées pour les atteindre, est proposée dans les sections suivantes.

1er objectif : Décrire le patron de covariation au sein des régions du cerveau d'une espèce modèle de salamandre afin d'identifier la présence de contraintes fonctionnelles et/ou développementales, et ce durant l'ontogénie.

Ce premier objectif visait à détecter des évidences de l'influence des modèles concerté et mosaïque de l'évolution du cerveau au cours du développement d'une espèce modèle de salamandre, en se basant sur le patron de covariation morphologique. Pour ce faire, un échantillon de 77 larves d'axolotl mexicain (*Ambystoma mexicanum*), réparties en quatre stades de développement post-éclosion distincts, a été utilisé. La morphologie

tridimensionnelle du cerveau a été obtenue par microtomographie à rayons X avec amélioration de contraste, une méthode permettant de visualiser avec précision les structures internes de façon non invasive (Gignac et Kley, 2014).

L'analyse de la modularité et de l'intégration morphologique a ensuite servi à explorer la contribution relative des modèles mosaïque et concerté à la structuration du cerveau au cours du développement. Ces deux concepts ont été étudiés à l'aide de la morphométrie géométrique. Contrairement aux approches reposant sur des mesures de morphométrie classique (linéaires ou volumétriques), la morphométrie géométrique exploite les coordonnées cartésiennes de points, appelés points références (du terme anglais « landmarks »), positionnés à des emplacements homologues sur les structures morphologiques étudiées (Bookstein, 1996; Zelditch *et al.*, 2012). Cette méthode présente l'avantage majeur de conserver l'information géométrique complète de la structure, permettant ainsi une représentation multidimensionnelle efficace de la forme (Zelditch *et al.*, 2012). Elle maximise la quantité d'information morphologique analysée, en comparaison avec les méthodes basées sur des combinaisons de mesures linéaires ou de rapports simples (Zelditch *et al.*, 2012). Dans le cadre des analyses d'intégration morphologique, les points références sont considérés comme intégrés lorsqu'ils varient de manière corrélée, reflétant ainsi des interconnexions développementales ou fonctionnelles entre différentes parties des structures biologiques (Klingenberg, 2014; Klingenberg et Marugán-Lobón, 2013). Le signal de modularité, quant à lui, peut être estimé en mettant en relation le degré d'intégration à l'intérieur et à l'extérieur de différents groupes de points références prédéterminés (Klingenberg, 2014; Klingenberg *et al.*, 2001).

Pour évaluer et comparer les patrons d'intégration morphologique et de modularité, une série de six hypothèses *a priori* de modularité a été formulée. Ces hypothèses reposaient sur des divisions régionales proposées antérieurement dans la littérature (Redies et Puelles, 2001), et des divisions s'appuyant sur des informations issues du développement embryonnaire et des fonctions associées aux principales régions cérébrales (Butler et Hodos, 2005; Corfield *et al.*, 2015; Finlay et Darlington, 1995; Finlay *et al.*, 2001; Gonzalez-Voyer *et al.*, 2009; Yopak *et*

al., 2010). Afin d'évaluer la qualité d'ajustement de ces hypothèses aux données de forme, trois approches ont été mises en œuvre : la méthode du ratio de covariance développé par Adams (2016), la méthode des moindres carrés partiels (Adams, 2014b) et la méthode EMMLi proposée par Goswami et Finarelli (2016).

En complément des analyses de forme, des mesures volumétriques ont été utilisées pour examiner la taille relative des différentes régions cérébrales, fournissant ainsi une perspective intégrée sur la variation conjointe de la forme et du volume. Les relations allométriques entre le volume de chaque région et celui du reste du cerveau ont été évaluées à l'aide de régressions linéaires des moindres carrés ordinaires et de régressions segmentées. Cette approche a permis de caractériser les patrons d'allométrie des régions du cerveau au cours du développement larvaire de l'axolotl.

Cet objectif a également permis de réaliser une première description de certaines étapes du développement morphologique du cerveau de l'axolotl. En effet, aucune description détaillée des changements de forme des structures cérébrales au cours du premier mois suivant l'éclosion n'était disponible dans la littérature. Ce type de description peut s'avérer utile pour établir des liens entre la morphologie du cerveau et la maturation d'autres structures anatomiques durant les premières semaines de vie, une période considérée comme critique pour la survie de nombreuses espèces (Skelly et Kiesecker, 2001; Van Buskirk et Smith, 1991; Vonesh et De la Cruz, 2002).

2^{em} objectif : Étudier le patron de covariation au sein des régions du cerveau chez les salamandres afin d'identifier la présence de contraintes fonctionnelles et/ou développementales, selon une perspective phylogénétique.

Le deuxième objectif visait à évaluer le patron de covariation du cerveau au sein d'un échantillon d'espèces de salamandres, afin d'évaluer l'influence des modèles d'évolution concertée ou mosaïque, tout en tenant compte des effets de l'allométrie et de la phylogénie. La méthode de morphométrie géométrique a été utilisée sur les cerveaux de 76 espèces différentes afin d'étudier la modularité et l'intégration morphologique. Les représentations

en trois dimensions des cerveaux ont aussi été obtenues par microtomographie à rayons X avec amélioration de contraste. Un ensemble de sept hypothèses de modularité *a priori* ainsi que deux hypothèses *a posteriori* ont été utilisées pour analyser le patron de covariation du cerveau. Les données de points références ont permis de générer une variable de taille (appelée la taille du centroïde) qui a été utilisée dans les analyses sur l'allométrie évolutive. Cela a permis de décrire des changements morphologiques du cerveau associés à l'allométrie au sein des salamandres actuelles. La phylogénie de Jetz et Pyron (2018) a été utilisée pour considérer l'effet des liens de parenté entre les espèces.

De plus, l'endocaste a aussi été étudié avec la même méthode que le cerveau afin de comparer la covariation du cerveau à celui de l'endocaste. L'endocaste étant une structure particulièrement intéressante pour estimer la morphologie du cerveau chez de nombreux groupes éteints de vertébrés (Bertrand *et al.*, 2019; Challands *et al.*, 2020; Clement *et al.*, 2021; Early *et al.*, 2020; Weisbecker *et al.*, 2021), ce genre de résultats peut s'avérer utile pour mieux comprendre l'évolution du cerveau. La modularité et l'intégration morphologique de l'endocaste ont été étudiées en utilisant 11 hypothèses *a priori*. Ces hypothèses ont été établies afin de permettre la comparaison du signal de modularité avec les hypothèses testées pour le cerveau, mais aussi afin de tester des hypothèses plus spécifiques à des caractéristiques crâniennes.

3^{em} objectif : Évaluer l'influence de facteurs allométriques, phylogénétiques, développementaux et écologiques sur l'évolution du cerveau chez les salamandres.

Ce troisième objectif consistait à mettre en relation l'allométrie, la phylogénie, des stratégies développementales et des facteurs écologiques avec l'évolution du cerveau chez les salamandres. Plus précisément, l'objectif était de comprendre le degré d'influence de ces facteurs sur l'évolution du cerveau. Pour réaliser cet objectif, la méthode de morphométrie géométrique a été utilisée sur les cerveaux de 76 espèces de salamandres. Des analyses ont été réalisées en comparant la forme du cerveau selon des types de cycle de vie, de microhabitats et de langue. Pour chacun de ces trois facteurs, un type a été attribué pour chaque espèce. Cet objectif a également permis de comparer les taux d'évolution et la

disparité morphologique du cerveau entre des groupes basés sur leur type de cycle de vie, de microhabitat et de langue. Comme pour le deuxième objectif, l'endocaste a aussi été inclus dans les analyses. Cela a permis de tester si cette structure permet d'obtenir des conclusions similaires à celles du cerveau lors de l'étude des taux d'évolution et de la disparité. Cet objectif a également permis de décrire des changements morphologiques du cerveau entre des espèces appartenant à des microhabitats ou à des cycles de vie différents.

CHAPITRE 1
EXPLORER LE DEVELOPPEMENT LARVAIRE DU CERVEAU DE L'AXOLOTL : IMPLICATIONS SUR LES CONTRAINTES DEVELOPPEMENTALES ET FONCTIONNELLES

Laurent Houle[1], Olivier Larouche[2] and Richard Cloutier[1,3]

[1] Laboratoire de Paléontologie et Biologie évolutive, Université du Québec à Rimouski, 300 Allée des Ursulines, Rimouski, Quebec G5L 3A1, Canada

[2] Biology Department, Western Carolina University, I University Dr., Cullowhee, NC, 28723, United States

[3] Center of Excellence on the Evolution of Life, Basin Studies and Applied Paleontology; Paleontological Research and Education Center, Mahasarakham University, Maha Sarakham 44150, Thailand

Cet article, intitulé « *Exploring Larval Axolotl Brain Development: Insights into Developmental and Functional Constraints* », a été soumis (en révision) en 2025 dans la revue *Evolution & Development*. J'ai conçu l'étude et élaboré la méthodologie, récolté les données, analysé des données, produit les résultats et les figures, rédigé l'article, incluant la recherche bibliographique, et coordonné les révisions et commentaires des coauteurs. Olivier Larouche a contribué à l'analyse des données et à la production des résultats et des figures, et a révisé l'article. Richard Cloutier a initié le projet et financé les travaux de recherche, contribué à la conception de l'étude et de la méthodologie, contribué à l'analyse des données et a révisé l'article.

1.1 RESUME

L'évolution du cerveau chez les vertébrés a été conceptualisée selon deux hypothèses principales : les modèles d'évolution mosaïque et concertée. Le modèle mosaïque propose que les structures cérébrales soient principalement façonnées par des contraintes fonctionnelles, tandis que le modèle concerté met l'accent sur le rôle des contraintes développementales. Les objectifs de cette étude étaient (1) de décrire les variations de forme et de volume du cerveau au cours du développement larvaire de l'axolotl mexicain (*Ambystoma mexicanum*), et (2) d'identifier les contraintes fonctionnelles et développementales pouvant intervenir durant la maturation cérébrale post-éclosion. Au total, 77 larves réparties en quatre stades de développement ont été analysées à l'aide de la morphométrie géométrique 3D et de mesures volumétriques dérivées d'imageries micro-CT avec augmentation du contraste via l'iode. Afin de caractériser les relations entre les différentes régions du cerveau, nous avons utilisé des analyses d'intégration morphologique et de modularité, fournissant ainsi une évaluation poussée des changements dans les patrons de covariation au cours du développement post-éclosion. Nos résultats montrent que la limite entre le télencéphale et le diencéphale ainsi que la région de l'hypothalamus présentent un faible niveau de variation morphologique durant la période étudiée. Cette stabilité pourrait influencer la formation de la suture coronale, un élément clé de la morphogenèse du crâne chez les tétrapodes. À l'inverse, les structures sensorielles subissent des modifications importantes. Les bulbes olfactifs et le mésencéphale présentent une croissance allométrique positive au début du développement post-éclosion, suivie d'une croissance isométrique à des stades plus tardifs. Ces transitions suggèrent une importance précoce des régions cérébrales liées aux fonctions sensorielles, possiblement sous l'influence de contraintes fonctionnelles. Les résultats révèlent également une correspondance générale entre le volume des régions cérébrales et le volume cérébral total, ce qui concorde avec le modèle concerté. Les analyses de modularité, d'intégration morphologique et de volumes indiquent qu'un ensemble de contraintes fonctionnelles et développementales pourrait conjointement façonner le développement du cerveau chez l'axolotl.

Mots clés : *Ambystoma mexicanum*, ontogénie, neurobiologie, modularité, intégration

1.2 ABSTRACT

Brain evolution in vertebrates has been conceptualized through two major hypotheses: the mosaic and concerted evolution models. The mosaic evolution model suggests that brain structures are primarily shaped by functional constraints, whereas the concerted evolution model emphasizes the role of developmental constraints. Our objectives in this study were (1) to describe brain shape and volume changes during Mexican axolotl (Ambystoma mexicanum) larvae development, and (2) to identify possible functional and developmental constraints during post-hatching brain maturation. A total of 77 larvae, spanning four developmental stages, were examined using 3D geometric morphometrics and volumetric measurements derived from iodine micro-CT imaging. To understand the relationships among brain regions, we employed morphological integration and modularity analyses, providing a comprehensive assessment of changes in shape covariation patterns during post-hatching development. Our results reveal that the telencephalon-diencephalon boundary and hypothalamus region exhibit a low level of morphological variation throughout larval development. This stability may influence the positioning of the coronal suture, a key feature in tetrapod skull morphogenesis. In contrast, sensory structures undergo significant changes. The olfactory bulbs and optic tectum display positive allometric growth during early post-hatching development, transitioning to isometric growth at later stages. These shifts suggest an early developmental emphasis on sensory related brain areas, potentially driven by functional constraints. Results revealed a general correspondence between brain region volume and total brain volume, which aligns with the concerted model. Modular, morphological integration and volumetric analyses suggest that an interplay of functional and developmental constraints might be involved in axolotl brain development.

Keywords: *Ambystoma mexicanum*, ontogeny, neurobiology, modularity, integration

1.3 INTRODUCTION

Two main hypotheses have been proposed to explain the evolution of vertebrate brains: the mosaic and concerted evolution models. The mosaic model suggests that individual brain regions can evolve independently, with morphological differences driven by adaptive divergence in function and selective pressures (Barton and Harvey, 2000). In contrast, the concerted model suggests that the brain evolves as an integrated unit, shaped primarily by global developmental constraints such as the timing and duration of neurogenesis (Finlay *et al.*, 2001). To detect the influence of these models, many studies have relied on how brain regions scale with total brain size, using allometric relationships between regional and whole-brain volumes (e.g., Finlay and Darlington, 1995; Finlay *et al.*, 2001; Gonzalez-Voyer *et al.*, 2009; Gutiérrez-Ibáñez *et al.*, 2014; Montgomery *et al.*, 2016). Under a concerted model, brain regions are expected to follow shared scaling trends with total brain size, reflecting strong developmental integration, whereas mosaic evolution is inferred when particular regions deviate from these trends or show patterns of co-variation that are independent of overall brain size (Barton and Harvey, 2000; Gutiérrez-Ibáñez *et al.*, 2014; Schumacher and Carlson, 2022). These two hypotheses are not mutually exclusive, and their respective contributions on brain structure variation remains debated (Barton and Harvey, 2000; D'Aniello *et al.*, 2019; Willemet, 2020). While several studies support the mosaic evolution model across diverse vertebrate groups (Barton and Harvey, 2000; Gómez-Robles *et al.*, 2014; Gonzalez-Voyer *et al.*, 2009), others find stronger evidence for the concerted evolution (Dumitru and Frugård Opdal, 2024; Finlay *et al.*, 2001; Stearns, 2018). In amphibians, both models were found to be involved in the evolution of brain size in anurans (Liao *et al.*, 2015). While these two evolutionary models have been mostly conducted at a macroevolutionary scale, intraspecific analyses using shape and volume variation should also be useful, given that part of the macroevolutionary patterns of covariation may arise from intraspecific variation.

Several authors have observed a general trend of complexification of brain structure throughout vertebrate evolution (Hodos, 1988; Hofman, 1982; Jerison, 2012). However,

some groups like amphibians, coelacanths and lungfishes exhibit relatively simple brain morphologies (Dutel *et al.*, 2019; Northcutt, 1986; Roth *et al.*, 1993). Salamanders, in particular, retain a Bauplan similar to early tetrapods and thus can increase our understanding of the complex processes underlying vertebrate evolution (Bonett *et al.*, 2022; Kawano *et al.*, 2024; Schwarz *et al.*, 2023). Among salamanders, the Mexican axolotl (*Ambystoma mexicanum*) is considered as a valuable model species (Bölük *et al.*, 2022; Vieira *et al.*, 2020; Voss *et al.*, 2009). Numerous studies have used axolotls as a model to address developmental and evolutionary questions (Denis *et al.*, 2013; Hincapie *et al.*, 2022; Malacinski, 1978), including many focused on brain structure and development (Amamoto *et al.*, 2016; Feng *et al.*, 2023; Fritzsch *et al.*, 2005). A key biological feature of the axolotl is its paedomorphosis, whereby individuals retain larval characteristics throughout life due to a failure to undergo metamorphosis (Gould, 1977; Shaffer, 1993). This condition is tightly linked to extremely low circulating levels of thyroid hormones (TH; Brown and Cai, 2007), which are major regulators of vertebrate brain development, neurogenesis, and neural differentiation (Tata, 2006). Because TH play a central role in orchestrating early brain maturation in most vertebrates (Mourouzis *et al.*, 2020), the persistent TH deficiency in axolotls provides a unique context in which to examine brain development in the relative absence of typical endocrine triggers. Although some salamander groups, particularly plethodontids, have been associated with secondary brain simplification, this pattern is not observed in the axolotl (Roth *et al.*, 1997), which retains functional and developmental features comparable to those of other vertebrates (Maddin *et al.*, 2016; Roth and Walkowiak, 2015).

The vertebrate brain is a complex organ that exhibits considerable disparity in shape and size and has been associated with the diversification of several vertebrate lineages (Balanoff *et al.*, 2016; Barton *et al.*, 1995; Pollen *et al.*, 2007). Comparative analyses demonstrate that brain regions can be linked to organismal functions critical for survival (Gonzalez-Voyer *et al.*, 2016; Nieuwenhuys *et al.*, 2014; Striedter, 2005). For example, in taxa highly reliant on visual and olfactory sensory information, such as sharks (Yopak and Lisney, 2012) and insectivorous mammals (Barton *et al.*, 1995), typically exhibit enlarged optic tecta and olfactory bulbs (Jerison, 2012). Conversely, primates and marine mammals display a

disproportionately enlarged telencephalon and cerebellum, associated with complex cognitive functions (Jerison, 2012). Even intraspecifically, the relative size and shape of brain regions can also change during ontogeny in response to specific physiological and environmental demands. These changes can include drastic morphological changes, such as those occurring during metamorphosis or even seasonal variations (Kollros, 1981; Lázaro *et al.*, 2018; Yaskin, 2011). Such great versatility of shape and highlights the importance of studying the morphological evolution of the brain.

This study has two main objectives: (1) to describe patterns of post hatching morphological development of the brain of *A. mexicanum* larvae, and (2) to examine if the variation of the shapes and relative volumes of brain regions could suggest an effect of functional and developmental constraints on developing brain regions. To address these objectives, we combine geometric morphometrics analyses with volumetric measurements (Slice, 2007; Zelditch *et al.*, 2012). Geometric morphometrics provides a powerful statistical framework to capture complex shape variation, quantify relative size differences, and assess morphological integration and modularity (Zelditch *et al.*, 2012). Morphological integration refers to the strength of correlations among morphological traits, whereas modularity describes the tendency of organism to be subdivided into partially independent groups of traits called modules (Olson and Miller, 1958). These two concepts have also been linked to detecting the relative influence of the concerted and mosaic models: high modularity is generally interpreted as support for the mosaic model (Gómez-Robles *et al.*, 2014), whereas strong morphological integration is more consistent with the concerted model (Gómez-Robles *et al.*, 2014; Mitteroecker and Bookstein, 2008). Quantifying morphological integration and modularity patterns promote a better understanding of morphological evolution and development since it allows a deep investigation of the covariation among sets of morphological regions. Our first hypothesis was that brain morphology undergoes its greatest changes immediately after hatching, before stabilizing during later development. For the second hypothesis, we expected that both functional and developmental constraints contribute to the development of the axolotl brain, which would be consistent with patterns observed in other vertebrates (Moore and DeVoogd, 2017; Noreikiene *et al.*, 2015).

1.4 MATERIAL & METHODS

1.4.1 Sample and husbandry

We analysed 80 post-hatching larvae of *A. mexicanum* collected at four developmental stages (47, 50, 52, 54; Nye *et al.* (2003)). All larvae originated from a single clutch (one male and one female leucistic adults) produced at Carleton University (Ottawa, Canada) under Canadian Council on Animal Care protocol #102951. Adults were obtained from the *Ambystoma* Genetic Stock Center (University of Kentucky, USA). One adult specimen was included as representative of the adult brain shape and volume conditions (University of Calgary Animal Care Committee protocol AC15-0020).

Eggs were incubated at 18°C in a 40% Holtfreter's solution. After hatching, larvae were reared in 20% Holtfreter's at 19°C under a 12:12 light:dark cycle and fed daily (baby brine shrimp, later bloodworms). Individuals were isolated at forelimb bud formation to prevent injury owing to limb bud biting behavior and to ensure accurate staging. Once in their individual compartments, the specimens were fed a diet of blood worms once per day. Specimens were staged daily using the Bordzilovskaya *et al.* (1989) and Nye *et al.* (2003) normal tables of development. Four developmental stages were selected: 47, 50, 52 and 54 according to Nye *et al.* (2003). These stages were selected to cover most of the first month of free foraging larval period and the beginning of the ossification of the skull roof. A sample of 20 specimens were euthanized on the same day for each stage using a 4% tricaine methanesulfonate (MS-222) solution (Sigma-Aldrich E10521, St. Louis, MO) buffered using sodium bicarbonate (pH of 7.1).

Specimens were fixed in a 4% neutral-buffered formalin (Thermo Fisher Scientific SF1004, Waltham, MA) solution for 4 hours. After fixation, larvae were washed in distilled water and, dehydrated gradually using 15%, 30%, and 50% (2 hours in each solution) ethanol solutions, and then stored in 70% ethanol. Among the specimens that were euthanized, three (one from stage 50 and two from stage 52) were removed from downstream analyses because

their brains appeared to be damaged due to handling (Table 1.1). The adult specimen was euthanized in 5% MS-222; the specimen was kept in the solution until cardiac activity ceased entirely (approx. 1h), and was then fixed in 10% neutral-buffered formalin for 24h.

Table 1.1 Description of the developmental stages and corresponding days post-hatching for *A. mexicanum* larvae included in the sample.

Developmental stage (Nye *et al.*, 2003)	Day post hatching	Sample size for analyses
47	10	20
50	16	19
52	22	18
54	28	20
Adult	-	1

1.4.2 Staining and imaging procedures

All larvae were stained in a solution composed of 0.3% phosphotungstic acid (PTA) and 70% ethanol following Metscher (2009). The adult specimen was stained in an 11.75% iodine solution (I_2KI) for five days. Specimens were scanned using a Bruker Skyscan 1173 at a resolution of 8.1 μm. For all the scans of larvae, the exposure time was usually 1325 ms, the voltage and current were set at 77 kV and 79 μA, respectively. The reconstruction of images was done using the NRecon software (Bruker Corporation).

The segmentation of the brains was performed using the Dragonfly software v.2022.2 (Dragonfly 2022.2). A standardisation of the grayscale domain of each image was performed to eliminate high greyscale domain variation across images of each specimen (gradient domain fusion filter in Dragonfly). A deep learning model was created to help the

segmentation process. The model had a U-Net architecture using a 2.5D method (adjusting segmentation using the two previous and next images), five layers and 112 pixels starting squares. The model was trained using between 10 and 50 images per specimen from various areas of the brain. The first draft of the segmentation process was produced by the model. Each image was then manually adjusted by the same observer (LH). The region of interest from the segmentation process was converted in a 3D surface mesh and then smoothed to reduce imperfections (Laplacian smoothing).

1.4.3 Geometric morphometrics

A sample of 28 fixed landmarks, 26 curve semilandmarks and 127 surface semilandmarks were used to capture the shape information of the brain (Figure 1.1, Table A1). The landmarks were placed using the Checkpoint software (Stratovan Corporation). All shape analyses were performed in R (v.4.4.3; R Core Team, 2024). An automated procedure was used to apply surface semilandmarks on meshes using the placePatch function in the "Morpho" package v.2.12 (Schlager, 2017). We used the findMeanSpec function from the "geomorph" package v.4.0.8 (Baken *et al.*, 2021) to identify the specimen closest to the mean shape, which was then selected as the atlas for automatic surface semilandmark placement. A generalized Procrustes analysis was performed on the landmark coordinates in order to control for differences in scaling, orientation and positioning of the configurations of landmarks (Rohlf and Slice, 1990).

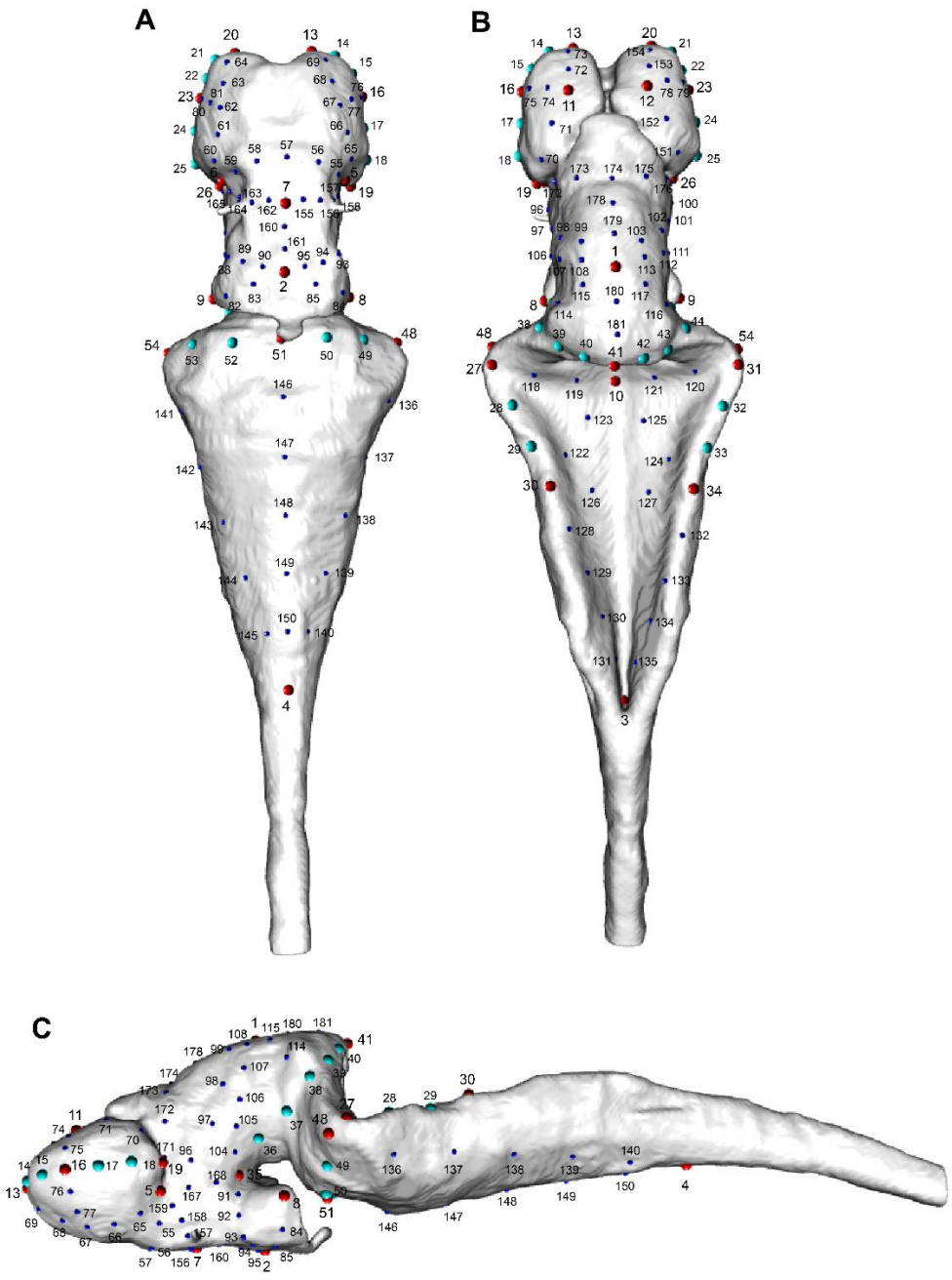

Figure 1.1 Ventral (A), dorsal (B) and lateral (C) views of the landmarks placed on the brain of *A. mexicanum* larvae. Large red spheres represent fixed landmarks, large cyan spheres represent curve semilandmarks, and small dark blue spheres represent surface semilandmarks.

A fluctuating asymmetry analysis was performed to quantify and exclude the shape changes resulting from bilateral asymmetry in the data (Klingenberg *et al.*, 2002). To assess

repeatability of morphometrics data collection, measurement error was calculated following the method developed by Collyer and Adams (2024) using the measurement.error function from the "RRPP" package v.2.0.4 (Collyer and Adams, 2019). The total measurement error represented 5.6% of the entire shape variation, and 94.3% of this amount represented random measurement error. Systematic measurement error was not significant ($R^2 = 0.0007$, $Z = -0.271$, $p = 0.612$), and was not significantly different among developmental stages ($R^2 = 0.003$, $Z = 1.54$, $p = 0.072$). The variation associated with measurement error was removed from the shape data using the fluctuating asymmetry analysis.

A Procrustes ANCOVA was used to examine the influence of (log) centroid size and developmental stages on the symmetrical component of shape variation, as well as to examine the interaction between the two independent variables. A Procrustes linear regression was performed to examine whether shape variation is influenced by size variation (Collyer *et al.*, 2015). Three-dimensional deformation grids comparing stages were used to interpret size-related shape changes. Since the effect of size on shape was significant and substantial ($F_{1,77} = 56.738$, $Z = 3.472$, $R^2 = 0.612$, $P = 0.001$), two datasets were generated, one that preserves the effect of size on shape, and one that controls for allometry. For the latter shape dataset, the residuals from the Procrustes linear regression between shape and size were added to the consensus shape.

Principal component analyses (PCA) were performed to compare the morphospace occupation of developmental stages while including or excluding the effect of size. Three-dimensional deformation grids were used to investigate shape changes along the principal components. Procrustes distance histograms were performed to evaluate if the variation among stages was associated with higher or lower Procrustes distances than the one within each stage. Procrustes ANOVAs and pairwise comparisons were used to investigate shape differences among developmental stages for both datasets (i.e., with and without the effect of size on shape). Pairwise comparisons were made for the Procrustes distances among mean shape and for the variance among stages using the pairwise function from the "RRPP" package v.2.0.4 (Collyer and Adams, 2019).

1.4.4 Volumetric measurements

The brain of each specimen was numerically dissected into six morphological partitions (olfactory bulbs, telencephalon, hypothalamus, thalamus, mesencephalon, and rhombencephalon) using the Dragonfly software v.2022.2 (Dragonfly 2022.2). The limits of each partition followed Lazcano *et al.* (2021). Specifically, the end of the telencephalon lobes was used an anatomical landmark to separate the telencephalon and hypothalamus (Figure A1). The anterior end of the lateral ventricle was used as the delineation between the olfactory bulb and the rest of the telencephalon (Figure A1). The diencephalic-mesencephalic boundary was taken to be where the hypothalamus separates from the rest of the brain (slightly anterior to the delineation between the hypothalamus ventralis and dorsalis; Figure A1). The posterior end of the rhombencephalon was considered to be at the closure of the medulla oblongata. The volume of each partition was measured using the labeled voxels of the region of interest in Dragonfly.

The statistical methods applied to the volumetric data consisted of three main analyses: (1) allometric regressions of brain region volumes, (2) mean $\log_{10}$-shape ratio (LSR) comparisons, and (3) a volumetric data PCA. A model selection approach was used to produce a regression model between the volume of each brain region and the total brain volume minus the volume of that specific region. Both ordinary least squares (OLS) and piecewise regressions were computed for each brain region. Piecewise regressions consist in a model composed of several (two or more) linear regressions associated with different segments of data (Muggeo, 2003). The best model was selected based on the results of an extra sum of squares F-test between the OLS and the piecewise model for each brain region. Akaike Information Criterion (AIC) values were also considered in the model selection. Assumptions for the linear regression were assessed visually. The piecewise models were produced using the "segmented" package v.2.1-3 (Fasola *et al.*, 2018). This approach allowed for an investigation of the possible negative or positive allometric growth of individual brain regions, and to examine possible allometric shifts during development (Kilmer and Rodríguez, 2017). A LSR standardisation was also applied to the volume data (Mosimann,

1970) to compare the relative volume of brain regions among developmental stages. This approach involves calculating a ratio between the volume of each individual region and the geometric mean across all volumes, and then applying a logarithmic transformation to this ratio (Mosimann, 1970). A permutation one-way ANOVA and permutation pairwise t tests were performed for each volume partition to test if there was a difference of the volume LSR among developmental stages. A Bonferroni correction was applied to the *p* values of the permutation pairwise *t*-tests. A PCA was performed on the LSR data to verify if shape and volume data were correlated. To test the fit between brain shape and volume PCA scores, a Mantel test was used between each of the shape datasets (including and excluding the effect of size on shape) scores and the volume PCA scores using the "vegan" package v.2.6-6.1 (Oksanen, 2016).

1.4.5 Morphological integration and modularity analyses

The datasets with and without allometric effects on shape were both analyzed for patterns of morphological integration and modularity. Individuals from different developmental stages were analysed separately. We compared six different *a priori* modularity hypotheses (Table 1.2, Annexe B). The signal of modularity was estimated using the covariance ratio (CR) method (Adams, 2016) and the maximum-likelihood approach (EMMLi v.0.0.3) developed by Goswami and Finarelli (2016). The CR coefficient represents the ratio between the covariances among modules and the within module covariances based on covariance matrices over all specimens and associated with variables of each module (Adams, 2016). To assess the strength of modular signal, the observed value is compared to a distribution of random CR values (null hypothesis; Adams, 2016). An effect size was also estimated, where increasingly negative values correspond to a stronger modular signal (Adams and Collyer, 2019). The effect size can also be used in pairwise comparisons to determine if the strength of modularity differ statistically among hypotheses (Adams and Collyer, 2019). This method was performed using the modularity.test and compare.CR functions from the "geomorph" package v.4.0.8 (Baken *et al.*, 2021). The EMMLi analysis, a maximum likelihood-based method, compares correlation coefficients between and within

modules and estimates a model $\log_{10}$ likelihood for each hypothesis (Goswami and Finarelli, 2016). To select the most supported hypothesis, EMMLi uses the corrected Akaike Information Criterion (AICc; Goswami and Finarelli, 2016). Using this method, the hypothesis with the lowest AIC would represent the best supported model (Goswami and Finarelli, 2016). This method also tests if the within module correlations are equal or unequal across all modules considered in a hypothesis, as well as if the between modules correlations are equal or unequal (Goswami and Finarelli, 2016). Consequently, four models are compared for each hypothesis of three or more modules, while two models are compared for a two modules hypothesis (Goswami and Finarelli, 2016).

Table 1.2 Name and description of hypotheses used in modularity analyses on *A. mexicanum* larvae. Brackets delimit hypothesized modules.

Hypothesis	**Description**	**Number of modules**	
Hypothesis 1	[Dorsal landmarks] and [ventral landmarks]	2	
Hypothesis 2	[Forebrain + hindbrain] and [midbrain]	2	
Hypothesis 3	[Forebrain], [midbrain], and [hindbrain]	3	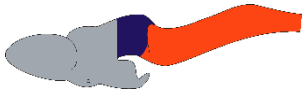
Hypothesis 4	[Telencephalon], [diencephalon], [mesencephalon], and [rhombencephalon]	4	

Hypothesis 5	[Olfactory bulbs], [telencephalon], [diencephalon], [mesencephalon], and [rhombencephalon]	5	
Hypothesis 6	[Olfactory bulbs], [telencephalon], [hypothalamus], [thalamus], [mesencephalon], and [rhombencephalon]	6	

All morphological integration analyses were implemented using the "geomorph" package v.4.0.8 (Baken *et al.*, 2021). To assess the level of morphological integration for each modularity hypothesis, partial least-squares analyses were performed (integration.test function; Collyer *et al.*, 2015). Using this method, a low PLS value represent a low level of inter-module integration (Collyer *et al.*, 2015). In addition, regressions between the variance of partial warps and their associated bending energy (globalIntegration function) were produced to assess the strength of integration of the shape of each developmental stage (Bookstein, 2015). The relative eigenvalue index (Vrel) was also used to compare the level of integration among developmental stages using their associated effect size (Conaway and Adams, 2022).

1.5 RESULTS

1.5.1 Description of shape and volume changes in post hatching axolotls

The centroid size of brain coordinates had a significant effect on shape and accounted for 61.2% of the total variation ($F_{1,75}$ = 38.439, Z = 5.469, R^2 = 0.612, P = 0.001). This substantial effect can mostly be attributed to the divergence between stage 47 and the three other stages (Figure 1.2). The Procrustes ANCOVA showed that there were no significant

differences among slopes for the four developmental stages concerning the relationship between brain shape and centroid size ($F_{3,69} = 1.258$, $Z = 1.302$, $R^2 = 0.019$, $P = 0.092$).

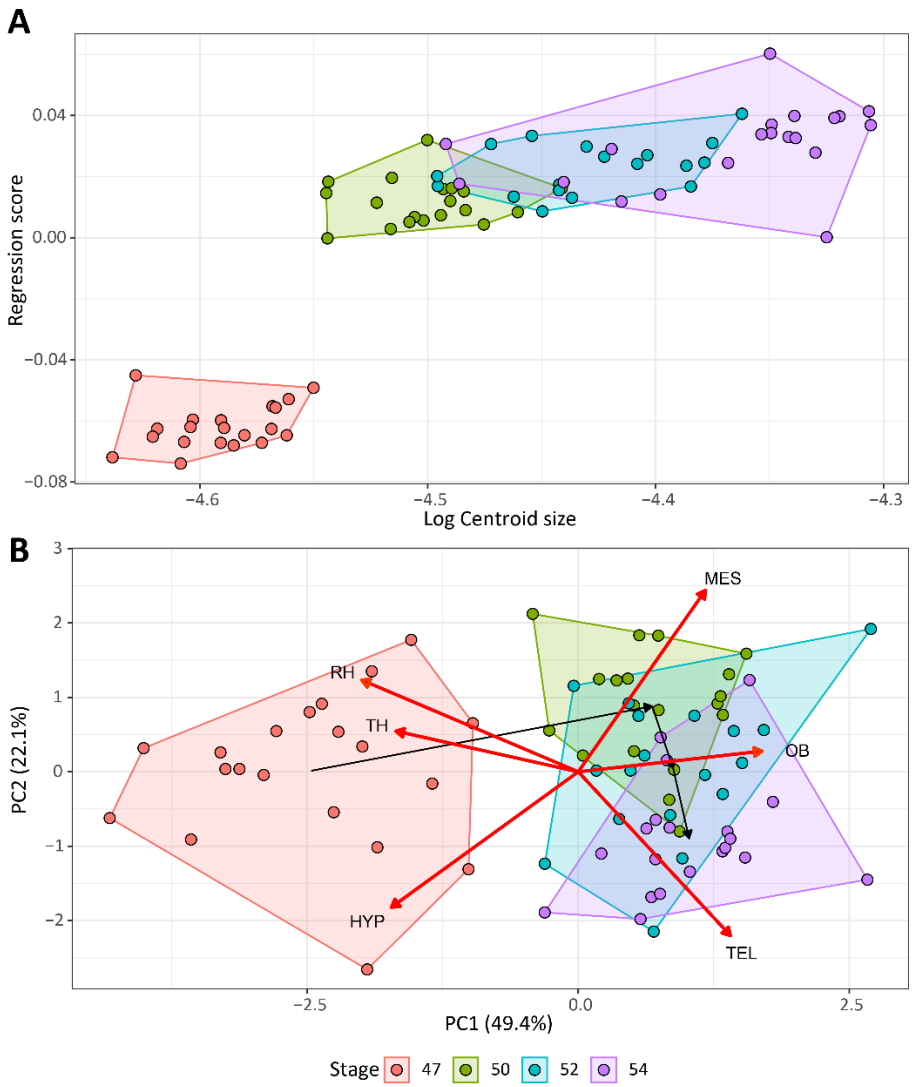

Figure 1.2 Regression analysis of 3D brain shape (regression scores) against log10-centroid size (A) and volumetric data PCA (B) showing differences among four developmental stages (polygons) of *A. mexicanum* larvae. Red arrows in plot B represent loadings of volumetric data. OB, olfactory bulbs. TEL, telencephalon. HYP, hypothalamus. TH, thalamus. MES, mesencephalon. RH, rhombencephalon. Percentages of explained variation are provided in parentheses for each PCA axis.

For the dataset including allometry, the PCA and Procrustes ANOVA showed a visible difference between stage 47 and the other stages, and also differences, albeit of a

smaller magnitude, among stages 50, 52 and 54 (Figure 1.3 and Table A2). The Procrustes variance among developmental stages did not significantly differ (Table A2). The Procrustes distance histogram shows that the within stage variation is composed of mostly small distances, while the among stages variation consist of a wide range from small to large distances (Figure A2). This diversity of small and large Procrustes distances might reflect the substantial divergence between stages 47 and 50, and the much smaller differences observed among the other stages (Figure 1.3). These differences account for most of the explained variation of the first principal component of the shape PCA (Figure 1.3). The shape deformation associated with the transition from stage 47 to 50 is similar to the size-related shape changes observed from the shape allometric regression (Figure A3 and A4). These changes consist of an elongation of the olfactory bulbs, a ventral depression of the mesencephalon, and an anterior and lateral constriction of the medulla oblongata (Figure 1.3, Figure A4). This last region also shows a dorsal elevation of its posterior end. From stage 50 to 52, shape changes are similar to those from stage 47 to 50, but with a much smaller magnitude (Figure A4). The transition between stage 52 and 54 is mostly associated with the posterior retraction of the ventral section of the medulla oblongata (Figure A4). Using the dataset where the effect of size on shape is removed, the patterns observed in the deformation grids are similar, but with lower magnitudes (Figure A5). Developmental stages still explain 25.2% of the total variation, and there is still no significant difference in Procrustes variance across stages (Table A3).

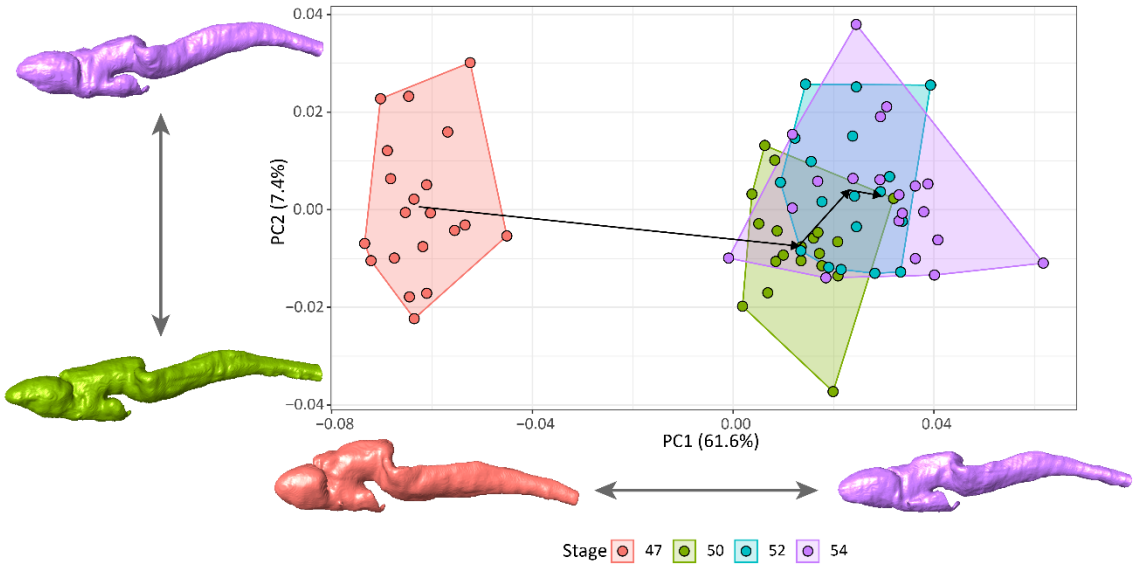

Figure 1.3 Size-included shape data PCA showing differences among four developmental stages (polygons) of *A. mexicanum* larvae. Brain meshes illustrate the shapes at the positive and negative extremes of each principal component axis. OB, olfactory bulbs. TEL, telencephalon. HYP, hypothalamus. TH, thalamus. MES, mesencephalon. RH, rhombencephalon. Percentages of explained variation are provided in parentheses for each PCA axis.

The Mantel tests showed that volume PCA was correlated with both the dataset including allometry ($P < 0.001$, $r = 0.665$) and the one excluding allometry ($P < 0.001$, $r = 0.265$). Both the volume PCA and mean LSR values indicated that stage 47 was substantially different than other developmental stages (Figure 1.2 and 1.4). Volume LSR of stage 47 for all partitions differed significantly from the three other stages (Figure 1.4). Stage 47 was associated with a small relative volume for the olfactory bulbs, telencephalon and mesencephalon, and large volumes for the hypothalamus, thalamus and rhombencephalon (Figure 1.4). From stage 47 to 50, the volume of brain regions exhibited drastic changes: the olfactory bulbs and mesencephalon increased in relative volume while the volumes of the hypothalamus, thalamus and rhombencephalon decreased (Figure 1.4). From stage 50 to 54, the volume of the olfactory bulbs, the thalamus, hypothalamus and rhombencephalon did not differ significantly (Figure 1.4). During that same period, the telencephalon progressively increases in relative size (Figure 1.4) while the volume of the mesencephalon finally decreases at stage 54 (Figure 1.4). A decrease in the relative volume of the thalamus,

hypothalamus, mesencephalon, and rhombencephalon, along with an increase in the relative volume of the olfactory bulbs and telencephalon, is observed when comparing stage 54 to adult data.

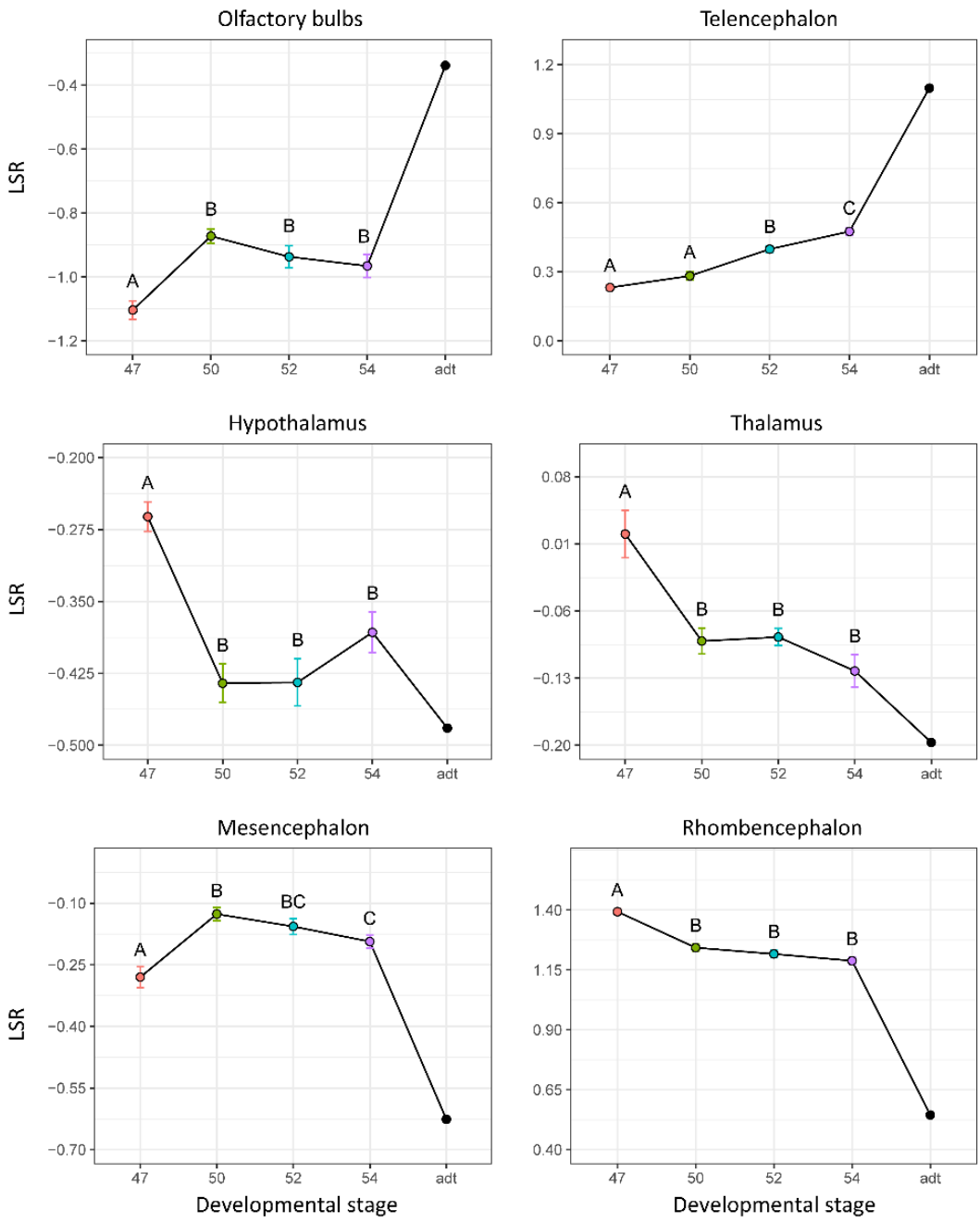

Figure 1.4 Comparison of the mean log10-shape ratio (LSR) of six volume partitions of the brain of *A. mexicanum* larvae across four developmental stages (Stages 47, 50, 52, and 54)

and one adult specimen (adt). Error bars represent the standard error and letters refer to permutation pairwise t-tests results.

1.5.2 Investigating support for a mosaic or concerted evolution of brain regions

Allometric regressions of volumetric measurements (Table A4) indicated that the olfactory bulbs, thalamus and mesencephalon are associated with allometric shifts with a breakpoint approximately at stage 50 (Figure 1.5 and Table A5). Stage 47 is associated specifically with a positive allometric growth for the olfactory bulbs and the mesencephalon and a negative allometric growth for the thalamus. The telencephalon exhibits positive allometry while the hypothalamus and rhombencephalon grew at a lower rate than the rest of the brain (Figure 1.5 and Table A5). While differences among brain regions are present, the predictive capability of linear models were generally strong (R^2 value ranging from 0.777 to 0.922; Table A5).

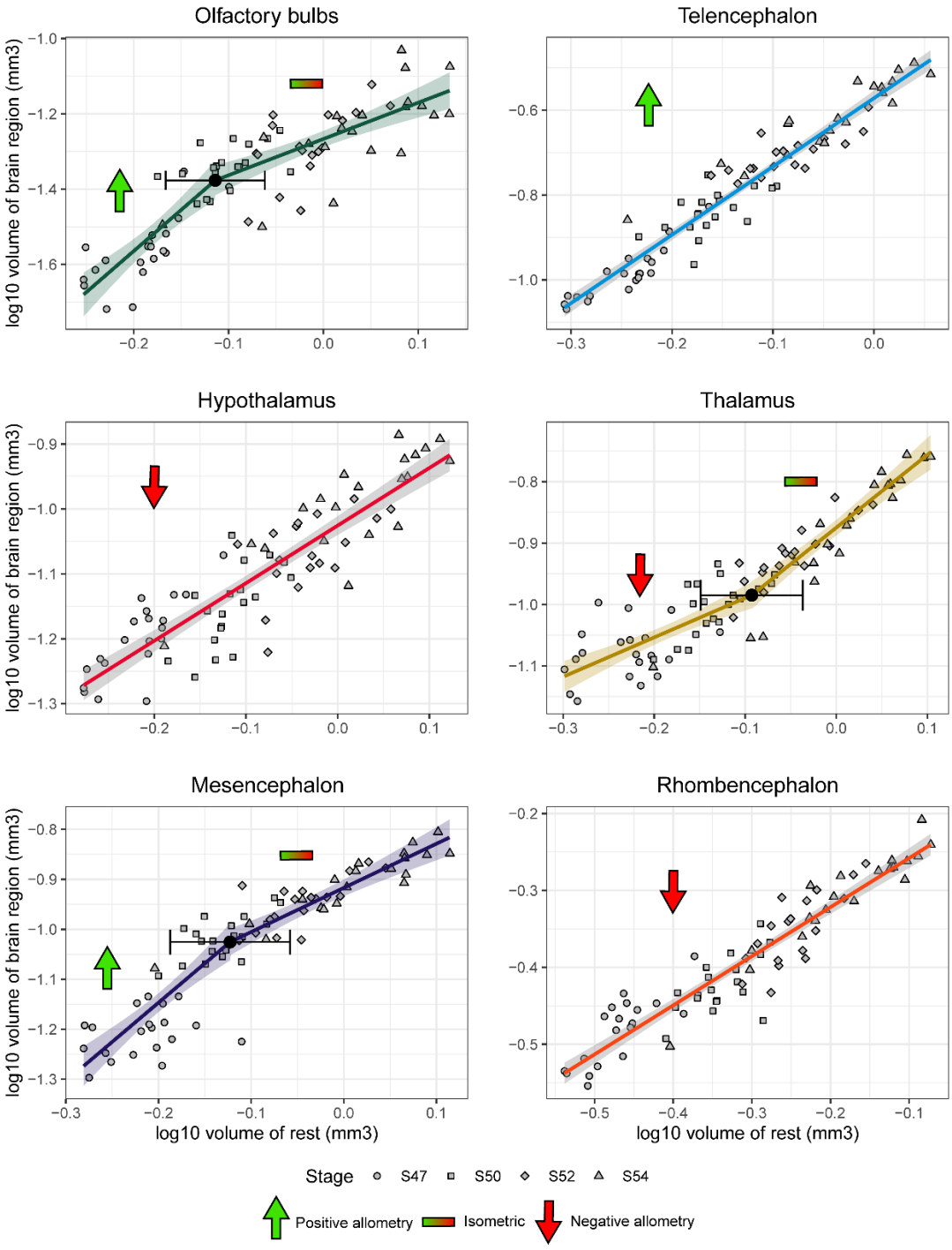

Figure 1.5 Best supported regression model comparing the volume of each brain region with the total volume of the brain minus the volume of the region (log_{10} transformation applied to x and y) for *A. mexicanum* larvae. Shaded areas represent the 95% confidence interval of

each regression line. Black dots indicate a breakpoint in the regression model and the error bars represent its 95% confidence interval.

The results of modular analyses for the datasets including and excluding allometry reported the same general conclusions. Therefore, only the results associated with the shape dataset controlling for allometry are presented in the main text (see Table A11 for the allometry included results). The best-supported hypotheses using the covariance ratio method on all larvae were hypotheses four, five, and six, which all showed similarly strong modular signals with effect sizes ranging from –8.5 to –8.9, whereas hypotheses one, two, and three exhibited much weaker values, between –3 and –5 (Table 1.3). The differences among these three hypotheses were associated with the separation of the olfactory bulb from the rest of the telencephalon between Hypotheses 4 and 5, and the separation of the thalamus and hypothalamus for Hypotheses 5 and 6. Specific investigation of CR values across modules of these three hypotheses revealed that the hypothalamus is systematically less integrated to other modules (Figure 1.6 and Figure A6). This may be linked to the lack of shape variation associated with this region. The olfactory bulb, when considered as a separate module, seems to be generally more integrated than the rest of the telencephalon with other modules (Figure A6).

Table 1.3 Results of morphological integration analyses using partial least squares (PLS) and modularity analyses using the covariance ratio (CR) for the six a priori hypotheses for the brain of *A. mexicanum* larvae. Hypotheses are described in Table 1.2.

	CR method			**Morphological integration**		
Hypothesis	**CR**	**P-value**	**Z**	**PLS**	**P-value**	**Z**
1	0.901	0.002	-3.934	0.923	0.001	4.304
2	0.886	0.001	-5.341	0.900	0.001	5.276
3	0.878	0.001	-5.769	0.917	0.001	8.519
4	0.816	0.001	-8.540	0.885	0.001	9.509

5	0.796	0.001	-8.872	0.887	0.001	7.096
6	0.776	0.001	-8.736	0.847	0.001	7.041

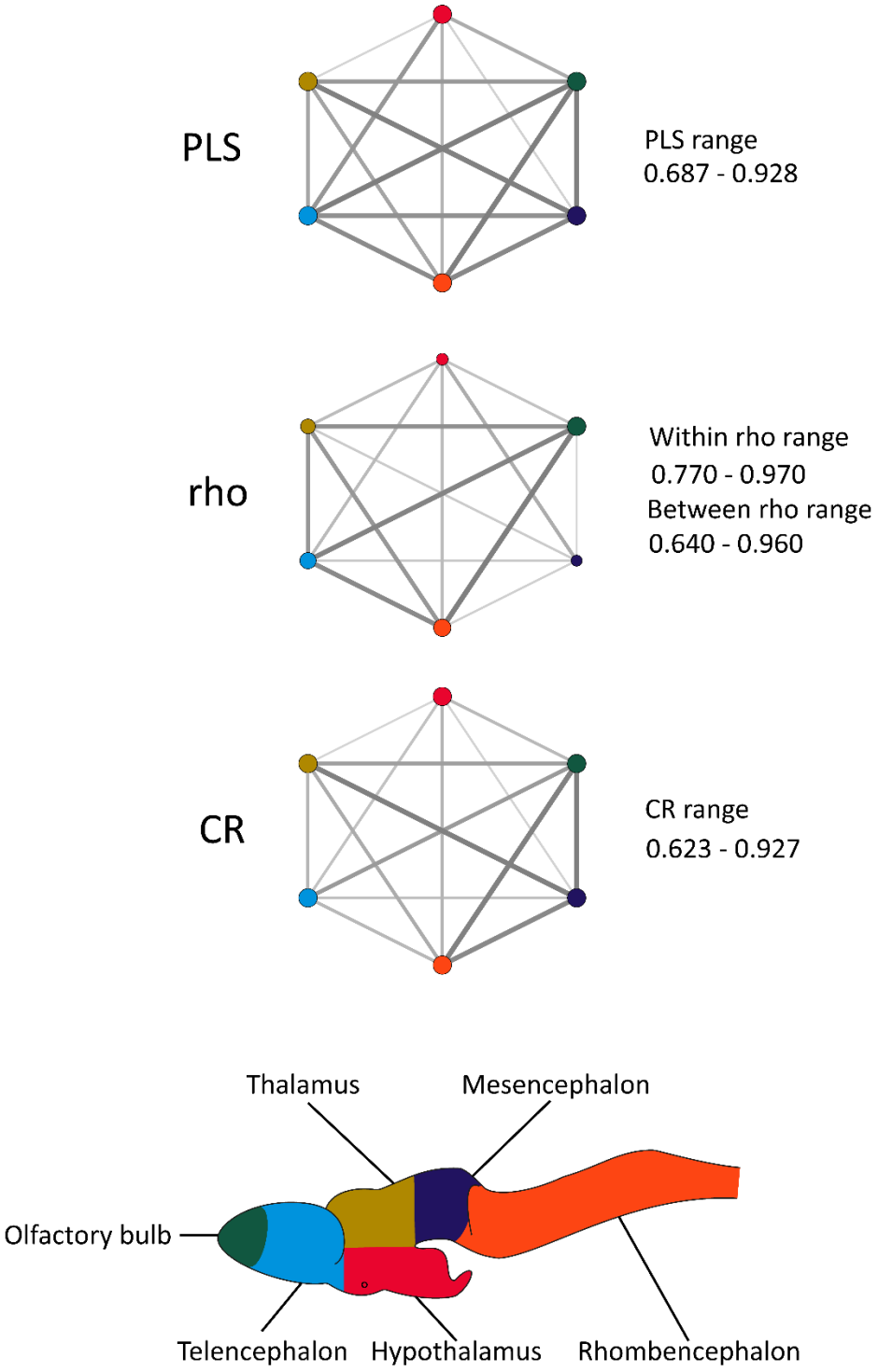

Figure 1.6 Network representations of the strength of morphological integration from the covariance ratio (CR), the EMMLi (rho) and the partial least squares (PLS) analyses for the brain shape of *A. mexicanum* larvae. Edge width in each network represents the strength of

the association between two modules. Note that the edge width is based on values within each analysis (i.e., not directly comparable between networks). For the EMMLi analysis, the edge width represents the correlation between two modules and the size of nodes represents the relative within module correlation.

Using the EMMLi analysis, Hypothesis 6 was the best-supported hypothesis (with variations observed in the strength of correlations both within and between modules) since it presented the lowest AIC value of all tested models (Table 1.4). This indicates that correlation strengths are not uniform across all modules (within correlations) or between module pairs (between correlations) in Hypothesis 6. The evaluation of these correlations for Hypothesis 6 revealed a somewhat different pattern compared to the CR method. The hypothalamus is less correlated with other modules, but the mesencephalon also exhibits this pattern (Figure 1.6). In this analysis, the olfactory bulbs showed strong correlations with the telencephalon, thalamus, and rhombencephalon, whereas correlations between the olfactory bulbs and the hypothalamus remained weak (Figure 1.6). The hypothalamus stands out as being the least integrated region using both the EMMLi and CR methods (Figure 1.6).

Table 1.4 Results of modularity hypotheses comparison using the EMMLi methods for the six *a priori* hypotheses for the brain of *A. mexicanum* larvae. Hypotheses are described in Table 1.2.

Hypothesis	K	AICc	ΔAICc
1	4	833281.941	130544.140
2	4	885704.137	182966.335
3	7	809423.868	106686.066
4	11	732786.505	30048.703
5	16	724795.690	22057.889
6	22	702737.802	0.000

Taken individually, each developmental stage exhibited significant modular signal using the CR approach (Table A6). While Hypothesis 1 was significantly different than hypotheses with more complex modular organisation (such as Hypotheses 4, 5 and 6), nonsignificant results were found among other hypotheses (Table A7). This may be related to a lack of statistical power owing to insufficient sample sizes for each developmental stage. Hypothesis 6 was best supported by the EMMLi analyses for every developmental stage (Table A6). These results seem to indicate that the modular signal was strong, and that the modularity pattern is generally conserved among developmental stages.

Concerning morphological integration, the brain shape of *A. mexicanum* larvae can be considered as disintegrated (slopes between -1 and 0) following Bookstein (2015) concept (Table A8). In this context, disintegration can be interpreted as a major contribution from small-scale variation on the brain shape, whereas integration would be associated to a major contribution from large-scale variation. Stage 47 is the least integrated developmental stage (Table A8). The pairwise PLS analyses indicate an intermediate level of integration among brain regions (Table 1.3). The level of morphological integration estimated using the relative eigenvalue index does not vary significantly among developmental stages (Table A9). Pairwise comparisons of PLS effect sizes among hypotheses revealed that hypotheses 3, 4, 5 and 6 had a significantly lower level of inter-module integration than hypothesis 1 and 2 (Table A10). These results in association with the similar Procrustes variance comparison indicates that the level of morphological integration appears to be fairly constant among developmental stages.

1.6 DISCUSSION

This study combines analyses of shape and volumetric data to characterize brain development of axolotl larvae across four developmental stages. Our results show that the shape and relative volumes of brain regions change during development, providing insights into the relationship between these observed brain patterns and skull development. Additionally, our analyses of modularity and morphological integration, combined with

volumetric analyses, suggest that patterns of morphological variation in the brains of post-hatching axolotl support both the mosaic and concerted model of evolution of the brain.

1.6.1 Evidence for the role of developmental constraints

The vertebrate skull roof consists of bones originating from different embryonic tissues, and although the contributing tissues vary among lineages, their proper arrangement depends on signaling centers that may be conserved across vertebrates (Maddin *et al.*, 2016; Teng *et al.*, 2019). In axolotls, the pattern of cranial neural crest (CNC) contributions to the bony skull is similar of that observed in amniotes (Piekarski *et al.*, 2014). Specifically, the neurocranium of amniotes and axolotls shows a distinct separation at the coronal suture, with CNC-derived bony structures located anteriorly, and non-CNC-derived bony structures positioned posteriorly (Maddin *et al.*, 2016; Piekarski *et al.*, 2014). In amniotes, the boundary between the telencephalon and diencephalon (near the optic chiasm) has been suggested as a key determinant of the frontoparietal suture location (Teng *et al.*, 2019). Our findings on the relative shape and volume stability of the hypothalamus region are consistent with observations in squamates after mid-stage development (Ollonen *et al.*, 2024). These results may support the hypothesis that this region plays a role in determining the location of the frontoparietal suture in tetrapods (Atkins *et al.*, 2020), as these two paired bones begin to ossify between stages 47 and 50 of Nye *et al.* (2003) ‘s table. This interpretation is consistent with the growing evidence that embryonic brain signaling centers play a crucial role in guiding suture formation (Teng *et al.*, 2019). However, further work on suture specification cues is needed to better understand the dynamics of the coronal suture formation and the role of the telencephalon-diencephalon boundary.

1.6.2 Evidence for the role of functional constraints

The olfactory and visual systems have been revealed as highly important in feeding success in amphibian larvae (Rot-Nikcevic *et al.*, 2005). The larval period is also a moment of rearrangement and maturation of several visual, olfactory and vomeronasal structures

(Cuny and Malacinski, 1986; Eisthen, 2000; Eisthen *et al.*, 1994). Early hatched predatory larvae, such as the axolotl, use several sensory mechanisms for foraging and sensing predators (Różański and Żuwała, 2020). The axolotl eyes are well developed at hatching, but the lens and the retina are associated with several modifications until the late juvenile phase (Cuny and Malacinski, 1986). Rearrangement of olfactory structures are also observed in salamander larvae (Eisthen, 2000; Eisthen *et al.*, 1994; Różański and Żuwała, 2020). Such reorganization might also be associated with brain morphological variation. For instance, visual experience in fishes has been associated with the relative size of the optic tectum (Hall and Tropepe, 2018; Soares *et al.*, 2005). In our results, olfactory bulbs and the mesencephalon (including the optic tectum) seem to exhibit a similar relative volumetric growth in post-hatching axolotls with a positive allometry in stage 47 followed by an isometric growth in later stages. Notably, among all brain regions, only the mesencephalon showed positive allometric growth during the developmental period examined, while also being characterized by a smaller relative volume in adults. This might be the result of a stronger investment in sensory system related structures in the early free-swimming larval life. Therefore, the differential growth of the optic tectum and olfactory bulbs may be influenced by visual and olfactory input acting as a functional constraint. Furthermore, the specific grouping of regions recovered in the best-supported modularity hypothesis highlights that certain sensory structures tend to covary more closely with one another, consistent with their shared roles in early larval behavior and sensory processing. The strong correlations identified by the EMMLi analysis between the olfactory bulbs and the telencephalon, thalamus, and rhombencephalon may reflect early integration among sensory-processing regions involved in odor detection, sensory evaluation, and foraging-related behaviors (Butler and Hodos, 2005). In contrast, the weak correlation between the olfactory bulbs and the hypothalamus could suggest that interoceptive or valence-related pathways may not yet be strongly integrated at these early developmental stages, or that these connections mature later in ontogeny.

1.6.3 Morphological integration and modularity patterns support both the concerted and mosaic models

Morphological integration is generally viewed as supporting the concerted model of brain evolution (Gómez-Robles *et al.*, 2014; Mitteroecker and Bookstein, 2008), whereas high modularity is typically interpreted as evidence for the mosaic model (Gómez-Robles *et al.*, 2014). Both the mosaic and concerted models have been proposed to explain vertebrate brain evolution in vertebrates (Gutiérrez-Ibáñez *et al.*, 2014; Hoops *et al.*, 2017; Moore and DeVoogd, 2017). For instance, Watanabe *et al.* (2021) found both integrated and modular patterns shaping the evolution of the brain of avian and non-avian coelurosaurians. Evidence supporting the mosaic model has been observed in specific contexts and vertebrate groups (Barton and Harvey, 2000; Gómez-Robles *et al.*, 2014; Hager *et al.*, 2012). For example, in teleosts, observed mosaic changes of specific brain regions associated with electrosensory systems were considered as support for independent size changes related to functional constraints (Schumacher and Carlson, 2022). The modular organisation of the brain has been suggested to promote mosaic evolution in chimpanzees and humans (Gómez-Robles *et al.*, 2014). Studies of salamander skulls have revealed high levels of modularity (Bon *et al.*, 2020; Fabre *et al.*, 2020), which is consistent with some of our observations in the axolotl brain. Our results indicate that visual and olfactory demands are associated with patterns of brain shape and volume, and the high level of modularity observed further suggests that mosaic processes may contributed to axolotl brain evolution.

Our results also provide evidence consistent with the concerted model. Although volumetric analyses revealed distinct regional trends, brain region volumes still generally scale with overall brain size. Additionally, while the brain shape does show limited support for global integration, the brain still exhibits a fair amount of integration among modules (Figure 1.6). These results suggest that developmental constraints may be affecting all brain regions, lending some support for the concerted model.

In conclusion, our study provides new insights into the brain development of axolotl larvae, highlighting significant changes in brain shape and volume between stages 47 and 50.

Our results suggest that both developmental and functional constraints might play a role in the developing brain of axolotls. Additionally, the stability of the telencephalon-diencephalon boundary and hypothalamus volume throughout development may influence the positioning of the frontoparietal suture, as proposed in other tetrapods. These findings underscore the interplay of evolutionary and developmental factors in shaping brain and skull development in vertebrates. However, future studies might expand the developmental sequence of brain change to allow a more comprehensive understanding of the morphological variation in the developing brain of salamanders.

1.7 ACKNOWLEDGMENTS

We thank Hillary Maddin for donating axolotl specimens, as well as Jade Atkins, Alanna Cantelon, and Bassel Arnaout for helping us with husbandry, fixation, and with other parts of the preparation of the experimental protocol. This work was funded by grants from the Natural Sciences and Engineering Research Council of Canada (NSERC) and the Fonds de recherche du Québec – Nature et technologies (FRQNT).

CHAPITRE 2
MODULARITE ET INTEGRATION MORPHOLOGIQUE DU CERVEAU ET DE L'ENDOCASTE CHEZ LES CAUDATA

Laurent Houle[1], Olivier Larouche[2] and Richard Cloutier[1,3]

[1] Laboratoire de Paléontologie et Biologie évolutive, Université du Québec à Rimouski, 300 Allée des Ursulines, Rimouski, Quebec G5L 3A1, Canada

[2] Biology Department, Western Carolina University, 1 University Dr., Cullowhee, NC, 28723, United States

[3] Center of Excellence on the Evolution of Life, Basin Studies and Applied Paleontology; Paleontological Research and Education Center, Mahasarakham University, Maha Sarakham 44150, Thailand

Cet article, intitulé « *Modularity and Morphological Integration of the Brain and Endocast of Caudata* », a été soumis (en révision) en 2026 dans la revue *Evolutionary Biology*. J'ai conçu l'étude et élaboré la méthodologie, récolté les données, analysé des données, produit les résultats et les figures, rédigé l'article, incluant la recherche bibliographique, et coordonné les révisions et commentaires des coauteurs. Olivier Larouche a contribué à l'analyse des données et à la production des résultats et des figures, et a révisé l'article. Richard Cloutier a initié le projet et financé les travaux de recherche, contribué à la conception de l'étude et de la méthodologie, contribué à l'analyse des données et a révisé l'article.

2.1 RESUME

Les modèles concerté et mosaïque de l'évolution du cerveau formulent des prédictions contrastées quant à la manière dont les régions cérébrales covarient au cours du temps, mais ces prédictions sont rarement évaluées conjointement pour le cerveau et les endocastes crâniens, qui constituent le principal proxy neuroanatomique utile pour les fossiles. Le modèle concerté met l'accent sur des changements coordonnés et liés à la taille entre les régions cérébrales, tandis que le modèle mosaïque prédit des adaptations régionales spécifiques dictées par des contraintes fonctionnelles. Les amphibiens, en particulier les salamandres, représentent un système comparatif pertinent pour étudier l'évolution du cerveau chez les tétrapodes en raison de leur combinaison de traits aquatiques et terrestres. Nous avons quantifié la variation de forme, la modularité et l'intégration morphologique du cerveau et de l'endocaste chez 83 spécimens représentant 76 espèces de salamandres couvrant les dix familles de Caudata, à l'aide de la morphométrie géométrique et de méthodes comparatives phylogénétiques. Nous avons évalué le rôle de l'allométrie évolutive, des contraintes développementales et fonctionnelles, ainsi que des relations phylogénétiques dans la structuration de ces structures morphologiques. Les formes du cerveau et de l'endocaste présentent des patrons allométriques marqués, ainsi qu'une modularité significative associée à des niveaux intermédiaires d'intégration entre modules, globalement compatibles avec des effets de proximité spatiale. Les contraintes fonctionnelles semblent également influencer les patrons de covariation observés au niveau du bulbe olfactif, du mésencéphale et du rhombencéphale. Nos résultats indiquent que des processus à la fois concertés et mosaïques contribuent à l'évolution du cerveau et de l'endocaste chez les salamandres. Bien que le cerveau et l'endocaste présentent un signal phylogénétique significatif, la faible concordance entre les patrons observés au niveau du cerveau et de l'endocaste suggère que ce dernier ne reflète que partiellement la structure phylogénétique associée au cerveau. Si les régions antérieures et postérieures montrent une forte correspondance cerveau-endocaste, les analyses de modularité révèlent un découplage au niveau du mésencéphale. Dans l'ensemble, ces résultats soutiennent un scénario évolutif mixte et indiquent que les endocastes des salamandres constituent des proxies informatifs mais régionalement variables de la morphologie cérébrale.

Mots clés : Amphibiens, Salamandres, Morphométrie géométrique, Neuroanatomie, Neurocrâne, Signal phylogénétique, Allométrie évolutive, Modularité, Intégration morphologique

2.2 ABSTRACT

The concerted and mosaic models of brain evolution make contrasting predictions about how brain regions covary through time, yet these predictions are rarely evaluated jointly for brains and cranial endocasts, the primary neuroanatomical proxy available for fossils. The concerted model emphasizes coordinated, size-related changes across brain regions, whereas the mosaic model predicts region-specific adaptations driven by functional demands. Amphibians, particularly salamanders, provide a valuable comparative system for investigating tetrapod brain evolution owing to their combination of aquatic and terrestrial traits. We quantified 3D shape variation, modularity, and morphological integration of the brain and endocast across 83 specimens representing 76 salamander species from all ten caudate families using geometric morphometrics and phylogenetic comparative methods. We assessed the roles of evolutionary allometry, developmental and functional constraints, and phylogenetic relationships in shaping these systems. Brain and endocast shapes exhibited allometric patterns, as well as significant modularity with intermediate levels of inter-module integration, broadly consistent with effects of spatial proximity. Functional constraints likely influence covariation in the olfactory bulb, mesencephalon, and rhombencephalon. Our results indicate that both concerted and mosaic processes contribute to salamander brain and endocast evolution. Although both systems showed significant phylogenetic signal, low concordance between brain- and endocast-level patterns suggests that endocasts only partially reflect the underlying phylogenetic structure of the brain. While anterior and posterior regions showed strong brain-endocast correspondence, modularity analyses revealed decoupling in the midbrain. Our findings support a mixed evolutionary scenario and indicate that salamander endocasts are informative but regionally variable proxies for salamander brain morphology.

Keywords: Amphibians, Salamanders, Geometric morphometrics, Neuroanatomy, Neurocranium, Phylogenetic signal, Evolutionary allometry, Modularity, Morphological integration

2.3 INTRODUCTION

The evolution of brain regions in vertebrates is an interesting topic in evolutionary biology. Concerning the morphological evolution of the brain, two major hypotheses are opposed: the concerted and mosaic models. For the concerted evolution model, developmental constraints are proposed to play a dominant role in vertebrate brain evolution (Finlay *et al.*, 2001). According to this hypothesis, brain regions would likely evolve in a coordinated fashion and total brain size would be the determinant in predicting the size of individual brain regions (Finlay *et al.*, 2001). On the other hand, the mosaic model suggest that functional constraints should be predominantly implicated in shaping brain evolution (Barton and Harvey, 2000). Brain regions with a shared function should then be more likely to co-evolve with one another almost independently from regions associated with different functions (Barton and Harvey, 2000). These models represent opposite ends of a continuum between developmental and functional influences and are not mutually exclusive. Several authors have found support for both hypotheses in various vertebrate groups, including anurans (Liao *et al.*, 2015), birds (Gutiérrez-Ibáñez *et al.*, 2014; Moore and DeVoogd, 2017) and squamates (Hoops *et al.*, 2017). This pattern is also evident in hominins, particularly within the genus *Homo*, where studies on both development and evolution have shown strong integration among brain regions, reinforcing the importance of coordinated developmental processes in brain evolution (de Sousa et al., 2023; Sansalone et al., 2023). Evaluating these models across broad evolutionary scales, however, requires access to brain morphological information across both extant and extinct taxa. Because neural tissues are rarely preserved in the fossil record, cranial endocasts are commonly used as proxies for brain morphology, allowing comparative and macroevolutionary analyses to be extended deep into vertebrate history (Challands *et al.*, 2020; Clement *et al.*, 2021; Clement *et al.*, 2015; Jerison, 2012).

Extant amphibians (lissamphibians) have been instrumental to our understanding of the brain-endocast relationship in early tetrapods (Clement *et al.*, 2021) as well as in some extinct amphibians (Dempster, 1935; Romer and Edinger, 1942). Due to their intermediate position between aquatic and terrestrial lifeforms, amphibians provide a perspective on the transition

from water to land. In terms of locomotion, habitat preference, and overall morphological traits, salamanders in particular have been, to some extent, regarded as suitable modern analogs for extinct groups of significant evolutionary relevance, including early tetrapods (Clement *et al.*, 2021). Their relatively conservative body plan and versatile locomotor abilities make them especially useful in comparative studies of functional anatomy and evolutionary transitions (Barclay, 1946; Ijspeert *et al.*, 2007; O'Reilly *et al.*, 2000; Wassersug, 1989; Zamora-Camacho, 2023). Considering the brain, salamanders have been proposed to present secondary simplification that may complement current knowledge of brain structure in other groups (Roth *et al.*, 1993; Roth *et al.*, 1997; Roth *et al.*, 1990). This secondary simplification refers to the observed simplicity of brain morphology and organization when considering the phylogenetic position of salamanders (Roth *et al.*, 1997). This simplicity contrasts with the general trend of increasing complexity observed across vertebrate brain evolution. Thus, salamanders may provide additional insights and help consolidate our understanding of brain evolution in tetrapods.

A useful tool for studying brain morphology in both extinct and extant species is the analysis of the endocranial space; the cavity within the neurocranium in which the brain is housed (Macrini, 2006). Many authors have used the cranial endocast (henceforth to be referred to as the endocast) as a proxy of brain shape in fossils of several vertebrate groups (Allemand *et al.*, 2023; Bertrand *et al.*, 2019; Early *et al.*, 2020; Romer and Edinger, 1942; Weisbecker *et al.*, 2021). Although direct evidence of soft tissue is rarely preserved in fossils, analyzing endocasts can allow inferences concerning the relative size and organisation of major brain regions, facilitating comparisons between extinct and extant species (Allemand *et al.*, 2023; Early *et al.*, 2020). This approach can help reconstruct the history of brain structure and evolution, assess changes in sensory and cognitive capabilities, and test hypotheses about the relationship between brain morphology and ecological or behavioral traits in deep time. The endocast has been recognized as a reliable proxy for brain morphology in several vertebrate groups, including birds (Early *et al.*, 2020) and mammals (Jerison, 2012; Macrini *et al.*, 2007). However, in other taxa, such as certain fish, endocast shape does not fully reflect brain morphology (Challands *et al.*, 2020; Dutel *et al.*, 2019). In salamanders, this relationship

appears to be only partially reliable: in some species like the mudpuppy, the endocast provides a poor approximation of brain morphology, while in others it captures more anatomical detail (Romer and Edinger, 1942). Challands *et al.* (2020) reported for two species of salamanders (*Ambystoma mexicanum* and *Cynops sp.*) that some regions of the endocast correspond more closely to the brain than others; for example, the mesencephalon tends to show a weaker fit. These findings on a few species highlight the need to assess whether, in general, the endocast is a reliable morphological proxy for the brain in a larger sample of salamanders.

The relationship between brain and endocast is deeply rooted in development. Several regions of the tetrapod brain have been proposed as signaling centers involved in the formation of specific cranial sutures. For instance, in birds, Schowing (1968) demonstrated that removal of the midbrain–hindbrain border resulted in the loss of the parietal bone, suggesting that particular brain regions may be critical for the development and spatial arrangement of neurocranial bones. More recently, Fabbri *et al.* (2017) examined skull morphology across a sample of reptiles and birds and showed that the frontal bone consistently overlies the forebrain, whereas the parietal bone is positioned above the midbrain. Comparable patterns have been reported in mammals, where the coronal suture typically aligns with the mid-region of the forebrain (Blümel *et al.*, 2019), approximately corresponding to the telencephalon–diencephalon boundary and the location of the pineal gland during development (Sood, 1980). This correspondence is further supported by molecular evidence from mouse models, which indicates that the coronal suture aligns with the telencephalon–diencephalon boundary (Deckelbaum *et al.*, 2012). The telencephalon–diencephalon border (or telencephalon-midbrain in squamates) has been proposed to be implicated in the formation of the coronal suture in several tetrapod taxa (Ollonen *et al.*, 2024; Teng *et al.*, 2019). Although the exact mechanisms by which these brain-derived signals influence skull roof development remain largely unknown, evidence of a conserved spatial relationship between the telencephalon–midbrain border and the coronal suture in squamates provides some support for this developmental link (Ollonen *et al.*, 2024).

The influence of allometry on the evolution of amphibian skull morphology has been documented in several studies (Bardua *et al.*, 2021; Bardua *et al.*, 2019; Sherratt *et al.*, 2014). In anurans, the oticooccipital region has been identified as one of the most strongly affected by size variation (Bardua *et al.*, 2021). Based on these patterns, Bardua *et al.* (2021) proposed an amphibian cranial evolutionary allometry (ACREA) model, suggesting that increases in body size led to wider skulls, instead of the facial elongation typically observed in mammals under the progressive preoptic preponderance (Robb, 1935) or craniofacial evolutionary allometry (Cardini *et al.*, 2015; Cardini and Polly, 2013). However, this pattern might be less pronounced in salamanders, for which skull shape evolution does not show a strong allometric signal (Fabre *et al.*, 2020). In addition to influencing the skull, body size also affects brain structure in amphibians. In anurans, relative proportions of brain regions vary predictably with overall brain size (Liao *et al.*, 2015), while in plethodontid salamanders, miniaturization has been associated with shifts in both brain region proportions and neuronal organization (Roth *et al.*, 1997; Roth *et al.*, 1990). Notably, *Thorius* species exhibit an increased relative brain and eye volume compared to larger plethodontids, highlighting the complex neuroanatomical consequences of extreme size reduction (Roth *et al.*, 1990). This suggests that allometric constraints might be important in shaping the amphibian brain evolution.

To analyze these complex anatomical relationships with greater precision, recent advances in imaging and morphometric methods have proven invaluable. The recent advent of geometric morphometrics, along with the growing accessibility of micro-CT imaging, has significantly transformed the fields of evolutionary biology (Adams *et al.*, 2004; Boerckel *et al.*, 2014; Brainerd *et al.*, 2010; Gignac and Kley, 2014; Heimel *et al.*, 2019; Mitteroecker and Gunz, 2009; Richtsmeier *et al.*, 2002; van Rietbergen *et al.*, 1995). Geometric morphometrics is a useful quantitative method that uses homologous anatomical points (known as landmarks) to capture and analyze the shape of biological structures (Zelditch *et al.*, 2012). By focusing on spatial relationships between these landmarks, this approach provides a detailed and statistically robust representation of morphological variation (Zelditch *et al.*, 2012). Unlike traditional linear morphometric techniques, geometric

morphometrics captures the geometry of entire forms, allowing the precise visualization and quantification of shape differences (Zelditch *et al.*, 2012). When combined with high-resolution 3D imaging technologies such as micro-CT, this method enables the study of complex anatomical structures, such as the brain and the corresponding endocast, permitting new insights into evolutionary patterns, developmental processes, and functional adaptations.

Geometric morphometrics also facilitates the investigation of broader evolutionary concepts such as modularity and morphological integration. These concepts describe how shape variation is structured among different morphological traits. Modularity refers to the tendency of certain groups of morphological traits to form semi-independent units, or modules, that can vary somewhat independently from other parts of the organism (Klingenberg, 2008; Wagner, 1996). In contrast, morphological integration reflects the degree of coordinated variation among traits (Olson and Miller, 1958). A higher level of integration indicates stronger relationships among the shape changes of different structures. Exploring modularity and integration can help identify evolutionary pathways, shedding light on how specific traits have diversified or remained conserved across lineages.

In this study, we analyzed the 3D shape of the brain and endocast in 76 salamander species by means of geometric morphometrics to investigate patterns of morphological variation, modularity and phylogenetic structure. We aimed to quantify the strength of modular signals and morphological integration within the brain and endocast, and to evaluate whether patterns of covariation among modules reflect underlying developmental or functional constraints. We also evaluated the degree to which endocast shape serves as a reliable proxy for brain shape, and whether the two systems exhibit comparable patterns of modular organization. Additionally, we examined the extent to which these patterns are shaped by shared ancestry and allometric effects.

2.4 MATERIALS & METHODS

2.4.1 Sample

The sample used for this study was composed of 83 specimens, representing 76 species from the Caudata order. All ten families of Caudata were sampled, representing 40 of the 69 recognized genera. Species selection aimed to capture the existing diversity within each genus, while also being constrained by the availability of specimens in museum collections. Most of the specimens were obtained from museum collections, but six were not listed in a collection (Table E1). *Ambystoma mexicanum* and *Pseudobranchus striatus* specimens were collected from captive colony under the Calgary Animal Care Committee protocol AC15-0020; specimens were euthanized using MS-222 5% (w/v) until cardiac activity had stopped. Two *Necturus maculosus* specimens were acquired from Ward's Science as fixed dissection specimens. Two *Nothophthalmus viridescens* specimens (Mauricie, Québec, Canada) were collected under the Parks Canada Agency permit LMNP-2023-45363 and were also euthanized in MS-222 5% (w/v).

2.4.2 Assessment for various fixation and staining procedures

Specimens of *Ambystoma mexicanum*, *Pseudobranchus striatus* and *Notophthalmus viridescens* collected in this study were fixed in neutral buffered formalin (NBF) 10% (w./v.). All other specimens used were alcohol-preserved specimens. All specimens were stained using iodine (see Table E1 for specimen-wise exposure times and concentrations). We acknowledge the possibility that variation in fixation and staining protocols may lead to differences in brain deformation caused by these techniques (Hedrick *et al.*, 2018; Tytiuk *et al.*, 2018; Weisbecker, 2012), although Weisbecker (2012) suggested that volume deformation of the brain owing to fixation and contrast agents may not greatly influence the shape information of soft tissues.

2.4.3 Imaging procedures

Specimens were scanned at one of three different facilities, with the reconstruction software varying according to the specific micro-CT scanner used (Table E2). Segmentation of all specimens was performed in the Dragonfly software, v.2022.2 for Windows (Dragonfly 2022.2) using a deep learning model. The model had a U-Net architecture using a 2.5D method (adjusting segmentation using information from the two previous and following images from the image stacks) and a five-layer structure. The initial number of pixels used in the U-Net process was adjusted to account for the pixel size of each set of images. The model was trained using between 10 and 50 images per specimen from various areas of the brain and endocast. The model produced the first draft of the segmentation process. Each image was then manually adjusted to correct any mistakes introduced by the segmentation model. Following segmentation, the 3D surface meshes of the brain and endocast were generated directly in Dragonfly. Prior to export, the meshes underwent a post-processing step consisting of Laplacian smoothing in Dragonfly to reduce surface imperfections.

2.4.4 Morphometric analyses

For each specimen, two linear measurements (Figure C1) were estimated using the Dragonfly software (measured in mm): (1) the distance from the anterior-most point of the premaxilla to the position of the median area of the coronal suture, and (2) the distance from the anterior-most point of the premaxilla to the optic chiasm. The values were $\log_{10}$ transformed. A Pearson correlation was calculated to assess the spatial relationship between the positions of the coronal suture and the optic chiasm. The normality assumption for the Pearson correlation was verified using a Shapiro-Wilk test with the "performance" R package v.0.12.2 (Lüdecke *et al.*, 2021; R Core Team, 2025).

2.4.5 Geometric morphometrics analyses

To investigate shape, 28 fixed landmarks, 26 curve semilandmarks, and 87 surface semilandmarks were placed on brains. An additional 19 fixed landmarks and 174 surface

semilandmarks were placed on endocasts (Figure E1 and E2). The software Stratovan Checkpoint (Stratovan Corporation) was used to perform landmark placement, and shape analyses were done in the R environment (R Core Team, 2025). A generalized Procrustes analysis was performed on shape coordinates using the gpagen function from the "geomorph" package v.4.0.10 (Baken *et al.*, 2021) and sliding of semilandmarks was conducted using Procrustes distances (Adams *et al.*, 2004; Gower, 1975; Gunz *et al.*, 2005). Each specimen was digitized twice to evaluate the error associated with landmark positioning. To remove the asymmetric shape and to quantify the landmark positioning error (considered as the residuals from the asymmetry analysis), a fluctuating asymmetry analysis was conducted on the shape data using the bilat.symmetry from the "geomorph" package v.4.0.10 (Baken *et al.*, 2021; Klingenberg *et al.*, 2002; Lazić *et al.*, 2015; Mardia *et al.*, 2000). The landmark positioning error represented 5.0 % of the total shape variation. The symmetric shape was considered as the shape dataset without allometric correction. The shape of species associated with more than one specimen were averaged. A second dataset was also produced by extracting the residuals from a Procrustes linear regression of the symmetric shape data as a function of the log of centroid size, thus removing the effect of size on shape. This Procrustes linear regression was performed using the ProcD.lm function from the "geomorph" package v.4.0.10 (Baken *et al.*, 2021). The residual coordinates from this regression were then added to the sample mean shape to reconstruct shape variation independent of allometry; this dataset is hereafter referred to as the allometry-corrected data. Phylomorphospaces were produced for the symmetric shape and allometry-corrected data to investigate shape changes along components for the brain and the endocast using the gm.prcomp function from the "geomorph" package v.4.0.10 (Baken *et al.*, 2021). A Mantel test was performed using the "vegan" package v.2.7-2 (Oksanen, 2016) to estimate the correlation between the brain and endocast phylomorphospace occupations. Phylogenetically aligned component analyses (PACA) were also produced using the gm.prcomp function from the "geomorph" package v.4.0.10 (Baken *et al.*, 2021) to highlight the effect of phylogeny on brain and endocast shapes. To visualize shape changes, 3D convex hulls were used to compare individuals associated with PC extremes for visualization of shape changes.

2.4.6 Phylogeny

A maximum clade credibility (MCC) tree was generated using TreeAnnotator in BEAST v1.10.4 (Drummond and Rambaut, 2007), based on 1000 posterior trees derived from the phylogeny of Jetz and Pyron (2018) constructed with a molecular supermatrix of 15 genes (10 nuclear and 5 mitochondrial). The common ancestor tree algorithm was used to avoid problems with estimation of negative branch lengths (Heled and Bouckaert, 2013). The MCC tree was pruned to include only the species of this study. The branch lengths of the MCC tree were scaled using the posterior branch-specific evolutionary rates from Bayesian analyses. Using a variable rates model and a reversible-jump Markov chain Monte Carlo (rjMCMC) algorithm for continuous traits, three separate analyses [(1) brain shape, (2) endocast shape, and (3) combined dataset] were performed in BayesTraitsV4. The variable rates model identifies deviations from a uniform Brownian motion model of trait evolution across a phylogeny, without requiring prior knowledge of where these shifts occur (Baker *et al.*, 2015; Venditti *et al.*, 2011). It does so by estimating a set of scalars for each branch that maximize the fit of the trait data to a homogeneous Brownian motion model (Baker *et al.*, 2015). The result is a rescaled phylogenetic tree, where each branch is lengthened or shortened to reflect the inferred evolutionary rate, effectively transforming the tree to better conform to Brownian motion dynamics (Baker *et al.*, 2015). The quantitative trait matrices used in the Bayesian analyses consisted of the scores of all retained phylogenetic principal component (PCA) axes from the shape data. For each dataset, enough PC axes were retained to account for more than 95% of the total shape variation, resulting in 27 axes for the brain, 18 for the endocast, and 29 for the combined dataset analyses, respectively. The Bayesian analyses were each conducted with four independent chains of 500 000 000 iterations. Sampling was performed every 50 000 iterations, and 55 000 000 iterations were excluded as burn-in. The convergence of MCMC chains is an important feature to verify when a reversible jump method is used since it uses a larger number of parameters than standard Brownian motion models (Green, 1995; Pagel and Meade, 2006). The convergence of the chains was assessed by investigating the trace and density plots (Figure B3, Figure B4, Figure

B5, Figure B6, Figure B7 and Figure B8), calculating the effective sample size of each parameter (Table E3, Table E4 and Table E5) and producing a Gelman and Rubin's convergence diagnostic (Table E6, Table E7 and Table E8). The effective sample size estimation (effectiveSize function) and the convergence diagnostic (gelman.diag function) were performed using the "coda" R package v.0.19-4.1 (Plummer *et al.*, 2006).

2.4.7 Evolutionary allometry

To assess evolutionary allometry, a Procrustes based phylogenetic generalized least squares (PGLS) analysis was performed for the symmetric shape data with the centroid size (log transformed) as the independent variable using the procD.pgls function in "geomorph" v.4.0.10 (Baken *et al.*, 2021). The phylogeny described above was used in this analysis. The standardized shape score (regression score) from the linear regression between the shape and size can be used as a simplified univariate representation of shape data (Adams *et al.*, 2013; Drake and Klingenberg, 2008). These regression scores were used to visualize the shape-size relationship for the brain, the endocast and the combined dataset.

2.4.8 Modularity and morphological integration

The degree of modular signal in the brain and the endocast was tested using a covariance ratio (CR) and a maximum-likelihood approaches (Adams and Felice, 2014). The allometry-corrected data was used for all modularity and morphological integration analyses. Phylogenetic relationships were accounted for in these analyses. The brain shape was analysed separately from the endocast shape as a first step. A selection of seven *a priori* modularity hypotheses for the brain shape (Table 2.1) and eleven *a priori* hypotheses for the endocast shape were tested (Table 2.2). Justification for the *a priori* hypotheses are described in Appendix D. Based on the integration pattern found among modules of the best supported *a priori* hypothesis of the brain, two *a posteriori* hypotheses were tested to investigate if better supported hypotheses could be detected.

Table 2.1 Names and descriptions of nine modularity hypotheses for salamander brain shape. Brackets delimit hypothesized modules.

	Hypothesis	Description	Number of modules	
a priori	Hypothesis 1A	[Dorsal landmarks], and [ventral landmarks]	2	
	Hypothesis 2A	[Forebrain and hindbrain], and [midbrain]	2	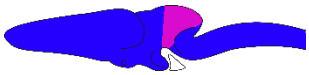
	Hypothesis 3A	[Forebrain], [midbrain], and [hindbrain]	3	
	Hypothesis 4A	[Telencephalon], [diencephalon], [mesencephalon], and [rhombencephalon]	4	
	Hypothesis 5A	[Telencephalon], [hypothalamus], [thalamus], [mesencephalon], and [rhombencephalon]	5	
	Hypothesis 6A	[Olfactory bulbs], [telencephalon], [diencephalon], [mesencephalon], and [rhombencephalon]	5	
	Hypothesis 7A	[Olfactory bulbs], [telencephalon], [hypothalamus], [thalamus], [mesencephalon], and [rhombencephalon]	6	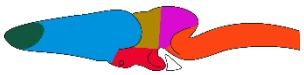
a posteriori	Hypothesis 8	[Olfactory bulbs], [telencephalon], [hypothalamus], [thalamus and mesencephalon], and [rhombencephalon]	5	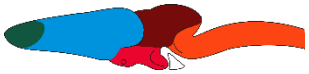
	Hypothesis 9	[Telencephalon], [hypothalamus], [thalamus and mesencephalon], and [rhombencephalon]	4	

Table 2.2 Names and descriptions of 11 modularity hypotheses for salamander endocast shape. Brackets delimit hypothesized modules.

Hypothesis	Description	Number of modules	
Hypothesis 1B	[Dorsal landmarks], and [ventral landmarks]	2	
Hypothesis 2B	[Forebrain and hindbrain], and [midbrain]*	2	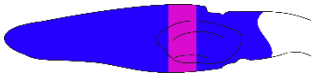
Hypothesis 3B	[Forebrain], [midbrain] and [hindbrain]*	3	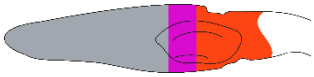
Hypothesis 4B	[Telencephalon], [diencephalon], [mesencephalon] and [rhombencephalon]*	4	
Hypothesis 5B	[Telencephalon], [hypothalamus], [thalamus], [mesencephalon] and [rhombencephalon]*	5	
Hypothesis 6B	[Olfactory bulb], [telencephalon], [diencephalon], [mesencephalon] and [rhombencephalon]*	5	
Hypothesis 7B	[Olfactory bulb], [telencephalon], [hypothalamus], [thalamus], [mesencephalon] and [rhombencephalon]*	6	
Hypothesis 10	[CNC derived bones], and [mesodermal bones]	2	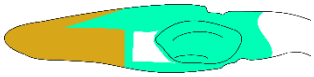
Hypothesis 11	[Otic region landmarks], and the [rest]	2	
Hypothesis 12	[frontal], [parietal], [parasphenoid], [orbitosphenoid], [occipito-otic area]	5	
Hypothesis 13	[frontal], [parietal], [anterior parasphenoid], [posterior parasphenoid], [orbitosphenoid], [occipito-otic area]	6	

In order to compare covariation patterns among brain modules, among endocast modules, and between brain–endocast modules, we needed a common modular partition for the combined dataset. First, we selected the best-supported modularity hypothesis identified for the brain. Then, we selected the two best-supported hypotheses identified for the endocast. Each endocast hypothesis was then combined with the best brain hypothesis to generate a unified set of modules spanning both structures. This procedure produced two alternative modular hypotheses for the complete dataset (brain and endocast). The pattern of covariation of these two combined hypotheses was subsequently compared (Table 2.3).

Table 2.3 Names and descriptions of two modularity hypotheses for the combined salamander dataset. Brackets delimit hypothesized modules.

Hypothesis	**Description**		**Number of modules**
	Brain	**Endocast**	
Hypothesis 14	[Olfactory bulbs], [telencephalon], [hypothalamus], [thalamus], [mesencephalon], and [rhombencephalon] 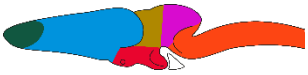	[Olfactory bulbs], [telencephalon], [hypothalamus], [thalamus], [mesencephalon], and [rhombencephalon] 	12
Hypothesis 15	[Olfactory bulbs], [telencephalon], [hypothalamus], [thalamus], [mesencephalon], and [rhombencephalon] 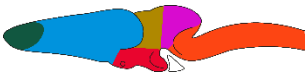	[Telencephalon], [hypothalamus], [thalamus], [mesencephalon], and [rhombencephalon] 	11

For the CR approach, analyses of modularity were performed using the phylo.modularity function (Adams *et al.*, 2014) from the "geomorph" package v.4.0.10 (Baken *et al.*, 2021) and hypotheses were compared using their multivariate effect size (Adams et Collyer, 2019). Partial least squares (PLS) analyses were used to evaluate the degree of phylogenetic morphological integration of modules using the phylo.integration function (Adams *et al.*,

2014) from the "geomorph" package v.4.0.10 (Baken *et al.*, 2021). The sample effect sizes of the PLS analysis were compared among modules to investigate if some modules exhibited higher levels of integration than other. Additionally, the globalIntegration function from the "geomorph" package v.4.0.10 (Baken *et al.*, 2021) was used to estimate overall level of integration of the brain and endocast according to Bookstein method (Bookstein, 2015). For the maximum-likelihood approach, phylogenetically informed EMMLi analyses (Goswami and Finarelli, 2016) were performed for the brain shape, the endocast shape and the combined dataset using the "EMMLiv2" package v.0.0.3 (Goswami and Finarelli, 2016). Under each modularity hypothesis, EMMLi fits a maximum-likelihood model in which within-module and between-module correlations are treated as modeled parameters (Goswami and Finarelli, 2016). These parameters are estimated as the set of optimal within- and between-module correlation values that maximize the likelihood fit of the observed trait correlation matrix under the specified modularity hypothesis (Goswami and Finarelli, 2016). Thus, these values do not represent simple descriptive correlations, but model-derived parameters reflecting the strength of association within and between modules under a hypothesis. This method uses the AICc values to select the best-supported hypothesis of modularity based on traits correlations (Goswami and Finarelli, 2016). To visualize the level of integration among modules of each hypothesis, graphical networks were produced using the qgraph function in "qgraph" package v.1.9.8 (Epskamp *et al.*, 2012). In all networks, values of association among modules were present only if they were above 0.5.

2.4.9 Phylogenetic signal

The phylogenetic signal of brain and endocast shape was evaluated using effect size estimation from likelihood (Collyer *et al.*, 2022). The phylogeny described above was used in these analyses. We conducted six separate tests of phylogenetic signal with the physignal.z function in "geomorph" v.4.0.10 (Baken *et al.*, 2021), using the burn-in optimization procedure (Collyer *et al.*, 2022). These tests assessed (1) brain shape, (2) endocast shape, and (3) combined brain and endocast shape (combined dataset), each performed both before and after accounting for the effect of allometry. We additionally quantified the phylogenetic

signal of centroid size using the same method. Finally, using the best-supported modularity hypothesis for the combined brain–endocast dataset, we evaluated the phylogenetic signal of each module independently and compared their relative signal strength based on effect sizes.

2.4.10 Intraspecific variation

To investigate the importance of intraspecific shape variation in the brain and the endocast, two specimens were included for seven of the species in this study (i.e., *Batrachuperus pinchonii*, *Notophthalmus viridescens*, *Isthmura bellii*, *Necturus maculosus*, *Taricha granulosa, Bolitoglossa subpalmata* and *Plethodon vehiculum*). For four of these species, a male and a female were used (i.e., *B. pinchonii, B. subpalmata, I. bellii, N. viridiscens*). The morphospace occupation of all individuals (including species with one specimen) was visualized using three PCAs (brain, endocast, and combined dataset). Frequencies of distances among Procrustes coordinates frequencies were calculated within species with multiple specimens, among species means and across all specimens using the dist function from the "stats" package v.4.5.0 (R Core Team, 2025). These frequencies were compared using density histograms.

2.5 RESULTS

2.5.1 Evolutionary allometry

Size significantly affected shape, notwithstanding that it explained a modest proportion of the total variation (brain: $R^2 = 0.076$, $p = 0.032$; endocast: $R^2 = 0.060$, $p = 0.023$; combined dataset: $R^2 = 0.080$, $p = 0.033$). Plotting the regression scores against centroid size provides a direct way to visualize shape–size relationships and to evaluate the presence of allometric signal (Drake and Klingenberg, 2008). When a clear relationship (i.e., a visible trend or slope) is observed between regression scores (grossly representing shape) and centroid size, this indicates that shape varies with size and therefore that an allometric signal is present. Conversely, the absence of such a relationship indicates little to no allometric signal (Drake and Klingenberg, 2008). The allometric regressions showed that Plethodontids seem to show

less allometric signal than other families for both the brain and the endocast, since this group did not show a shape-size relationship. However, a general allometric signal (shape-size relationship) is still visible in each case (Figure C2). For the combined dataset, a similar allometric trend is visible among families but with slightly different means (Figure C2). Shape variation related to size in the brain is primarily associated with the rhombencephalon and the telencephalon (Figure C3). *Thorius* exhibited a strongly curved telencephalon along the antero-posterior axis, a feature absent in the largest salamanders (Figure C3 A). Additionally, the anterior rhombencephalon of *Thorius* lies ventral to the posterior mesencephalon, producing a more robust dorso-ventral profile in this region (Figure C3 B). In contrast, the mesencephalon–rhombencephalon boundary is relatively flat in *Cryptobranchus alleganiensis* (Figure C3 B).

Larger species tend to have elongated, flatter endocast shapes along the antero-posterior and dorso-ventral axes with a much longer occipito-otic region (Figure C4 A, B). Smaller species exhibit more compact endocasts with increased dorso-ventral thickness (Figure C4 A, B). Laterally, small endocasts also appear diamond-shaped, with their widest section aligning with the posterior end of the curved telencephalon (Figure C4 B). These allometric differences (for both the brain and endocast) are mainly congruent with shape changes associated with the first PC of the phylomorphospace (Figure C5 and Figure C6).

2.5.2 Brain modularity and shape variation

The modular signal of the brain is strong and significant (Table 2.4). The CR effect size of all tested modular hypotheses differed significantly from the null (Table C2). Pairwise comparisons of CR coefficients revealed that Hypotheses 5A, 6A, 7A and 8 were significantly different from Hypothesis 1A, but no other differences were observed among the remaining hypotheses (Table C1). We therefore combined the results of the EMMLi method to select the best-supported hypotheses while considering the lowest CR effect sizes. Among the hypotheses tested, Hypothesis 7A received the strongest overall support, exhibiting both the lowest CR effect size and the lowest corrected AIC value using the

EMMLi method (Table 2.5). The morphological integration analysis yielded PLS coefficients ranging between 0.6 and 0.9, which can be interpreted as intermediate to high levels of integration (Table 2.4). Among modular hypotheses, sample effect size from PLS analyses were estimated to compare the level of integration. Hypothesis 7A was associated with the lowest sample effect size, which is congruent with this hypothesis exhibiting the highest level of modular signal (Table C2). This analysis also showed that Hypotheses 1A, 2A and 5A were associated with a significantly higher level of integration than Hypothesis 7A (Table C2).

Table 2.4 Results of morphological integration analyses using partial least squares (PLS) and modularity analyses of the salamander brain using the covariance ratio (CR) for the seven *a priori* and two *a posteriori* hypotheses. Results in bold represent the best supported hypothesis (Hypothesis 7A). The last line represents results from the global morphological integration analysis (Bookstein, 2015).

		CR method			**Morphological integration**		
	Hypothesis	**CR**	**P-value**	**Z**	**PLS**	**P-value**	**Z**
	Hypothesis 1A	0.853	0.001	-2.676	0.876	0.001	5.197
	Hypothesis 2A	0.706	0.002	-2.925	0.777	0.001	4.262
	Hypothesis 3A	0.618	0.001	-3.986	0.685	0.001	7.099
a priori	Hypothesis 4A	0.608	0.001	-4.437	0.680	0.001	9.924
	Hypothesis 5A	0.582	0.001	-5.277	0.660	0.001	11.209
	Hypothesis 6A	0.599	0.001	-5.217	0.671	0.001	10.670
	Hypothesis 7A	**0.573**	**0.001**	**-6.241**	**0.645**	**0.001**	**12.257**

a posteriori	Hypothesis 8	0.592	0.001	-5.065	0.663	0.001	9.638
	Hypothesis 9	0.598	0.001	-4.740	0.671	0.001	9.139
Global integration				-0.782			

Table 2.5 Results of modularity analyses using the phylogenetically informed EMMLi method for the seven *a priori* and two *a posteriori* hypotheses for salamander brains. Results in bold represent the best supported hypothesis (Hypothesis 7A).

	Hypothesis	**K**	**AICc**	**ΔAICc**
a priori	Hypothesis 1A	4	-48027.472	2246.797
	Hypothesis 2A	4	-47736.150	2538.120
	Hypothesis 3A	7	-49342.565	931.704
	Hypothesis 4A	11	-49801.509	472.760
	Hypothesis 5A	16	-50091.532	182.737
	Hypothesis 6A	16	-49979.123	295.147
	Hypothesis 7A	**22**	**-50274.270**	**0.000**
a posteriori	Hypothesis 8	16	-50033.026	241.244
	Hypothesis 9	11	-49845.246	429.024

Under Hypothesis 7A, pairwise CR and PLS comparisons consistently identified the olfactory bulb as the module showing the weakest correlations with all other modules, making it the most independent module according to these methods (Figure C7). In contrast, the EMMLi analysis identified the hypothalamus and rhombencephalon as the most independent modules (Figure C7). According to this last method, the strongest associations were found between the olfactory bulb and the rest of the telencephalon, and between the mesencephalon and the thalamus (Figure C7). The strong association between the olfactory bulb and the telencephalon was also supported by the CR and PLS analyses. This strong relationship among regions of the telencephalon is consistent with the high level of modular signal of Hypothesis 5A, in which the telencephalon is considered as one module (Table 2.4). Finally, *a posteriori* testing showed that grouping the thalamus and mesencephalon into a single module did not result in a better-supported modular hypothesis (Table 2.4).

The EMMLi method enables comparisons of both the strength of correlations among modules and the internal correlation level within each module (Goswami and Finarelli, 2016). Consequently, each modular hypothesis is assessed under four distinct correlation configurations: (1) fully heterogeneous, where both correlations among and within modules are allowed to vary; (2) partially constrained (within heterogeneous), where correlations among modules are held equal, but correlations within modules can vary; (3) partially constrained (among heterogeneous), where correlations within modules are held equal, but correlations among modules can vary; and (4) fully constrained, where both correlations among and within modules are assumed to be equal. Among the four configurations tested for Hypothesis 7A, the fully heterogeneous was found to be the best supported. Among the modules, the mesencephalon showed the weakest within-module level of correlation, while the hypothalamus showed the strongest (Figure C7).

In the allometry-corrected data, the first principal component of the phylomorphospace reflects a general lateral expansion of brain regions, particularly the telencephalon (including olfactory bulb), and to a lesser extent, a dorso-ventral expansion (Figure C5 A, B). The second principal component captures an antero-posterior elongation of the rhombencephalon

combined with a shortening of the telencephalon (Figure C8 A, B). Along this axis, the shape of the olfactory bulb also shifts from more pointed at PC2 minimum to noticeably rounder at PC2 maximum (Figure C8 A).

2.5.3 Endocast modularity and shape variation

Among the *a priori* endocast modular hypotheses, Hypotheses 5B and 7B received the strongest support using the CR method (Table 2.6). These two hypotheses were significantly different from all other hypotheses but were not significantly different from each other (Table C3). Both Hypotheses 5B and 7B identified modules of the brain, and differ in treating the olfactory bulb as an independent module (Hypothesis 7B), or as a part of the telencephalon's module (Hypothesis 5B; Table 2.2). The EMMLi method identified Hypothesis 13 as best supported (Table 2.7). Considering that the CR and EMMLi method did not lead to similar conclusions, Hypotheses 5B and 7B were retained as meaningful following the results of CR effect size comparison. Under these two hypotheses, the most independent module was the area surrounding the thalamus (Figure C9). Considering the EMMLi method, the two modules with the lowest internal integration were the area surrounding the mesencephalon, and the rhombencephalon (Figure C9). With regard to the integration levels among modules, a strong association between the olfactory bulb and telencephalon for Hypothesis 7B and also between the mesencephalon and rhombencephalon were found (Figure C9). Morphological integration levels were between 0.560 and 0.750, which is slightly lower than the levels observed for the brain (Table 2.6). Comparing the PLS sample effect sizes revealed that Hypotheses 5B and 7B were associated with significantly lower integration than Hypotheses 2B and 11 (Table C4).

Table 2.6 Results of morphological integration analyses using partial least squares (PLS) and modularity analyses of the salamander endocast using the covariance ratio (CR) method for the eleven *a priori* hypotheses. Results in bold represent the retained hypotheses (Hypotheses

5B, 7B and 13). The last line represents results from the global morphological integration analysis (Bookstein, 2015).

	CR method			Morphological integration		
Hypothesis	**CR**	**P-value**	**Z**	**PLS**	**P-value**	**Z**
Hypothesis 1B	0.679	0.001	-3.590	0.731	0.001	4.587
Hypothesis 2B	0.687	0.002	-2.899	0.724	0.001	3.861
Hypothesis 3B	0.642	0.001	-3.136	0.613	0.001	5.205
Hypothesis 4B	0.588	0.001	-4.163	0.626	0.001	5.854
Hypothesis 5B	**0.503**	**0.001**	**-6.949**	**0.565**	**0.001**	**6.856**
Hypothesis 6B	0.581	0.001	-4.500	0.609	0.001	6.611
Hypothesis 7B	**0.512**	**0.001**	**-7.290**	**0.562**	**0.001**	**7.768**
Hypothesis 10	0.602	0.001	-4.454	0.624	0.001	3.086
Hypothesis 11	0.663	0.001	-2.833	0.746	0.001	4.673
Hypothesis 12	0.570	0.001	-4.749	0.609	0.001	8.897
Hypothesis 13	**0.515**	**0.001**	**-5.946**	**0.537**	**0.001**	**9.518**
Global integration			-0.591			

Table 2.7 Results of modularity analyses using the phylogenetically informed EMMLi method for the eleven *a priori* hypotheses for salamander endocasts. Results in bold represent the retained hypotheses (Hypotheses 5B, 7B and 13).

Hypothesis	K	AICc	ΔAICc
Hypothesis 1B	4	-50329.918	4443.187
Hypothesis 2B	4	-49437.297	5335.808
Hypothesis 3B	7	-50847.743	3925.362
Hypothesis 4B	11	-51711.471	3061.633
Hypothesis 5B	**16**	**-51950.744**	**2822.361**
Hypothesis 6B	16	-52582.029	2191.076
Hypothesis 7B	**22**	**-52821.432**	**1951.672**
Hypothesis 10	4	-50409.653	4363.452
Hypothesis 11	4	-50184.081	4589.024
Hypothesis 12	16	-53836.350	936.754
Hypothesis 13	**22**	**-54773.105**	**0.000**

In the allometry-corrected endocast shape, PC1 was associated with a general antero-posterior elongation, particularly of the areas surrounding the telencephalon and rhombencephalon (Figure C6). PC1 was also linked to the lateral compression of these two areas, whereas the areas associated with the hypothalamus, thalamus and mesencephalon

remain generally unchanged (Figure C6 A, C). PC2 reflected a slight ventral expansion of the olfactory bulb and the anterior part of the rhombencephalon (Figure C10 B).

2.5.4 Endocast and brain associations

We compared the two hypotheses composed of the combination of the best-supported brain modular hypothesis with the two best-supported endocast modular hypotheses (Table 2.3). Comparing the CR effect size revealed that Hypothesis 14 was not significantly different from Hypothesis 15 (Table C5). Since Hypothesis 14 was associated with the lowest CR effect size and was found to be the best supported hypothesis using the EMMLi methods, it was considered as the overall best supported modular hypothesis (Table 2.8 and Table 2.9). The fully heterogeneous model was best supported for Hypothesis 14 using the EMMLi method (Table 2.9). PLS analyses revealed an intermediate level of morphological integration (between 0.5 and 0.6) and somewhat similar PLS sample effect sizes for the two hypotheses (Table 2.8 and Table C6).

Table 2.8 Results of morphological integration analyses using partial least squares (PLS) and modularity analyses using the covariance ratio (CR) method for the two hypotheses of the combined salamander dataset. Results in bold represent the retained hypothesis (Hypothesis 14). The last line represents results from the global morphological integration analysis (Bookstein, 2015).

	CR method			**Morphological integration**		
Hypothesis	**CR**	**P-value**	**Z**	**PLS**	**P-value**	**Z**
Hypothesis 14	**0.514**	**0.001**	**-11.753**	**0.571**	**0.001**	**12.383**
Hypothesis 15	0.510	0.001	-11.697	0.580	0.001	12.722
Global integration			-0.701			

Table 2.9 Results of modularity analyses using the phylogenetically informed EMMLi method for the two hypotheses for the combined salamander dataset. Results in bold represent the retained hypothesis (Hypothesis 14).

Hypothesis	K	AICc	ΔAICc
Hypothesis 14	**79**	**-237900.217**	**0.000**
Hypothesis 15	67	-237017.320	882.897

Pairwise comparisons of the strength of associations among modules revealed slightly more integration among modules of the brain compared with those of the endocast (Figure 2.1). A strong association between the olfactory bulb and telencephalon is apparent both for the brain and the endocast (Figure 2.1). The endocast exhibits a strong association between the mesencephalon and rhombencephalon for the CR and PLS methods that, although present, is not of the same magnitude for the brain (Figure 2.1).

When focusing on associations between brain and endocast modules, the olfactory bulb, telencephalon and hypothalamus are integrated with their surrounding area on the endocast for all methods (Figure 2.1). For the CR and PLS methods, the rhombencephalon also exhibit an association with its surrounding area on the endocast (Figure 2.1). Of all the modules, the endocast area surrounding the mesencephalon showed the lowest internal integration (Figure 2.1).

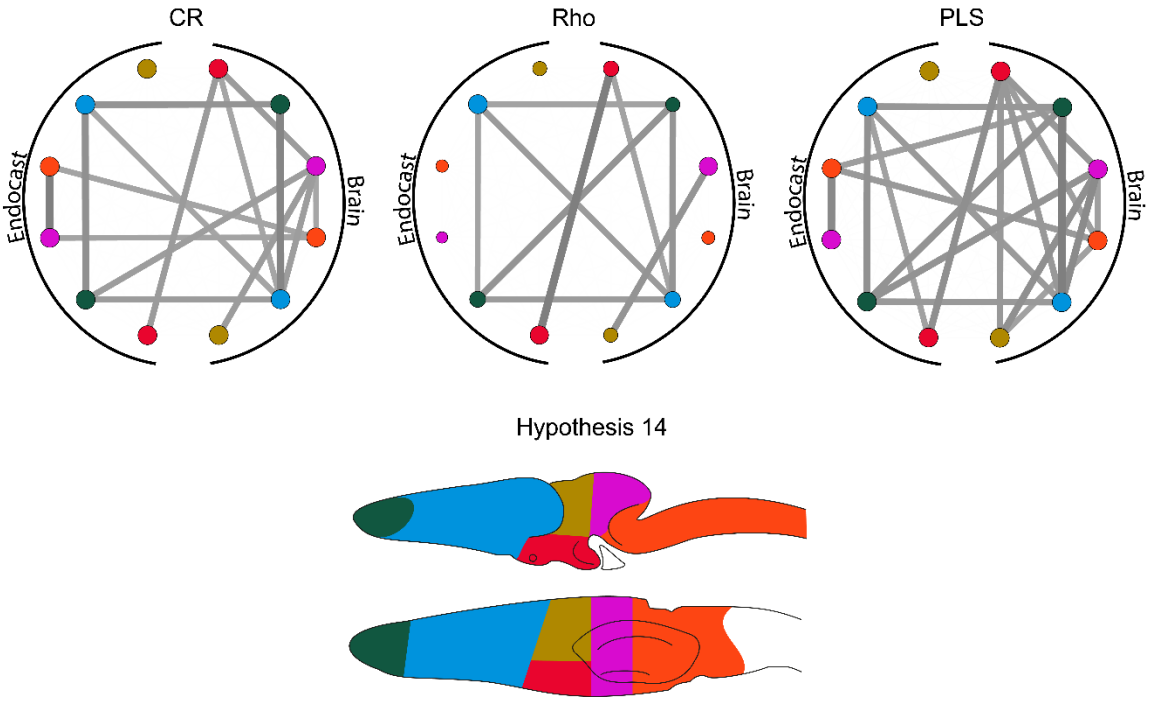

Figure 2.1 Network representations of the strength of morphological integration from the covariance ratio (CR), the EMMLi (rho) and the partial least squares (integration) analyses for the best supported hypothesis of the combined salamander dataset. Edge width in each network represents the strength of the association between two modules. Note that the edge width is based on values within each analysis (i.e., they are not directly comparable between networks). For the EMMLi analysis, the edge width represents the correlation between two modules and the size of nodes represents the within module correlation.

The correspondence between the morphospaces of the brain and of the endocast were tested using a Mantel test. A correlation of 0.613 ($p < 0.001$) and 0.492 ($p < 0.001$) were found for the symmetric shape and allometry-corrected data, respectively. While the brain and endocast shape are generally correlated, this suggest that they might describe slightly different patterns of evolutionary diversification. To further investigate the anatomical relationship between neurocranial and brain structures, we tested the alignment of the frontoparietal (coronal) suture with the telencephalon–diencephalon boundary using linear morphometric measurements. The optic chiasm, particularly the midpoint between the bases of the optic nerves, served as a reliable landmark for the telencephalon–diencephalon transition. There was a strong, significant correlation across species between the optic chiasm and the central point of the coronal suture ($r = 0.986$, $t_{74} = 51.607$, $p < 0.001$; Figure 2.2).

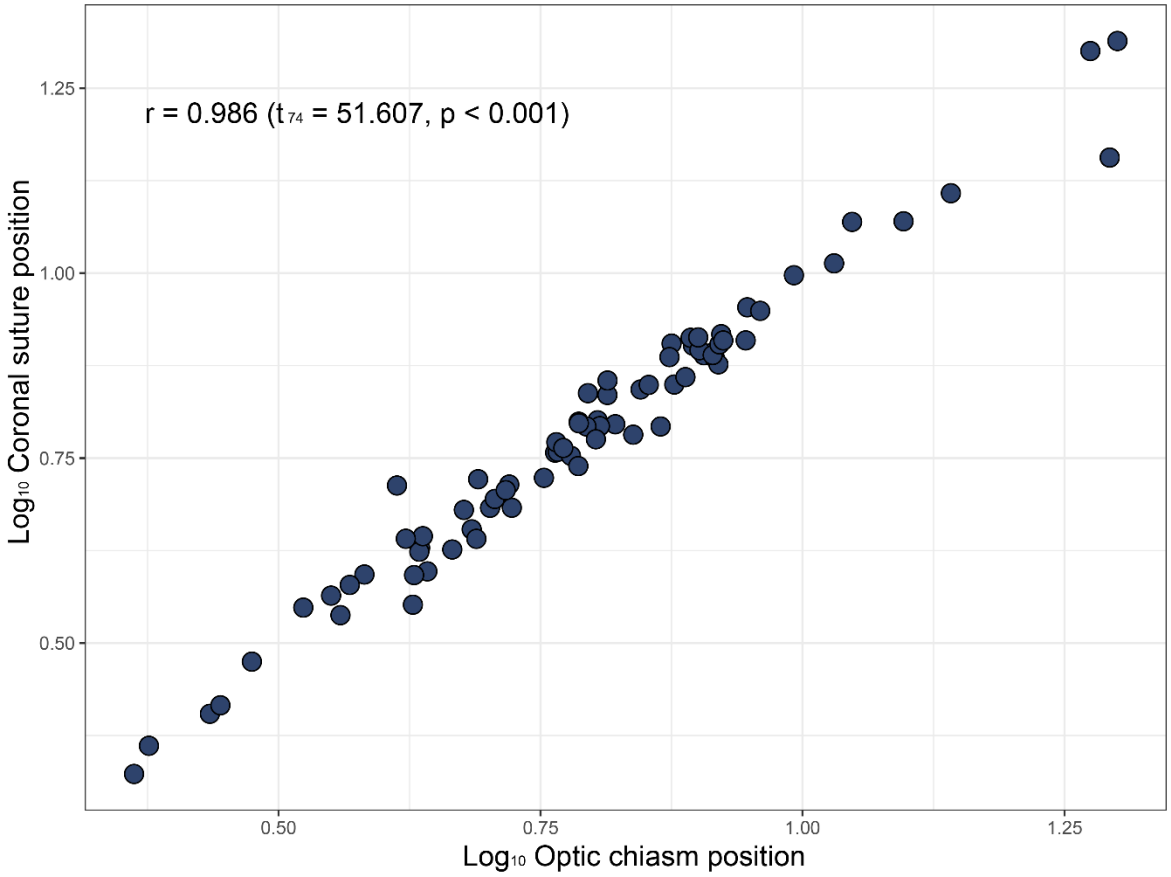

Figure 2.2 Relationship between the median point of the coronal suture and optic chiasm position measured in mm (log_{10} transformation) among 76 salamander species.

2.5.5 Phylogenetic signal

Phylomorphospaces and PACA showed that species are widely dispersed, with *Thorius* spp. generally occupying a unique space (Figure C11 and Figure C12). This pattern is congruent with a strong, significant phylogenetic signal in brain and endocast shapes (Table 2.10). Although K_{mult} values for brain (0.996) and endocast (0.934) shape were similar and close to 1, indicating patterns of shape evolution broadly consistent with a Brownian motion model, comparison of effect sizes (Z) revealed that the endocast exhibited a significantly stronger phylogenetic signal than the brain (Table 2.10). The PACA revealed that the *Hynobius* brain and endocast shapes are different when phylogenetic variation is optimized (Figure C12). The centroid size also exhibited a significant phylogenetic signal (K_{mult} = 0.902), indicating

that size variation is also phylogenetically structured (Table 2.10). To assess whether allometry drove most of the phylogenetic signal, we performed analyses on allometry-corrected data. These results indicates that the strong phylogenetic signal found in the endocast was entirely associated with the effect of size on shape since the removal of the allometric effect leads to the absence of phylogenetic signal (Table 2.10). However, the brain showed a persistent and significant phylogenetic signal after allometric correction (K_{mult} = 0.682), although this lower K_{mult} value suggests greater evolutionary lability than expected under a Brownian motion model (Table 2.10). This indicates contrasting patterns in phylogenetic signal between the brain and endocast in allometry-corrected data (Table 2.10).

Under Hypothesis 14, several brain and endocast modules displayed varying levels of phylogenetic signal (Table C7). Among the brain modules, all except the hypothalamus showed significant phylogenetic signal, with the telencephalon exhibiting the strongest signal (Table C7). For the endocast, the areas surrounding the telencephalon and rhombencephalon showed a significant phylogenetic signal (Table C7).

Table 2.10 Phylogenetic signal results for brain and endocast shape with and without an allometric correction. The results of a comparison of the effect size of phylogenetic signal between brain and endocast shape is also present.

		K_{mult}	Pagel's λ	Z	P-value	P-value effect size comparison
Symmetric shape	Brain	0.996	0.100	11.338	0.001	0.001
	Endocast	0.934	0.100	22.316	0.001	
	Combined dataset	1.080	0.100	13.545	0.001	
Centroid size	Combined dataset	0.902	0.100	3.446	0.002	
Allometry-corrected data	Brain	0.682	0.100	8.577	0.001	0.001
	Endocast	-	0.000	-	-	
	Combined dataset	0. 741	0.100	9.769	0.001	

2.5.6 Intraspecific shape variation

PCAs of all specimens for brain and endocast shapes revealed relatively high variation within the seven species that were represented by multiple individuals. In several cases, individuals from the same species were widely separated in morphospace, occasionally overlapping with the distributions of other species (Figure C13). Of the seven species represented by two specimens, four had a specimen of each sex. Generally, the shape of the brain and endocast of species represented by both sexes seems slightly more variable than the species represented by only one sex with the exception of the brain shape of *Taricha granulosa* (Figure C13). However, analysis of frequencies of distances of shape coordinates demonstrates that inter-specific differences were substantially larger than intra-specific ones, indicating that despite some overlap, interspecific variation remains the dominant source of shape differences across the morphospace (Figure C14).

2.6 DISCUSSION

This study offers new insights into the evolution of salamander neuroanatomy by jointly examining the shapes of the brain and endocast. We identified a relatively high degree of integration in brain morphology and phylogenetically conserved spatial boundaries between the brain and the dermal skull roof, which could provide some support to the concerted model of brain evolution. However, the presence of a strong modular signal in the brain and several patterns of morphological integration among modules support the mosaic evolutionary model. These findings suggest that both functional and developmental constraints interact in shaping the brain evolution in salamanders. In addition, the endocast exhibits a pronounced phylogenetic signal combined with a strong allometric component. Evolutionary allometry is emerging as a driver of shape variation, particularly in association with miniaturized taxa. Together, these results underscore the complex interplay between developmental, functional, phylogenetic and allometric factors that influence neuroanatomical evolution in salamanders.

2.6.1 Evolutionary allometry and the role of body size

Our results reveal a clear allometric signal in both brain and endocast morphology. Shape variation along the main allometric axis for the brain is characterized by a general antero-posterior elongation and dorso-ventral flattening in larger species, whereas smaller species, particularly those in miniaturized *Thorius*, exhibit more compact, dorsoventrally expanded brains with a distinctive curvature of the telencephalon. Similar allometric trends are also exhibited by the endocast shape, with a diamond compact shape in small species and elongated and dorsoventrally compressed endocasts in larger ones. These morphological trends suggest that reductions in body size are accompanied by coordinated shape changes in the brain and surrounding structures, likely reflecting both developmental scaling and biomechanical constraints. Miniaturization appears to be associated with some of the shape changes in our results. Previous studies including miniature species of salamanders showed that extreme size reduction were associated with the loss of some cranial elements, altered proportions of brain regions, and compensatory changes in the density of neurons in some regions such as the optic tectum (Fabre *et al.*, 2020; Roth *et al.*, 1997; Roth *et al.*, 1990). The shape of the telencephalon and endocast in *Thorius* appears to be associated with a spatial reorganisation of the anterior brain owing to an increase in relative size of the eyes and brain (Roth *et al.*, 1997; Roth *et al.*, 1990). The shape of the brain in small salamanders somewhat reflect Haller's rule, whereby small vertebrates tend to exhibit globular brains (Baker *et al.*, 2025; Haller, 1762; Rensch, 1948; Tsuboi *et al.*, 2018). This supports a view in which size not only shapes the trajectory of morphological evolution through predictable allometric relationships, but also constrains the range of viable morphological solutions, particularly in lineages undergoing miniaturization.

Regarding the endocast, we observed substantial shape variation associated with allometry. Removing the allometric component markedly reduced the magnitude of the shape differences, indicating that allometry plays a major role in shaping the endocast. These results are broadly consistent with previous findings in anurans and caecilians, where braincase morphology was also shown to be strongly influenced by allometric effects (Bardua *et al.*,

2021; Bardua *et al.*, 2019). This suggests that allometric constraints on braincase shape may be a common pattern among amphibians, and perhaps among vertebrates.

2.6.2 Developmental constraints

In our results, the boundary between the telencephalon and diencephalon aligns closely with the coronal suture (frontal–parietal), a pattern reminiscent of the telencephalon–diencephalon boundary described as a conserved and developmentally stable zone in other vertebrate taxa (Ollonen *et al.*, 2024; Teng *et al.*, 2019). This spatial congruence suggests that some of the brain and skull module boundaries may co-evolve under shared positional or signaling constraints during development, and that such constraints may be highly conserved across salamander species. This congruence is developmentally plausible because the coronal suture is positioned at a neural crest–mesoderm interface whose placement is genetically regulated (e.g., En1-dependent), and this interface has been argued to track the telencephalon–diencephalon boundary across osteichthyans (Deckelbaum *et al.*, 2012; Teng *et al.*, 2019).

2.6.3 Functional constraints

The patterns of evolutionary modularity and covariation identified in our analyses may partially reflect functional constraints acting on the morphology of the brain and its surrounding structures. The significant and high level of modular signal for both the brain and endocast shapes are indicative of mosaic evolution. The olfactory bulb was the most independent module of the brain (while being strongly integrated to the rest of the telencephalon), which may reflect a specialization related to olfaction and chemosensory communication, a function of high ecological relevance in salamanders (Woodley, 2015). In addition to the telencephalon, our results show that the rhombencephalon, including the cerebellum, exhibits substantial shape variation relative to other modules. This suggests that the rhombencephalon may be subject to functional pressures that promote divergent morphological adaptations. As this region is involved in motor coordination and basic autonomic functions, its variation could reflect ecological differences in locomotor behavior,

as has been suggested for anurans (Manzano *et al.*, 2017). In salamanders, such divergence may partly arise from the difference between aquatic and terrestrial habitats, which likely imposes distinct locomotor demands and selective pressures. In amphibians, the optic tectum within the mesencephalon serves as a key hub for processing and integrating multimodal sensory inputs, particularly visual and somatosensory information, which may require extensive connectivity with other brain regions (González *et al.*, 2020). Our results indicated that the mesencephalon exhibits weak internal integration but relatively strong levels of integration with all other brain modules. This pattern may reflect its function as one of the primary integrative centers in the salamander brain (Roth *et al.*, 1990; Roth *et al.*, 1997).

More generally, the balance observed in our data between regional autonomy and coordinated shape variation is consistent with a mixed model of brain evolution, in which both developmental constraints and mosaic processes co-exist. This duality has been documented in anurans (Liao *et al.*, 2015), where allometric scaling explains most of the variation among brain regions (supporting constraint-based models), yet ecologically relevant brain regions (e.g., telencephalon, olfactory bulbs) vary independently in association with specific pressures like microhabitat types or predation. Our results echo this pattern; the strong allometric signal linking brain size and shape supports a constrained developmental framework, yet region-specific variation in shape and integration, particularly in sensory and posterior brain regions, points toward a possible functional specialization and partial release from global constraints.

2.6.4 Endocast and brain correspondence

The degree of integration between brain and endocast modules reveals a particularly strong correspondence in the anterior region, where the endocast closely reflects the morphology of the olfactory bulbs and telencephalon. To a lesser extent, the posterior portion of the endocast also exhibits a similar signal to that of the rhombencephalon. These associations likely reflect the influence of spatial cohesion among specific brain regions and adjacent skeletal structures. More generally, significant Mantel correlations support the overall morphological

congruence between the brain and endocast, indicating that shape variation is partially shared across the two structures. One striking example is the near-perfect alignment between the optic chiasm and the median point of the coronal suture, reinforcing a close anatomical and developmental correspondence between particular neural and cranial elements. This lends support to the notion that endocasts can serve as reasonable proxies of the brain morphology in salamanders. However, modularity analyses indicate a lack of strong integration between the mesencephalon and surrounding endocast regions. This finding aligns with previously documented spatial mismatches between the brain and the endocast in the mesencephalic region of salamanders (Challands *et al.*, 2020). Compared to other vertebrate groups, the degree of brain-endocast correspondence observed in salamanders appears broadly similar to that reported in squamates (Allemand *et al.*, 2023), and less pronounced than in birds (Early *et al.*, 2020; Keirnan *et al.*, 2025; Watanabe *et al.*, 2019).

2.6.5 Phylogenetic constraints

Our results provide strong evidence for phylogenetic influence on the shape of the brain and endocast. The significant phylogenetic signal observed in multiple brain and endocast regions, as well as for the centroid size, supports the hypothesis that shared ancestry constrains the morphological evolution of these systems. This is particularly evident in *Thorius*, which consistently occupies a distinct region of the phylomorphospace, and in the retention of phylogenetic signal in the brain even after correcting for allometric effects. Moreover, the fact that most K_{mult} estimates were close to 1 indicates that the evolution of these traits is broadly consistent with a Brownian motion model, suggesting that morphological divergence accumulated approximately in proportion to phylogenetic divergence. These patterns are similar to what was observed in previous studies on skull evolution, which have shown that cranial morphology in salamanders (Fabre *et al.*, 2020) and anurans (Hou *et al.*, 2022; Liao *et al.*, 2015) reflects deep phylogenetic relationships, often more strongly than the effects of ecological or functional factors.

The strong phylogenetic signal found in the overall endocast shape (symmetric shape data) is in line with the proposition that the braincase's early ontogenetic origin and isolation from environmental selective pressures promote a strong phylogenetic signal for this region of the skull (Bardua *et al.*, 2021; Cardini and Elton, 2008; Goswami and Polly, 2010). In contrast, brain morphology appears somewhat more evolutionarily labile, suggesting that, while constrained by the phylogeny, certain brain regions may respond more flexibly to ecological or functional demands. With respect to the phylogenetic signal of specific brain regions, our results differ from those of Liao *et al.* (2015); while these authors found the telencephalon to be more influenced by ecological factors in anurans, our findings suggest it is the most strongly constrained by shared ancestry among all brain regions in salamanders. Among all brain modules, only the two exhibiting the strongest phylogenetic signal had corresponding endocast regions that also showed significant phylogenetic signal. This suggests that a portion of the phylogenetic information present in brain morphology is not fully captured by the shape of the endocast.

2.6.6 Intraspecific variation and plasticity

The intraspecific variation observed in brain and endocast shape likely reflects a combination of biological processes known to generate morphological diversity among individuals of the same species. One possible contributor is sexual dimorphism, which is widespread in amphibians (Kupfer, 2007). Sexual size dimorphism (SSD), typically female-biased in salamanders, has been linked to fecundity selection, as larger female body size enhances reproductive output (Mai and Liao, 2019). However, sexual shape dimorphism (SShD) also occurs independently of size and may affect structures such as the skull, limbs, and trunk, often with sex-specific functional implications for locomotion or reproduction (Pogoda and Kupfer, 2018; Reinhard and Kupfer, 2015). For example, studies on *Salamandrina* have shown that males tend to have larger heads and limbs, while females have more voluminous trunks (Pogoda and Kupfer, 2018). In addition, differences in the distribution of neuromodulators, such as arginine vasotocin, between sexes suggest subtle variation in brain anatomy and neurochemistry (Boyd *et al.*, 1992). Sexual shape dimorphism of the brain and

endocast cannot be ruled out for most of the species that were represented by each sex in our data.

Beyond sexual dimorphism, phenotypic plasticity may also be a source of intraspecific variation. Experimental studies in anurans have demonstrated that environmental factors such as larval density and predation risk can induce lasting modifications in brain architecture across metamorphosis, particularly in the size of regions like the optic tectum and diencephalon (Gonda *et al.*, 2010; Trokovic *et al.*, 2011). These changes can involve both expansion and reorganization of brain regions. Furthermore, seasonal changes may contribute to the observed variation, especially in brain regions associated with chemosensation. In *Plethodon cinereus*, proliferation of cells in the telencephalon and olfactory epithelium increases significantly in spring, likely in preparation for mating and other seasonally-mediated behaviors (Dawley *et al.*, 2000). These patterns of plasticity and dimorphism, combined with possible age-related differences, may provide possible explanations for the shape variation observed within species.

2.7 CONCLUSION

Across Caudata, brain and endocast shapes exhibit detectable evolutionary allometry and pervasive patterns of modularity and integration, indicating that neither concerted nor mosaic models alone capture the full structure of neuroanatomical evolution. Miniaturized taxa, particularly *Thorius*, show pronounced departures in telencephalic and endocast geometry, consistent with size-related reorganization of the anterior brain and surrounding endocranial space. Modularity analyses identify the olfactory bulb as comparatively independent while remaining strongly integrated with the telencephalon, a pattern consistent with localized evolutionary flexibility embedded within broader integration.

Endocasts recover substantial aspects of brain morphology, especially in anterior (olfactory bulb and telencephalon) and, to a lesser extent, posterior (rhombencephalon) regions, but correspondence weakens in the mesencephalic region where modular decoupling is consistently detected. The near-perfect alignment between the optic chiasm and the coronal

suture further supports conserved spatial relationships between neural and cranial organization, suggesting persistent developmental constraints across salamanders. Finally, while phylogenetic signal is strong in both structures, the endocast signal is largely driven by allometric shape change, whereas the brain retains phylogenetic structure after allometric correction. Overall, salamander endocasts are best interpreted as informative, region-dependent proxies: reliable for some parts of the brain and cautionary for others, especially when making inferences about midbrain evolution in fossil taxa.

2.8 ACKNOWLEDGMENTS

We thank Jason Pardo for sharing scan images of *Ambystoma mexicanum* and *Pseudobranchus striatus*, as well as museum staff members Stéphanie Tessier (Canadian Museum of Nature), Amy Lathrop (Royal Ontario Museum), Rachunliu Kamei (Field Museum of Natural History), Joshua Mata (Field Museum of Natural History), Ana Motta (Kansas University Biodiversity Institute), Carol Spencer (Museum of Vertebrate Zoology), Lauren Vonnahme (American Museum of Natural History), and David A. Kizirian (American Museum of Natural History) for their assistance with specimen loans. This work was funded by grants from the Natural Sciences and Engineering Research Council of Canada (NSERC) and the Fonds de recherche du Québec – Nature et technologies (FRQNT).

CHAPITRE 3
ALLOMETRIE, PHYLOGENIE, CYCLE DE VIE ET MICROHABITAT COMME FACTEURS AFFECTANT L'EVOLUTION DE LA FORME DU CERVEAU ET DE L'ENDOCASTE CHEZ LES SALAMANDRES

Laurent Houle[1], Olivier Larouche[2] and Richard Cloutier[1,3]

[1] Laboratoire de Paléontologie et Biologie évolutive, Université du Québec à Rimouski, 300 Allée des Ursulines, Rimouski, Quebec G5L 3A1, Canada

[2] Biology Department, Western Carolina University, 1 University Dr., Cullowhee, NC, 28723, United States

[3] Center of Excellence on the Evolution of Life, Basin Studies and Applied Paleontology; Paleontological Research and Education Center, Mahasarakham University, Maha Sarakham 44150, Thailand

Cet article, intitulé « *Allometry, Phylogeny, Life cycle and Microhabitat as Drivers of Brain and Endocast Shape Evolution in Salamanders* », est en fin de préparation pour soumission dans le journal international *Evolution*. J'ai conçu l'étude et élaboré la méthodologie, récolté les données, analysé des données, produit les résultats et les figures, rédigé l'article, incluant la recherche bibliographique, et coordonné les révisions et commentaires des coauteurs. Olivier Larouche a contribué à l'analyse des données et à la production des résultats et des figures, et a révisé l'article. Richard Cloutier a initié le projet et financé les travaux de recherche, contribué à la conception de l'étude et de la méthodologie, contribué à l'analyse des données et a révisé l'article.

3.1 RESUME

Le cerveau des vertébrés est un organe complexe façonné par des contraintes développementales, des exigences fonctionnelles et l'histoire évolutive. Les salamandres constituent un modèle comparatif particulièrement informatif en raison de la grande diversité de leurs modes de développement et de leurs stratégies écologiques. Nous examinons ici l'ampleur de l'influence de la phylogénie, de l'allométrie, des microhabitats et des stratégies développementales sur l'évolution du cerveau et de l'endocaste chez les salamandres. À l'aide d'imagerie micro-CT à haute résolution et de morphométrie géométrique 3D, nous avons analysé la forme du cerveau et de l'endocaste chez 83 spécimens représentant 76 espèces couvrant l'ensemble des dix familles de salamandres. L'allométrie et la phylogénie ont été identifiées comme les principaux déterminants de la forme du cerveau et de l'endocaste, tandis que le cycle de vie et le microhabitat n'exerçaient que des effets limités et spécifiques à certaines régions. Des différences localisées ont été observées notamment au niveau des bulbes olfactifs et du télencéphale, mais l'architecture neuronale globale demeure largement conservée. Aucune preuve d'un effet macroscopique de la présence d'une langue balistique sur l'évolution du cerveau n'a été détectée. Les espèces strictement paedomorphes présentent une disparité morphologique plus élevée. Des changements des taux évolutifs au début de l'histoire des salamandres reflètent des patrons précédemment mis en évidence pour la morphologie crânienne, suggérant l'existence de mécanismes sous-jacents communs. Le télencéphale et le rhombencéphale affichent les taux d'évolution les plus élevés parmi les régions cérébrales, indiquant que l'intégration n'exclut pas une disparification régionale. Enfin, les endocastes reproduisent les principaux patrons évolutifs du cerveau, soutenant leur pertinence comme substituts chez les taxons actuels et fossiles de Caudata. Ensemble, ces résultats mettent en évidence un cadre évolutif généralement conservé, mais flexible du cerveau des salamandres, principalement façonné par la phylogénie et l'allométrie, tout en conservant une signature limitée des facteurs écologiques et développementaux.

Mots clés : Amphibiens, Tetrapodes, Morphométrie géométrique, Neuroanatomie, Disparité, Taux d'évolution, Écomorphologie

3.2 ABSTRACT

The vertebrate brain is a complex organ shaped by developmental constraints, functional demands, and evolutionary history. Salamanders offer an informative comparative model due to their wide range of developmental modes and ecological strategies. Here, we examine the extent of the influence of shared ancestry, allometry, microhabitat, and developmental strategies on brain and endocast evolution across the salamander radiation. Using high-resolution micro-CT imaging and 3D geometric morphometrics, we analyzed brain and endocast shape in 83 specimens representing 76 species across all ten salamander families. Allometry and phylogeny were identified as the main determinants of brain and endocast shape, while life cycle and microhabitat exerted only limited, region-specific effects. Localized differences were observed in areas such as the olfactory bulb and telencephalon, but overall neural architecture was largely conserved. No evidence was detected for large-scale effects of the presence of a ballistic tongue on brain evolution. Strict paedomorphs showed high morphological disparity. Evolutionary rate shifts early in salamander history mirror patterns previously identified in cranial morphology, suggesting shared underlying drivers. Telencephalon and rhombencephalon exhibited the highest evolutionary rates among brain regions, which further demonstrates that integration does not preclude localized disparification. Finally, endocasts capture the main evolutionary patterns of the brain, supporting their utility as proxies in both extant and fossil taxa in the Caudata. Together, our results highlight a conserved yet flexible framework in salamander neural evolution, shaped primarily by ancestry and allometry but also allowing limited ecological and developmental signatures.

Keywords: Amphibians, Tetrapods, Geometric morphometrics, Neuroanatomy, Disparity, Evolutionary rate, Ecomorphology

3.3 INTRODUCTION

Morphological evolution in vertebrates has long been understood as the product of interactions among processes such as shared ancestry, developmental constraints, and selective pressures often tied to differences in ecologies (Anelli *et al.*, 2024; Hodge *et al.*, 2025; Ord and Summers, 2015; Roux and Robinson-Rechavi, 2008). Within this framework, amphibians offer a useful comparative model because of their diverse life histories, ecological strategies (Duellman and Trueb, 1994), and patterns of morphological integration across tissues (Bardua *et al.*, 2020; Bardua *et al.*, 2019; Fabre *et al.*, 2020; Sherratt *et al.*, 2014; Tomašević Kolarov *et al.*, 2017). Salamanders, in particular, are characterized by an unusual diversity of developmental strategies, ranging from strict biphasy with complete metamorphosis, to direct development, to facultative and obligate paedomorphosis (Bonett and Blair, 2017; Ledbetter and Bonett, 2019). The wide range of ontogenetic trajectories, combined with an evolutionary history extending over 230 million years (MA; Schoch *et al.*, 2020), provides a unique opportunity to test how different drivers interact to shape morphological diversification at macroevolutionary scales.

The vertebrate brain is a complex tissue made of a mosaic of regions differing in their developmental origins, connectivity, and functional roles (Butler and Hodos, 2005; Nieuwenhuys *et al.*, 2014; Puelles and Rubenstein, 2003). Comparative work across vertebrates has revealed that some regions, such as the telencephalon or olfactory bulbs, can evolve at rates distinct from other regions (Liao *et al.*, 2015; Watanabe *et al.*, 2019). These differences can reflect functional specialization linked to senses, locomotion, or feeding strategies, but they can also be constrained by concerted allometric scaling and phylogenetic inertia (Montgomery *et al.*, 2016). In anurans, for example, the optic tectum and cerebellum show strong phylogenetic signal, suggesting that, in some cases, neural morphology can be deeply constrained by shared ancestry rather than ecological adaptation (Rodrigues *et al.*, 2025).

Allometry has been identified as one of the major drivers of morphological evolution in many vertebrates (Montgomery *et al.*, 2016; Pélabon *et al.*, 2014). Relative changes in growth rates and tempo of different regions of the body can produce variation in phenotypes, which might be selected and lead to diversification (Sansalone *et al.*, 2020; Sol and Price, 2008). On the contrary, conservation of developmental growth patterns may lead to the canalization of phenotypes (Lazić *et al.*, 2016; Sansalone *et al.*, 2020; Sol and Price, 2008). In anurans, allometric changes were identified as an important driver of the evolution of the cranium (Bardua *et al.*, 2021), while in salamanders, it was not found to be a major aspect of skull shape variation among species (Fabre *et al.*, 2020). These contrasting patterns suggest that different amphibian lineages may follow distinct evolutionary pathways depending on how tightly growth trajectories are regulated.

Life cycle strategy has repeatedly been identified as a major determinant of morphological evolution in salamanders (Bonett and Blair, 2017; Fabre *et al.*, 2020; Ledbetter and Bonett, 2019; Louppe *et al.*, 2025). Oviparous direct development (metamorphosis completed within a terrestrial egg, yielding a hatchling that is a miniature juvenile) is restricted to Plethodontidae among extant salamanders, indicating a single origin at the caudate level, with evidence for subsequent reversals to biphasic development within the family (Chippindale *et al.*, 2004; Mueller *et al.*, 2004; Wake and Hanken, 1996). In contrast, paedomorphosis has evolved repeatedly, while a biphasic life cycle has undergone multiple independent losses and reversals across salamander lineages (Bonett and Blair, 2017; Duellman and Trueb, 1994; Ledbetter and Bonett, 2019). These developmental transitions not only affect timing of metamorphosis but also influence adult body size, ecological niche, and morphological disparity (Rowe and Ludwig, 1991; Werner, 1988; Werner, 1986). Previous research on cranial morphology has shown that paedomorphic species often exhibit the highest disparity and fastest evolutionary rates, whereas direct developers appear more constrained (Fabre *et al.*, 2020; Louppe *et al.*, 2025). Such findings underscore the importance of metamorphosis in shaping morphological evolution, a conclusion that resonates with broader vertebrate studies where major life-history transitions can sometimes

correspond to macroevolutionary shifts (Kriwet *et al.*, 2009; Watanabe *et al.*, 2019; Winemiller and Rose, 1992).

In addition to life cycle strategies, ecological context can leave imprints on neural morphology in vertebrates (González-Forero and Gardner, 2018; Gonzalez-Voyer and Kolm, 2010; Liao *et al.*, 2015). Salamanders occupy a wide spectrum of microhabitats, including aquatic, terrestrial, arboreal, and cave environments, each associated with different sensory and locomotor demands (Blankers *et al.*, 2012; McEntire, 2016; Petranka, 1998). Brain regions associated with sensory processing or locomotor control can often vary according to habitat use, reflecting divergent selective regimes (Manzano *et al.*, 2017). Taylor *et al.* (1995) found that arboreal frogs have a relatively larger cerebellum than frogs from other habitats. Additionally, arboreal anurans exhibit distinctive optic tectum and cerebellar morphologies compared to fossorial species (Rodrigues *et al.*, 2025). Similarly, a great deal of variation in telencephalon size can be explained by habitat type across Chinese anurans (Liao *et al.*, 2015). Selection for an enlarged telencephalon in arboreal species may reflect the demands of maneuvering and navigating three-dimensional habitats, consistent with its role in spatial learning and memory (Salas *et al.*, 2003). In contrast to these findings, previous studies have also suggested that microhabitat effects on the brain can be subtle or localized, and that phylogenetic inertia may overshadow ecological convergence at broad scales (Blankers *et al.*, 2012; Liao *et al.*, 2015). Distinguishing the relative strength of these ecological versus phylogenetic influences would help in clarifying the evolutionary mechanisms underlying salamander brain diversity.

Feeding innovation provides an additional context for exploring neural evolution. In plethodontid salamanders, the evolution of ballistic tongue projection has been associated with major morphological shifts in the skull and forelimbs (Fabre *et al.*, 2020; Ledbetter and Bonett, 2019). At the neural level, ballistic feeders exhibit expanded retinotectal projections and altered tectal organization (Roth *et al.*, 1993; Roth *et al.*, 1997; Roth and Schmidt, 1993), highlighting how prey-capture strategies can shape brain circuitry. However, whether these anatomical reorganizations translate into large-scale morphometric changes in brain shape is

not well established. Integrating functional innovations with macroevolutionary analyses thus provides a means to assess whether ecological novelty leaves signatures in overall neural morphology or whether its effects are restricted to fine-scale neural architecture (Deban *et al.*, 2007; Deban *et al.*, 2020).

Another key axis of investigation lies in the relationship between the brain and the endocast. Endocasts, representing the internal mold of the braincase (endocranial cavity), have long been used as proxies for brain morphology and associated soft tissues in both extant and extinct taxa (Clement *et al.*, 2021; Clement *et al.*, 2015; Early *et al.*, 2020; Macrini *et al.*, 2007; Rogers, 1999; Weisbecker *et al.*, 2021). Yet the fidelity of this proxy can vary extensively among vertebrate groups (Challands *et al.*, 2020; Jerison, 2012; Rogers, 1999). For example, in the coelacanth *Latimeria chalumnae*, the brain occupies only a small proportion of the endocranial cavity, resulting in a marked mismatch between brain and endocast morphology, whereas in many other osteichthyans the correspondence is considerably tighter (Dutel *et al.*, 2019; Challands *et al.*, 2020). The brain-endocast relationship can also vary among species within the same vertebrate group (Allemand *et al.*, 2023; Hopson, 1979; Romer and Edinger, 1942; Watanabe *et al.*, 2019). If salamander endocasts can reliably reflect major brain shape variation and evolutionary dynamics, they could provide a powerful tool for extending analyses of neural evolution into fossil lineages. Conversely, mismatches between brain and endocast trends could highlight developmental and morphological decoupling between neural and skeletal tissues. Establishing the degree of correspondence is therefore critical for improving morphological inferences of fossil amphibians and tetrapods.

This study aims to evaluate the influence of five potential drivers of morphological evolution of the brain in salamanders which are: shared ancestry, allometry, metamorphosis, types of microhabitats and the presence or absence of a ballistic tongue. Additionally, we also aim to evaluate if the endocast can serve as a reliable proxy of the brain in an evolutionary context. To do so, we used 3D geometric morphometrics on digitalized brains and endocasts (using micro-CT imaging) from 76 salamander species. Our hypotheses are that shared ancestry and

allometry are likely to have a strong influence on brain morphological evolution, since these were found to be important for anurans and caecilians (Liao *et al.*, 2015; Maddin, 2011; Rodrigues *et al.*, 2025). Following the findings of Liao *et al.* (2015) in anurans, life cycle and microhabitat are likely to have regional effects on brain evolution. Since morphological and anatomical changes were reported in species associated with a ballistic tongue system (Roth *et al.*, 1997; Roth and Schmidt, 1993), we expect that the morphological evolution of the mesencephalon and telencephalon might be affected by the evolution of the ballistic tongue in several plethodontids.

3.4 MATERIALS & METHODS

3.4.1 Specimen sampling

To document morphological variation across salamanders, we assembled a dataset of 83 specimens representing 76 species (Table E1) distributed among all ten extant Caudata families. Our goal was to span the taxonomic and morphological breadth of the clade; consequently, 40 of the 69 currently recognized genera (AmphibiaWeb, 2025) were represented. Although the sampling design prioritized phylogenetic breadth, availability of material in museum collections strongly influenced the final composition of the dataset. Most individuals originated from museum collections (Table E1). In addition to museum specimens, six individuals were collected expressly for research purposes. Two *Necturus maculosus* specimens were acquired as pre-fixed dissection material from Ward's Science. Specimens of *Ambystoma mexicanum* and *Pseudobranchus striatus* were collected and euthanized in accordance with the Calgary Animal Care Committee protocol AC15-0020, using a 5% (w/v) MS-222 solution applied until cardiac activity ceased. Two *Notophthalmus viridescens* individuals were collected under Parks Canada permit LMNP-2023-45363.

3.4.2 Preservation and contrast staining

Preservation methods varied depending on the origin of the specimen. Individuals collected by us (*A. mexicanum*, *P. striatus*, *N. viridescens*) were fixed using 10% (w/v) neutral buffered

formalin (NBF), whereas all museum-derived material had been stored in alcohol. To enhance soft-tissue contrast for micro-CT imaging, all specimens were stained with iodine (Gignac and Kley, 2014; Gignac *et al.*, 2016; Metscher, 2009). Exposure times and iodine concentrations are listed in Table E1. Although fixation and staining protocols are known to influence soft-tissue volume, particularly through shrinkage or variable penetration, previous work show that chemical preparation can modify absolute volumes but may exert only limited influence on relative geometric configurations, suggesting that shape analyses remain robust even where volumetric distortion is possible (Hedrick *et al.*, 2018; Tytiuk *et al.*, 2018; Weisbecker, 2012).

3.4.3 Micro-CT imaging and segmentation

Three-dimensional imaging of the head was carried out through high-resolution micro-CT scanning performed at three facilities (see Table E2). Reconstruction parameters varied by scanner model and local protocols. Segmentation of brain and endocast structures was achieved in Dragonfly v.2022.2 (Dragonfly 2022.2) using a deep-learning approach. The model employed a U-Net architecture incorporating a 2.5D strategy, in which predictions for each slice were informed by neighbouring images. Pixel size and input parameters were adjusted for each specimen to reflect differences in scanning resolution. Between 10 and 50 slices per specimen were manually selected to train the model, sampling anatomically diverse regions of the brain and endocast. Automated segmentation served as initial drafts; each dataset was subsequently refined manually to correct misclassifications.

3.4.4 Landmark acquisition and geometric morphometrics

Landmarks were placed on brain and endocast meshes using Stratovan Checkpoint (Stratovan Corporation). For brains, we used 28 fixed points, 26 semilandmarks positioned along curves, and 87 on surfaces; endocasts were described using 19 fixed landmarks and 58 surface semilandmarks (Figures E1-E2). Each specimen was digitized twice to evaluate measurement repeatability. Landmark coordinates were aligned using a generalized

Procrustes analysis to remove positional, rotational, and scaling effects. Sliding of curve semilandmarks followed Procrustes distances (Zelditch *et al.*, 2012). Measurement error was quantified using a fluctuating asymmetry analysis (Klingenberg *et al.*, 2002), which indicated that digitizing error accounted for 5.0% of the total shape variation. Two shape datasets were generated. The first retained only the symmetric component of shape, obtained after removing asymmetry. To evaluate and correct for the influence of size, we then fitted a Procrustes distance–based regression of symmetric shape on log-centroid size. Residuals from this model were added back to the consensus shape to create an allometry-corrected dataset. Depending on the analytical context, either centroid size was included as a covariate or the corrected shape dataset was used directly.

3.4.5 Life cycle, microhabitat and tongue-type factors

Each species was scored for life cycle type, microhabitat, and the presence or absence of a ballistic tongue (Table F1). Life cycles were categorized into five groups: (1) complex cycle (e.g., viviparous), (2) direct development, (3) biphasic cycle, (4) strict paedomorphic cycle, and (5) facultative paedomorphic cycle. Because only three species exhibited a complex life cycle, this category was excluded from hypothesis-testing analyses. Microhabitat use was classified into five categories: (1) aquatic, (2) semiaquatic, (3) terrestrial, (4) cave, and (5) arboreal. As only three species were identified as cave specialists, this group was also excluded from hypothesis-testing analyses. For the tongue-type factor, only two types of tongue were used in this study: (1) ballistic tongue and (2) non-ballistic tongue. Data on life cycle strategies, microhabitat use, and presence/absence of a ballistic tongue were compiled from several different sources listed in Table F1.

3.4.6 Phylogeny

A sample of 1000 posterior trees from the molecular based phylogeny of Jetz and Pyron (2018) was used to produce a maximum clade credibility (MCC) tree using the TreeAnnotator program in BEAST v.1.10.4 (Drummond and Rambaut, 2007). Branch

lengths were obtained using the common ancestor tree algorithm, which avoids the problem of negative branch lengths (Heled and Bouckaert, 2013). The MCC tree was pruned and branch lengths were scaled using branch-specific evolutionary rates. These branch-specific evolutionary rates were obtained from the posterior results of a Bayesian analysis performed in BayesTraitsV4 using a variable rates model and reversible jump Markov chain Monte Carlo (rjMCMC) algorithm for continuous traits. To reduce the dimensionality of shape data, a phylogenetic principal component analysis (PCA) of the symmetric shape of the brain, endocast and entire dataset (brain and endocast together) were calculated and the PC axes that explained a cumulative 95% of the total variation (27, 18, 29 PC axes retained, respectively) were used as the continuous traits for the Bayesian analysis. For each dataset, four independent rjMCMC were done using 500 000 000 iterations, sampling every 50 000 iterations with 55 000 000 iterations as burn-in. A rjMCMC uses a higher number of parameters than a regular MCMC chain, testing for the chains convergence is therefore important (Green, 1995; Pagel and Meade, 2006). The trace and density plots were investigated to validate the convergence of chains (Figures E3-E8). Additionally, the effective sample size was estimated for each parameter and the Gelman and Rubin's convergence diagnostic was also performed on each chain (Tables E3-E8).

3.4.7 Principal component analyses, allometry analyses and phylogenetic generalized least square analyses (PGLS)

PCAs were performed for the brain and endocast shapes. The shape of six major brain regions (i.e., olfactory bulb, telencephalon, hypothalamus, thalamus, mesencephalon, and rhombencephalon) and their corresponding areas of the endocast were also used in separate PCAs. Additional PCAs were performed for the brain and endocast shapes adding the centroid size to produce a size-shape PCA as described in Mitteroecker *et al.* (2004). These two size-shape PCAs were produced using the plotAllometry function (Adams *et al.*, 2013; Adams and Nistri, 2010) from the "geomorph" package v.4.0.10 (Baken *et al.*, 2021).

All PGLS analyses were performed using the ProcD.pgls function (Adams, 2014b) from the "geomorph" package v.4.0.10 (Baken *et al.*, 2021). A PGLS model was produced for the

brain and endocast shape to assess the relationship between shape and centroid size. PGLS analyses of brain and endocast shapes were also performed against life cycle, microhabitat and tongue-type factors (with the centroid size as a covariate). In addition, PGLS analyses were carried out on the first principal component (PC1) from the brain and endocast shape PCA to assess the effects of life cycle, microhabitat and tongue-type factors. Further PGLS models were applied to the shape of the six major brain regions and their corresponding areas on the endocast to test for associations with life cycle, microhabitat and tongue-type factors. To assess the relationship between shape and size, shape regression scores (as described in Drake and Klingenberg (2008)) were estimated for the brain and endocast shape and plotted against the centroid size for each of these subsets of shape data.

3.4.8 Disparity, evolutionary rates analyses and phylogenetic signal

Brain and endocast shape evolutionary rates were estimated and compared among life cycle, microhabitat and tongue-type categories using the allometry-corrected data. The evolutionary rate of morphological evolution for each major brain region and their corresponding area of the endocast were estimated and compared using the compare.evol.rate function (Adams, 2014c) from the "geomorph" package v.4.0.10 (Baken *et al.*, 2021). Evolutionary rates associated with the centroid size were also estimated and compared among life cycle, microhabitat and tongue-type categories.

Morphological disparity was quantified using the morphol.disparity function from the "geomorph" package v.4.0.10 (Baken *et al.*, 2021) and compared among life cycle, microhabitat and tongue types for the brain and endocast shape (allometry-corrected data). Disparity was also compared among major brain regions and their corresponding endocast areas. Additionally, Spearman correlations were calculated to assess the relationship between disparity and evolutionary rate for each brain region and its endocast counterpart across life cycle, microhabitat and tongue types, as well as for the entire brain and endocast. Disparity through time analyses were performed for each brain region and their corresponding area of the endocast using the dtt function from the "geiger" package v.2.0.11 (Pennell *et al.*, 2014).

The degree of phylogenetic signal present in the brain and endocast shape was estimated using a standardized effect size developed by Collyer *et al.* (2022) and implemented in the "geomorph" package v.4.0.10 (Baken *et al.*, 2021). For each group in the life cycle, microhabitat and tongue-type factors, an effect size was estimated and later used to compare the phylogenetic signal among groups. In each case, Blomberg's multiple K (Adams, 2014a; Blomberg *et al.*, 2003) and Pagel's lambda (Pagel, 1999) were also estimated.

3.5 RESULTS

3.5.1 Evolutionary allometry

Evolutionary allometry had a significant effect on both brain and endocast shape (Table 3.1). It explained 7.5% of the total shape variation in the brain and 8.4% in the endocast. Furthermore, allometry accounted for 58.5% of the variance explained by PC1 in brain shape and 44.5% in endocast shape (Table 3.1; Figure 3.1).

Table 3.1 PGLS results for the brain and endocast shape and PC1 against types of life cycle, microhabitat and tongue. The centroid size was used as a covariate in all PGLS. Df = total degree of freedom. Bold-faced numbers indicate significant values.

Brain					
Response	Predictor	Df	F	R^2	P-value
Shape	Centroid size	75	5.982	0.075	**0.028**
PC1	Centroid size	75	104.260	0.585	**0.001**
Shape	Life cycle	72	1.607	0.063	0.206
PC1	Life cycle	72	8.076	0.131	**0.001**
Shape	Microhabitat	72	1.203	0.047	0.276
PC1	Microhabitat	72	6.573	0.115	**0.001**
Shape	Ballistic	75	2.569	0.032	0.221
PC1	Ballistic	75	2.128	0.012	0.153
Endocast					

Shape	Centroid size	75	6.748	0.084	**0.028**
PC1	Centroid size	75	59.409	0.445	**0.001**
Shape	Life cycle	72	1.759	0.069	0.170
PC1	Life cycle	72	5.894	0.124	**0.002**
Shape	Microhabitat	72	1.117	0.044	0.337
PC1	Microhabitat	72	3.189	0.077	**0.029**
Shape	Ballistic	75	2.887	0.035	0.208
PC1	Ballistic	75	4.074	0.029	0.053

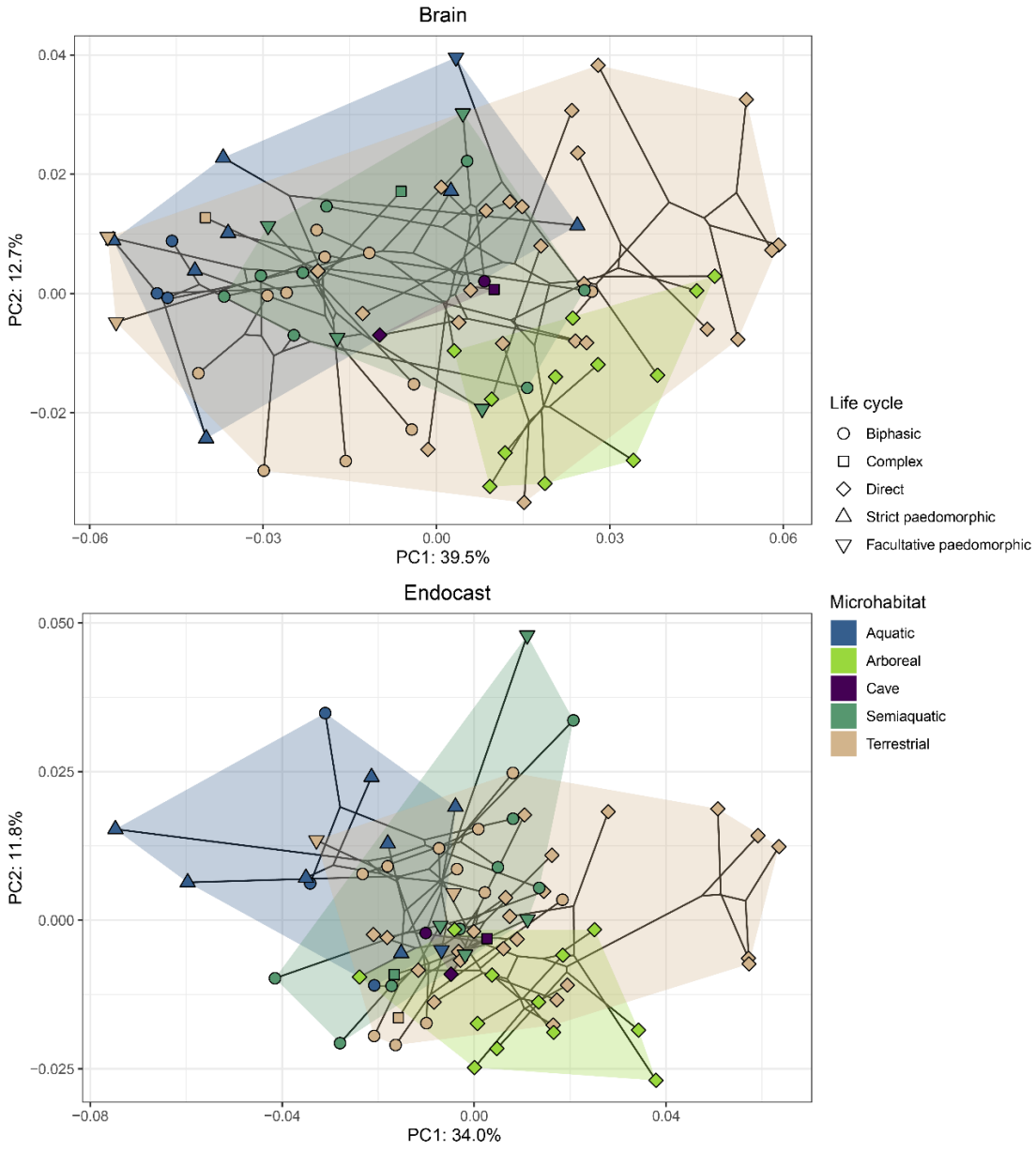

Figure 3.1 Phylomorphospace of the brain and endocast representing type of life cycle and microhabitat.

The life cycle factor did not explain significant differences in overall brain or endocast shape when centroid size was included as a covariate (Table 3.1). However, regional analyses highlighted specific patterns. The olfactory bulb exhibited a significant interaction between

centroid size and life cycle (Table F2), visible in regression scores of the shape data (Figure F1). This relationship also indicates that direct-developing species followed a distinct allometric trajectory compared to other life cycle types (Figure F1). The telencephalon also exhibits a significant difference among mean shape of life cycle categories (Table F2). Remaining regions of the brain and the endocast did not show any significant differences comparing the life cycle types (Table F2 and Figure F1). The comparison of life cycle categories using the size-shape PCA revealed that the allometry-related phylomorphospace occupation of biphasic species was visibly smaller than the one of all other life cycle types (Figure F2).

When centroid size was included as a covariate, microhabitat was not significantly associated with brain or endocast shape (Table 3.1). When considering individual brain regions, microhabitat had a significant effect on the shape of the olfactory bulb (Table F3). An interaction between centroid size and microhabitat was also detected for the shape of the region surrounding the hypothalamus (Figure F3). No other major brain regions or the endocast showed significant differences among microhabitat types (Table F3 and Figure F3). A size-shape PCA further indicated that the allometry-related phylomorphospace occupied by aquatic and terrestrial species was larger than that of the other microhabitat categories (Figure F4).

The tongue-type factor did not show any significant effects on brain or endocast shape when centroid size was included as a covariate (Table 3.1). For individual brain and endocast regions, the presence or absence of a ballistic tongue did not show any significant results (Table F4). A size-shape PCA supported the absence of an effect of the tongue-type factor by revealing no clear separation of the species with or without a ballistic tongue for either the brain or endocast (Figure F5). The allometry-related phylomorphospace occupation of the two groups were similar (Figure F5).

Together, these results indicate that evolutionary allometry had a significant influence on both brain and endocast shape, explaining a modest proportion of total shape variation but accounting for a large part of variation along the main axis of shape divergence (PC1). Life

cycle and microhabitat did not significantly affect overall brain or endocast shape once size was accounted for, although region-specific effects were detected, particularly in the olfactory bulb and, to a lesser extent, the telencephalon and hypothalamic region, often involving interactions with size. In contrast, tongue type had no detectable effect on either global or regional brain and endocast shape, and did not alter allometric trajectories or phylomorphospace occupation.

3.5.2 Phylogenetic signal

Phylogenetic signal of shape was strong and significant for both the brain and the endocast (Table F5). Within life cycle categories, both brain and endocast shapes exhibited a significant phylogenetic signal in biphasic and direct-developing species, whereas strict and facultative paedomorphic species did not (Table F5). Moreover, biphasic species displayed a significantly stronger phylogenetic signal than direct developers (Table F6). For brain shape in relation to microhabitat, aquatic, terrestrial, and semi-aquatic species did exhibit significant phylogenetic signal, whereas arboreal species did not (Table F5). These categories differed significantly from one another, with terrestrial species showing the strongest signal (Table F7). For the endocast, all microhabitat groups exhibited significant phylogenetic signal and differed significantly among themselves, with terrestrial species again showing the strongest signal (Table F5 and Table F7). Concerning the tongue-type, there was a significant phylogenetic signal for the shape of the brain and the endocast for both species that exhibit a ballistic tongue and species that do not (Table F8). Species with a ballistic tongue showed significantly higher phylogenetic signal (Table F8).

3.5.3 Life cycle

Life cycle categories accounted for 13.1% of the variation in brain shape PC1 and 12.4% in endocast shape PC1, both of which were statistically significant (Table 3.1). PCAs of major brain regions did not reveal clear separation among life cycle types (Figure F6), although mean shapes were associated with localized morphological differences (Figure F7). Direct-

developing species exhibited the shortest rhombencephalon along the anteroposterior axis, and both direct developers and strict paedomorphs showed a wider and more posteriorly elongated telencephalon relative to biphasic and facultative paedomorphic species. For the endocast, strict paedomorphs displayed the most elongated region surrounding the rhombencephalon. In contrast, the region surrounding the telencephalon was not notably wider in either direct developers or strict paedomorphs (Figure F8).

3.5.4 Microhabitat

Microhabitat categories significantly accounted for 11.5% of the variation in brain shape PC1 and 7.7% in endocast shape PC1 (Table 3.1). PCA did not reveal distinct clustering by microhabitat types, although a slight separation was observed between arboreal and aquatic species in the shape of the olfactory bulb and telencephalon (Figure F9). Arboreal species showed a wider and more anteriorly elongated olfactory bulb and telencephalon compared to aquatic species (Figure F10). Similarly, the endocast regions surrounding the olfactory bulb, telencephalon, and rhombencephalon were slightly wider in arboreal species (Figure F11).

3.5.5 Tongue-type

The tongue-type factor was not associated with a significant effect on brain and endocast shape (Table 3.1). Concerning individual brain and endocast regions, the morphospace occupation of species that possess a ballistic tongue overlaps extensively with that of species that do not (Figure F12). Overall, this indicates that ballistic tongue presence has no substantial effect on brain or endocast shape variation.

3.5.6 Disparity, evolutionary rate and rate shifts

Significant differences in the evolutionary rate of centroid size were detected across life cycle and microhabitat types, whereas no significant difference was found between species with and without a ballistic tongue (Table F9). Specifically, strict paedomorphic species exhibited a significantly higher rate compared to biphasic species and direct developers (Table F10).

Among microhabitats, aquatic species showed a significantly higher rate relative to arboreal species (Table F11). In contrast, the evolutionary rates of brain and endocast shape did not differ significantly across life cycle and microhabitat types (Table F9).

Two major rate shifts in brain and endocast shape evolution were identified early in salamander evolution. The first occurred ca. 185 MA, during the Lower Jurassic, between the Sirenidae and the remaining Salamandroidea, and the other ca. 156 MA, during the Late Jurassic, between the Cryptobranchidae and the remaining Cryptobranchoidea (traditionally referred to as the Hynobiidae; Figure 3.2 and Figure F13). These shifts may reflect transitions in body size, life cycle strategy, and microhabitat use.

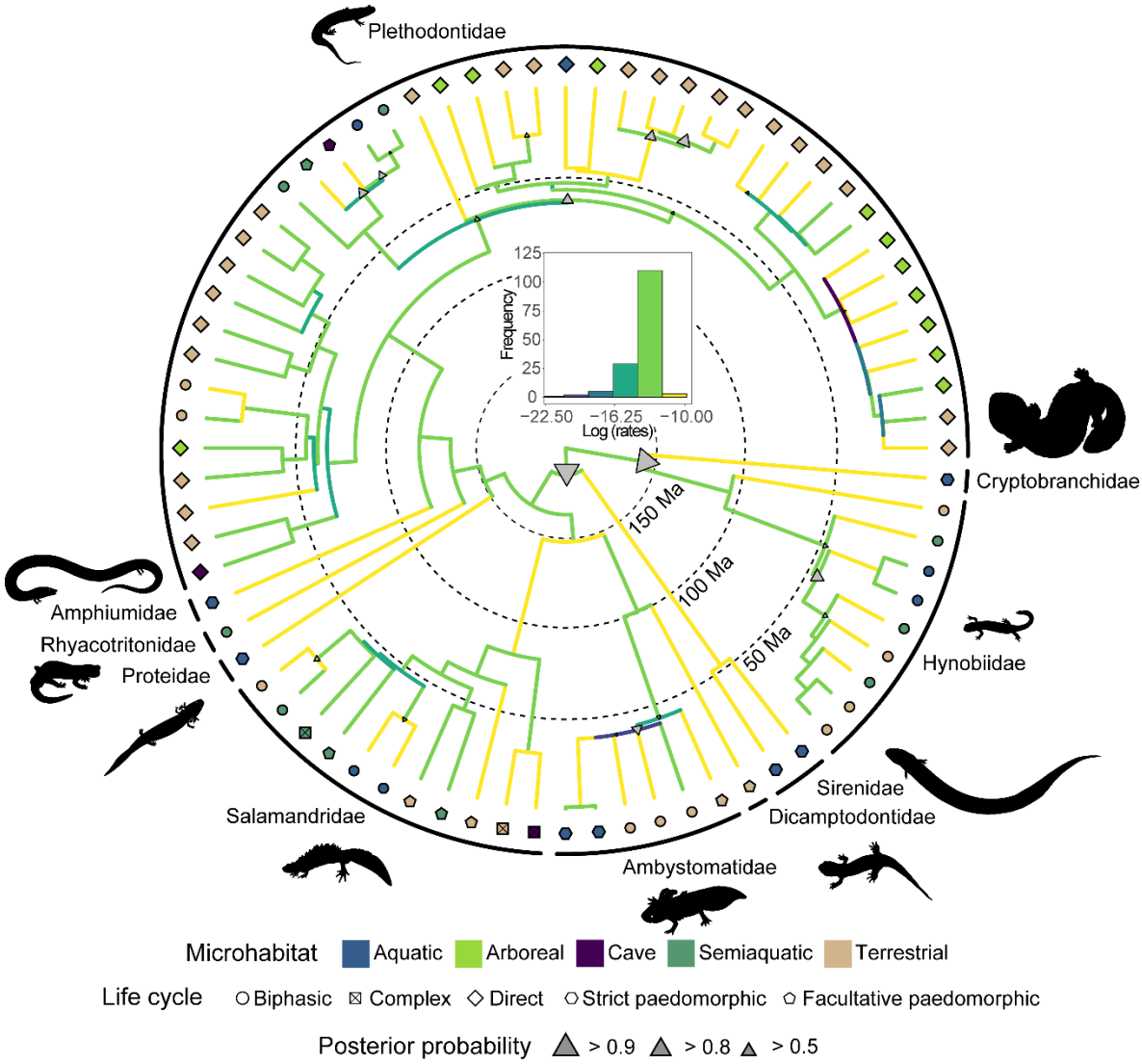

Figure 3.2 Evolutionary rates and rate shifts of the brain shape of salamanders. Branch colour gradients represent rates of brain shape evolution, with yellow colours indicating higher rates and purple colours indicating lower ones. The distribution plot shows the frequencies of log-transformed evolutionary rates. Grey triangles mark the stem branches of clades for which whole-clade rate shifts are supported, with the size of each triangle reflecting the posterior probability of the shift. Time is expressed in millions of years (MA). PhyloPic silhouettes were used except for Proteidae, which was made by the first author. PhyloPic credit: T. Michael Keesey (https://creativecommons.org/licenses/by/4.0/).

Rates of shape evolution also varied significantly among major brain regions (Table 3.2). The telencephalon was associated with the highest rate of all brain regions (Table 3.2). The olfactory bulb, thalamus and hypothalamus evolved at a significantly lower rate from that of

the telencephalon (Table 3.2). The hypothalamus and thalamus exhibited significantly lower rates compared to the mesencephalon and rhombencephalon, and the mesencephalon also evolved at a lower rate from the rhombencephalon (Table 3.2). For the endocast regions corresponding to brain areas, several differences were also detected. The corresponding region of the endocast associated with the olfactory bulb exhibited a significantly higher rate than regions of the endocast representing the telencephalon, hypothalamus, thalamus, and significantly lower than the one of the rhombencephalon (Table 3.2). The telencephalon region had a significantly higher rate than the one of the hypothalamus and lower than the one of the rhombencephalon. As in the brain, the hypothalamus and thalamus regions showed significantly lower rates from the mesencephalon and rhombencephalon. However, no significant difference in rate was found between the mesencephalon and rhombencephalon in the endocast (Table 3.2). Additionally, most brain regions and corresponding regions of the endocast were not significantly different, with the exception of the telencephalon and hypothalamus, for which the brain region had a significantly higher rate than the endocast counterpart (Table 3.2).

Table 3.2 Evolutionary rates of major brain regions and corresponding areas of the endocast. The first two lines present the evolutionary rate of each major brain and endocast region. The twelve subsequent lines present P-values form pairwise comparisons among major brain and endocast regions. Bold values represent a significant result ($p < 0.05$).

					Brain					Endocast		
	OB	TEL	HYP	THA	MES	RHO	OB	TEL	HYP	THA	MES	RHO
Rate	1.164 e-07	2.017 e-07	4.537 e-08	1.974 e-08	8.657 e-08	1.177 e-07	9.355 e-08	4.609 e-08	1.671 e-08	1.553 e-08	8.712 e-08	2.100 e-07
		TEL	HYP	THA	MES	RHO	OB	TEL	HYP	THA	MES	RHO
Brain	OB	**0.001**	0.080	0.074	1.000	1.000	0.997	**0.001**	**0.001**	0.431	1.000	**0.001**
	TEL	-	**0.001**	**0.001**	0.968	1.000	**0.001**	**0.001**	**0.001**	**0.001**	1.000	0.991
	HYP		-	0.371	**0.001**	**0.001**	**0.001**	0.979	**0.001**	0.711	1.000	**0.001**
	THA			-	**0.001**	**0.001**	**0.002**	0.867	1.000	0.961	**0.001**	**0.001**

	MES	-	**0.011**	1.000	**0.001**	**0.001**	**0.001**	1.000	**0.017**
	RHO		-	0.997	**0.001**	**0.001**	**0.001**	1.000	0.455
	OB			-	**0.001**	**0.001**	**0.035**	1.000	**0.001**
	TEL				-	**0.001**	0.983	1.000	**0.001**
Endocast	HYP					-	1.000	**0.001**	**0.001**
	THA						-	**0.001**	**0.001**
	MES							-	1.000

Disparity in brain and endocast shapes varied significantly among life cycle types, with strict paedomorphs exhibiting the highest values compared to all other categories (Table F12 and Table F13). Brain shape disparity also differed among microhabitat types: aquatic species differed significantly from arboreal and terrestrial species, and semiaquatic species differed from arboreal species (Table F14 and Table F15). These differences were not observed in endocast shape.

Subclade disparity through time for both brain and endocast shapes exceeded expectations under a Brownian motion model. Morphological disparity indices (MDI) were 0.503 for the brain and 0.486 for the endocast, indicating no significant temporal shifts. Analyses of individual brain regions and their corresponding endocast areas revealed similar patterns, with subclade disparity generally exceeding Brownian expectations (Figure F14). These patterns indicate higher within-clade disparity and substantial morphospace overlap among subclades, suggesting limited phylogenetic structuring of brain shape and the absence of early morphological diversification (Figure F14).

A significant correlation between evolutionary rate and disparity was detected for brain shape ($r = 0.886$, $p = 0.032$, $N = 6$; Figure 3.3), but not for endocast shape ($r = 0.771$, $p = 0.104$, $N = 6$; Figure 3.3). Among individual regions, the telencephalon and rhombencephalon showed the most pronounced differences between brain and endocast (Figure 3.3). Across life cycle and microhabitat types, few significant correlations between evolutionary rate and disparity

were detected (Table F16, Figure F15 and Figure F16). For the brain, significant correlations were found in facultative and strict paedomorphic species, as well as in semiaquatic species. These patterns were not mirrored in the corresponding endocast regions, in which only terrestrial species exhibited a significant correlation between evolutionary rate and disparity (Table F16 and Figure F16). Considering the tongue-type factor, a high and significant relationship was found for the species without a ballistic tongue for the brain (Table F16 and Figure F17).

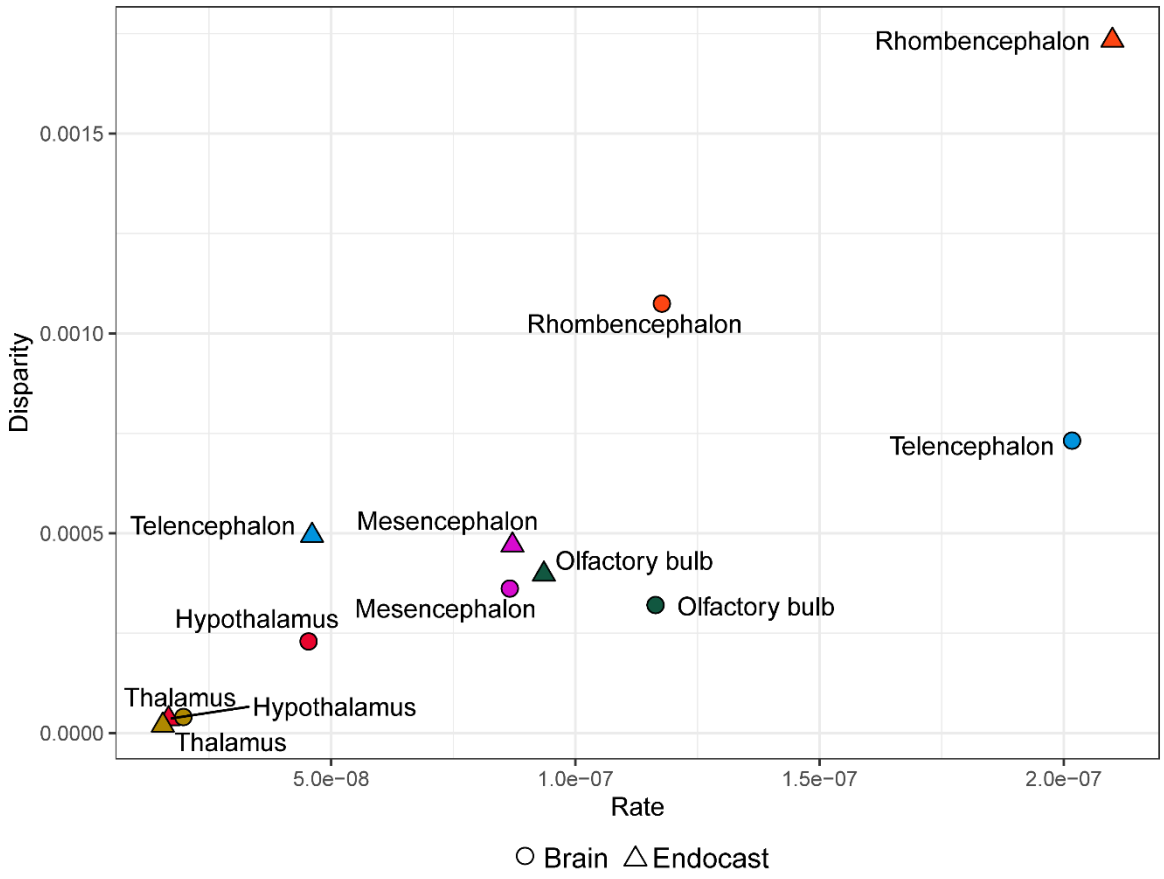

Figure 3.3 Relationship between disparity and evolutionary rate of major brain regions and corresponding areas of the endocast.

3.6 DISCUSSION

Our results show that salamander brain and endocast evolution is primarily governed by allometry and phylogenetic signal, contrasting with the stronger life-cycle imprint observed in the skull. Major rate shifts appear to coincide with historical transitions in life cycle, microhabitat use, and body size, reflecting the combined influence of developmental, ecological, and allometric factors. Paedomorphic species consistently exhibit high disparity, which aligns with previous findings for the skull and braincase (Fabre *et al.*, 2020; Szostakiwskyj and Anderson, 2022). While life cycle strategies structure variance, disparity, and evolutionary rates, their imprint on brain shape is weaker than for cranial morphology, with canalization effects evident mainly under complete metamorphosis. Microhabitat exerts

only localized effects, most notably on the olfactory bulb, whereas prey-capture innovation through ballistic feeding appears linked to neural microanatomy rather than large-scale morphometric change. Finally, despite partial mismatches, endocasts reliably capture the major evolutionary trends of the brain, confirming their value as proxies for studying both living and fossil salamanders.

3.6.1 Drivers of morphological evolution in salamanders

Allometry and phylogenetic signal clearly dominate as primary determinants of brain and endocast shapes. A comparable primacy of ancestry over ecology was found for the optic tectum and cerebellum in anurans (Rodrigues *et al.*, 2025), reinforcing a cross-amphibian pattern of strong phylogenetic inertia in neural morphology. Interestingly, this contrasts with salamander cranial evolution, in which life cycle rather than allometry was the main macroevolutionary driver of skull shape and rate (Fabre *et al.*, 2020). This brain–skull difference suggests that, despite neurocranial integration, nervous tissues may be more tightly constrained by size scaling and ancestry than the skull.

Over the past ~230 million years, salamanders have undergone multiple shifts in developmental strategies (Bonett and Blair, 2017; Fabre *et al.*, 2020; Ledbetter and Bonett, 2019). The biphasic life cycle is generally regarded as the ancestral condition within the group (Bonett and Blair, 2017; Duellman and Trueb, 1994). Direct development appears to have originated only once in salamander evolution, whereas the biphasic condition has been lost and regained repeatedly over the evolution of the Plethodontidae. Paedomorphosis is thought to have evolved independently on several occasions among salamanders (Denoël *et al.*, 2005). We detected two major rate shifts in brain and endocast evolution that align with previously identified skull shifts (Fabre *et al.*, 2020). The rate shift observed within cryptobranchoids may be linked to a change in life cycle strategy, as extant cryptobranchids and hynobiids differ in their developmental modes. It may also reflect contrasting degrees of aquatic dependence, with cryptobranchids being strictly aquatic (and paedomorphic) while hynobiids are associated with both aquatic and terrestrial habitats, and exhibit a complete

metamorphosis (Browne *et al.*, 2012; Fei and Ye, 2001). In addition, this shift coincides with a pronounced increase in body size, given that extant cryptobranchids are characterized by gigantism (Böhme *et al.*, 2012). The second rate shift may similarly be linked to major transitions in life cycle strategies, accompanied by differences in microhabitat use and body size between the Sirenidae and the remaining Salamandroidea. The association of ecological, allometric, and developmental influences therefore provides a plausible explanation for the repeated shifts in brain and endocast evolution observed across salamanders.

Our analyses also indicate that life cycle categories do not predict a clear separation in overall brain or endocast shape once centroid size is included as a covariate, yet they strongly structure PC1 variance, disparity, and evolutionary rates. For the skull, previous work shows a robust life-cycle imprint: paedomorphs exhibit the highest cranial disparity and fastest rates, whereas direct developers are most constrained, with biphasic species been intermediate (Fabre *et al.*, 2020; Louppe *et al.*, 2025). From our results, paedomorphic species also exhibited the highest disparity, which has been proposed to facilitate the persistence of these species in environment with usually poor access to food resources and mates (Bonett *et al.*, 2014; Wilbur and Collins, 1973). High morphological variation in the anterior braincase of paedomorphs has been reported previously (Szostakiwskyj and Anderson, 2022), which aligns with our results of a significantly higher shape disparity of brain and endocast shapes for paedomorphic species. Overall, the convergence of brain and braincase patterns underscores a tight morphological integration, suggesting that the directionality of evolutionary changes in paedomorphic lineages can be shared in both structures.

Bonett and Blair (2017) found that for the body form, direct developers exhibited a higher rate of evolution than biphasic species. In contrast, we did not find that to be the case for the brain, which aligns more closely to what was previously found for the skull (Fabre *et al.*, 2020). Across different tissues, evidence from salamander skulls (Fabre *et al.*, 2020), mandibles (Louppe *et al.*, 2025), and brains points to a consistent role of metamorphosis in shaping morphological opportunity, with effects that are robust in bones but comparatively

muted in the brain. Developmental canalization was proposed to reduce the morphological variation of species with multistage life cycles (Bonett and Blair, 2017). Following similar conclusions for what was observed for the skull (Fabre *et al.*, 2020), we found that only complete metamorphosis could be associated with brain shape canalization. Also, head shape has not been associated with a reduction of its variation at the intraspecific level (Bonett and Blair, 2017). Our results (at the interspecific level) on brains diverge from the ones of Bonett and Blair (2017), suggesting that micro- and macroevolutionary processes may differ.

Globally, microhabitat explains little of overall shape when centroid size is included as a covariate, except for the shape of olfactory bulbs for which arboreal species differed from aquatic species. This result follows other findings in anurans for which the microhabitat was found to influence brain morphology or size (Liao *et al.*, 2015; Rodrigues *et al.*, 2025). In other vertebrates, olfactory bulb characteristics were also found to be related to ecological factors including microhabitats (Avilés and Amo, 2018; Gittleman, 1991). The specific regional signal found for the olfactory bulb also aligns to findings associated with other vertebrates, such as mammals (Finlay and Darlington, 1995; Finlay *et al.*, 2001), where the olfactory bulb appears to exhibit increased evolutionary independence compared to other regions. Thus, while broad morphological conservatism persists, neural tissues retain localized ecological signatures, particularly in sensory-processing regions.

For plethodontid ballistic feeders, skull and limb morphology was demonstrated to be constrained, showing low values of disparity and rate of evolution (Fabre *et al.*, 2020; Ledbetter and Bonett, 2019). As for the brain, ballistic feeders were associated with expanded retinotectal projections and increased tectal neuron density (Roth *et al.*, 1993; Roth *et al.*, 1997; Roth and Schmidt, 1993). Here, we recovered no gross brain or endocast shape effect associated with ballistic feeders. This may suggest that prey-capture innovation involved microanatomical reorganization rather than large-scale morphometric changes, a result consistent with experimental work on feeding mechanics and neural circuitry (Deban *et al.*, 2007; Deban *et al.*, 2020).

3.6.2 Brain-endocast correspondence

While it is apparent that the brain-endocast relationship is not as reliable as for other vertebrate groups such as birds and mammals (Early *et al.*, 2020; Jerison, 1985), our results show a general fit between the major brain regions and their endocast counterparts in salamanders. A reduction in the magnitude of shape changes was observed between the brain and the endocast regarding life cycle and microhabitat types. Although the shape correspondence between the brain and endocast appears to be partial, nonetheless, the most important trends in regards to disparity and evolutionary rates were paralleled in both structures. The shape-size principal component analyses also showed a close correspondence of the shape variation among the first PC, indicating that size-related shape changes of the brain might be preserved in the endocast shape. Therefore, regarding primary shape changes, disparity and evolutionary rates, the endocast does appear to be a reliable proxy of brain shape in salamanders.

3.7 CONCLUSION

Taken together, these findings reinforce the view that salamander evolution is shaped primarily by allometry and constrained by phylogeny. Life cycle and microhabitat impose localized effects on the brain and endocast shape evolution. The combination of strong phylogenetic inertia, deep historical rate shifts, and localized ecological imprints offers a compelling parallel to cranial and mandibular evolution in salamanders (Fabre *et al.*, 2020; Louppe *et al.*, 2025) and to broader vertebrate patterns of ecomorphological diversification under integration constraints (Watanabe *et al.*, 2019).

3.8 ACKNOWLEDGEMENTS

Financial support for this research was provided by the Natural Sciences and Engineering Research Council of Canada (NSERC) and the Fonds de recherche du Québec – Nature et technologies (FRQNT). Access to scan images of two specimens was kindly provided by Jason Pardo, and specimen loans were made possible through the assistance of museum staff

members Stéphanie Tessier (Canadian Museum of Nature), Amy Lathrop (Royal Ontario Museum), Rachunliu Kamei (Field Museum of Natural History), Joshua Mata (Field Museum of Natural History), Ana Motta (Kansas University Biodiversity Institute), Carol Spencer (Museum of Vertebrate Zoology), Lauren Vonnahme (American Museum of Natural History), and David A. Kizirian (American Museum of Natural History).

CONCLUSION GÉNÉRALE

1. CONTEXTE, ORIGINALITE DE L'ETUDE ET RAPPEL DES OBJECTIFS

Dans cette thèse, les travaux de recherche réalisés permettent d'intégrer de l'information provenant de patrons observables sur des organismes vivants à des processus évolutifs majeurs chez les vertébrés, en particulier quant à l'évolution du cerveau. Trois objectifs principaux structuraient cette thèse doctorale. Le premier consistait à décrire le patron de covariation au sein des régions du cerveau d'une espèce modèle de salamandre afin d'identifier la présence de contraintes fonctionnelles et développementales, et ce durant l'ontogénie. Le deuxième objectif visait à étudier le patron de covariation au sein des régions du cerveau chez les salamandres afin d'identifier la présence de contraintes fonctionnelles et développementales, selon une perspective phylogénétique. Le troisième objectif avait pour but d'évaluer l'influence de facteurs allométriques, phylogénétiques, développementaux et écologiques sur l'évolution du cerveau chez les salamandres. Esteve-Altava (2017) a démontré que la majorité des études traitant de modularité dans un contexte évolutif se concentraient sur des aspects soit micro- ou macro-évolutifs, c'est-à-dire à l'échelle de l'individu ou de l'espèce, respectivement, et bien peu d'entre elles abordaient ces deux aspects simultanément (p. ex., Goswami *et al.*, 2014; Klingenberg *et al.*, 2001; Sears *et al.*, 2013). Les travaux de cette thèse permettent d'aborder des mécanismes évolutifs importants associés au cerveau des vertébrés en étudiant des patrons observables aux échelles micro- et macro-évolutives.

2. PRINCIPAUX RESULTATS

Les travaux liés au premier objectif ont conduit à plusieurs résultats. Parmi ceux-ci, les analyses ont permis d'identifier l'hypothèse de modularité cérébrale la mieux supportée selon

les trois approches statistiques employées. L'hypothèse proposant six modules (lobes olfactifs, télencéphale, thalamus, hypothalamus, mesencéphale et rhombencéphale) distincts s'est révélée la plus robuste, mettant en évidence un signal de modularité important au sein du cerveau de l'axolotl.

Le premier objectif a aussi permis de mettre en évidence des indices suggérant la présence de contraintes développementales au cours du développement de l'axolotl. Bien que le signal de modularité soit marqué, un certain degré d'intégration morphologique a été détecté entre les modules cérébraux. Cette intégration indique qu'un lien développemental subsiste entre certaines régions du cerveau, ce qui appuie en partie un modèle d'évolution concertée. Cette cohésion entre les régions du cerveau a déjà été documentée dans la littérature (Finlay et Darlington, 1995; Finlay *et al.*, 2001; Willemet, 2013). De plus, les analyses volumétriques ont, elles aussi, contribué à mettre en évidence la présence de contraintes développementales au sein du cerveau de l'axolotl. Ces analyses ont montré une correspondance forte entre le volume de chaque région et le volume du reste du cerveau. Bien qu'il ne s'agisse pas de relations isométriques, ces relations impliquent qu'un certain niveau de cohésion existe entre la taille d'une région et la taille totale du cerveau. Ce résultat, bien qu'attendu, constitue un support pour le modèle concerté de l'évolution.

Une autre contrainte développementale possible découle de la faible variation morphologique de la région de l'hypothalamus. En effet, la limite entre le télencéphale et le diencéphale est considérée chez plusieurs groupes de vertébrés comme pouvant avoir un rôle de guidage important dans la formation de certaines sutures osseuses, dont la suture coronale (entre l'os frontal et pariétal; Piekarski *et al.*, 2014; Teng *et al.*, 2019). L'hypothalamus, et plus précisément le chiasme optique, étant la section la plus ventrale du diencéphale et situé à proximité de la limite télencéphale-diencéphale, constitue un repère important dans l'étude des liens développementaux entre le neurocrâne et le cerveau (Ollonen *et al.*, 2024; Teng *et al.*, 2019). La stabilité de cette région, illustrée par les résultats de cet objectif, peut être

indicative d'un effet potentiel de guidage dans la formation d'autres structures anatomiques, telles que des os du crâne.

Le premier objectif a aussi permis de mettre en évidence la présence de contraintes fonctionnelles lors du développement de l'axolotl. En effet, le mésencéphale et les lobes olfactifs ont été associés à une croissance allométrique positive durant la première partie de la période de développement étudiée. Le mésencéphale est principalement impliqué dans le traitement visuel, tandis que les lobes olfactifs assurent des fonctions essentielles liées à l'olfaction (Hodos, 1988; Nieuwenhuys *et al.*, 2014). Le télencéphale a aussi présenté une relation allométrique positive durant toute la période étudiée, montrant que cette région, associée à l'intégration des informations sensorielles et à la prise de décision chez les salamandres (Hodos, 1988), connaît une croissance accrue par rapport à plusieurs autres régions du cerveau durant cette période. Ainsi, la présence de différences marquées dans la relation allométrique des régions du cerveau suggère la présence de contraintes associées aux fonctions spécifiques des régions. De plus, le fort signal de modularité détecté au sein de cette étude peut être indicatif d'une organisation morphologique mosaïque.

Finalement, une autre conclusion importante de ce premier objectif est la présence d'un moment de forts changements entre les stades de développement 47 et 50 de la table de Nye *et al.* (2003). Ce moment du développement est associé à un changement drastique du volume relatif du mésencéphale, du télencéphale et des lobes olfactifs. Ces changements pourraient être dus à une pression forte associée à l'alimentation, puisque les larves d'axolotl commencent à s'alimenter directement après l'éclosion. Ce début d'alimentation coïncide bien avec la période associée aux stades de 47 à 50 de la table de Nye *et al.* (2003), qui sont parmi les premiers après l'éclosion (Atkins *et al.*, 2020).

Un résultat majeur du deuxième objectif est associé à l'identification d'évidences de contraintes développementales au sein du cerveau chez les salamandres. La constance dans la relation entre la suture coronale et le chiasme optique au sein des salamandres peut être considérée comme une évidence de la présence de contraintes développementales. La

présence d'un niveau intermédiaire d'intégration morphologique entre les modules du cerveau démontre aussi un certain support pour le modèle concerté de l'évolution. Le mésencéphale est le module qui a présenté le plus faible niveau d'intégration interne et une assez forte intégration avec les modules environnants, ce qui peut suggérer un certain niveau d'association concertée.

Un fort signal de modularité a été identifié au sein du cerveau des salamandres. Les lobes olfactifs et le rhombencéphale ont été identifiés comme les plus indépendants des modules du cerveau, ce qui suggère une certaine indépendance évolutive de ces régions. Les lobes olfactifs étant associés à la détection et à l'intégration des informations chimiques (Hodos, 1988), cela conforte le rôle important de l'olfaction chez les salamandres. Quant au rhombencéphale, son rôle étant principalement lié à la coordination motrice et aux fonctions autonomes de base (Hodos, 1988), son indépendance pourrait être liée à la diversité de stratégies de locomotion (p. ex., aquatique, terrestre, arboricole) présentes chez les salamandres. Cette organisation modulaire au sein des régions du cerveau peut servir d'évidence en soutien au modèle mosaïque d'évolution.

Les deux premiers objectifs ont permis de suggérer la présence de contraintes développementales à des échelles différentes. La stabilité de la zone de transition entre le télencéphale et le diencéphale à des niveaux micro- et macro-évolutifs est un élément intéressant qui est compatible avec le rôle potentiel de cette région dans la formation de la suture coronale. Le degré d'intégration morphologique inter-modules du cerveau dans les travaux des deux premiers objectifs montre aussi une présence de contraintes développementales à des échelles intraspécifique et interspécifique.

De plus, les deux premiers chapitres démontrent la présence d'indépendance entre certaines régions du cerveau. Que ce soit au niveau d'une seule espèce ou d'un échantillon de plusieurs espèces, le signal de modularité était fort dans les deux cas. L'hypothèse la plus supportée dans ces deux objectifs s'est avérée être la même (lobes olfactifs, télencéphale, thalamus, hypothalamus, mésencéphale et rhombencéphale). Cela pourrait impliquer que les modules

évolutifs (à l'échelle de l'espèce) et variationnels (à l'échelle de l'individu) sont similaires et fortement conservés au cours du développement et de l'évolution chez les salamandres. Selon les résultats des deux premiers chapitres, les lobes olfactifs représentent une région qui est morphologiquement assez indépendante sur le plan développemental et évolutif. Cette indépendance particulière a aussi été notée chez d'autres groupes de vertébrés, comme les mammifères (Finlay et Darlington, 1995; Finlay *et al.*, 2001). Cependant, une différence notable est associée au mésencéphale qui a été associé à un niveau d'indépendance assez grand à l'échelle développementale et une intégration plus forte avec les autres modules à l'échelle interspécifique.

Le troisième objectif a, entre autres, permis de préciser l'importance du rôle des stratégies de cycle de vie dans l'évolution du cerveau chez les salamandres. L'influence des cycles de vie est limitée quant à l'évolution du cerveau, ce qui contraste avec un signal plus fort dans le cas d'autres structures comme le crâne (Fabre *et al.*, 2020). Les microhabitats ont eux aussi une influence limitée quant à l'évolution du cerveau chez les salamandres. Des différences ont toutefois été trouvées entre des espèces aquatiques et arboricoles quant à la forme des lobes olfactifs. Le type de langue a aussi été testé comme une force potentielle influençant l'évolution des salamandres. Suite aux analyses, la présence d'une langue à projection balistique chez certaines espèces n'a pas d'influence directe sur la morphologie générale du cerveau.

Le deuxième et troisième objectifs ont permis de montrer l'importance de l'allométrie et de la phylogénie comme des forces majeures dirigeant l'évolution du cerveau chez les salamandres. La forme du cerveau chez les espèces de grande taille semble aplatie dorso-ventralement alors que le cerveau des espèces miniatures est plus globuleux et compact. Cette tendance allométrique a déjà été observée au niveau d'autres structures associées à la tête, telles que le crâne (Bardua *et al.*, 2021; Fabre *et al.*, 2020). L'influence des relations phylogénétiques, reflétant une contrainte évolutive importante, a déjà été mise en évidence pour certaines structures cérébrales chez les amphibiens (Rodrigues *et al.*, 2025), de manière

comparable à celle observée dans cet objectif.Les deux derniers objectifs illustrent tous les deux le lien entre le cerveau et l'endocaste. L'adéquation entre l'hypothèse de modularité la plus supportée du cerveau et celle de l'endocaste démontre une correspondance morphologique entre les deux structures. De plus, les travaux du troisième objectif indiquent que l'importance relative des différentes forces guidant l'évolution morphologique du cerveau est similaire à celle détectée pour l'endocaste. Cela implique la possibilité d'une représentation assez fidèle de la morphologie du cerveau par l'endocaste, même dans des contextes évolutifs variés (p. ex., allométrie, phylogénie, écomorphologie).

3. PORTEE DE L'ETUDE

Cette thèse a permis de produire un portrait nouveau et complet du développement morphologique et de l'évolution du cerveau chez les salamandres, ce qui n'a pas été fait dans la littérature auparavant. En effet, le groupe des salamandres n'a pas été étudié de façon intégrative quant à la morphologie du cerveau en utilisant un échantillon complet des familles du groupe (p. ex., Lazcano *et al.*, 2021; Romer et Edinger, 1942; Roth *et al.*, 1990; Roth et Schmidt, 1993). Les travaux de cette thèse sont complémentaires à l'étude de Fabre *et al.* (2020) sur l'évolution du crâne chez les salamandres. Ces nouvelles informations offriront des bases de comparaison plus solides avec d'autres groupes de vertébrés et pourraient contribuer à améliorer notre compréhension de l'évolution des amphibiens, voire des premiers tétrapodes.

Les spécimens de salamandres utilisés dans le cadre de cette étude ont été scannés dans un micro-tomographe à rayons X. Les images résultantes de ces scans ont été rendues disponibles sur un site web dédié au partage de ce genre d'information (MorphoSource). Ainsi, les images issues de cette thèse pourront servir de matériel utile dans le cadre d'autres études sur la morphologie de structures associées à la tête de salamandres actuelles.

L'espèce étudiée dans le cadre du premier objectif (*Ambystoma mexicanum*) est utilisée comme un modèle dans le domaine du développement et de la régénération (Pan *et al.*, 2023;

Voss *et al.*, 2009). La description du développement morphologique du cerveau durant le premier mois de vie post-éclosion pourrait s'avérer grandement utile dans l'avancement des connaissances sur cette espèce. L'axolotl mexicain fait aussi partie des espèces utilisées dans l'étude des liens de signalisation développementale entre le cerveau et le crâne (Maddin *et al.*, 2016; Piekarski *et al.*, 2014; Teng *et al.*, 2019). Les résultats de cette étude suggérant une stabilité de la zone entre le télencéphale et le diencéphale pourraient servir à d'autres chercheurs afin d'investiguer plus en profondeur cette période du développement et cette zone spécifique du cerveau dans de futurs travaux.

Les résultats des deux derniers objectifs ont permis de valider l'utilité de l'endocaste pour estimer la morphologie du cerveau chez les salamandres. Ce résultat s'imbrique dans les nombreux efforts visant à mieux comprendre l'évolution du cerveau durant les périodes clés de l'évolution (Challands *et al.*, 2020; Clement *et al.*, 2021). Ces résultats offrent, par exemple, la possibilité d'effectuer des études incluant l'endocaste d'espèces de salamandres fossiles et actuelles et de pouvoir formuler des conclusions assez fiables sur la morphologie du cerveau, comme il est commun de faire chez des groupes comme les mammifères (p. ex., Bertrand *et al.*, 2019; Weisbecker *et al.*, 2021).

4. LIMITATIONS DE L'ETUDE

Le micro-tomographe à rayons X utilisé dans cette étude a permis d'obtenir une résolution tout à fait adéquate des structures cérébrales globales. Cependant, la résolution la plus fine étant 8,1 micromètres, il est possible que cela ait empêché de représenter fidèlement la glande pituitaire chez certaines des spécimens adultes utilisés pour les deux derniers objectifs. En effet, la glande pituitaire n'a pas été représentée dans les analyses, puisque la résolution des images ne permettait pas une segmentation claire de cette structure chez plusieurs spécimens. Cette structure est positionnée très près de plusieurs vaisseaux sanguins et nerfs (Nieuwenhuys *et al.*, 2014), ce qui peut rendre difficile une segmentation précise de cette région.

De plus, il est possible que la glande pituitaire ait été affectée par une source de déformation potentielle des tissus nerveux. En effet, sur plusieurs spécimens, cette structure fine apparaissait légèrement déformée. Étant une structure séparée spatialement du cerveau chez les salamandres (Lazcano *et al.*, 2021), il est possible qu'une légère déformation ait pu affecter plus spécifiquement cette région, rendant plus difficile sa segmentation. Dans le cadre de cette étude, un protocole strict limitant la déformation des tissus nerveux a été employé, mais il est connu que les spécimens de musée peuvent présenter de la déformation au niveau des structures molles comme le cerveau (Gignac *et al.*, 2016). Cependant, il est important de mentionner que Weisbecker (2012) a indiqué que la présence d'une légère déformation du cerveau ne limitait pas la portée des analyses de forme.

Les divisions faites entre les différentes régions du cerveau dans cette étude ont été basées sur des repères anatomiques. Cette technique est globalement fiable, peu coûteuse et rapide, mais elle n'est pas nécessairement la méthode la plus précise pour définir des régions distinctes. En effet, certaines techniques telles que le marquage avec des anticorps fluorescents peuvent permettre de mieux déterminer les limites entre des régions du cerveau (Perens et Hecksher-Sørensen, 2022; Perens *et al.*, 2021). Il est donc important de reconnaître que les délimitations régionales utilisées dans cette étude doivent être interprétées avec prudence, puisqu'elles peuvent entraîner une simplification ou une approximation des frontières anatomiques réelles.

Dans les analyses des deux derniers objectifs, un échantillon de 76 espèces et de 83 spécimens de salamandres a été utilisé. Ainsi, la variation intraspécifique a été peu représentée. Or, il est connu que certaines espèces de salamandres peuvent présenter du dimorphisme sexuel quant à certains aspects morphologiques (Bruce, 2000; Ficetola *et al.*, 2013; Wang *et al.*, 2023). Il est important de considérer que les résultats des deux derniers objectifs ne prennent en compte que très peu de cette source de variation morphologique potentielle.

5. PERSPECTIVES DE RECHERCHE DANS LE DOMAINE CONCERNE

Le premier objectif a permis de montrer le patron de covariation du cerveau lors du premier mois de vie d'une espèce modèle chez les salamandres. Dans ce contexte, il pourrait être intéressant d'étendre la période du développement considérée en incluant des stades avant l'éclosion et des stades juvéniles et adultes. Cela permettrait d'avoir un portrait plus complet des changements associés à la covariation morphologique des régions du cerveau au cours du développement. Cependant, certaines limitations associées à l'homologie des points références et à la délimitation des régions seraient à considérer. Aussi, puisqu'il est possible d'induire la métamorphose de façon contrôlée en laboratoire chez l'axolotl (Monaghan *et al.*, 2014; Prahlad et DeLanney, 1965; Ussing et Rosenkilde, 1995), il pourrait être intéressant de tester l'effet de cette phase de transition majeure sur le patron de covariation du cerveau en comparant des individus métamorphosés et paedomorphes. De plus, étudier la morphologie du cerveau lors du développement chez d'autres espèces de salamandres serait très pertinent afin de représenter de potentielles différences entre des familles taxonomiques distinctes. Des espèces possédant des caractéristiques contrastées seraient un moyen efficace de comparer les patrons de covariation des structures cérébrales (p. ex., espèces aquatiques et arboricoles).

Le deuxième objectif a permis de caractériser le patron de covariation entre les régions cérébrales chez les salamandres en intégrant une perspective phylogénétique. Dans ce contexte, l'étude de la modularité du cerveau à l'échelle populationnelle représenterait une avenue particulièrement intéressante. En effet, certaines espèces de salamandres présentent des différences marquées entre populations, notamment en lien avec la taille corporelle ou même avec la stratégie de cycle de vie adoptée (Romano et Ficetola, 2010; Semlitsch et Gibbons, 1985; Semlitsch *et al.*, 1990). Comparer le patron de covariation observé au sein des populations à celui mesuré à l'échelle de l'espèce offrirait ainsi l'occasion d'évaluer la stabilité ou la variabilité des processus évolutifs selon le niveau d'organisation considéré, et de mieux cerner les mécanismes qui façonnent l'évolution cérébrale à différentes échelles.

Le troisième objectif a permis de montrer l'effet de plusieurs facteurs sur l'évolution du cerveau chez les salamandres. Dans le cadre de cette étude, l'allométrie, les liens de parenté, le type de langue, le microhabitat et le type de cycle de vie ont été utilisés comme éléments potentiels guidant l'évolution du cerveau de ce groupe. Cependant, d'autres facteurs pourraient aussi être pertinents à tester. Il est connu que plusieurs espèces de salamandres présentent un dimorphisme sexuel (Bruce, 2000; Ficetola *et al.*, 2013; Wang *et al.*, 2023). Il pourrait être intéressant de tester l'effet du sexe sur l'évolution du cerveau et d'explorer l'intensité d'un dimorphisme potentiel de forme et de taille du cerveau chez des espèces de salamandres.

6. RECHERCHES FUTURES

Une avenue intéressante quant à de futures recherches dans le domaine de cette étude serait l'utilisation de spécimens frais plutôt que des spécimens provenant de collections de musée d'histoire naturelle (comme dans les deux derniers objectifs). Les spécimens frais peuvent permettre un niveau de déformation minimal qui est requis pour des analyses plus poussées que celles portant sur la forme générale des structures. En effet, en utilisant des spécimens frais en plus d'autres techniques spécialisées pour limiter au maximum la déformation fine des tissus cérébraux, il est possible d'étudier le volume des structures avec une plus grande précision et même d'être en mesure d'estimer la densité neuronale des régions. Ainsi, il serait possible d'acquérir une définition à l'échelle cellulaire plutôt qu'une échelle macroscopique comme celle utilisée dans cette étude. Le fait d'utiliser des spécimens frais plutôt que des spécimens de musée offrirait la possibilité d'utiliser des solutions de fixation plus adaptées aux études sur la morphologie interne, telles que le paraformaldéhyde par exemple, qui est connu pour être un meilleur fixateur que le formaldéhyde neutre largement utilisé dans les collections de musées d'histoire naturelle (Metscher, 2009). De plus, une technique intéressante afin de limiter la déformation des structures cérébrales est l'utilisation d'hydrogel polymérisé qui permet de mieux conserver la conformation naturelle de structures

molles comme le cerveau (Wong *et al.*, 2013). Ces méthodes peuvent augmenter la précision des analyses plus poussées à des échelles fines d'organisation tissulaire.

De plus, l'utilisation de techniques d'histologie combinées à des anticorps fluorescents représente une avenue particulièrement prometteuse pour améliorer la délimitation des régions cérébrales, en comparaison avec une approche reposant sur des repères anatomiques macroscopiques. Par exemple, Lazcano *et al.* (2021) montrent que les colorations histologiques et l'immunohistochimie permettent de distinguer finement différents types cellulaires et couches neuronales dans le cerveau de l'axolotl, fournissant une résolution tissulaire bien supérieure à celle obtenue par l'imagerie morphologique seule. Pour des études nécessitant un niveau de détails anatomiques fin, cette précision est essentielle pour identifier correctement les frontières entre structures adjacentes, qui peuvent paraître continues ou difficiles à distinguer, particulièrement pour des stades développement précoces.

Cette précision devient particulièrement cruciale dans un contexte développemental. Durant les phases pré-éclosion et post-éclosion, les frontières entre régions cérébrales sont encore en formation, les tissus sont en croissance rapide et certaines structures sont peu différenciées. Les techniques fluorescentes permettent alors de suivre l'émergence progressive de noyaux ou de couches neuronales, de visualiser des patrons de maturation (p. ex., myélinisation, différenciation cellulaire) et d'identifier des régions qui seraient impossibles à distinguer visuellement à partir de la morphologie externe. Ainsi, l'intégration de ces nouvelles méthodes offrirait un cadre plus robuste pour mesurer la forme, le volume et la densité neuronale des régions cérébrales au cours du développement, réduisant l'incertitude associée aux délimitations basées uniquement sur des repères anatomiques.

ANNEXE A : INFORMATION SUPPLÉMENTAIRE DU CHAPITRE 1

Table A1. Description of landmarks used on the brain of *A. mexicanum* larvae. curveSM = curve semilandmark. surfaceSM = surface semilandmark.

Landmark number	Type	Side	Description
1	fixed	Median	Medio-dorsal point of optic tectum
2	fixed	Median	Ventral-most point of hypothalamus dorsalis
3	fixed	Median	Dorsal posterior end of medulla oblongata
4	fixed	Median	Ventral point parallel to posterior end of medulla oblongata
5	fixed	Left	Left ventral border between forebrain bundle and hypothalamus dorsalis
6	fixed	Right	Right ventral border between forebrain bundle and hypothalamus dorsalis
7	fixed	Median	Medio-ventral point of optic chiasm
8	fixed	Left	Left lateral-most point of hypothalamus dorsalis
9	fixed	Right	Right lateral-most point of hypothalamus dorsalis
10	fixed	Median	Medio-dorsal point of anterior medulla oblongata
11	fixed	Left	Left dorsal-most point of telencephalon
12	fixed	Right	Right dorsal-most point of telencephalon
13	fixed	Left	Left anterior most point of olfactory bulb
14	curveSM	Left	Semilandmark in lateral region of left olfactory bulb
15	curveSM	Left	Semilandmark in lateral region of left olfactory bulb
16	fixed	Left	Left lateral and posterior end of olfactory bulb
17	curveSM	Left	Semilandmark in lateral region of left olfactory bulb
18	curveSM	Left	Semilandmark in lateral region of left olfactory bulb
19	fixed	Left	Left posterior end of telencephalon
20	fixed	Right	Right anterior most point of olfactory bulb
21	curveSM	Right	Semilandmark in lateral region of right olfactory bulb
22	curveSM	Right	Semilandmark in lateral region of right olfactory bulb
23	fixed	Right	Right lateral and posterior end of olfactory bulb
24	curveSM	Right	Semilandmark in lateral region of right olfactory bulb
25	curveSM	Right	Semilandmark in lateral region of right olfactory bulb
26	fixed	Right	Right posterior end of telencephalon
27	fixed	Left	Left lateral and anterior most point of white matter of medulla oblongata
28	curveSM	Left	Semilandmark on the left crest of white matter of medulla oblongata
29	curveSM	Left	Semilandmark on the left crest of white matter of medulla oblongata

Landmark number	Type	Side	Description
30	fixed	Left	Left dorsal point at lateral constriction of medulla oblongata
31	fixed	Right	Right lateral and anterior most point of white matter of medulla oblongata
32	curveSM	Right	Semilandmark on the right crest of white matter of medulla oblongata
33	curveSM	Right	Semilandmark on the right crest of white matter of medulla oblongata
34	fixed	Right	Right dorsal point at lateral constriction of medulla oblongata
35	fixed	Left	Left border between tegmentum and hypothalamus dorsalis
36	curveSM	Left	Semilandmark in the lateral region of tegmentum
37	curveSM	Left	Semilandmark in the lateral region of tegmentum
38	curveSM	Left	Semilandmark in the lateral region of optic tectum
39	curveSM	Left	Semilandmark in the lateral region of optic tectum
40	curveSM	Left	Semilandmark in the posterior and dorsal region of cerebellum
41	fixed	Median	Medio-posterior point of cerebellum
42	curveSM	Right	Semilandmark in the posterior and dorsal region of cerebellum
43	curveSM	Right	Semilandmark in the lateral region of optic tectum
44	curveSM	Right	Semilandmark in the lateral region of optic tectum
45	curveSM	Right	Semilandmark in the lateral region of tegmentum
46	curveSM	Right	Semilandmark in the lateral region of tegmentum
47	fixed	Right	Right border between tegmentum and hypothalamus dorsalis
48	fixed	Left	Left lateral and anterior most point of grey matter of medulla oblongata
49	curveSM	Left	Semilandmark in the anterior region of grey matter of medulla oblongata
50	curveSM	Left	Semilandmark in the anterior region of grey matter of medulla oblongata
51	fixed	Median	Median ventral and anterior most point of grey matter of medulla oblongata
52	curveSM	Right	Semilandmark in the anterior region of grey matter of medulla oblongata
53	curveSM	Right	Semilandmark in the anterior region of grey matter of medulla oblongata
54	fixed	Right	Right lateral and anterior most point of grey matter of medulla oblongata
55	surfaceSM	Left	Semilandmark in the ventral region of forebrain bundle
56	surfaceSM	Left	Semilandmark in the ventral region of forebrain bundle
57	surfaceSM	Median	Semilandmark in the ventral region of forebrain bundle
58	surfaceSM	Right	Semilandmark in the ventral region of forebrain bundle
59	surfaceSM	Right	Semilandmark in the ventral region of forebrain bundle
60	surfaceSM	Left	Semilandmark in the ventral region of telencephalon
61	surfaceSM	Left	Semilandmark in the ventral region of telencephalon
62	surfaceSM	Left	Semilandmark in the ventral region of telencephalon
63	surfaceSM	Left	Semilandmark in the ventral region of olfactory bulb
64	surfaceSM	Left	Semilandmark in the ventral region of olfactory bulb
65	surfaceSM	Right	Semilandmark in the ventral region of telencephalon
66	surfaceSM	Right	Semilandmark in the ventral region of telencephalon
67	surfaceSM	Right	Semilandmark in the ventral region of telencephalon

Landmark number	Type	Side	Description
68	surfaceSM	Right	Semilandmark in the ventral region of olfactory bulb
69	surfaceSM	Right	Semilandmark in the ventral region of olfactory bulb
70	surfaceSM	Left	Semilandmark in the dorsal region of dorsal pallium
71	surfaceSM	Left	Semilandmark in the dorsal region of dorsal pallium
72	surfaceSM	Left	Semilandmark in the dorsal region of olfactory bulb
73	surfaceSM	Left	Semilandmark in the dorsal region of olfactory bulb
74	surfaceSM	Left	Semilandmark in the lateral region of lateral pallium
75	surfaceSM	Left	Semilandmark in the lateral region of lateral pallium
76	surfaceSM	Left	Semilandmark in the lateral region of striatum
77	surfaceSM	Left	Semilandmark in the lateral region of striatum
78	surfaceSM	Right	Semilandmark in the lateral region of lateral pallium
79	surfaceSM	Right	Semilandmark in the lateral region of lateral pallium
80	surfaceSM	Right	Semilandmark in the lateral region of striatum
81	surfaceSM	Right	Semilandmark in the lateral region of striatum
82	surfaceSM	Right	Semilandmark in the ventral region of hypothalamus ventralis
83	surfaceSM	Right	Semilandmark in the ventral region of hypothalamus ventralis
84	surfaceSM	Left	Semilandmark in the ventral region of hypothalamus ventralis
85	surfaceSM	Left	Semilandmark in the ventral region of hypothalamus ventralis
86	surfaceSM	Right	Semilandmark in the lateral region of hypothalamus dorsalis
87	surfaceSM	Right	Semilandmark in the lateral region of hypothalamus dorsalis
88	surfaceSM	Right	Semilandmark in the lateral region of hypothalamus dorsalis
89	surfaceSM	Right	Semilandmark in the lateral region of hypothalamus dorsalis
90	surfaceSM	Right	Semilandmark in the lateral region of hypothalamus dorsalis
91	surfaceSM	Left	Semilandmark in the lateral region of hypothalamus dorsalis
92	surfaceSM	Left	Semilandmark in the lateral region of hypothalamus dorsalis
93	surfaceSM	Left	Semilandmark in the lateral region of hypothalamus dorsalis
94	surfaceSM	Left	Semilandmark in the lateral region of hypothalamus dorsalis
95	surfaceSM	Left	Semilandmark in the lateral region of hypothalamus dorsalis
96	surfaceSM	Left	Semilandmark in the lateral region of ventral thalamus
97	surfaceSM	Left	Semilandmark in the lateral region of ventral thalamus
98	surfaceSM	Left	Semilandmark in the lateral region of dorsal thalamus
99	surfaceSM	Left	Semilandmark in the lateral region of optic tectum
100	surfaceSM	Right	Semilandmark in the lateral region of ventral thalamus
101	surfaceSM	Right	Semilandmark in the lateral region of ventral thalamus
102	surfaceSM	Right	Semilandmark in the lateral region of dorsal thalamus
103	surfaceSM	Right	Semilandmark in the lateral region of optic tectum
104	surfaceSM	Left	Semilandmark in the lateral region of tegmentum
105	surfaceSM	Left	Semilandmark in the lateral region of tegmentum

Landmark number	Type	Side	Description
106	surfaceSM	Left	Semilandmark in the lateral region of tegmentum
107	surfaceSM	Left	Semilandmark in the dorsal region of optic tectum
108	surfaceSM	Left	Semilandmark in the dorsal region of optic tectum
109	surfaceSM	Right	Semilandmark in the lateral region of tegmentum
110	surfaceSM	Right	Semilandmark in the lateral region of tegmentum
111	surfaceSM	Right	Semilandmark in the lateral region of tegmentum
112	surfaceSM	Right	Semilandmark in the dorsal region of optic tectum
113	surfaceSM	Right	Semilandmark in the dorsal region of optic tectum
114	surfaceSM	Left	Semilandmark in the dorsal region of optic tectum
115	surfaceSM	Left	Semilandmark in the dorsal region of optic tectum
116	surfaceSM	Right	Semilandmark in the dorsal region of optic tectum
117	surfaceSM	Right	Semilandmark in the dorsal region of optic tectum
118	surfaceSM	Left	Semilandmark in the anterior region of white matter of medulla oblongata
119	surfaceSM	Left	Semilandmark in the anterior region of white matter of medulla oblongata
120	surfaceSM	Right	Semilandmark in the anterior region of white matter of medulla oblongata
121	surfaceSM	Right	Semilandmark in the anterior region of white matter of medulla oblongata
122	surfaceSM	Left	Semilandmark in the anterior region of white matter of medulla oblongata
123	surfaceSM	Left	Semilandmark in the anterior region of white matter of medulla oblongata
124	surfaceSM	Right	Semilandmark in the anterior region of white matter of medulla oblongata
125	surfaceSM	Right	Semilandmark in the anterior region of white matter of medulla oblongata
126	surfaceSM	Left	Semilandmark in the dorsal region of white matter of medulla oblongata at lateral constriction
127	surfaceSM	Right	Semilandmark in the dorsal region of white matter of medulla oblongata at lateral constriction
128	surfaceSM	Left	Semilandmark in the posterior region of white matter of medulla oblongata
129	surfaceSM	Left	Semilandmark in the posterior region of white matter of medulla oblongata
130	surfaceSM	Left	Semilandmark in the posterior region of white matter of medulla oblongata
131	surfaceSM	Left	Semilandmark in the posterior region of white matter of medulla oblongata
132	surfaceSM	Right	Semilandmark in the posterior region of white matter of medulla oblongata
133	surfaceSM	Right	Semilandmark in the posterior region of white matter of medulla oblongata
134	surfaceSM	Right	Semilandmark in the posterior region of white matter of medulla oblongata
135	surfaceSM	Right	Semilandmark in the posterior region of white matter of medulla oblongata
136	surfaceSM	Left	Semilandmark in the lateral and anterior region of grey matter of medulla oblongata
137	surfaceSM	Left	Semilandmark in the lateral and anterior region of grey matter of medulla oblongata
138	surfaceSM	Left	Semilandmark in the lateral and posterior region of grey matter of medulla oblongata
139	surfaceSM	Left	Semilandmark in the lateral and posterior region of grey matter of medulla oblongata
140	surfaceSM	Left	Semilandmark in the lateral and posterior region of grey matter of medulla oblongata

Landmark number	Type	Side	Description
141	surfaceSM	Right	Semilandmark in the lateral and anterior region of grey matter of medulla oblongata
142	surfaceSM	Right	Semilandmark in the lateral and anterior region of grey matter of medulla oblongata
143	surfaceSM	Right	Semilandmark in the lateral and posterior region of grey matter of medulla oblongata
144	surfaceSM	Right	Semilandmark in the lateral and posterior region of grey matter of medulla oblongata
145	surfaceSM	Right	Semilandmark in the lateral and posterior region of grey matter of medulla oblongata
146	surfaceSM	Median	Semilandmark in the median and anterior region of grey matter of medulla oblongata
147	surfaceSM	Median	Semilandmark in the median and anterior region of grey matter of medulla oblongata
148	surfaceSM	Median	Semilandmark in the median and posterior region of grey matter of medulla oblongata
149	surfaceSM	Median	Semilandmark in the median and posterior region of grey matter of medulla oblongata
150	surfaceSM	Median	Semilandmark in the median and posterior region of grey matter of medulla oblongata
151	surfaceSM	Right	Semilandmark in the dorsal region of dorsal pallium
152	surfaceSM	Right	Semilandmark in the dorsal region of dorsal pallium
153	surfaceSM	Right	Semilandmark in the dorsal region of olfactory bulb
154	surfaceSM	Right	Semilandmark in the dorsal region of olfactory bulb
155	surfaceSM	Left	Semilandmark in the ventral region of optic chiasm
156	surfaceSM	Left	Semilandmark in the ventral region of optic chiasm
157	surfaceSM	Left	Semilandmark in the lateral region of optic chiasm
158	surfaceSM	Left	Semilandmark in the lateral and anterior region of hypothalamus dorsalis
159	surfaceSM	Left	Semilandmark in the lateral and anterior region of hypothalamus dorsalis
160	surfaceSM	Median	Semilandmark in the median and posterior region of optic chiasm
161	surfaceSM	Median	Semilandmark in the medio-ventral region of hypothalamus dorsalis
162	surfaceSM	Right	Semilandmark in the ventral region of optic chiasm
163	surfaceSM	Right	Semilandmark in the ventral region of optic chiasm
164	surfaceSM	Right	Semilandmark in the lateral region of optic chiasm
165	surfaceSM	Right	Semilandmark in the lateral and anterior region of hypothalamus dorsalis
166	surfaceSM	Right	Semilandmark in the lateral and anterior region of hypothalamus dorsalis
167	surfaceSM	Left	Semilandmark in the dorso-lateral border of hypothalamus dorsalis and ventral thalamus
168	surfaceSM	Left	Semilandmark in the dorso-lateral border of hypothalamus dorsalis and ventral thalamus
169	surfaceSM	Right	Semilandmark in the dorso-lateral border of hypothalamus dorsalis and ventral thalamus
170	surfaceSM	Right	Semilandmark in the dorso-lateral border of hypothalamus dorsalis and ventral thalamus
171	surfaceSM	Left	Semilandmark in the lateral region of ventral thalamus

Landmark number	Type	Side	Description
172	surfaceSM	Left	Semilandmark in the lateral region of ventral thalamus
173	surfaceSM	Left	Semilandmark in the lateral region of dorsal thalamus
174	surfaceSM	Median	Semilandmark in the dorsal region of dorsal thalamus
175	surfaceSM	Right	Semilandmark in the lateral region of dorsal thalamus
176	surfaceSM	Right	Semilandmark in the lateral region of ventral thalamus
177	surfaceSM	Right	Semilandmark in the lateral region of ventral thalamus
178	surfaceSM	Median	Semilandmark in the dorsal region of dorsal thalamus
179	surfaceSM	Median	Semilandmark in the dorsal region of dorsal thalamus
180	surfaceSM	Median	Semilandmark in the dorsal region of optic tectum
181	surfaceSM	Median	Semilandmark in the dorsal region of optic tectum

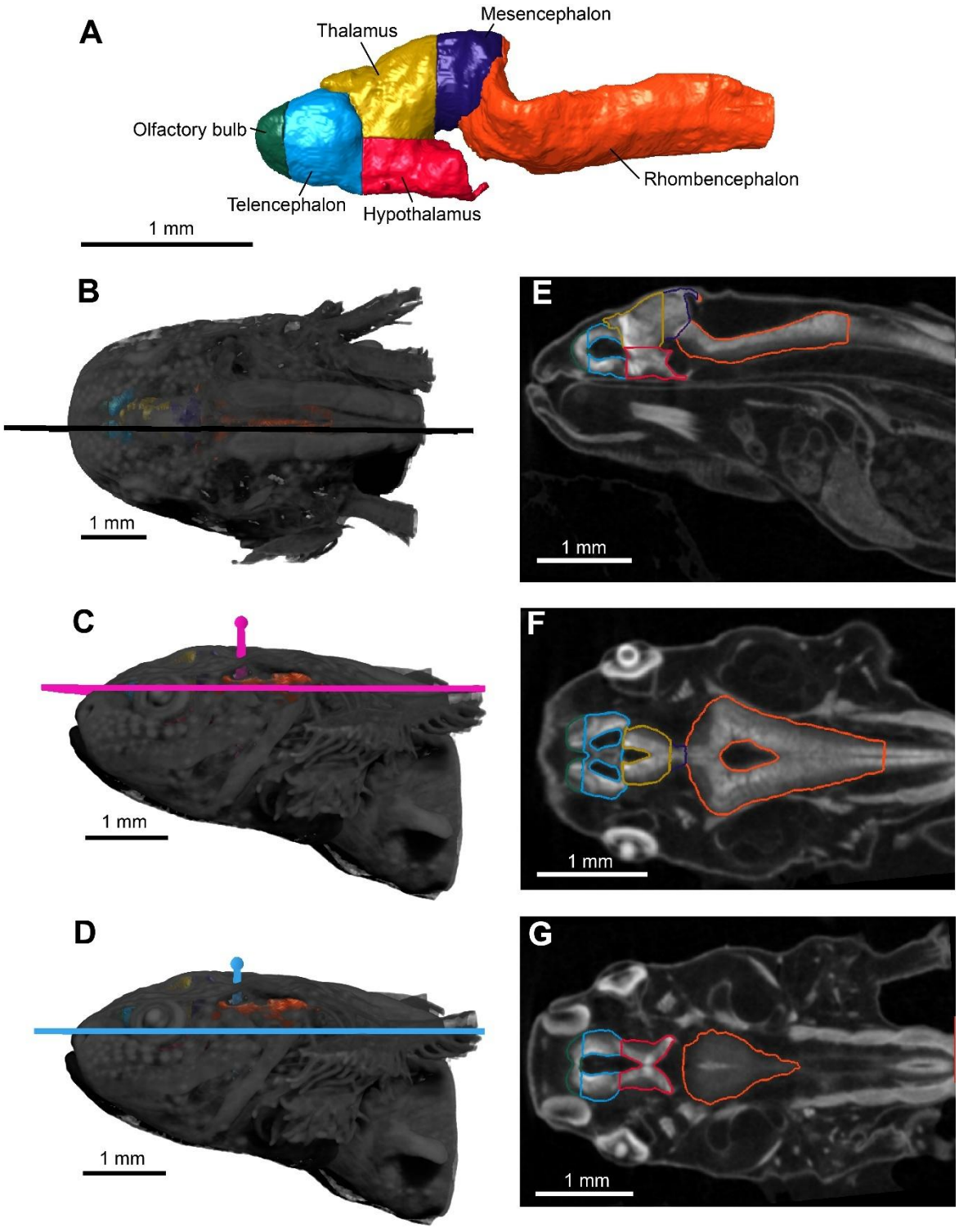

Figure A1. Representation of delineation of volume partitions from a 3D point of view (A) and from CT images of different parts of a specimen (B, C, D, E, F, G). A sagittal view near

the median section of the specimen is shown (E) and a black line represent the area associated with that view (B). Also, two transversal views are presented (F and G) and the area corresponding to these views are indicated by a pink (C) and blue lines (D), respectively.

Table A2. Size-included Procrustes ANOVA and pairwise distance between least-squares means and shape variance comparisons results for the size-included brain shape of *A. mexicanum* larvae. The first line presents the Procrustes ANOVA results and the subsequent lines present the effect size (Z) of the pairwise distance between means and shape variance comparisons. P-values from the pairwise comparisons are in parentheses. Bold values represent significant results.

	R^2	F	Z	P-value
ANOVA	0.612	38.439	5.469	**0.001**
		Procrustes distances		
Developmental stage	47	50	52	54
50	3.088 (**0.001**)			
52	3.434 (**0.001**)	1.003 (0.195)		
54	3.283 (**0.001**)	1.647 (0.051)	0.598 (0.298)	
		Variance		
Developmental stage	47	50	52	54
50	0.910 (0.199)			
52	-1.585 (0.933)	0.762 (0.251)		

54	-0.878 (0.799)	1,169 (0.135)	-0.687 (0.742)	

Table A3. Size-excluded Procrustes ANOVA and pairwise distance between least-squares means and shape variance comparisons results for the size-excluded brain shape of *A. mexicanum* larvae. The first line present the Procrustes ANOVA results and the subsequent lines present the effect size (Z) of the pairwise distance between means and shape variance comparisons. P-values from the pairwise comparisons are in parentheses. Bold values represent significant results.

	R^2	F	Z	P-value
ANOVA	0.252	8.214	4.665	**0.001**
		Procrustes distances		
Developmental stage	47	50	52	54
50	4.326 (**0.001**)			
52	3.216 (**0.001**)	2.124 (**0.015**)		
54	1.542 (0.065)	3.189 (**0.001**)	2.082 (**0.021**)	
		Variance		
Developmental stage	47	50	52	54
50	0.345 (0.379)			
52	-1.023 (0.834)	0.639 (0.284)		
54	0.396 (0.368)	1.407 (0.088)	0.026 (0.489)	

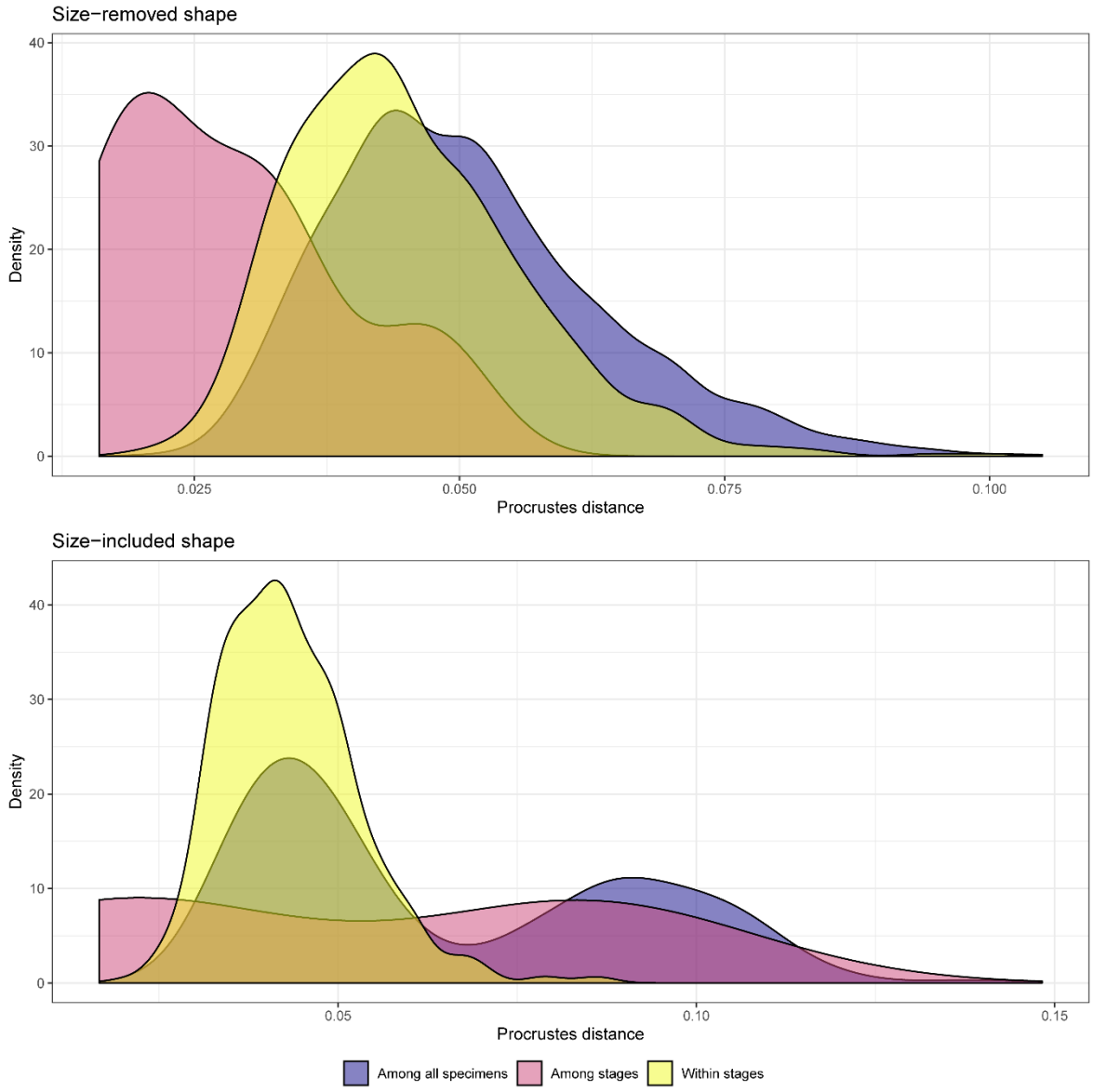

Figure A2. Density plots of the frequency of Procrustes distances associated with among stages variation, within stages variation and variation among all specimens of *A. mexicanum* larvae.

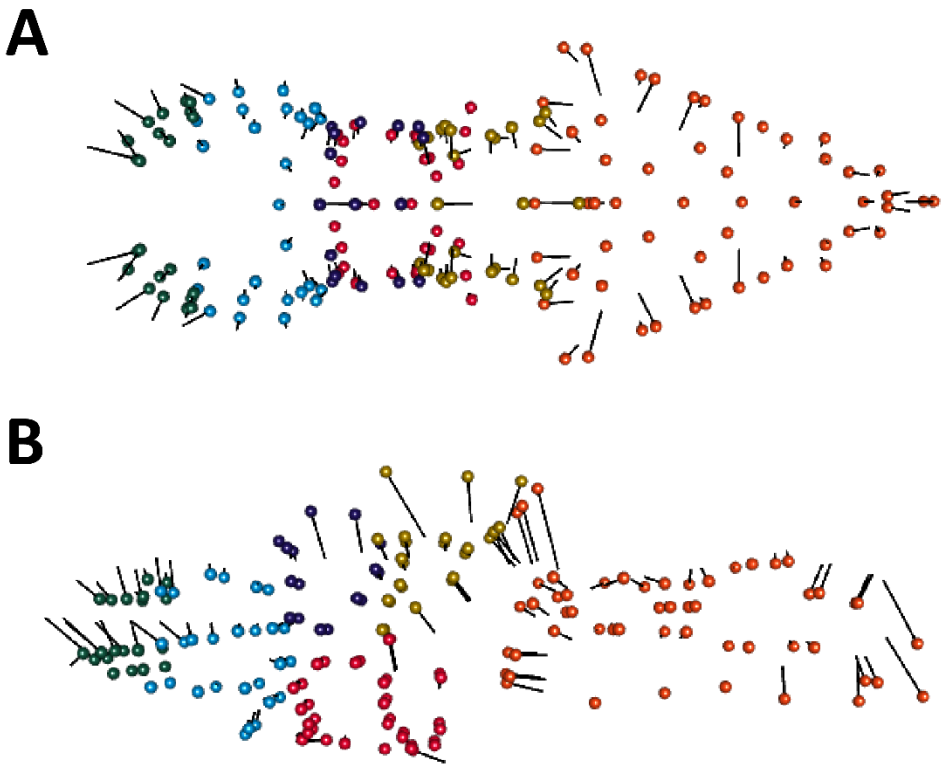

Figure A3. Dorsal (A) and lateral (B) views of the shape variation from the Procrustes linear regression. Colors represent the six different brain regions of *A. mexicanum* larvae: olfactory bulb (dark green), telencephalon (light blue), thalamus (dark purple), hypothalamus (red), mesencephalon (gold), and rhombencephalon (orange).

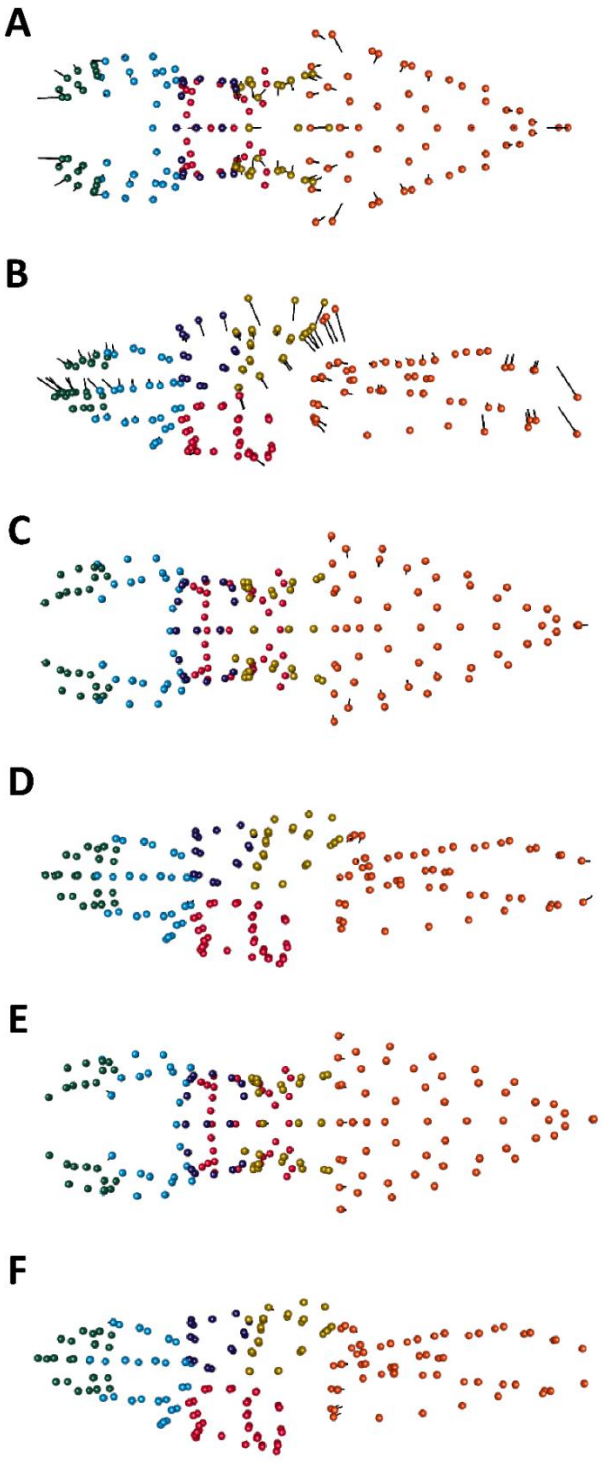

Figure A4. Dorsal and lateral views of the shape variation from the size-included dataset between the mean shape of stage 47 and stage 50 (A, B), the mean shape of stage 50 and 52

(C, D), and the mean shape of stage 52 and 54 (E, F) of *A. mexicanum* larvae. Colors represent the six different brain regions: olfactory bulb (dark green), telencephalon (light blue), thalamus (dark purple), hypothalamus (red), mesencephalon (gold), and rhombencephalon (orange).

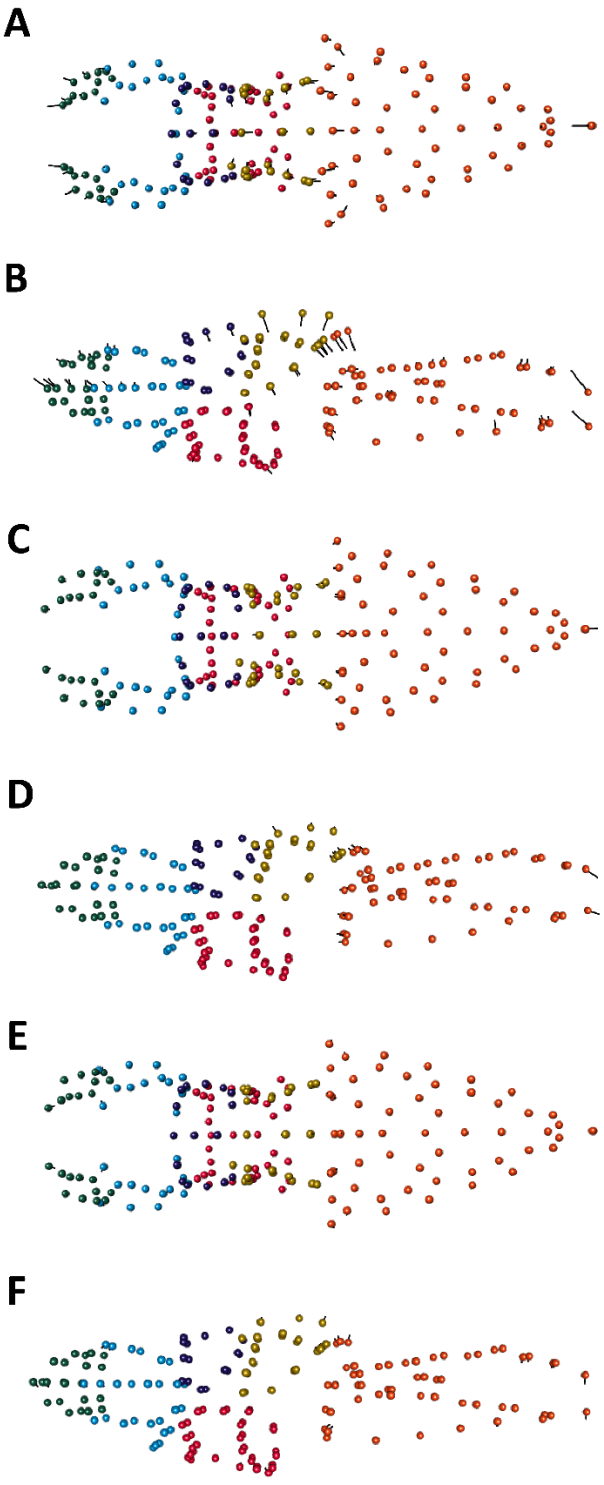

Figure A5. Dorsal and lateral views of the shape variation from the size-removed dataset between the mean shape of stage 47 and stage 50 (A, B), the mean shape of stage 50 and 52

(C, D), and the mean shape of stage 52 and 54 (E, F) of *A. mexicanum* larvae. Colors represent the six different brain regions: olfactory bulb (dark green), telencephalon (light blue), thalamus (dark purple), hypothalamus (red), mesencephalon (gold), and rhombencephalon (orange).

Table A4. Extra sum of squares F-test results and AIC values for the allometric model selection of brain volumetric data for *A. mexicanum* larvae. Bold values indicate that the piecewise model had a significantly better fit to the data.

Brain region	extra sum of squares F-test		Linear model AIC	Piecewise model AIC
	F	P-value		
Olfactory bulbs	6.311	**0.003**	-166.925	-175.206
Telencephalon	0.647	0.527	-259.610	-256.962
Hypothalamus	0.898	0.412	-242.553	-240.424
Thalamus	6.693	**0.002**	-272.980	-281.944
Mesencephalon	4.815	**0.011**	-225.429	-230.969
Rhombencephalon	1.926	0.153	-326.192	-326.151

Table A5. Coefficients (± 95% confidence interval) associated with the best supported regression model of brain region volumes of *A. mexicanum* larvae. Each line present results of a different model.

Brain region	Best supported regression model	Slope	Intercept	R^2
Olfactory bulbs	Piecewise	slope 1: 2.184 ± 0.678 slope 2: 0.964± 0.309	-1.128 ± 0.122	0.777
Telencephalon	Linear	1.611 ± 0.107	-0.799 ± 0.010	0.922

Thalamus	Piecewise	slope 1: 0.641± 0.195 slope 2: 1.186 ± 0.225	-0.925 ± 0.037	0.867
Hypothalamus	Linear	0.888 ± 0.106	-1.114 ± 0.011	0.785
Mesencephalon	Piecewise	slope 1: 1.570 ± 0.420 slope 2: 0.883 ± 0.229	-0.833 ± 0.084	0.837
Rhombencephalon	Linear	0.638 ± 0.052	-0.398 ± 0.006	0.886

Table A6. Results of morphological integration analyses using partial least squares (PLS) and modularity analyses using the covariance ratio (CR) and EMMLi methods for the six a priori hypotheses for each developmental stage of brain shape of *A. mexicanum* larvae. The results in bold represent best supported hypotheses.

	CR method			EMMLi			Morphological integration			Stage
Hypothesis	CR	P-value	Z	K	AICc	ΔAICc	PLS	P-value	Z	
1	0.941	0.024	-1.878	4	181242.440	40463.639	0.957	0.001	3.802	47
2	0.882	0.001	-2.840	4	170171.452	29392.650	0.877	0.011	2.345	
3	0.839	0.001	-4.397	7	165138.557	24359.756	0.869	0.001	3.209	
4	0.802	0.001	-5.780	11	147769.785	6990.983	0.873	0.001	4.535	
5	0.758	0.001	-6.731	16	145813.314	5034.512	0.846	0.001	5.212	
6	**0.712**	**0.001**	**-7.466**	**22**	**140778.801**	**0.000**	**0.798**	**0.001**	**4.839**	
1	0.889	0.001	-3.537	4	173655.567	41521.308	0.907	0.001	2.730	50
2	0.806	0.001	-4.025	4	162970.205	30835.946	0.844	0.020	2.085	
3	0.774	0.001	-5.653	7	156852.864	24718.605	0.814	0.001	3.126	
4	0.754	0.001	-6.730	11	139166.433	7032.174	0.813	0.001	3.723	

5	0.731	0.001	-6.948	16	137349.728	5215.469	0.806	0.001	4.248	
6	**0.728**	**0.001**	**-6.914**	**22**	**132134.259**	**0.000**	**0.810**	**0.001**	**4.486**	
1	0.885	0.001	-5.087	4	156246.603	37155.987	0.904	0.002	2.661	
2	0.807	0.001	-5.350	4	146676.074	27585.458	0.853	0.025	2.005	
3	0.799	0.001	-6.881	7	141566.624	22476.008	0.852	0.001	3.626	52
4	0.753	0.001	-8.665	11	125361.243	6270.627	0.811	0.001	4.121	
5	0.762	0.001	-8.315	16	123685.084	4594.468	0.811	0.001	4.473	
6	**0.733**	**0.001**	**-8.389**	**22**	**119090.616**	**0.000**	**0.792**	**0.001**	**4.398**	
1	0.937	0.003	-2.555	4	179548.179	41095.403	0.944	0.001	3.516	
2	0.845	0.001	-4.345	4	167831.260	29378.485	0.939	0.001	3.639	
3	0.840	0.001	-5.421	7	162487.849	24035.073	0.930	0.001	4.169	54
4	0.781	0.001	-7.507	11	145370.834	6918.058	0.879	0.001	3.862	
5	0.769	0.001	-7.802	16	143484.421	5031.645	0.883	0.001	4.067	
6	**0.757**	**0.001**	**-7.934**	**22**	**138452.776**	**0.000**	**0.855**	**0.001**	**4.268**	

Table A7. P-values from pairwise covariance ratio effect size associated with modularity hypotheses for brain shape of *A. mexicanum* larvae. Bold values represent significant results.

Modularity hypothesis	No modules	1	2	3	4	5	Stage
1	**0.000**						
2	**0.000**	0.462					
3	**0.000**	0.336	0.323				
4	**0.000**	**0.039**	0.056	0.098			All
5	**0.000**	**0.012**	**0.022**	**0.037**	0.287		
6	**0.000**	**0.005**	**0.010**	**0.016**	0.162	0.329	
1	**0.030**						
2	**0.002**	0.192					47

Modularity hypothesis	No modules	1	2	3	4	5	Stage
3	**0.000**	0.062	0.298				
4	**0.000**	**0.019**	0.165	0.316			
5	**0.000**	**0.006**	0.084	0.175	0.314		
6	**0.000**	**0.002**	**0.043**	0.093	0.184	0.337	
1	**0.000**						50
2	**0.000**	0.160					
3	**0.000**	0.072	0.394				
4	**0.000**	**0.041**	0.326	0.422			
5	**0.000**	**0.027**	0.271	0.350	0.419		
6	**0.000**	**0.027**	0.267	0.345	0.413	0.494	
1	**0.000**						52
2	**0.000**	0.086					
3	**0.000**	**0.049**	0.471				
4	**0.000**	**0.008**	0.271	0.269			
5	**0.000**	**0.011**	0.294	0.296	0.469		
6	**0.000**	**0.004**	0.197	0.187	0.377	0.350	
1	**0.005**						54
2	**0.000**	**0.045**					
3	**0.000**	**0.031**	0.478				
4	**0.000**	**0.003**	0.255	0.203			
5	**0.000**	**0.001**	0.181	0.131	0.375		
6	**0.000**	**0.001**	0.132	0.087	0.280	0.394	

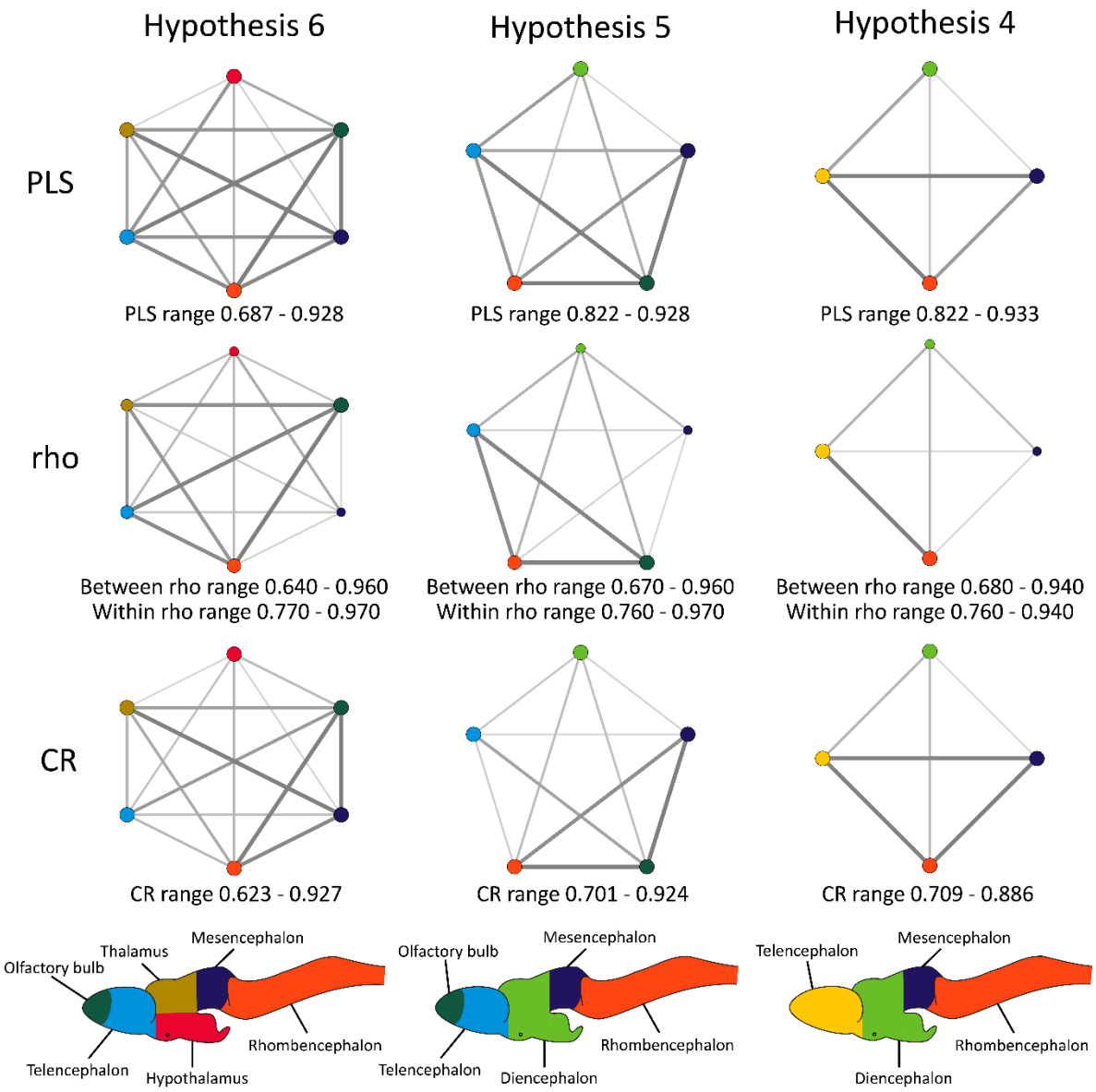

Figure A6. Network representations of the strength of morphological integration from the covariance ratio (CR), the EMMLi (rho) and the partial least squares (PLS) analyses for three a priori hypotheses for the brain shape of *A. mexicanum* larvae. Edge width in each network represents the strength of the association between two modules. Note that the edge width is based on values within each analysis (i.e., not directly comparable between networks). For the EMMLi analysis, the edge width represents the correlation between two modules and the size of nodes represents the within module correlation.

Table A8. Global integration results for each studied developmental stage of *A. mexicanum* larvae.

Stage	Global integration slope
All	-0.865
47	-0.743
50	-0.821
52	-0.892
54	-0.881

Table A9. P-values from the pairwise comparison of the effect size of relative eigenvalue index comparing differences in integration level among studied developmental stages of *A. mexicanum* larvae.

Stage	47	50	52
50	0.841		
52	0.907	0.757	
54	0.452	0.347	0.541

Table A10. P-values from the pairwise comparison of the effect size of the pairwise PLS values of each modularity hypothesis for the brain shape of *A. mexicanum* larvae. Bold values represent significant results.

Hypothesis	1	2	3	4	5
2	**0.033**				
3	**0.034**	**0.042**			
4	**0.048**	**0.047**	0.388		

5	**0.017**	**0.012**	0.096	0.181	
6	**0.035**	**0.020**	0.181	0.285	0.365

Table A11. Results from modularity and morphological integration analyses for each developmental stage of *A. mexicanum* larvae. The table include three different methods (CR, PLS and EMMLi, from left to right) separated by vertical doted lines. Results including (I) and excluding (E) allometry are presented. For the EMMLi method, the type of within and between module correlations assumed for each model was presented (Type). Hyp. = Hypothesis. CR = Covariance ratio value. P = P-value. Z = effect size. K = Number of parameters. PP = posterior probability. Stg = Stage. Allo. = Allometry. SEW = Separate within correlations. SAW = Same within correlations. SEB = Separate between correlations. SAB = Same between correlations.

Hyp.	CR	P	Z	PLS	P	Z	K	AICc	ΔAICc	PP	Type	Stg	Allo.
H1	0.95	0.05	-1.72	0.97	0.00	3.79	3.00	1866 25.22	3670 4.47	0	SEW SEB	47	I
							4.00	1866 27.22	3670 6.47	0	SAW SEB	47	
							3.00	1866 25.22	3670 4.47	0	SEW SAB	47	
							4.00	1866 27.22	3670 6.47	0	SAW SAB	47	
H2	0.87	0.01	-3.12	0.90	0.01	2.59	4.00	1767 55.27	2683 4.51	0	SEW SEB	47	I
							3.00	1774 81.03	2756 0.27	0	SAW SEB	47	
							4.00	1767 55.27	2683 4.51	0	SEW SAB	47	
							3.00	1774 81.03	2756 0.27	0	SAW SAB	47	
H3	0.83	0.00	-4.59	0.84	0.00	3.01	7.00	1730 14.30	2309 3.54	0	SEW SEB	47	I
							5.00	1772 49.89	2732 9.13	0	SAW SEB	47	
							5.00	1811 10.93	3119 0.17	0	SEW SAB	47	

Hyp.	CR	P	Z	PLS	P	Z	K	AICc	ΔAICc	PP	Type	Stg	Allo.
							3.00	185346.52	35425.76	0	SAW SAB	47	
H4	0.80	0.00	-5.82	0.85	0.00	4.20	11.00	156757.11	6836.35	0	SEW SEB	47	I
							8.00	163932.52	14011.77	0	SAW SEB	47	
							6.00	174696.55	24775.79	0	SEW SAB	47	
							3.00	181871.97	31951.21	0	SAW SAB	47	
H5	0.75	0.00	-6.65	0.81	0.00	4.65	16.00	154490.81	4570.05	0	SEW SEB	47	I
							12.00	161905.92	11985.16	0	SAW SEB	47	
							7.00	176592.50	26671.74	0	SEW SAB	47	
							3.00	184007.61	34086.85	0	SAW SAB	47	
H6	0.71	0.00	-7.34	0.78	0.00	4.19	22.00	149920.76	0.00	1	SEW SEB	47	I
							17.00	154903.00	4982.24	0	SAW SEB	47	
							8.00	176850.82	26930.06	0	SEW SAB	47	
							3.00	181833.08	31912.32	0	SAW SAB	47	
H1	0.94	0.02	-1.88	0.96	0.00	3.80	4.00	181242.44	40463.64	0	SEW SEB	47	E
							3.00	181314.68	40535.87	0	SAW SEB	47	
							4.00	181242.44	40463.64	0	SEW SAB	47	
							3.00	181314.68	40535.87	0	SAW SAB	47	
H2	0.88	0.01	-2.84	0.88	0.01	2.35	4.00	170171.45	29392.65	0	SEW SEB	47	E

Hyp.	CR	P	Z	PLS	P	Z	K	AICc	ΔAICc	PP	Type	Stg	Allo.
							3.00	170888.86	3011 0.06	0	SAW SEB	47	
							4.00	170171.45	2939 2.65	0	SEW SAB	47	
							3.00	170888.86	3011 0.06	0	SAW SAB	47	
H3	0.84	0.00	-4.40	0.87	0.00	3.21	7.00	165138.56	2435 9.76	0	SEW SEB	47	E
							5.00	170568.94	2979 0.14	0	SAW SEB	47	
							5.00	174511.24	3373 2.44	0	SEW SAB	47	
							3.00	179941.63	3916 2.83	0	SAW SAB	47	
H4	0.80	0.00	-5.78	0.87	0.00	4.53	11.00	147769.78	6990. 98	0	SEW SEB	47	E
							8.00	155937.09	1515 8.29	0	SAW SEB	47	
							6.00	167898.77	2711 9.97	0	SEW SAB	47	
							3.00	176066.08	3528 7.27	0	SAW SAB	47	
H5	0.76	0.00	-6.73	0.85	0.00	5.21	16.00	145813.31	5034. 51	0	SEW SEB	47	E
							12.00	154135.77	1335 6.97	0	SAW SEB	47	
							7.00	170039.24	2926 0.44	0	SEW SAB	47	
							3.00	178361.71	3758 2.91	0	SAW SAB	47	
H6	0.71	0.00	-7.47	0.80	0.00	4.84	22.00	140778.80	0.00	1	SEW SEB	47	E
							17.00	146367.16	5588. 36	0	SAW SEB	47	
							8.00	170306.49	2952 7.68	0	SEW SAB	47	

Hyp.	CR	P	Z	PLS	P	Z	K	AICc	ΔAICc	PP	Type	Stg	Allo.
							3.00	175894.86	35116.06	0	SAW SAB	47	
H1	0.93	0.02	-1.96	0.94	0.00	2.89	4.00	175814.86	40622.98	0	SEW SEB	50	I
							3.00	175982.03	40790.15	0	SAW SEB	50	
							4.00	175814.86	40622.98	0	SEW SAB	50	
							3.00	175982.03	40790.15	0	SAW SAB	50	
H2	0.80	0.00	-3.44	0.83	0.09	1.38	4.00	165721.33	30529.45	0	SEW SEB	50	I
							3.00	166286.45	31094.57	0	SAW SEB	50	
							4.00	165721.33	30529.45	0	SEW SAB	50	
							3.00	166286.45	31094.57	0	SAW SAB	50	
H3	0.75	0.00	-4.94	0.82	0.01	2.65	7.00	159928.11	24736.23	0	SEW SEB	50	I
							5.00	165919.04	30727.16	0	SAW SEB	50	
							5.00	168689.59	33497.71	0	SEW SAB	50	
							3.00	174680.52	39488.64	0	SAW SAB	50	
H4	0.72	0.00	-6.02	0.77	0.01	2.45	11.00	142281.97	70909.09	0	SEW SEB	50	I
							8.00	150458.88	15267.00	0	SAW SEB	50	
							6.00	162478.71	27286.83	0	SEW SAB	50	
							3.00	170655.62	35463.74	0	SAW SAB	50	
H5	0.70	0.00	-6.27	0.77	0.00	3.45	16.00	140381.63	51895.75	0	SEW SEB	50	I

Hyp.	CR	P	Z	PLS	P	Z	K	AICc	ΔAICc	PP	Type	Stg	Allo.
							12.00	148790.76	13598.88	0	SAW SEB	50	
							7.00	164384.96	29193.08	0	SEW SAB	50	
							3.00	172794.10	37602.22	0	SAW SAB	50	
H6	0.69	0.00	-7.35	0.77	0.00	4.27	22.00	135191.88	0.00	1	SEW SEB	50	I
							17.00	140815.98	5624.10	0	SAW SEB	50	
							8.00	164688.24	29496.36	0	SEW SAB	50	
							3.00	170312.36	35120.48	0	SAW SAB	50	
H1	0.89	0.00	-3.54	0.91	0.00	2.73	4.00	173655.57	41521.31	0	SEW SEB	50	E
							3.00	173816.95	41682.69	0	SAW SEB	50	
							4.00	173655.57	41521.31	0	SEW SAB	50	
							3.00	173816.95	41682.69	0	SAW SAB	50	
H2	0.81	0.00	-4.03	0.84	0.02	2.09	4.00	162970.21	30835.95	0	SEW SEB	50	E
							3.00	163582.44	31448.18	0	SAW SEB	50	
							4.00	162970.21	30835.95	0	SEW SAB	50	
							3.00	163582.44	31448.18	0	SAW SAB	50	
H3	0.77	0.00	-5.65	0.81	0.00	3.13	7.00	156852.86	24718.60	0	SEW SEB	50	E
							5.00	163216.52	31082.26	0	SAW SEB	50	
							5.00	166071.92	33937.66	0	SEW SAB	50	

Hyp.	CR	P	Z	PLS	P	Z	K	AICc	ΔAICc	PP	Type	Stg	Allo.
							3.00	172435.58	40301.32	0	SAW SAB	50	
H4	0.75	0.00	-6.73	0.81	0.00	3.72	11.00	139166.43	7032.17	0	SEW SEB	50	E
							8.00	147698.12	15563.86	0	SAW SEB	50	
							6.00	159833.17	27698.91	0	SEW SAB	50	
							3.00	168364.86	36230.60	0	SAW SAB	50	
H5	0.73	0.00	-6.95	0.81	0.00	4.25	16.00	137349.73	5215.47	0	SEW SEB	50	E
							12.00	146077.16	13942.91	0	SAW SEB	50	
							7.00	161811.27	29677.01	0	SEW SAB	50	
							3.00	170538.72	38404.46	0	SAW SAB	50	
H6	0.73	0.00	-6.91	0.81	0.00	4.49	22.00	132134.26	0.00	1	SEW SEB	50	E
							17.00	138016.36	5882.10	0	SAW SEB	50	
							8.00	162121.88	29987.62	0	SEW SAB	50	
							3.00	168003.99	35869.74	0	SAW SAB	50	
H1	0.91	0.00	-3.84	0.94	0.00	3.27	4.00	158700.46	38811.28	0	SEW SEB	52	I
							3.00	158888.38	38999.20	0	SAW SEB	52	
							4.00	158700.46	38811.28	0	SEW SAB	52	
							3.00	158888.38	38999.20	0	SAW SAB	52	
H2	0.80	0.00	-4.91	0.88	0.01	2.22	4.00	148740.78	28851.61	0	SEW SEB	52	I

Hyp.	CR	P	Z	PLS	P	Z	K	AICc	ΔAICc	PP	Type	Stg	Allo.
							3.00	149285.08	29395.90	0	SAW SEB	52	
							4.00	148740.78	28851.61	0	SEW SAB	52	
							3.00	149285.08	29395.90	0	SAW SAB	52	
H3	0.77	0.00	-6.52	0.84	0.00	2.93	7.00	142949.36	23060.18	0	SEW SEB	52	I
							5.00	148959.12	29069.94	0	SAW SEB	52	
							5.00	151576.69	31687.51	0	SEW SAB	52	
							3.00	157586.45	37697.27	0	SAW SAB	52	
H4	0.72	0.00	-8.18	0.79	0.00	3.62	11.00	126301.21	6412.03	0	SEW SEB	52	I
							8.00	134492.46	14603.29	0	SAW SEB	52	
							6.00	145607.51	25718.33	0	SEW SAB	52	
							3.00	153798.77	33909.59	0	SAW SAB	52	
H5	0.73	0.00	-7.83	0.79	0.00	4.03	16.00	124618.14	4728.97	0	SEW SEB	52	I
							12.00	132953.63	13064.45	0	SAW SEB	52	
							7.00	147517.60	27628.42	0	SEW SAB	52	
							3.00	155853.10	35963.92	0	SAW SAB	52	
H6	0.71	0.00	-7.87	0.77	0.00	4.22	22.00	119889.18	0.00	1	SEW SEB	52	I
							17.00	125481.26	5592.08	0	SAW SEB	52	
							8.00	147830.29	27941.12	0	SEW SAB	52	

Hyp.	CR	P	Z	PLS	P	Z	K	AICc	ΔAICc	PP	Type	Stg	Allo.
							3.00	153422.39	33533.22	0	SAW SAB	52	
H1	0.89	0.00	-5.09	0.90	0.00	2.66	4.00	156246.60	37155.99	0	SEW SEB	52	E
							3.00	156332.28	37241.66	0	SAW SEB	52	
							4.00	156246.60	37155.99	0	SEW SAB	52	
							3.00	156332.28	37241.66	0	SAW SAB	52	
H2	0.81	0.00	-5.35	0.85	0.03	2.00	4.00	146676.07	27585.46	0	SEW SEB	52	E
							3.00	147285.62	28195.01	0	SAW SEB	52	
							4.00	146676.07	27585.46	0	SEW SAB	52	
							3.00	147285.62	28195.01	0	SAW SAB	52	
H3	0.80	0.00	-6.88	0.85	0.00	3.63	7.00	141566.62	22476.01	0	SEW SEB	52	E
							5.00	146954.64	27864.02	0	SAW SEB	52	
							5.00	149683.48	30592.86	0	SEW SAB	52	
							3.00	155071.50	35980.88	0	SAW SAB	52	
H4	0.75	0.00	-8.67	0.81	0.00	4.12	11.00	125361.24	62706.63	0	SEW SEB	52	E
							8.00	133061.91	13971.30	0	SAW SEB	52	
							6.00	143704.66	24614.04	0	SEW SAB	52	
							3.00	151405.33	32314.71	0	SAW SAB	52	
H5	0.76	0.00	-8.31	0.81	0.00	4.47	16.00	123685.08	45944.47	0	SEW SEB	52	E

Hyp.	CR	P	Z	PLS	P	Z	K	AICc	ΔAICc	PP	Type	Stg	Allo.
							12.00	131567.58	12476.96	0	SAW SEB	52	
							7.00	145617.25	26526.64	0	SEW SAB	52	
							3.00	153499.76	34409.14	0	SAW SAB	52	
H6	0.73	0.00	-8.39	0.79	0.00	4.40	22.00	119090.62	0.00	1	SEW SEB	52	E
							17.00	124336.95	5246.33	0	SAW SEB	52	
							8.00	145960.10	26869.48	0	SEW SAB	52	
							3.00	151206.45	32115.83	0	SAW SAB	52	
H1	0.99	0.37	-0.74	0.96	0.00	3.85	4.00	184268.13	44039.66	0	SEW SEB	54	I
							3.00	184446.24	44217.77	0	SAW SEB	54	
							4.00	184268.13	44039.66	0	SEW SAB	54	
							3.00	184446.24	44217.77	0	SAW SAB	54	
H2	0.74	0.00	-14.40	0.87	0.00	2.87	4.00	172181.30	31952.84	0	SEW SEB	54	I
							3.00	172860.83	32632.36	0	SAW SEB	54	
							4.00	172181.30	31952.84	0	SEW SAB	54	
							3.00	172860.83	32632.36	0	SAW SAB	54	
H3	0.76	0.00	-7.86	0.86	0.00	3.70	7.00	165259.09	25030.62	0	SEW SEB	54	I
							5.00	172478.85	32250.38	0	SAW SEB	54	
							5.00	175663.11	35434.64	0	SEW SAB	54	

Hyp.	CR	P	Z	PLS	P	Z	K	AICc	ΔAICc	PP	Type	Stg	Allo.
							3.00	182882.87	42654.40	0	SAW SAB	54	
H4	0.72	0.00	-7.11	0.80	0.00	3.77	11.00	147472.87	7244.40	0	SEW SEB	54	I
							8.00	156922.13	16693.66	0	SAW SEB	54	
							6.00	169261.66	29033.19	0	SEW SAB	54	
							3.00	178710.92	38482.46	0	SAW SAB	54	
H5	0.72	0.00	-7.31	0.82	0.00	4.38	16.00	145696.20	5467.73	0	SEW SEB	54	I
							12.00	155321.25	15092.78	0	SAW SEB	54	
							7.00	171400.36	31171.89	0	SEW SAB	54	
							3.00	181025.42	40796.95	0	SAW SAB	54	
H6	0.71	0.00	-7.81	0.80	0.00	4.27	22.00	140228.47	0.00	1	SEW SEB	54	I
							17.00	146798.69	6570.22	0	SAW SEB	54	
							8.00	171702.10	31473.63	0	SEW SAB	54	
							3.00	178272.34	38043.87	0	SAW SAB	54	
H1	0.94	0.00	-2.56	0.94	0.00	3.52	4.00	179548.18	41095.40	0	SEW SEB	54	E
							3.00	179600.11	41147.34	0	SAW SEB	54	
							4.00	179548.18	41095.40	0	SEW SAB	54	
							3.00	179600.11	41147.34	0	SAW SAB	54	
H2	0.84	0.00	-4.34	0.94	0.00	3.64	4.00	167831.26	29378.48	0	SEW SEB	54	E

Hyp.	CR	P	Z	PLS	P	Z	K	AICc	ΔAICc	PP	Type	Stg	Allo.
							3.00	168678.21	30225.43	0	SAW SEB	54	
							4.00	167831.26	29378.48	0	SEW SAB	54	
							3.00	168678.21	30225.43	0	SAW SAB	54	
H3	0.84	0.00	-5.42	0.93	0.00	4.17	7.00	162487.85	24035.07	0	SEW SEB	54	E
							5.00	168274.19	29821.42	0	SAW SEB	54	
							5.00	172258.19	33805.41	0	SEW SAB	54	
							3.00	178044.53	39591.76	0	SAW SAB	54	
H4	0.78	0.00	-7.51	0.88	0.00	3.86	11.00	145370.83	6918.06	0	SEW SEB	54	E
							8.00	153703.78	15251.00	0	SAW SEB	54	
							6.00	165786.68	27333.90	0	SEW SAB	54	
							3.00	174119.62	35666.85	0	SAW SAB	54	
H5	0.77	0.00	-7.80	0.88	0.00	4.07	16.00	143484.42	5031.65	0	SEW SEB	54	E
							12.00	152021.75	13568.97	0	SAW SEB	54	
							7.00	167909.92	29457.14	0	SEW SAB	54	
							3.00	176447.26	37994.48	0	SAW SAB	54	
H6	0.76	0.00	-7.93	0.85	0.00	4.27	22.00	138452.78	0.00	1	SEW SEB	54	E
							17.00	144220.04	5767.27	0	SAW SEB	54	
							8.00	168186.88	29734.11	0	SEW SAB	54	

Hyp.	CR	P	Z	PLS	P	Z	K	AICc	ΔAICc	PP	Type	Stg	Allo.
							3.00	1739 54.17	3550 1.39	0	SAW SAB	54	

ANNEXE B : JUSTIFICATION DES HYPOTHÈSES DE MODULARITÉ UTILISÉES DANS LE CHAPITRE 1

The first hypothesis follows ideas discussed in Ollonen *et al.* (2024), which highlight distinct developmental and topological behaviours of dorsal and ventral brain regions in squamates, with dorsal regions exhibiting greater variation and ventral regions maintaining more conservative trajectories. This pattern echoes the well-established dorsoventral organization of the vertebrate brain, in which dorsal and ventral domains correspond to genetically and developmentally distinct territories (Butler et Hodos, 2005; Jessell, 2000; Puelles, 2013; Puelles et Rubenstein, 2003).

The second hypothesis builds on evidence for the partial developmental and functional independence of the midbrain relative to both the forebrain and hindbrain. The mesencephalon forms a cohesive visuomotor integration center composed of the tectum and tegmentum, supporting orienting reflexes, multimodal integration, and motor gating (Butler et Hodos, 2005; Roth *et al.*, 1997; Striedter, 2005). Its identity is established and maintained by the isthmic organizer (IsO), which imposes a sharp developmental boundary through FGF8–Wnt signalling (Kiecker et Lumsden, 2005; Rhinn et Brand, 2001).

The third hypothesis is based on the classical tripartite organization of the vertebrate brain, where the forebrain, midbrain, and hindbrain arise from distinct embryonic compartments separated by stable molecular and morphogenetic boundaries (Puelles et Rubenstein, 2003; Redies et Puelles, 2001). These territories are patterned by independent signaling centers that regulate regional identity and growth (Kiecker et Lumsden, 2005).

The fourth hypothesis aligns with the neuromeric model, which subdivides the forebrain into telencephalic and diencephalic domains, in addition to the mesencephalon and rhombencephalon. These four regions constitute discrete embryonic divisions that are molecularly delimited, developmentally autonomous, and preserved as coherent radial units into adulthood (Nieuwenhuys *et al.*, 2014; Redies et Puelles, 2001).

The fifth hypothesis further separates the olfactory bulb from the remainder of the telencephalon based on its distinct functional and developmental properties. The olfactory bulb acts as a primary sensory system devoted to odor detection and early signal transformation and relies on specialized circuitry and direct sensory input that is largely segregated from higher-order telencephalic processing (Butler et Hodos, 2005; Corfield *et al.*, 2015). In contrast, the rest of the telencephalon integrates multisensory information, supports associative and spatial processing, and scales more predictably with overall brain size following conserved developmental patterns in some vertebrates (Finlay et Darlington, 1995; Finlay *et al.*, 2001). Comparative studies show that olfactory bulb size can vary independently from total telencephalic volume and can reflects ecological reliance on olfaction rather than overall brain enlargement (Gonzalez-Voyer *et al.*, 2009; Yopak *et al.*, 2010).

The sixth hypothesis retains the major developmental divisions of the brain while separately modelling regions with strongly divergent functional roles. The olfactory bulb functions as a dedicated sensory processor with evolutionary and developmental scaling patterns often decoupled from those of the remaining telencephalon (Corfield *et al.*, 2015; Finlay et Darlington, 1995; Finlay *et al.*, 2001; Gonzalez-Voyer *et al.*, 2009; Yopak *et al.*, 2010). The telencephalon supports higher-order associative and spatial processing (Striedter, 2005), while within the diencephalon, the thalamus acts as the principal sensory relay system and the hypothalamus regulates neuroendocrine function, homeostasis, and motivational behaviours (Butler et Hodos, 2005; Northcutt, 2002). The midbrain forms a cohesive visuomotor integration center, and the rhombencephalon coordinates motor pattern generation, balance, and autonomic control (Butler et Hodos, 2005; Nieuwenhuys *et al.*, 2014; Northcutt, 2002). Together, these marked functional dissociations support modelling the olfactory bulb, telencephalon, thalamus, hypothalamus, mesencephalon, and rhombencephalon as six distinct modules.

ANNEXE C : INFORMATION SUPPLÉMENTAIRE DU CHAPITRE 2

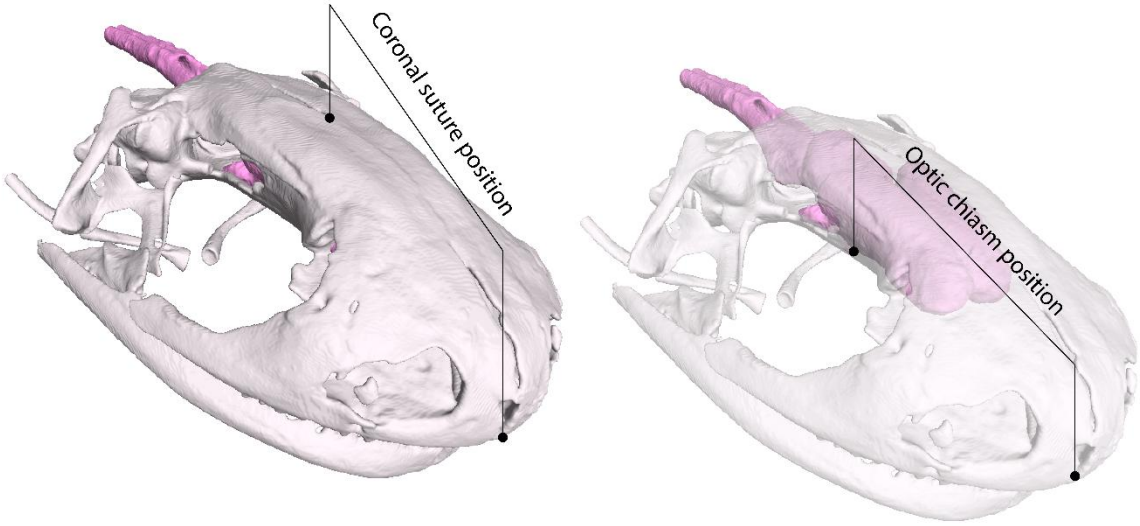

Figure C1 Two linear measurements used in this study represented using the skull and brain of *Hynobius leechii*.

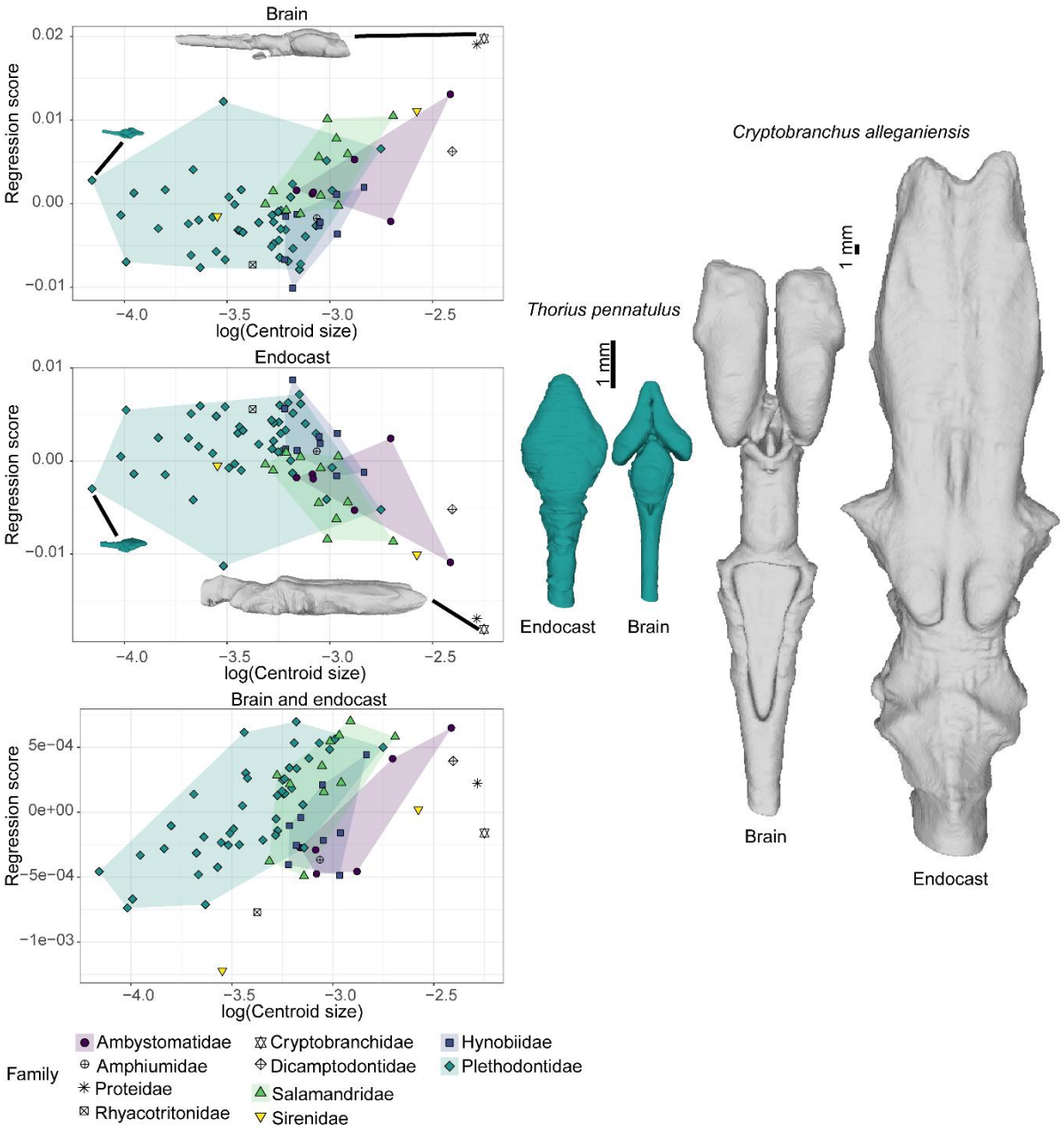

Figure C2 Relationship between the regression score and the centroid size (log transformation).

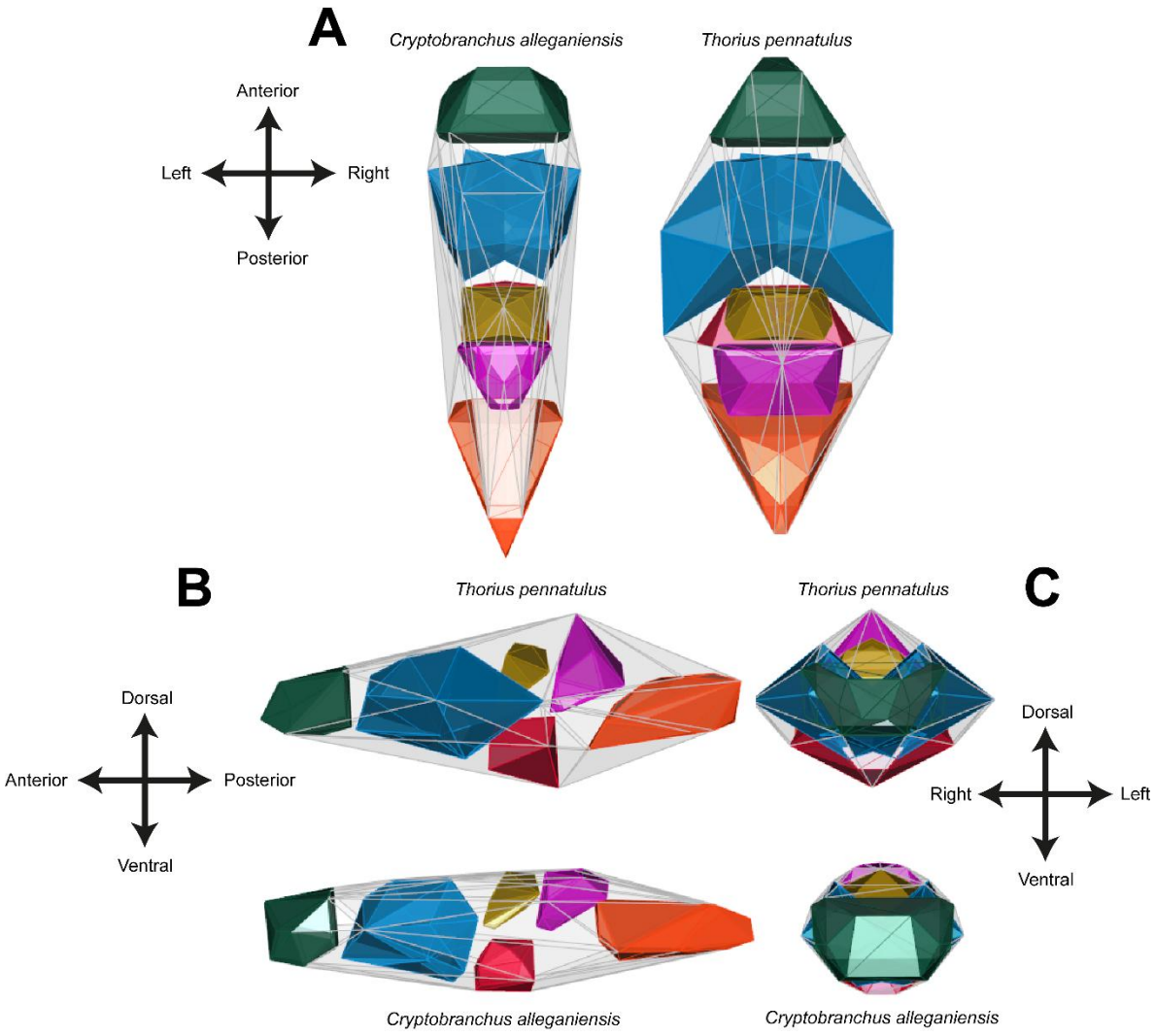

Figure C3 Comparison of landmarks of brain symmetric shape between the two extremes of the first PC of the size-shape PCA in dorsal (A), lateral (B) and front (C) views. The convex hulls in 3D are associated with the landmarks and boundaries refer to the modules of Hypothesis 7A (dark green = olfactory bulb, blue = rest of telencephalon, yellow = thalamus, red = hypothalamus, pink = mesencephalon and orange = rhombencephalon).

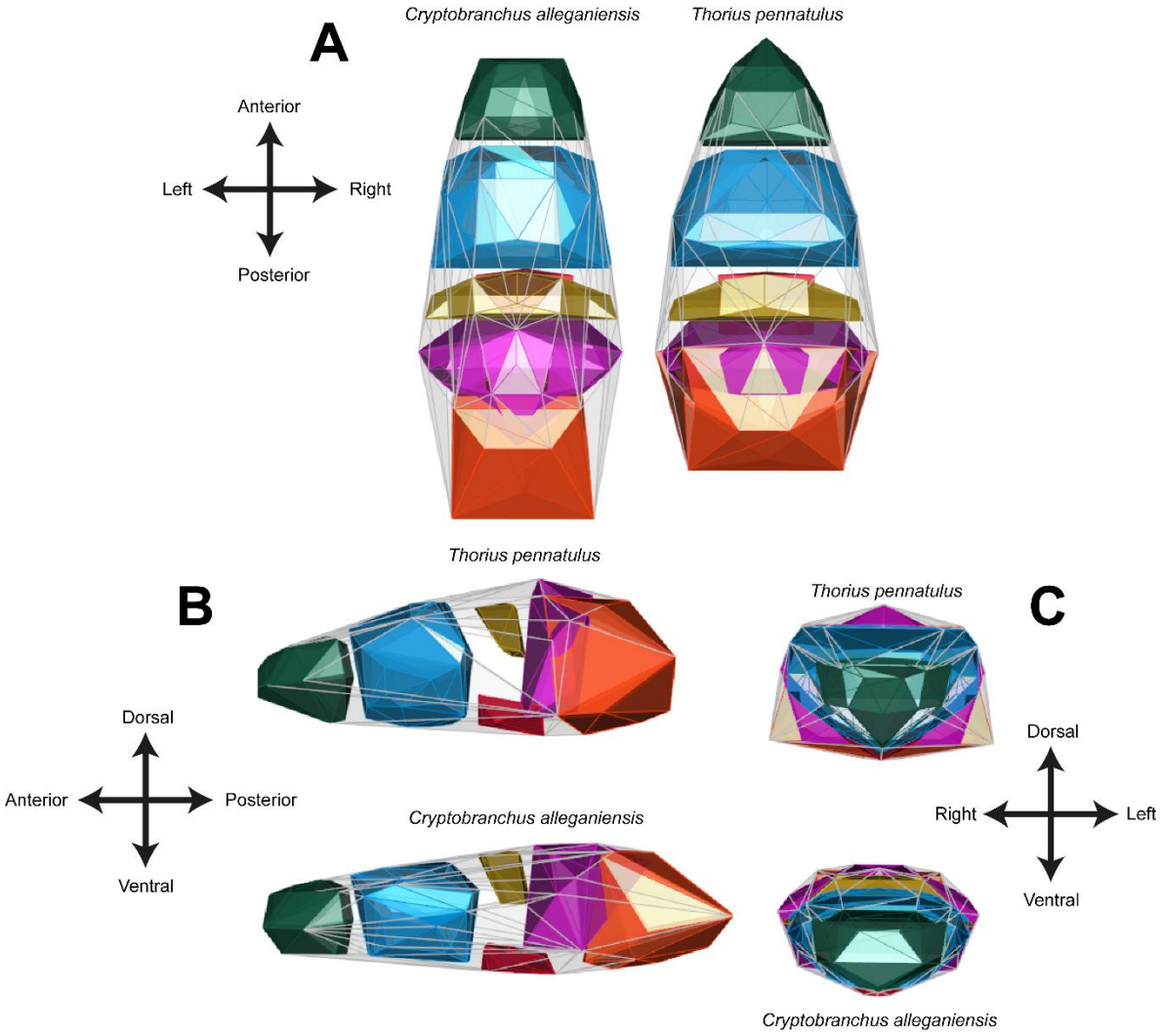

Figure C4 Comparison of landmarks of endocast symmetric shape between the two extremes of the first PC of the size-shape PCA in dorsal (A), lateral (B) and front (C) views. The convex hulls in 3D are associated with the landmarks and boundaries refer to the modules of Hypothesis 7B (dark green = olfactory bulb, blue = rest of telencephalon, yellow = thalamus, red = hypothalamus, pink = mesencephalon and orange = rhombencephalon).

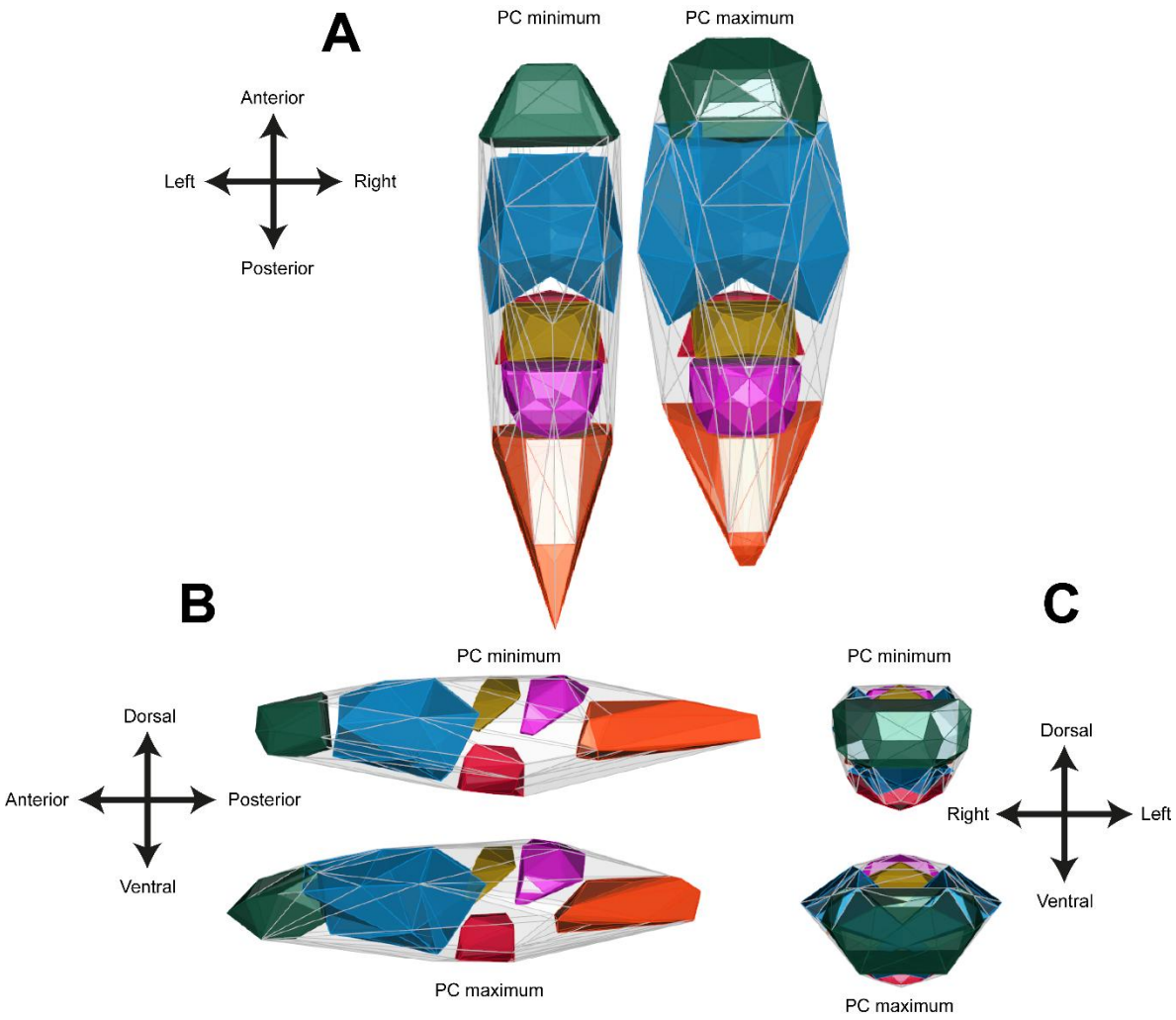

Figure C5 Comparison of brain landmarks between the two PC1 extremes of the allometry-corrected shape PCA in dorsal (A), lateral (B) and front (C) views. The convex hulls in 3D are associated with the landmarks and boundaries refer to the modules of Hypothesis 7A (dark green = olfactory bulb, blue = rest of telencephalon, yellow = thalamus, red = hypothalamus, pink = mesencephalon and orange = rhombencephalon).

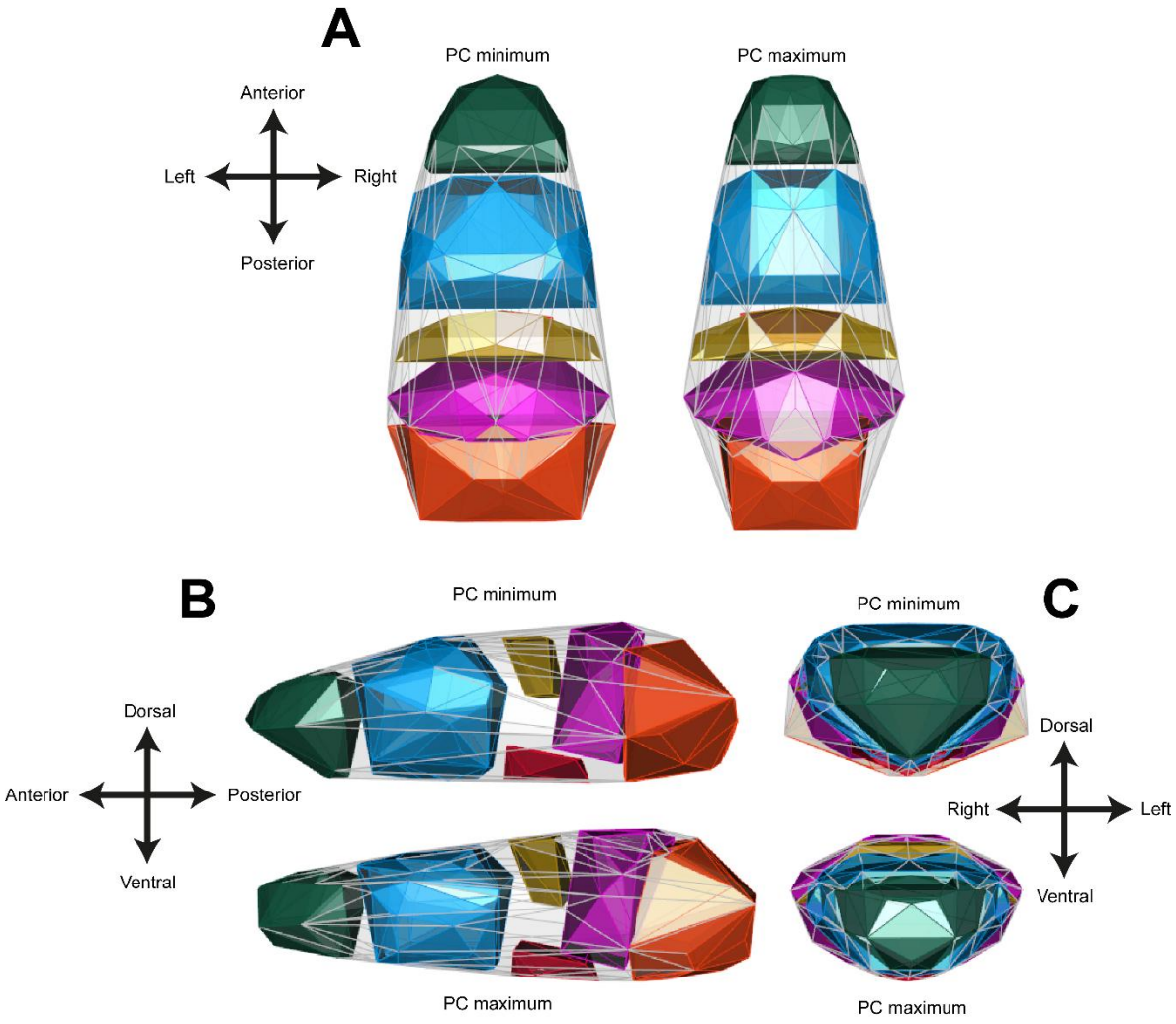

Figure C6 Comparison of endocast landmarks between the two PC1 extremes of the allometry-corrected shape PCA in dorsal (A), lateral (B) and front (C) views. The convex hulls in 3D are associated with the landmarks and boundaries refer to the modules of Hypothesis 7B (dark green = olfactory bulb, blue = rest of telencephalon, yellow = thalamus, red = hypothalamus, pink = mesencephalon and orange = rhombencephalon).

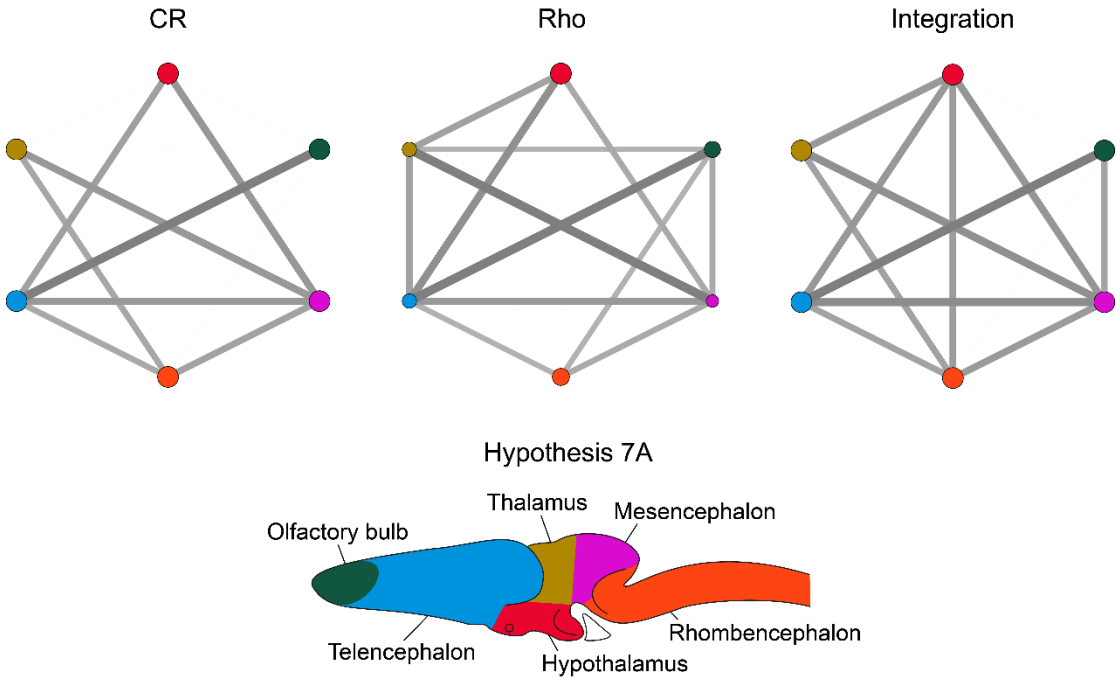

Figure C7 Network representations of the strength of morphological integration from the covariance ratio (CR), the EMMLi (rho) and the partial least squares (integration) analyses for the modular Hypothesis 7A. Edge width in each network represents the strength of the association between two modules. Note that the edge width is based on values within each analysis (i.e., not directly comparable between networks). For the EMMLi analysis, the edge width represents the correlation between two modules and the size of nodes represents the within module correlation.

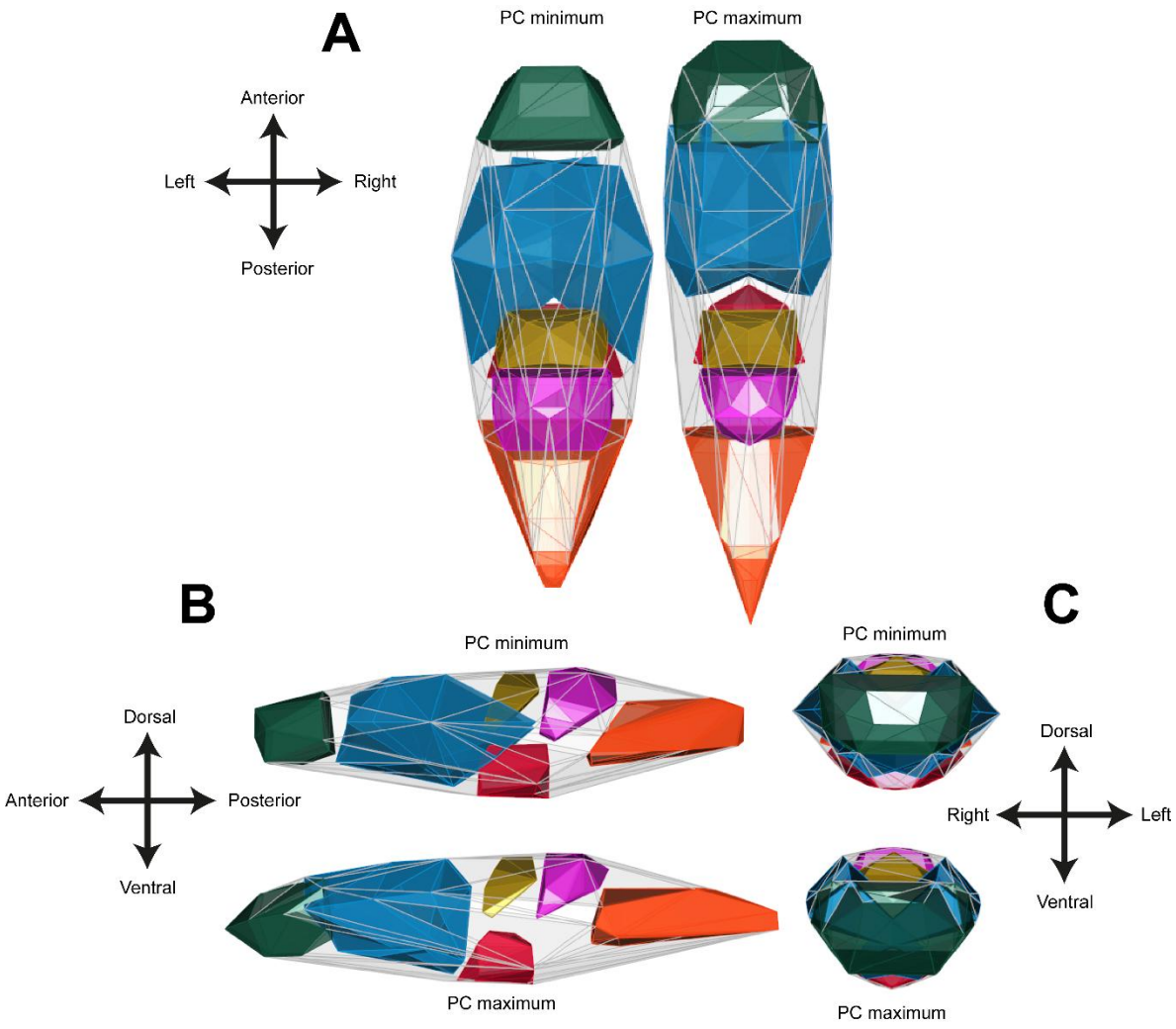

Figure C8 Comparison of brain landmarks between the two PC2 extremes of the allometry-corrected shape PCA in dorsal (A), lateral (B) and front (C) views. The convex hulls in 3D are associated with the landmarks and boundaries refer to the modules of Hypothesis 7A (dark green = olfactory bulb, blue = rest of the telencephalon, yellow = thalamus, red = hypothalamus, pink = mesencephalon and orange = rhombencephalon).

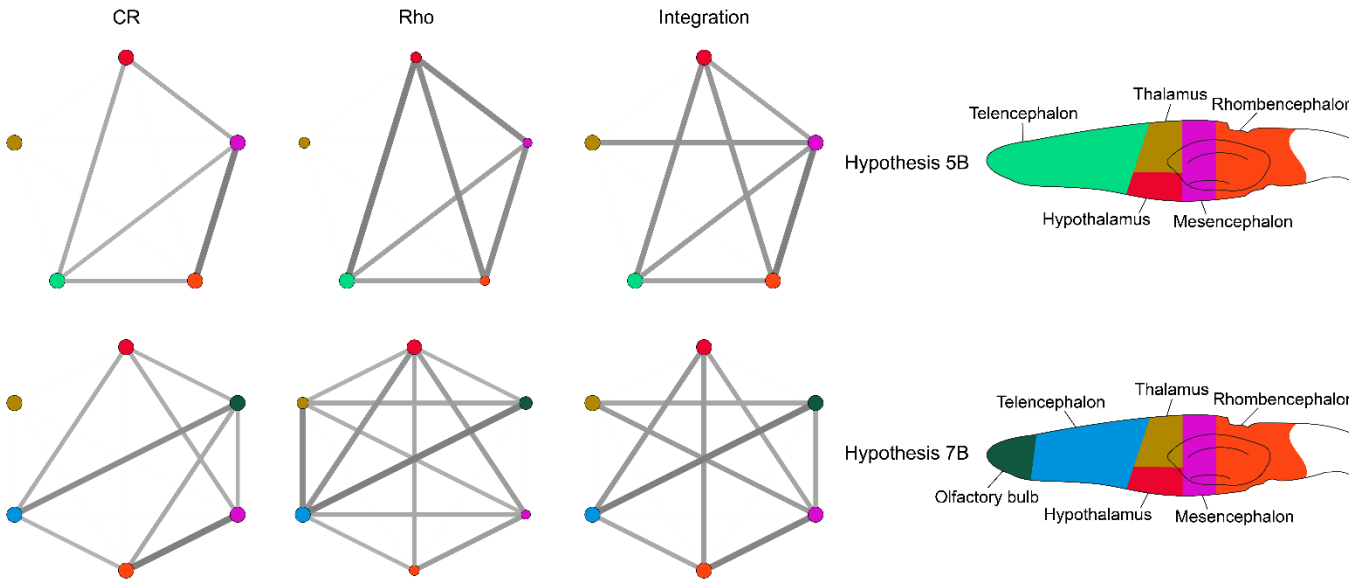

Figure C9 Network representations of the strength of morphological integration from the covariance ratio (CR), the EMMLi (rho) and the partial least squares (integration) analyses for two hypotheses of the endocast shape. Edge width in each network represents the strength of the association between two modules. Note that the edge width is based on values within each analysis (i.e., not directly comparable between networks). For the EMMLi analysis, the edge width represents the correlation between two modules and the size of nodes represents the within module correlation.

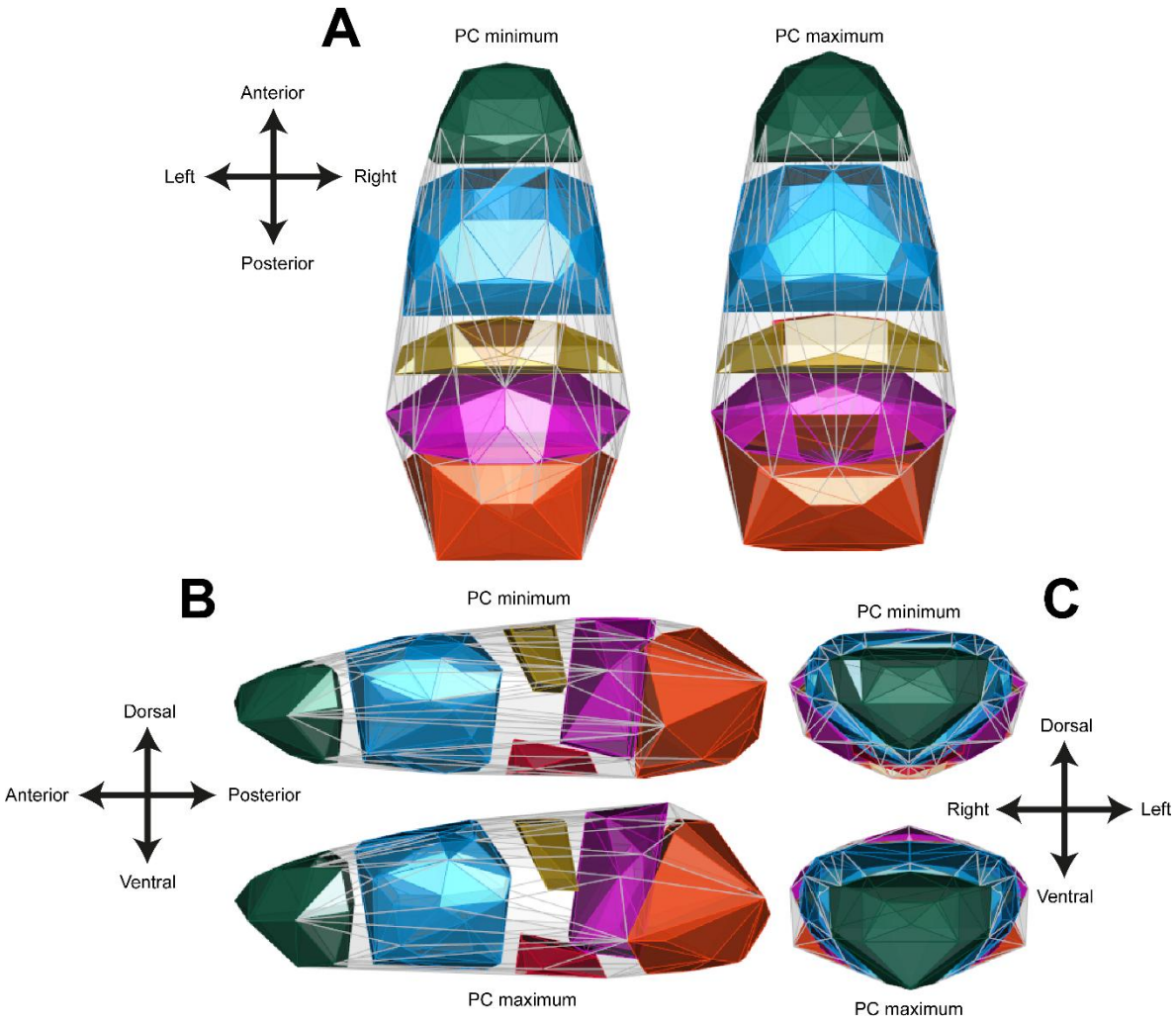

Figure C10 Comparison of endocast landmarks between the two PC2 extremes of the allometrycorrected shape PCA in dorsal (A), lateral (B) and front (C) views. The convex hulls in 3D are associated with the landmarks and boundaries refer to the modules of Hypothesis 7B (purple = frontal, cyan = parietal, grey = orbitosphenoid, green = anterior half of parasphenoid, dark blue = posterior half of parasphenoid, orange = occipito-otic area).

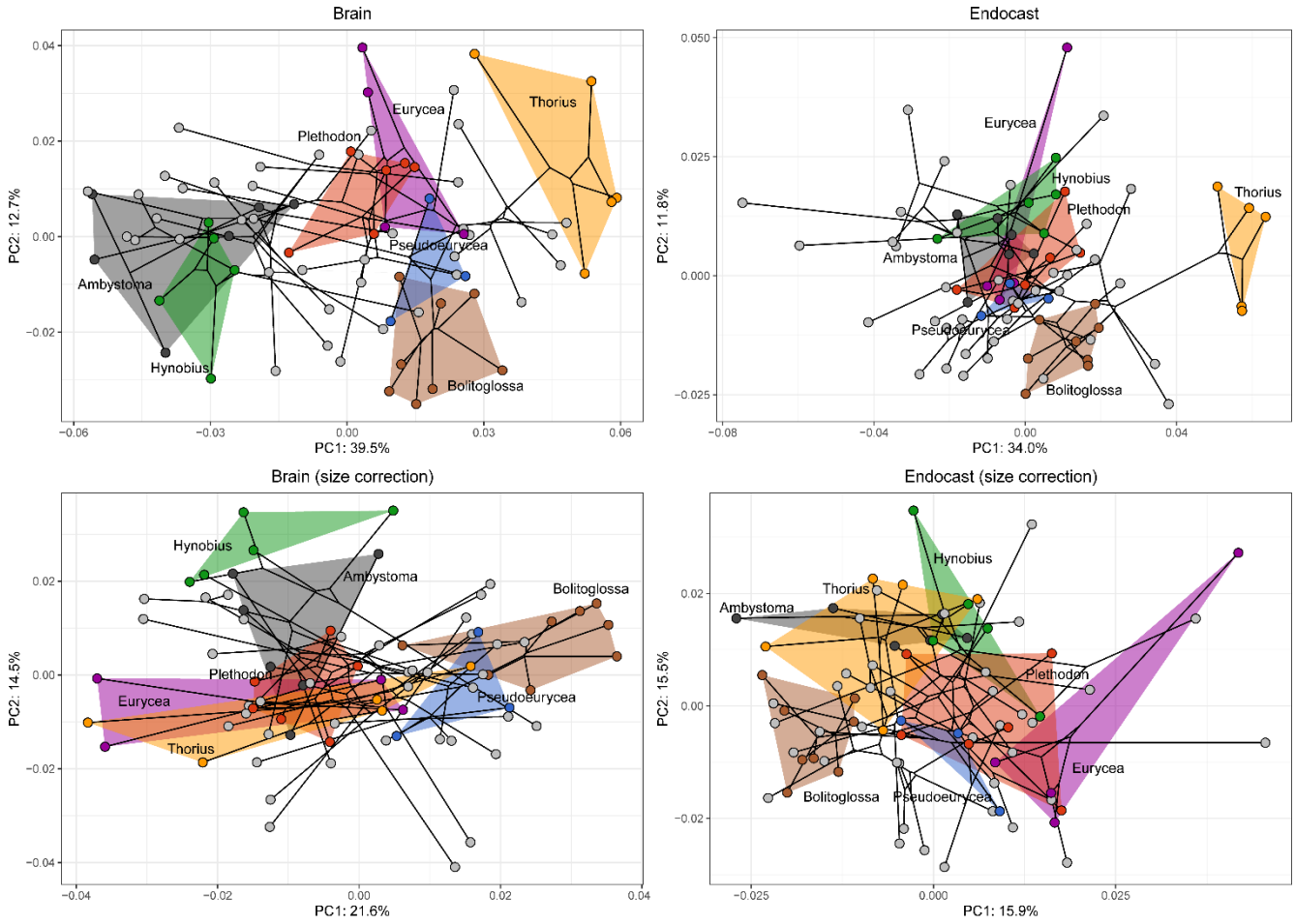

Figure C11 Phylomorphospace of brain (A, C) and endocast (B, D) shape with and without allometric correction.

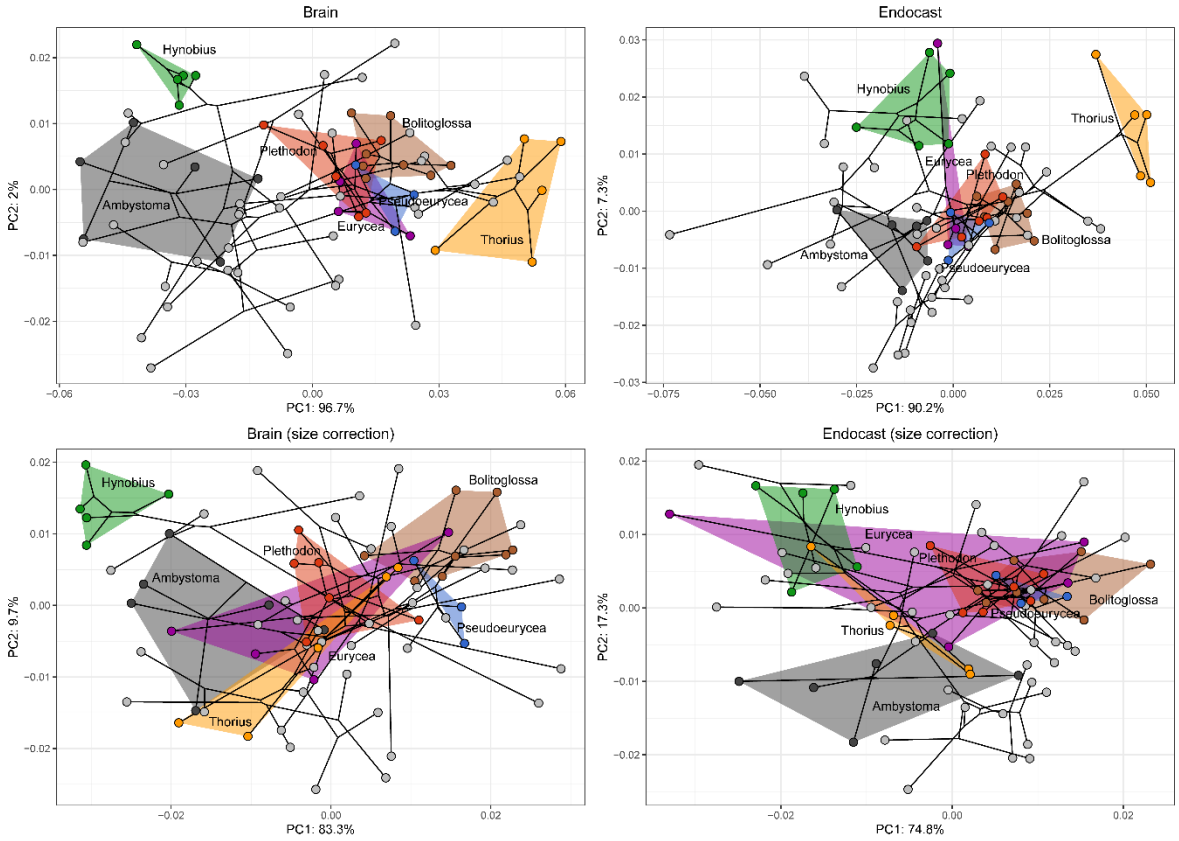

Figure C12 Phylogenetically aligned component analysis (PACA) of brain (A, C) and endocast (B, D) shape with and without allometric correction.

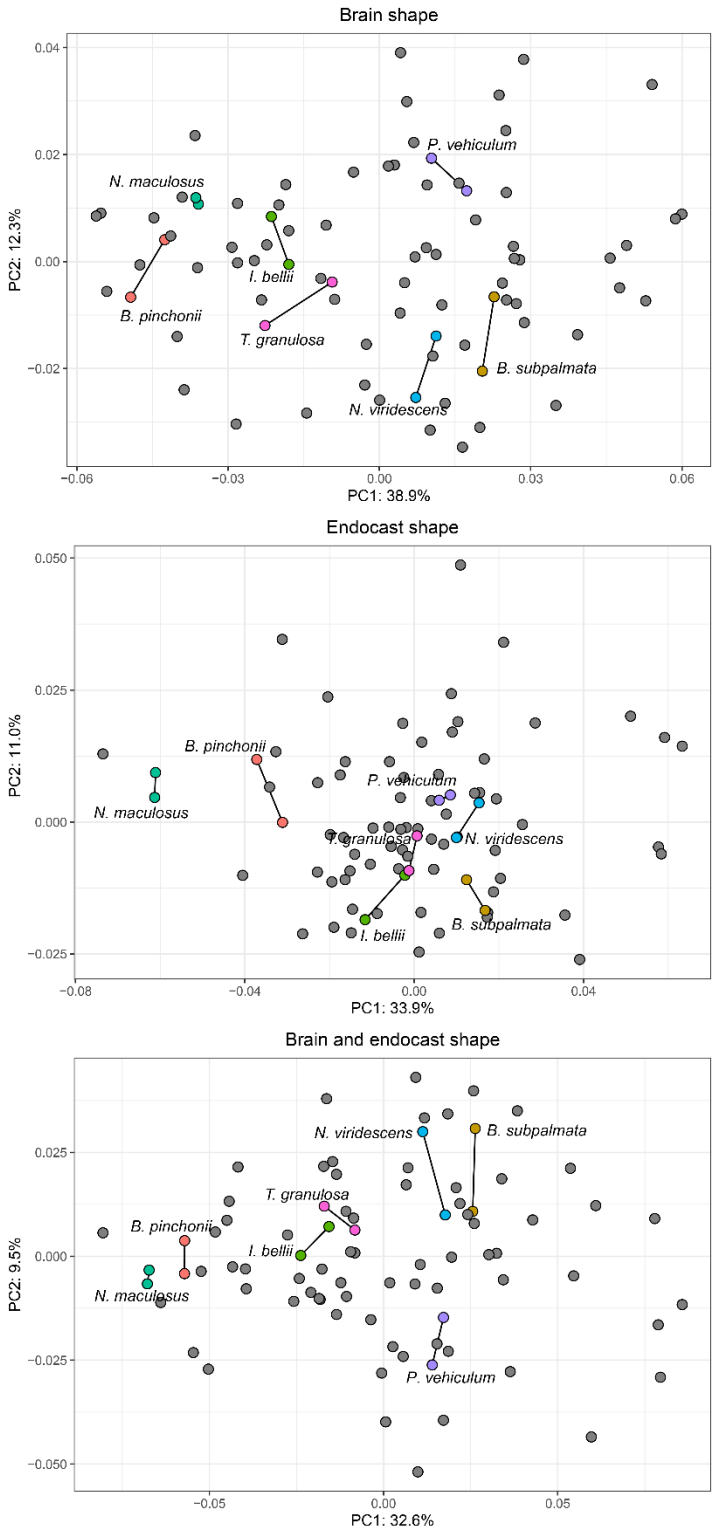

Figure C13 PCA plots showing intraspecific and interspecific shape variation in the sample.

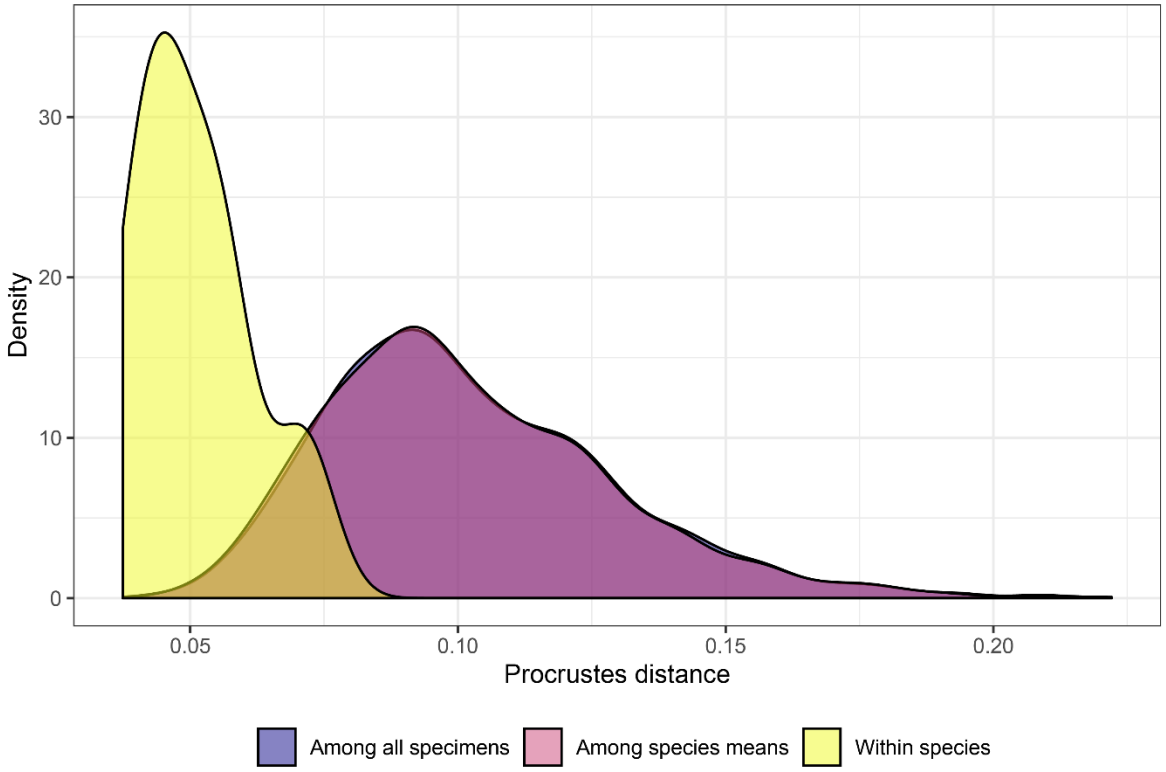

Figure C14 Procrustes coordinate distances histogram for the combined shape dataset of salamanders.

Table C1 Pairwise effect size (lower diagonal) and p-value (upper diagonal) comparison of modular signal of nine hypotheses for the brain shape. Bold values represent significant results ($p < 0.05$) and grey areas represent results associated with the best supported hypothesis.

Hypothesis	No module	1A	2A	3A	4A	5A	6A	7A	8	9
No module		**0.004**	**0.002**	**0.000**	**0.000**	**0.000**	**0.000**	**0.000**	**0.000**	**0.000**
1A	2.676		0.186	0.100	0.085	**0.010**	**0.021**	**0.002**	**0.028**	0.064
2A	2.925	0.892		0.416	0.409	0.137	0.213	0.058	0.244	0.366
3A	3.986	1.281	0.211		0.495	0.160	0.255	0.062	0.294	0.445

4A	4.437	1.369	0.230	0.012		0.151	0.248	0.054	0.288	0.447
5A	5.277	2.329	1.093	0.996	1.033		0.353	0.302	0.311	0.179
6A	5.217	2.039	0.795	0.659	0.681	0.378		0.177	0.452	0.289
7A	6.241	2.948	1.575	1.542	1.608	0.519	0.928		0.147	0.067
8	5.065	1.917	0.693	0.543	0.559	0.494	0.121	1.048		0.332
9	4.740	1.524	0.343	0.139	0.134	0.918	0.558	1.498	0.434	

Table C2 Sample effect size of PLS coefficients for each modular hypothesis for the brain shape (first two lines). Pairwise effect size (lower diagonal) and p-value (upper diagonal) comparison of PLS correlation coefficients of nine hypotheses for the brain shape. Bold values represent significant results ($p < 0.05$) and grey areas represent results associated with the best supported hypothesis.

Hypothesis	1A	2A	3A	4A	5A	6A	7A	8	9
Z	5.197	4.262	3.432	4.896	4.392	3.164	2.645	2.732	3.968

Hypothesis	1A	2A	3A	4A	5A	6A	7A	8	9
1A		0.206	**0.048**	**0.031**	0.097	**0.001**	**0.001**	**0.001**	**0.036**
2A	0.820		0.202	0.174	0.334	**0.017**	**0.016**	**0.011**	0.178
3A	1.669	0.836		0.494	0.323	0.109	0.103	0.078	0.488
4A	1.873	0.938	0.015		0.301	0.060	0.058	**0.037**	0.479
5A	1.301	0.430	0.459	0.522		**0.031**	**0.031**	**0.020**	0.299
6A	3.051	2.131	1.230	1.558	1.860		0.457	0.396	0.092

7A	3.030	2.137	1.265	1.569	1.868	0.107		0.444	0.087
8	3.216	2.306	1.421	1.792	2.058	0.263	0.140		0.062
9	1.804	0.922	0.031	0.053	0.528	1.331	1.360	1.542	

Table C3 Pairwise effect size (lower diagonal) and p-value (upper diagonal) comparison of modular signal of eleven hypotheses for the endocast shape. Bold values represent significant results ($p < 0.05$) and grey areas represent results associated with the best supported hypotheses.

Hypothesis	No module	1B	2B	3B	4B	5B	6B	7B	10	11	12	13
No module		**0.000**	**0.002**	**0.001**	**0.000**	**0.000**	**0.000**	**0.000**	**0.000**	**0.002**	**0.000**	**0.000**
1B	3.590		0.437	0.473	0.364	**0.001**	0.446	**0.002**	0.251	0.408	0.397	0.158
2B	2.899	0.158		0.465	0.316	**0.001**	0.384	**0.003**	0.218	0.473	0.341	0.139
3B	3.136	0.068	0.087		0.346	**0.001**	0.420	**0.003**	0.241	0.438	0.375	0.156
4B	4.163	0.347	0.480	0.396		**0.002**	0.406	**0.006**	0.369	0.289	0.455	0.263
5B	6.949	3.230	3.182	3.152	2.952		**0.000**	0.256	**0.004**	**0.001**	**0.001**	**0.005**
6B	4.500	0.137	0.294	0.201	0.239	3.315		**0.002**	0.277	0.354	0.445	0.170
7B	7.290	2.836	2.789	2.755	2.527	0.656	2.927		**0.016**	**0.002**	**0.002**	**0.017**
10	4.454	0.671	0.778	0.702	0.334	2.614	0.591	2.155		0.196	0.319	0.398
11	2.833	0.232	0.068	0.157	0.557	3.262	0.375	2.877	0.856		0.312	0.120
12	4.749	0.262	0.409	0.319	0.114	3.221	0.137	2.820	0.471	0.491		0.206
13	5.946	1.003	1.086	1.012	0.635	2.592	0.954	2.112	0.259	1.173	0.822	

Table C4 Sample effect size of PLS coefficients for each modular hypothesis for the endocast shape (first two lines). Pairwise effect size (lower diagonal) and p-value (upper diagonal) comparison of PLS correlation coefficients of eleven hypotheses for the endocast shape. Bold values represent significant results ($p < 0.05$) and grey areas represent results associated with the best supported hypotheses.

Hypothesis	1B	2B	3B	4B	5B	6B	7B	10	11	12	13
Z	4.587	3.861	2.157	2.939	2.150	2.770	1.918	3.086	4.673	1.683	1.545

Hypothesis	1B	2B	3B	4B	5B	6B	7B	10	11	12	13
1B		0.265	**0.041**	0.255	0.064	0.162	0.092	0.230	0.246	0.090	0.066
2B	0.628		**0.023**	0.128	**0.033**	0.081	**0.047**	0.115	0.491	**0.046**	**0.034**
3B	1.738	2.005		0.168	0.418	0.260	0.422	0.187	**0.012**	0.461	0.481
4B	0.658	1.135	0.963		0.222	0.380	0.251	0.470	0.106	0.236	0.192
5B	1.523	1.835	0.206	0.767		0.327	0.494	0.245	**0.020**	0.471	0.413
6B	0.985	1.402	0.643	0.305	0.447		0.350	0.408	0.061	0.327	0.276
7B	1.326	1.675	0.196	0.671	0.015	0.385		0.273	**0.033**	0.468	0.416
10	0.739	1.202	0.888	0.074	0.691	0.232	0.603		0.093	0.256	0.210
11	0.686	0.022	2.252	1.248	2.057	1.549	1.837	1.325		**0.033**	**0.023**

12	1.342	1.685	0.098	0.721	0.073	0.449	0.079	0.656	1.833		0.449
13	1.510	1.827	0.046	0.870	0.220	0.595	0.213	0.805	1.994	0.127	

Table C5 Pairwise effect size (lower diagonal) and p-value (upper diagonal) comparison of modular signal of two hypotheses for the combined shape dataset. Bold values represent significant results ($p < 0.05$) and grey areas represent results associated with the best supported hypothesis.

Hypothesis	No module	14	15
No module		**0.000**	**0.000**
14	11.753		0.306
15	11.697	0.507	

Table C6 Sample effect size of PLS coefficients for each modular hypothesis for the combined shape dataset (first two lines). Pairwise effect size (lower diagonal) and p-value (upper diagonal) comparison of PLS correlation coefficients of two hypotheses for the combined dataset. Bold values represent significant results ($p < 0.05$) and grey areas represent results associated with the best supported hypothesis.

Hypothesis	14	15
Z	2.774	2.668

Hypothesis	14	15
14		0.392
15	0.273	

Table C7 Phylogenetic signal results for each module of Hypothesis 14. Bold values represent significant results ($p < 0.05$) and the grey area represents results associated with the endocast. OLF = Olfactory bulb, HYP = Hypothalamus, MES = Mesencephalon, RHM = Rhombencephalon, TEL = Telencephalon, THA = Thalamus.

	OLF	HYP	MES	RHM	TEL	THA	OLF	HYP	MES	RHM	TEL	THA
K	0.477	-	0.488	0.693	0.558	0.466	-	-	-	0.618	0.576	-
Pagel's λ	0.100	0.000	0.100	0.100	0.100	0.100	0.000	0.000	0.000	0.100	0.100	0.000
Z	3.895	-	3.541	5.939	8.823	2.468	-	-	-	7.572	8.136	-
P-value	**0.001**	-	**0.001**	**0.001**	**0.001**	**0.008**	**-**	**-**	**-**	**0.001**	**0.001**	-

ANNEXE D : JUSTIFICATION DES HYPOTHÈSES DE MODULARITÉ UTILISÉES DANS LE CHAPITRE 2

Common hypotheses for the brain and endocast

Hypotheses 1A and 1B are inspired by the framework proposed by Ollonen *et al.* (2024), which documents contrasting developmental and topological dynamics between dorsal and ventral brain regions in squamates. In this context, dorsal regions tend to display higher morphological variation, whereas ventral regions follow more conservative evolutionary trajectories. This pattern is consistent with the fundamental dorsoventral organization of the vertebrate brain, where dorsal and ventral domains correspond to genetically distinct and developmentally segregated territories established early in embryogenesis (Butler et Hodos, 2005; Jessell, 2000; Puelles, 2013; Puelles et Rubenstein, 2003).

Hypotheses 2A and 2B are grounded in evidence supporting the relative developmental and functional independence of the midbrain from both the forebrain and hindbrain. The mesencephalon constitutes an integrated visuomotor processing center formed by the tectum and tegmentum, which together support orienting responses, multimodal sensory integration, and motor gating (Butler et Hodos, 2005; Roth *et al.*, 1997; Striedter, 2005). Its distinct identity is established and maintained by the isthmic organizer, which creates a sharp developmental boundary via FGF8–Wnt signaling interactions (Kiecker et Lumsden, 2005; Rhinn et Brand, 2001).

Hypotheses 3A and 3B build on the classical tripartite organization of the vertebrate brain, in which the forebrain, midbrain, and hindbrain arise from separate embryonic compartments delineated by stable molecular and morphogenetic boundaries (Puelles et Rubenstein, 2003; Redies et Puelles, 2001). These major brain divisions are patterned by distinct signaling centers that independently regulate regional growth and identity throughout development (Kiecker et Lumsden, 2005).

Hypotheses 4A and 4B follow the neuromeric model of brain organization, which further subdivides the forebrain into telencephalic and diencephalic domains in addition to the mesencephalon and rhombencephalon. These four regions represent discrete embryonic units that are molecularly defined, developmentally autonomous, and retained as coherent radial domains into adulthood (Nieuwenhuys *et al.*, 2014; Redies et Puelles, 2001).

Hypotheses 5A and 5B explicitly distinguish the thalamus from the hypothalamus based upon deeply conserved developmental and functional differences across vertebrates, including amphibians. Although both structures originate within the diencephalon, they arise from distinct prosomeric subdivisions characterized by separate genetic regulatory environments and divergent morphogenetic trajectories (Puelles, 2013; Puelles et Rubenstein, 2003). In salamanders, as in other vertebrates, the thalamus develops primarily from prosomere p2 and serves as the main relay for ascending sensory pathways, distributing multimodal information to telencephalic targets (Butler et Hodos, 2005; Nieuwenhuys *et al.*, 2014). In contrast, the hypothalamus derives from ventral prosomeric territories patterned by Shh-dependent ventralization processes and a conserved molecular signature distinguishing it from dorsal diencephalic regions, a pattern well documented in amphibians and other vertebrates (Domínguez *et al.*, 2010; Domínguez *et al.*, 2015; Puelles et Rubenstein, 2003; Shimogori *et al.*, 2010). Functionally, salamander hypothalamic regions regulate homeostasis, neuroendocrine output, feeding, and osmoregulation, whereas the thalamus primarily supports multimodal sensory processing and relay to pallial areas (Butler et Hodos, 2005; Northcutt, 2002). These pronounced developmental and functional divergences justify treating the thalamus and hypothalamus as independent modules.

Hypotheses 6A and 6B further isolate the olfactory bulb from the remainder of the telencephalon, reflecting its distinctive developmental origin and functional specialization. The olfactory bulb operates as a primary sensory system dedicated to odor detection and early signal processing, relying on specialized circuitry and direct sensory input that is largely segregated from higher-order telencephalic processing streams (Butler et Hodos, 2005; Corfield *et al.*, 2015). By contrast, the remaining telencephalon integrates multisensory

information, supports associative and spatial cognition, and often scales predictably with overall brain size under conserved developmental programs in some vertebrate lineages (Finlay et Darlington, 1995; Finlay *et al.*, 2001). Comparative analyses indicate that olfactory bulb size may evolve independently of total telencephalic volume and instead reflects ecological dependence on olfaction rather than generalized brain enlargement (Gonzalez-Voyer *et al.*, 2009; Yopak *et al.*, 2010).

Hypotheses 7A and 7B retain the major developmental divisions of the brain while explicitly separating regions with strongly divergent functional roles. The olfactory bulb functions as a specialized sensory processor whose developmental and evolutionary scaling patterns are frequently decoupled from those of the remaining telencephalon (Corfield *et al.*, 2015; Finlay et Darlington, 1995; Finlay *et al.*, 2001; Gonzalez-Voyer *et al.*, 2009; Yopak *et al.*, 2010). The telencephalon supports higher-order associative and spatial processing (Striedter, 2005), whereas within the diencephalon, the thalamus acts as the principal sensory relay system and the hypothalamus regulates neuroendocrine function, homeostasis, and motivational states (Butler et Hodos, 2005; Northcutt, 2002). The midbrain constitutes a cohesive visuomotor integration center, and the rhombencephalon coordinates motor pattern generation, balance, and autonomic control (Butler et Hodos, 2005; Nieuwenhuys *et al.*, 2014; Northcutt, 2002). Collectively, these functional dissociations support modelling the olfactory bulb, telencephalon, thalamus, hypothalamus, mesencephalon, and rhombencephalon as six distinct modules.

Additional hypotheses for the endocast

Hypothesis 10 separates bones derived from the cranial neural crest (CNC) from bones derived from the mesoderm based on their conserved developmental origins and distinct patterning mechanisms. Fate-mapping studies in the axolotl show a sharp and stable boundary in the skull roof, with the frontal bone derived entirely from CNC and the parietal from mesoderm (Maddin *et al.*, 2016). This partition closely matches the ancestral tetrapod condition documented in comparative maps across vertebrates, including salamanders, amniotes, and fishes (Piekarski *et al.*, 2014). Moreover, CNC- and mesoderm-derived bones

follow different genetic programs, form independent ossification centers (Piekarski *et al.*, 2014), and may exhibit distinct evolutionary and functional behaviours. These conserved embryonic differences support modelling CNC-derived and mesoderm-derived bones as two separate modules.

Hypothesis 11 separates the occipito-otic region from the rest of the endocast based on its coherent developmental origin, conserved topological position, and highly specialized vestibular function. In salamanders, the otic capsule and adjoining occipital elements form a unified posterior neurocranial complex derived from paraxial mesoderm, contrasting with the mixed CNC–mesodermal origins of more anterior cranial regions (Maddin *et al.*, 2016). This otic–occipital unit shows a stable developmental organization; the cranial vault forms well anterior to the otic capsule in axolotls, highlighting the consistent positional and developmental separation between the otic region and the remainder of the skull (Maddin *et al.*, 2016). Functionally, the otic capsule houses the semicircular canals, utricle, and saccule, the core vestibular organs responsible for detecting angular and linear accelerations and maintaining equilibrium in vertebrates (Eatock et Songer, 2011; Fritzsch et Straka, 2014; Maddin et Anderson, 2012). Comparative analyses also suggest that this region evolves under distinct functional and developmental constraints (Clack, 2016; Fabre *et al.*, 2020; Maddin *et al.*, 2016). In salamanders, Fabre *et al.* (2020) found that the otic and occipital regions form a strongly integrated morphological module that remains relatively stable across ontogenetic transitions, in contrast to more variable skull regions associated with feeding or respiration. Together, the cohesive embryonic origin, consistent posterior topological placement, and specialized vestibular function of the otic region support modelling the occipito-otic complex as an independent morphological module within the endocast.

Hypothesis 12 models each bone surrounding the endocast (frontal, parietal, orbitosphenoid, parasphenoid, and occipito-otic complex) as an independent module based on their distinct developmental origins, ossification sequences, and functional roles. Across amphibians, cranial bones arise from discrete embryonic compartments, either CNC or mesoderm, and follow bone-specific ossification trajectories that generate heterogeneous developmental

constraints (Bardua *et al.*, 2019; Fabre *et al.*, 2020). The frontal and orbitosphenoid contribute to the protection of anterior brain regions and typically ossify earlier in development, whereas the parietal and parasphenoid form part of the cranial roof and braincase floor and exhibit different timing and patterns of ossification (Fabre *et al.*, 2020; Weisbecker et Mitgutsch, 2010). Comparative analyses further show that cranial bones do not evolve as a single integrated unit, but instead display heterogeneous evolutionary rates and integration strengths depending on their developmental origin and biomechanical role (Bardua *et al.*, 2020; Fabre *et al.*, 2020). These distinct developmental and functional trajectories support treating each major neurocranial bone as a potential quasi-autonomous evolutionary module.

Hypothesis 13 builds on the rationale of Hypothesis 12 but further subdivides the parasphenoid into anterior and posterior modules to reflect its mixed embryonic origin and heterogeneous developmental constraints. In amphibians, the anterior portion of the parasphenoid is generally derived from cranial neural crest, whereas the posterior portion arises from paraxial mesoderm, resulting in a bone that integrates two distinct embryonic compartments with different patterning mechanisms and ossification pathways (Maddin *et al.*, 2016; Piekarski *et al.*, 2014). Separating the parasphenoid into anterior and posterior units therefore provides a biologically informed way to capture potential modular boundaries rooted in their distinct developmental origins.

ANNEXE E : INFORMATION SUPPLÉMENTAIRE COMMUNE AUX CHAPITRES 2 ET 3

Table E1 List of the salamander specimens used in this study. Museums: AMNH = American Museum of Natural History, New York, USA; CMN = Canadian Museum of Nature, Ottawa, Canada; CSU = Colorado State University, Denver, USA; FLMNH = Florida Museum of Natural History, Gainesville, USA; FMNH = Field Museum of Natural History, Chicago, USA; KUBI = Kansas University Biodiversity Institute, Lawrence, USA; MVZ = Museum of Vertebrate Zoology, Berkeley, USA; ROM = Royal Ontario Museum, Toronto, Canada; SMNS = Stuttgart State Museum of Natural History, Stuttgart, Germany. Data manager: LH = Laurent Houle, JP = Jason Pardo.

Species	Data manager	Museum	Specimen ID	Iodine concentration (% v/w)	Iodine exposure time (days)
Ambystoma andersoni	LH	FMNH	228429	3	12
Ambystoma gracile	LH	CMN	18713	3	6
Ambystoma laterale	LH	CMN	36591	3	6
Ambystoma mexicanum	JP	Not in a collection	-	11.75	5
Ambystoma opacum	LH	CMN	12497	3	4
Ambystoma texanum	LH	CMN	10211	3	4
Amphiuma pholeter	Morphosource	FLMNH	162027	unknown	unknown
Aneides aeneus	LH	CMN	7556	1.5	4
Aneides ferreus	LH	CMN	34740	3	3
Aquiloeurycea cephalica	LH	KUBI	53962	1.5	3
Batrachoseps pacificus	LH	KUBI	17849	1.5	4
Batrachuperus pinchonii	LH	FMNH	28148B	3	4

Species	Data manager	Museum	Specimen ID	Iodine concentration (% v/w)	Iodine exposure time (days)
Batrachuperus pinchonii	LH	FMNH	28148A	3	4
Batrachuperus tibetanus	LH	ROM	40080	3	3
Bolitoglossa adspersa	LH	KUBI	110367	1.5	3
Bolitoglossa altamazonica	LH	KUBI	220585	1.5	3
Bolitoglossa chica	LH	KUBI	179519	1.5	2
Bolitoglossa helmrichi	LH	KUBI	186122	1.5	2
Bolitoglossa rufescens	LH	KUBI	26222	1.5	3
Bolitoglossa schizodactyla	LH	KUBI	116639	3	2
Bolitoglossa sima	LH	KUBI	119454	1.5	3
Bolitoglossa subpalmata	LH	KUBI	66728	1.5	4
Bolitoglossa subpalmata	LH	KUBI	66640	1.5	4
Chiropterotriton chiropterus	LH	KUBI	100755	1.5	3
Cryptobranchus alleganiensis	Morphosource	FLMNH	10881	unknown	unknown
Cryptotriton veraepacis	LH	MVZ	167991	1.5	2
Cynops pyrrhogaster	LH	CMN	13924	3	5
Dendrotriton bromeliacius	LH	MVZ	103235	1.5	2
Desmognathus monticola	LH	CMN	25385	3	4
Desmognathus ochrophaeus	LH	ROM	15969	1.5	3

Species	Data manager	Museum	Specimen ID	Iodine concentration (% v/w)	Iodine exposure time (days)
Dicamptodon ensatus	Morphosource	FLMNH	149094	unknown	unknown
Ensatina eschscholtzii	LH	CMN	34782	1.5	3
Eurycea bislineata	LH	CMN	8154	1.5	3
Eurycea cirrigera	LH	KUBI	144442	1.5	3
Eurycea lucifuga	LH	CMN	34465	1.5	3
Eurycea multiplicata	LH	KUBI	175858	1.5	2
Gyrinophilus porphyriticus	LH	CMN	29950	3	4
Hydromantes genei	LH	FMNH	71113	3	7
Hydromantes platycephalus	LH	MVZ	233372	1.5	3
Hynobius leechii	LH	KUBI	152356	1.5	3
Hynobius nebulosus	Morphosource	FLMNH	24315	unknown	unknown
Hynobius sonani	LH	MVZ	197242	3	4
Hynobius tsuensis	LH	KUBI	151832	3	4
Hynobius yiwuensis	LH	MVZ	231134	3	4
Ichthyosaura alpestris	LH	CMN	4332	1.5	4
Isthmura bellii	LH	FMNH	36885A	3	10
Isthmura bellii	LH	KUBI	129225	3	11
Lissotriton montandoni	LH	FMNH	11770	1.5	8

Species	Data manager	Museum	Specimen ID	Iodine concentration (% v/w)	Iodine exposure time (days)
Lyciasalamandra luschani	LH	MVZ	230161	1.5	3
Necturus maculosus	LH	Not in a collection	-	3	7
Necturus maculosus	LH	Not in a collection	-	3	7
Notophthalmus viridescens	LH	Not in a collection	-	1.5	3
Notophthalmus viridescens	LH	Not in a collection	-	1.5	2
Nototriton picadoi	LH	KUBI	203192	1.5	2
Oedipina complex	LH	FMNH	152580	1.5	3
Oedipina cyclocauda	LH	KUBI	34749	1.5	2
Onychodactylus japonicus	LH	MVZ	129401	3	4
Pachytriton brevipes	LH	AMNH	18542	3	4
Plethodon dunni	LH	CMN	34793	1.5	3
Plethodon elongatus	LH	CMN	34755	1.5	3
Plethodon glutinosus	LH	CMN	16933	3	4
Plethodon hoffmani	LH	CMN	21019	1.5	3
Plethodon vandykei	Morphosource	CSU	MWI 0039	unknown	unknown
Plethodon vehiculum	Morphosource	CSU	MWI 0042	unknown	unknown
Plethodon vehiculum	Morphosource	CSU	MWI 0043	unknown	unknown
Pseudobranchus striatus	JP	Not in a collection	-	unknown	unknown

Species	Data manager	Museum	Specimen ID	Iodine concentration (% v/w)	Iodine exposure time (days)
Pseudoeurycea leprosa	LH	KUBI	182503	1.5	3
Pseudoeurycea rex	LH	KUBI	59283	1.5	3
Pseudoeurycea saltator	LH	KUBI	136515	1.5	2
Rhyacotriton olympicus	LH	CMN	34779	1.5	4
Salamandra salamandra	LH	KUBI	144178	3	12
Salamandrella keyserlingii	LH	KUBI	212725	1.5	2
Siren intermedia	Morphosource	SMNS	15426	unknown	unknown
Taricha granulosa	LH	CMN	16068	3	4
Taricha granulosa	LH	FMNH	85374	3	4
Thorius boreas	LH	KUBI	136521	1.5	2
Thorius lunaris	LH	KUBI	106887	1.5	2
Thorius macdougalli	LH	KUBI	110050	1.5	2
Thorius pennatulus	LH	KUBI	106865	1.5	2
Thorius spilogaster	LH	KUBI	106926	1.5	2
Triturus cristatus	LH	CMN	4331	3	5
Triturus marmoratus	LH	KUBI	144198	3	4
Tylototriton ziegleri	LH	ROM	35339	3	3

Table E2 List of scanning facilities that produced the images used for this study.

Scanning facility	Scanner	Specimen scanned	Reconstruction sofware
Nanoscale Research Facility (University of Florida, USA)	General Electric phoenix v|tome|x m 240	FLMNH-162027, FLMNH-10881, FLMNH-149094, FLMNH-24315	Datos|x
VetCore Facility for Research (University of Veterinary Medicine Vienna)	Zeiss Xradia microXCT-400	SMNS-15426	Zeiss Advanced Reconstruction Toolbox (ART)
Département de biologie, chimie et géographie and Institut des sciences de la mer (Université du Québec à Rimouski)	Bruker Skyscan 1173	All other specimens (see Table E1)	NRecon

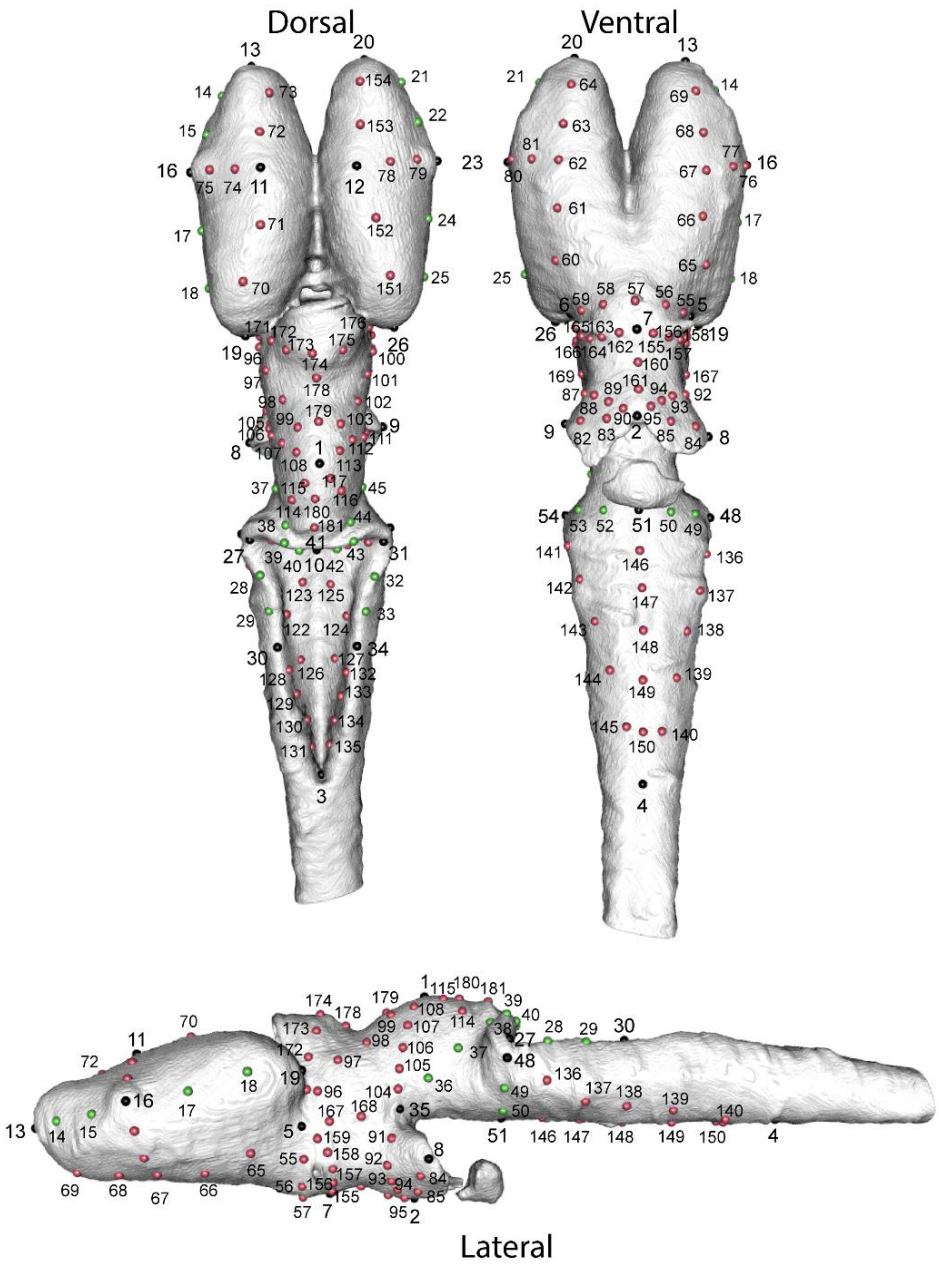

Figure E1 Landmarks used in this study on the brain of *Ambystoma mexicanum*. Black, red and green spheres represent fixed landmarks (28), surface semilandmarks (87) and curve semilandmarks (26), respectively.

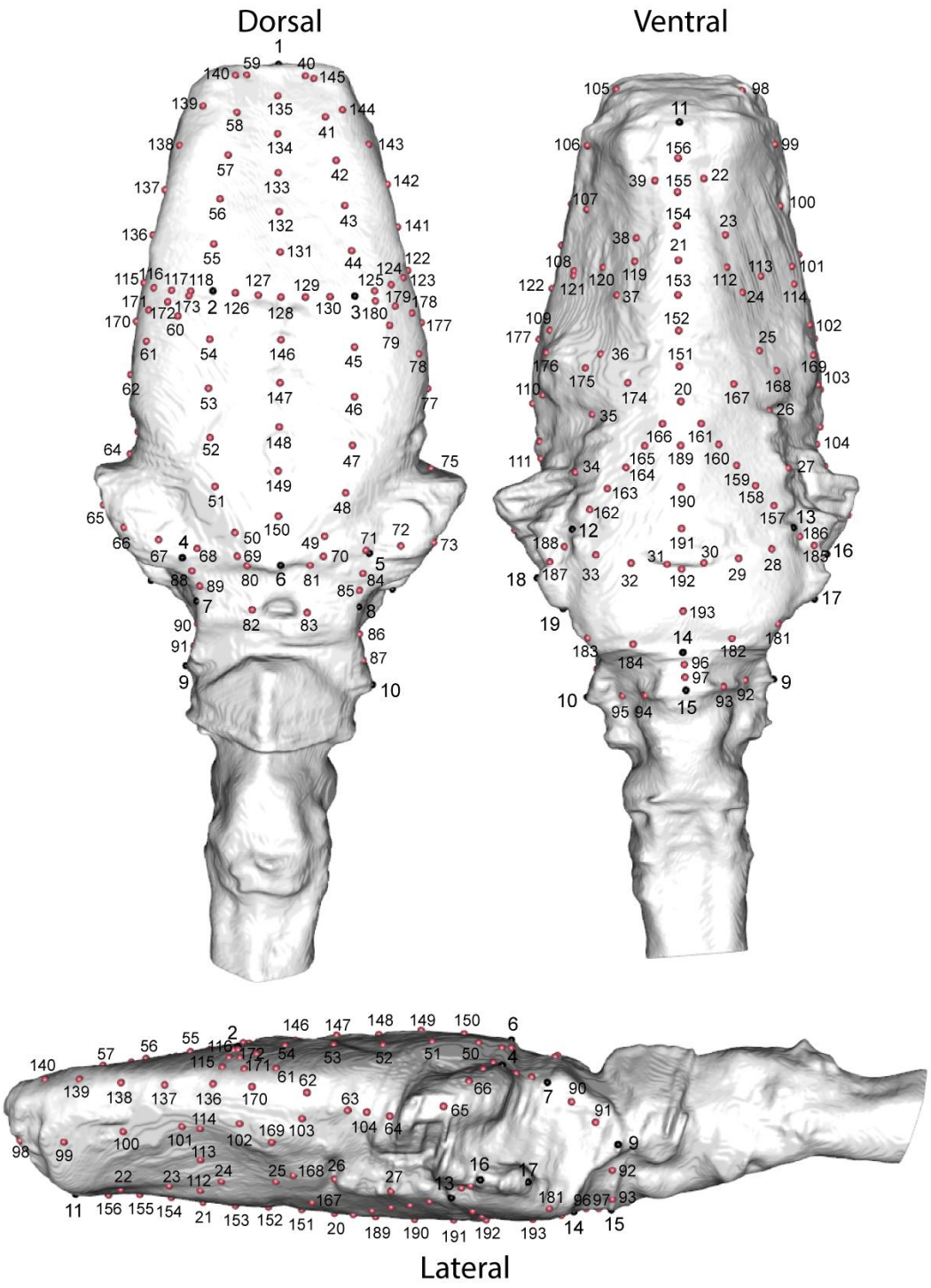

Figure E2 Landmarks used in this study on the endocast of *Pseudoeurycea leprosa*. Black and red spheres represent fixed landmarks (19) and surface semilandmarks (174), respectively.

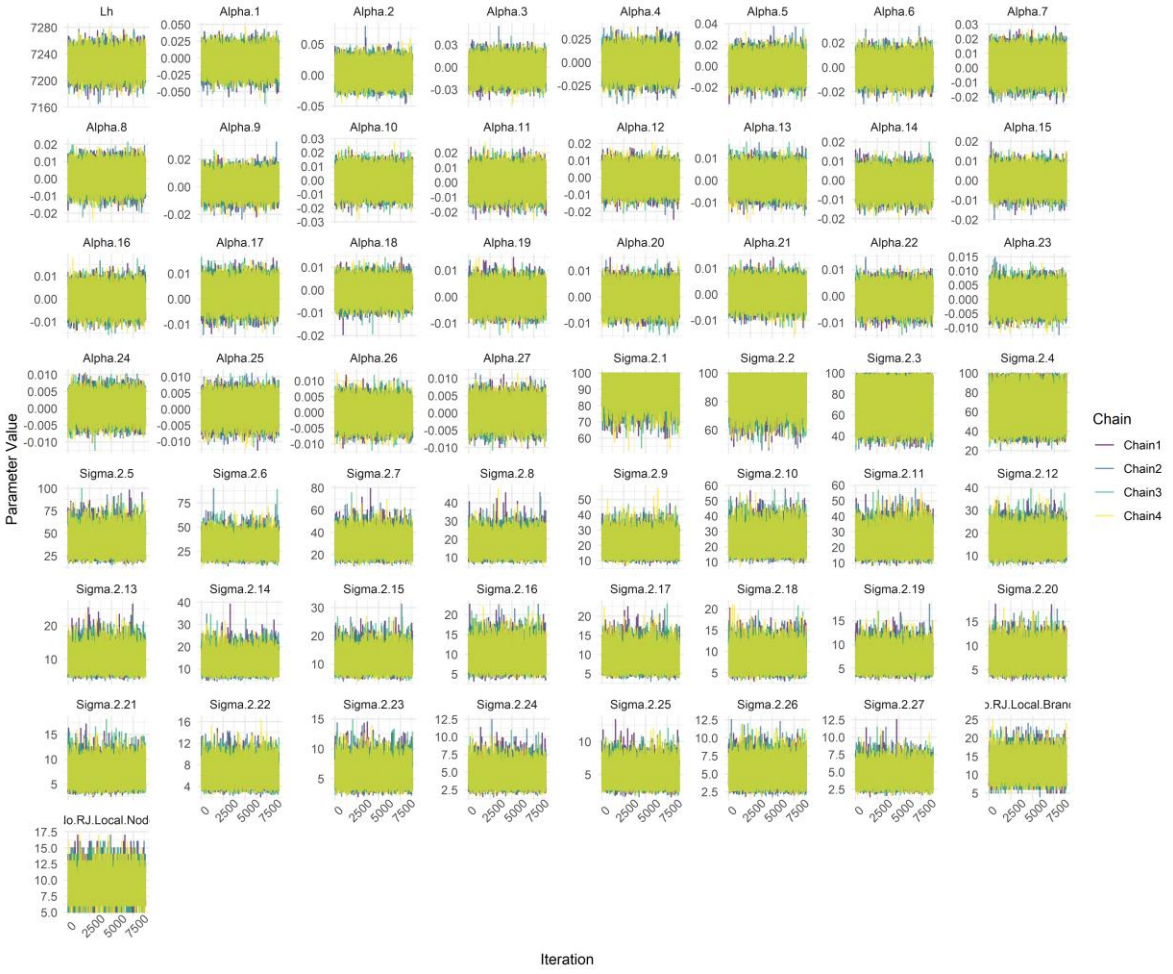

Figure E3 Trace plots of each parameter for four independent MCMC chains for the phylogenetic Bayesian analysis performed on brain shape. Lh = Likelihood.

Figure E4 Parameter values density for four independent chains for the phylogenetic Bayesian analysis performed on the brain shape. Lh = Likelihood.

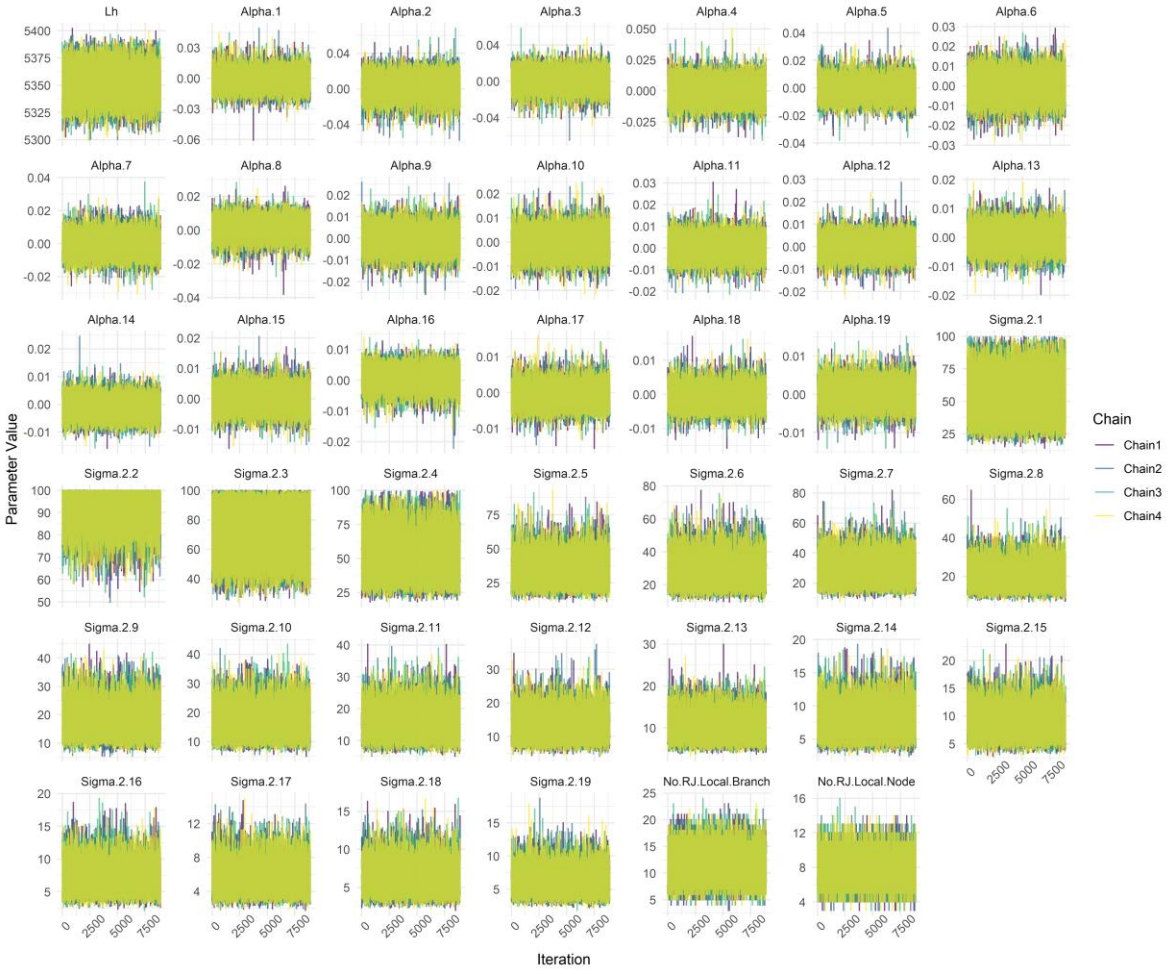

Figure E5 Trace plots of each parameter for four independent MCMC chains for the phylogenetic Bayesian analysis performed on endocast shape. Lh = Likelihood.

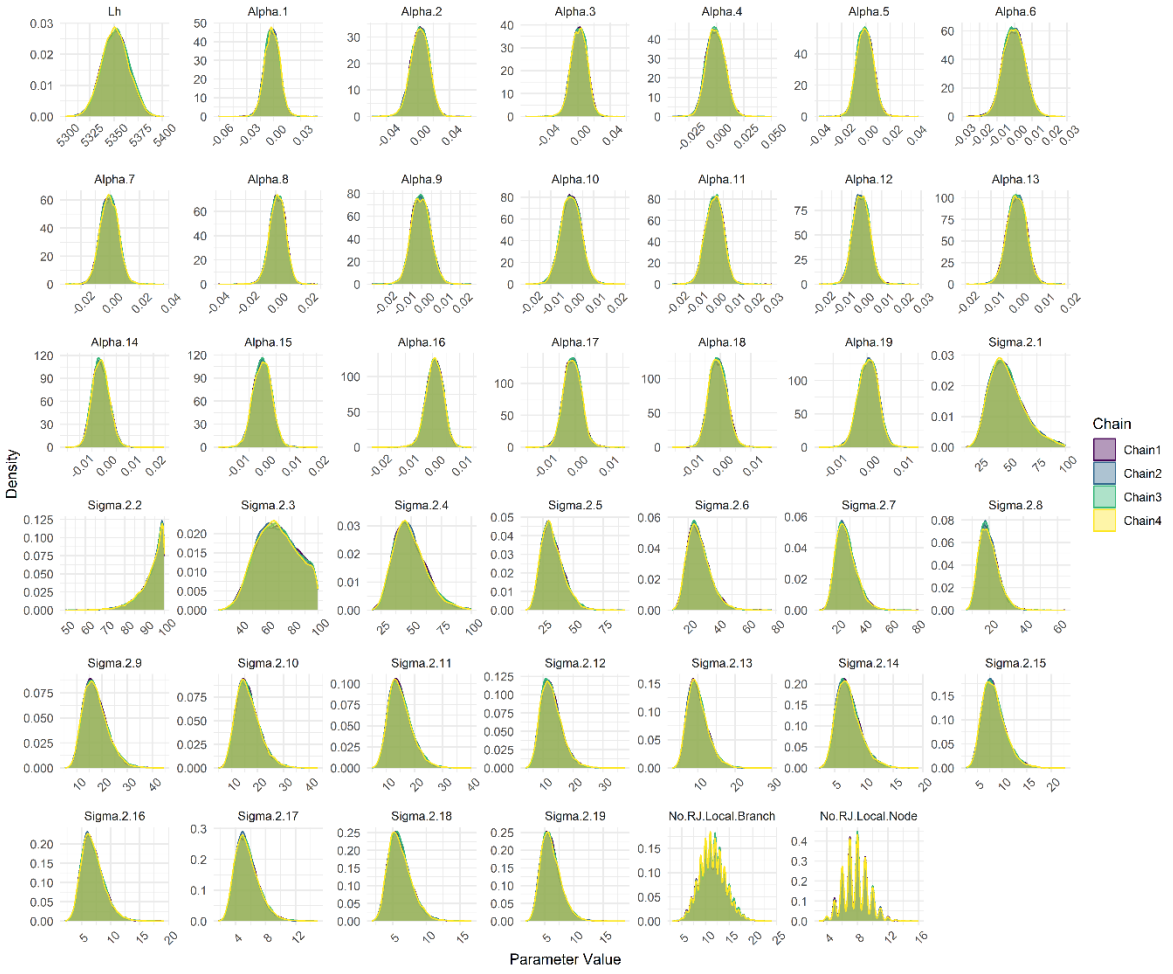

Figure E6 Parameter values density for four independent chains for the phylogenetic Bayesian analysis performed on the endocast shape. Lh = Likelihood.

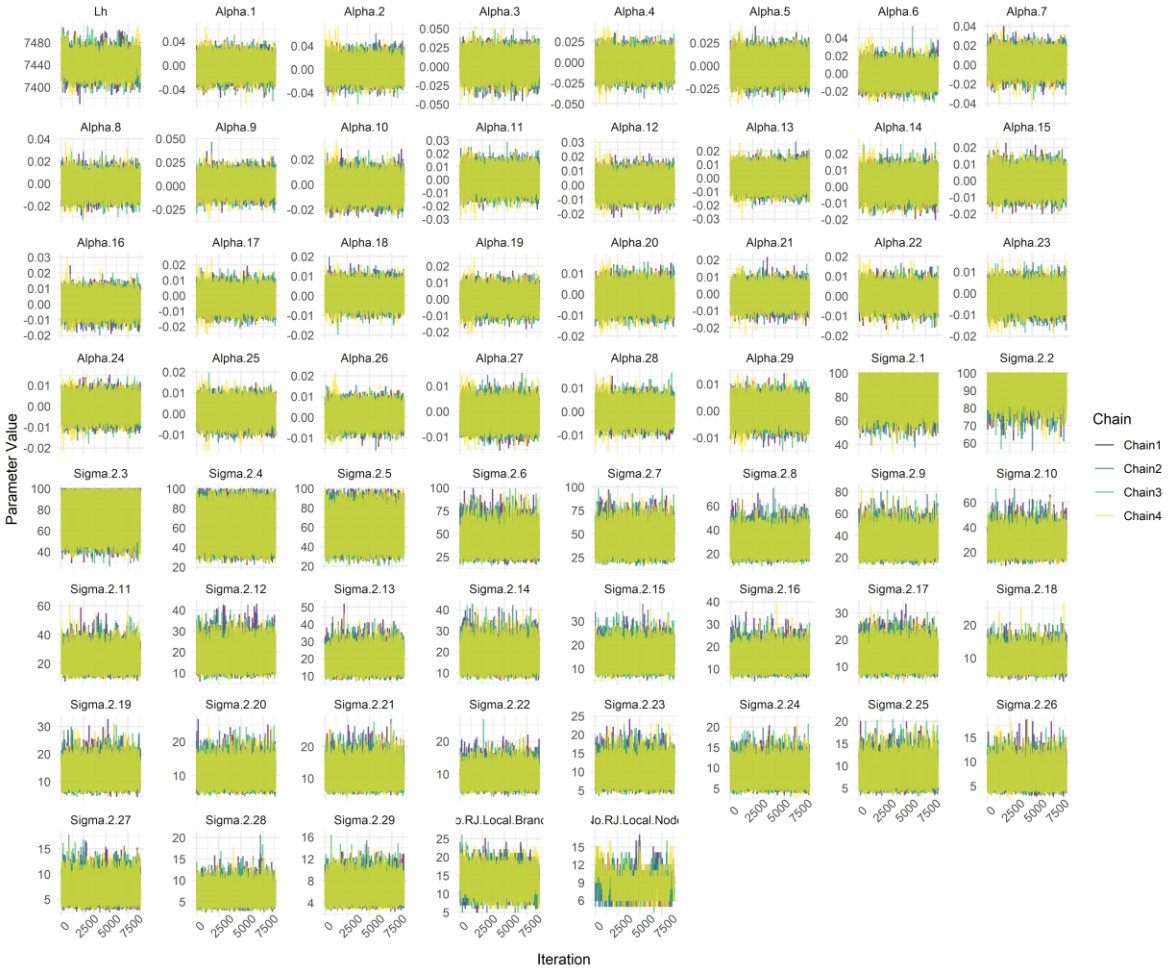

Figure E7 Trace plots of each parameter for four independent MCMC chains for the phylogenetic Bayesian analysis performed on the combined dataset. Lh = Likelihood.

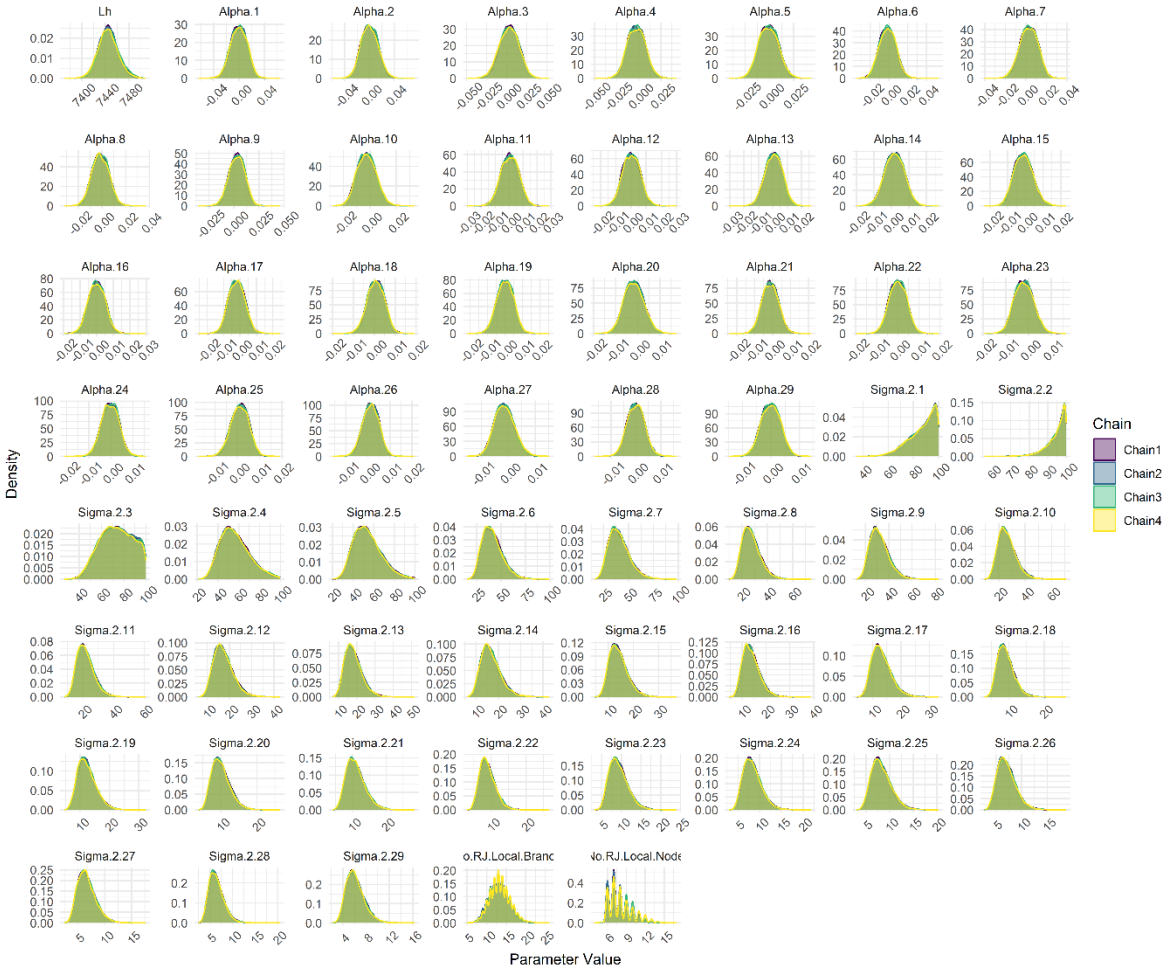

Figure E8 Parameter values density for four independent chains for the phylogenetic Bayesian analysis performed on the combined dataset. Lh = Likelihood.

Table E3 Effective sample size for each parameter of four independent MCMC chains for the phylogenetic Bayesian analysis performed on the brain shape.

Parameter	Chain 1	Chain 2	Chain 3	Chain 4	Parameter	Chain 1	Chain 2	Chain 3	Chain 4
Likelihood	4430	4071	5282	2712	Sigma.2.1	8900	8900	8900	8900
Alpha.1	8900	8900	8900	7645	Sigma.2.2	7155	8154	8272	8150
Alpha.2	8900	8900	8900	8900	Sigma.2.3	8018	7659	7402	6795
Alpha.3	8900	9608	9416	8900	Sigma.2.4	6763	7718	8081	7889

Parameter	Chain 1	Chain 2	Chain 3	Chain 4	Parameter	Chain 1	Chain 2	Chain 3	Chain 4
Alpha.4	8900	8900	8900	8900	Sigma.2.5	6138	7409	7495	7674
Alpha.5	8900	8900	8900	8629	Sigma.2.6	7859	7089	7444	7905
Alpha.6	8900	8900	8900	8900	Sigma.2.7	8050	6939	7409	7614
Alpha.7	8900	8065	8900	8900	Sigma.2.8	8002	7817	7037	7491
Alpha.8	8900	8831	8316	8900	Sigma.2.9	7680	7389	7074	7846
Alpha.9	9265	8900	9351	8900	Sigma.2.10	7360	7338	7251	7391
Alpha.10	8900	8156	8885	9152	Sigma.2.11	7697	7645	7387	7880
Alpha.11	8900	8950	9234	8900	Sigma.2.12	7559	7536	7486	7825
Alpha.12	8900	9343	8900	8900	Sigma.2.13	6970	8054	7714	7725
Alpha.13	9268	8900	8900	8900	Sigma.2.14	7440	7510	7179	8022
Alpha.14	8348	8900	8900	8900	Sigma.2.15	6106	6738	7258	6394
Alpha.15	8900	8900	8900	8900	Sigma.2.16	7375	7949	6525	7696
Alpha.16	8900	8900	8900	8900	Sigma.2.17	7206	7491	6792	7825
Alpha.17	8900	8900	9660	8900	Sigma.2.18	7707	7923	7633	8076
Alpha.18	8900	8900	10313	8900	Sigma.2.19	7201	6581	7382	7773
Alpha.19	8900	9304	7862	8452	Sigma.2.20	7978	7865	7139	7626
Alpha.20	8900	8900	8900	9663	Sigma.2.21	7114	7907	7480	7419
Alpha.21	9211	8900	8900	8900	Sigma.2.22	6855	7905	7424	7818
Alpha.22	9206	9235	8900	9237	Sigma.2.23	8045	7020	7417	7825
Alpha.23	8900	8900	8900	8900	Sigma.2.24	6736	7573	7524	7426
Alpha.24	8900	8900	8900	8900	Sigma.2.25	6566	7314	6510	7658
Alpha.25	8900	8900	8900	8900	Sigma.2.26	7986	7334	6971	7961
Alpha.26	8900	8900	8625	8900	Sigma.2.27	6724	5864	7377	7361
Alpha.27	8900	8900	8900	8900	No. reverse jump local branch	6175	4649	5500	5370

Parameter	Chain 1	Chain 2	Chain 3	Chain 4	Parameter	Chain 1	Chain 2	Chain 3	Chain 4
					No. reverse jump local node	1550	2020	1905	1565

Table E4 Effective sample size for each parameter of four independent MCMC chains for the phylogenetic Bayesian analysis performed on the endocast shape.

Parameter	Chain 1	Chain 2	Chain 3	Chain 4	Parameter	Chain 1	Chain 2	Chain 3	Chain 4
Likelihood	3139	3113	3077	3291	Sigma.2.1	8414	7683	8374	8115
Alpha.1	8900	9289	8900	7619	Sigma.2.2	8325	8900	8433	8827
Alpha.2	8770	8116	8900	8900	Sigma.2.3	8116	7638	7597	7982
Alpha.3	8900	8900	8900	8900	Sigma.2.4	6855	7519	7171	7251
Alpha.4	7966	7544	7587	7777	Sigma.2.5	7141	7559	7899	6511
Alpha.5	8900	8900	9896	8900	Sigma.2.6	7630	7318	6841	7165
Alpha.6	8079	8900	7999	8278	Sigma.2.7	7479	7401	6745	8149
Alpha.7	8900	8900	8900	8900	Sigma.2.8	6863	7397	7931	7917
Alpha.8	8900	8900	8900	8838	Sigma.2.9	8126	8032	7879	8306
Alpha.9	8900	8329	8249	9067	Sigma.2.10	7516	7801	7942	7705
Alpha.10	8900	8900	8313	8900	Sigma.2.11	6942	7515	7960	6721
Alpha.11	8453	6972	7876	8069	Sigma.2.12	7980	8234	7476	8076
Alpha.12	9948	8900	8900	8900	Sigma.2.13	7157	7566	7370	7530
Alpha.13	8557	8900	8900	8900	Sigma.2.14	6545	6805	6791	7473
Alpha.14	5831	5813	5835	5629	Sigma.2.15	7277	7256	7253	7279
Alpha.15	8900	8900	8900	8900	Sigma.2.16	7381	7255	7647	7822
Alpha.16	8900	8900	8603	8710	Sigma.2.17	8124	7514	8000	7694
Alpha.17	8442	8900	8900	8900	Sigma.2.18	8139	7999	7478	7382
Alpha.18	8175	8193	7450	7669	Sigma.2.19	6462	7115	7179	7421

Parameter	Chain 1	Chain 2	Chain 3	Chain 4	Parameter	Chain 1	Chain 2	Chain 3	Chain 4
Alpha.19	8900	8900	8291	8900	No. reverse jump local branch	6607	6099	6557	6611
					No. reverse jump local node	4456	3930	4184	4253

Table E5 Effective sample size for each parameter of four independent MCMC chains for the phylogenetic Bayesian analysis performed on the combined dataset.

Parameter	Chain 1	Chain 2	Chain 3	Chain 4	Parameter	Chain 1	Chain 2	Chain 3	Chain 4
Likelihood	184	505	180	210	Sigma.2.1	8335	9195	8551	8900
Alpha.1	8292	8469	8317	8900	Sigma.2.2	8070	8361	9387	8189
Alpha.2	8900	8508	7257	8480	Sigma.2.3	7954	7971	7226	6754
Alpha.3	7623	8333	8009	7634	Sigma.2.4	7765	7892	7694	6572
Alpha.4	8900	8900	8900	8900	Sigma.2.5	7424	7567	7168	6887
Alpha.5	7101	8164	8299	8900	Sigma.2.6	7829	7325	6789	7723
Alpha.6	8900	8900	8900	9092	Sigma.2.7	7730	7740	7491	6788
Alpha.7	8564	5477	8136	8143	Sigma.2.8	7219	7884	7347	7966
Alpha.8	8527	8528	8378	8634	Sigma.2.9	7397	7672	7678	7218
Alpha.9	8720	8144	7739	8900	Sigma.2.10	6775	7469	7121	7402
Alpha.10	7890	7450	7689	5126	Sigma.2.11	7066	7880	7690	7682
Alpha.11	8015	8900	7050	8636	Sigma.2.12	7368	7767	7687	7422
Alpha.12	8635	8900	8358	8900	Sigma.2.13	7054	6892	7091	6462
Alpha.13	8367	7986	7881	7753	Sigma.2.14	7792	7627	7532	7658
Alpha.14	8953	7538	8900	8900	Sigma.2.15	7201	7635	7255	7201
Alpha.15	7418	8969	7026	6574	Sigma.2.16	7362	7515	7393	7857
Alpha.16	8900	7651	8615	8900	Sigma.2.17	6883	7590	6264	6926

Parameter	Chain 1	Chain 2	Chain 3	Chain 4	Parameter	Chain 1	Chain 2	Chain 3	Chain 4
Alpha.17	8900	8461	8900	8900	Sigma.2.18	7359	7688	7867	7458
Alpha.18	8900	7161	8900	8481	Sigma.2.19	7475	7003	7329	6571
Alpha.19	9212	6605	8900	8577	Sigma.2.20	7503	7275	7239	7454
Alpha.20	8900	7718	6012	8253	Sigma.2.21	6144	7480	7059	7245
Alpha.21	8900	8601	8366	8900	Sigma.2.22	7976	7732	7725	7447
Alpha.22	8900	8900	8148	8900	Sigma.2.23	7542	6881	6624	6661
Alpha.23	8617	8900	8611	8900	Sigma.2.24	7698	7078	7620	7419
Alpha.24	8556	8900	8515	8295	Sigma.2.25	6602	7378	6938	6453
Alpha.25	7896	8900	7450	8148	Sigma.2.26	6549	6991	7585	6451
Alpha.26	8278	6291	4170	3577	Sigma.2.27	7839	7287	8130	7618
Alpha.27	7486	7905	7102	7181	Sigma.2.28	7762	6916	7419	7990
Alpha.28	8900	8900	8900	8900	Sigma.2.29	7520	7754	7326	7096
Alpha.29	8900	9297	8402	8900	No. reverse jump local branch	658	2414	1157	512
					No. reverse jump local node	188	181	197	139

Table E6 Gelman and Robin's convergence diagnostic results for each parameter considering four independent MCMC chains performed on the brain shape. Additionally, the multivariate potential scale reduction factor (PSRF) is provided. est. = estimate. CI = confidence interval.

Parameter	Point est.	Upper CI	Parameter	Point est.	Upper CI
Likelihood	1.00	1.00	Sigma.2.1	1.00	1.00
Alpha.1	1.00	1.00	Sigma.2.2	1.00	1.00
Alpha.2	1.00	1.00	Sigma.2.3	1.00	1.00

Parameter	Point est.	Upper CI	Parameter	Point est.	Upper CI
Alpha.3	1.00	1.00	Sigma.2.4	1.00	1.00
Alpha.4	1.00	1.00	Sigma.2.5	1.00	1.00
Alpha.5	1.00	1.00	Sigma.2.6	1.00	1.00
Alpha.6	1.00	1.00	Sigma.2.7	1.00	1.00
Alpha.7	1.00	1.00	Sigma.2.8	1.00	1.00
Alpha.8	1.00	1.00	Sigma.2.9	1.00	1.00
Alpha.9	1.00	1.00	Sigma.2.10	1.00	1.00
Alpha.10	1.00	1.00	Sigma.2.11	1.00	1.00
Alpha.11	1.00	1.00	Sigma.2.12	1.00	1.00
Alpha.12	1.00	1.00	Sigma.2.13	1.00	1.00
Alpha.13	1.00	1.00	Sigma.2.14	1.00	1.00
Alpha.14	1.00	1.00	Sigma.2.15	1.00	1.00
Alpha.15	1.00	1.00	Sigma.2.16	1.00	1.00
Alpha.16	1.00	1.00	Sigma.2.17	1.00	1.00
Alpha.17	1.00	1.00	Sigma.2.18	1.00	1.00
Alpha.18	1.00	1.00	Sigma.2.19	1.00	1.00
Alpha.19	1.00	1.00	Sigma.2.20	1.00	1.00
Alpha.20	1.00	1.00	Sigma.2.21	1.00	1.00
Alpha.21	1.00	1.00	Sigma.2.22	1.00	1.00
Alpha.22	1.00	1.00	Sigma.2.23	1.00	1.00

Parameter	Point est.	Upper CI	Parameter	Point est.	Upper CI
Alpha.23	1.00	1.00	Sigma.2.24	1.00	1.00
Alpha.24	1.00	1.00	Sigma.2.25	1.00	1.00
Alpha.25	1.00	1.00	Sigma.2.26	1.00	1.00
Alpha.26	1.00	1.00	Sigma.2.27	1.00	1.00
Alpha.27	1.00	1.00	No. reverse jump local branch	1.00	1.00
			No. reverse jump local node	1.00	1.00
Multivariate PSRF			1.00		

Table E7 Gelman and Robin's convergence diagnostic results for each parameter considering four independent MCMC chains performed on the endocast shape. Additionally, the multivariate potential scale reduction factor (PSRF) is provided. est. = estimate. CI = confidence interval.

Parameter	Point est.	Upper CI	Parameter	Point est.	Upper CI
Likelihood	1.00	1.00	Sigma.2.1	1.00	1.00
Alpha.1	1.00	1.00	Sigma.2.2	1.00	1.00
Alpha.2	1.00	1.00	Sigma.2.3	1.00	1.00
Alpha.3	1.00	1.00	Sigma.2.4	1.00	1.00
Alpha.4	1.00	1.00	Sigma.2.5	1.00	1.00
Alpha.5	1.00	1.00	Sigma.2.6	1.00	1.00
Alpha.6	1.00	1.00	Sigma.2.7	1.00	1.00

Parameter	Point est.	Upper CI	Parameter	Point est.	Upper CI
Alpha.7	1.00	1.00	Sigma.2.8	1.00	1.00
Alpha.8	1.00	1.00	Sigma.2.9	1.00	1.00
Alpha.9	1.00	1.00	Sigma.2.10	1.00	1.00
Alpha.10	1.00	1.00	Sigma.2.11	1.00	1.00
Alpha.11	1.00	1.00	Sigma.2.12	1.00	1.00
Alpha.12	1.00	1.00	Sigma.2.13	1.00	1.00
Alpha.13	1.00	1.00	Sigma.2.14	1.00	1.00
Alpha.14	1.00	1.00	Sigma.2.15	1.00	1.00
Alpha.15	1.00	1.00	Sigma.2.16	1.00	1.00
Alpha.16	1.00	1.00	Sigma.2.17	1.00	1.00
Alpha.17	1.00	1.00	Sigma.2.18	1.00	1.00
Alpha.18	1.00	1.00	Sigma.2.19	1.00	1.00
Alpha.19	1.00	1.00	No. reverse jump local branch	1.00	1.00
			No. reverse jump local node	1.00	1.00
Multivariate PSRF			1.00		

Table E8 Gelman and Robin's convergence diagnostic results for each parameter considering four independent MCMC chains performed on the combined dataset. Additionally, the

multivariate potential scale reduction factor (PSRF) is provided. est. = estimate. CI = confidence interval.

Parameter	Point est.	Upper CI	Parameter	Point est.	Upper CI
Likelihood	1.00	1.00	Sigma.2.1	1.00	1.00
Alpha.1	1.00	1.00	Sigma.2.2	1.00	1.00
Alpha.2	1.00	1.00	Sigma.2.3	1.00	1.00
Alpha.3	1.00	1.00	Sigma.2.4	1.00	1.00
Alpha.4	1.00	1.00	Sigma.2.5	1.00	1.00
Alpha.5	1.00	1.00	Sigma.2.6	1.00	1.00
Alpha.6	1.00	1.00	Sigma.2.7	1.00	1.00
Alpha.7	1.00	1.00	Sigma.2.8	1.00	1.00
Alpha.8	1.00	1.00	Sigma.2.9	1.00	1.00
Alpha.9	1.00	1.00	Sigma.2.10	1.00	1.00
Alpha.10	1.00	1.00	Sigma.2.11	1.00	1.00
Alpha.11	1.00	1.00	Sigma.2.12	1.00	1.00
Alpha.12	1.00	1.00	Sigma.2.13	1.00	1.00
Alpha.13	1.00	1.00	Sigma.2.14	1.00	1.00
Alpha.14	1.00	1.00	Sigma.2.15	1.00	1.00
Alpha.15	1.00	1.00	Sigma.2.16	1.00	1.00
Alpha.16	1.00	1.00	Sigma.2.17	1.00	1.00
Alpha.17	1.00	1.00	Sigma.2.18	1.00	1.00

Parameter	Point est.	Upper CI	Parameter	Point est.	Upper CI
Alpha.18	1.00	1.00	Sigma.2.19	1.00	1.00
Alpha.19	1.00	1.00	Sigma.2.20	1.00	1.00
Alpha.20	1.00	1.00	Sigma.2.21	1.00	1.00
Alpha.21	1.00	1.00	Sigma.2.22	1.00	1.00
Alpha.22	1.00	1.00	Sigma.2.23	1.00	1.00
Alpha.23	1.00	1.00	Sigma.2.24	1.00	1.00
Alpha.24	1.00	1.00	Sigma.2.25	1.00	1.00
Alpha.25	1.00	1.00	Sigma.2.26	1.00	1.00
Alpha.26	1.00	1.00	Sigma.2.27	1.00	1.00
Alpha.27	1.00	1.00	Sigma.2.28	1.00	1.00
Alpha.28	1.00	1.00	Sigma.2.29	1.00	1.00
Alpha.29	1.00	1.00	No. reverse jump local branch	1.00	1.00
			No. reverse jump local node	1.01	1.01
Multivariate PSRF			1.01		

ANNEXE F : INFORMATION SUPPLÉMENTAIRE DU CHAPITRE 3

Table F1 Scoring of each species to a microhabitat, a life cycle and a tongue-type.

Species	Microhabitat	Reference Microhabitat	Life cycle	Reference Life cycle	Ballistic tongue	Reference Ballistic tongue
Ambystoma andersoni	Aquatic	(Baken and Adams, 2019)	Strict paedomorphic	(Shaffer *et al.*, 2004)	No	(Deban *et al.*, 2020)
Ambystoma gracile	Terrestrial	(Ponssa *et al.*, 2022)	Facultative paedomorphic	(Ponssa *et al.*, 2022)	No	(Deban *et al.*, 2020)
Ambystoma laterale	Terrestrial	(Baken and Adams, 2019)	Biphasic	(Raffaëlli, 2007)	No	(Deban *et al.*, 2020)
Ambystoma mexicanum	Aquatic	(Baken and Adams, 2019; Ponssa *et al.*, 2022)	Strict paedomorphic	(Ponssa *et al.*, 2022)	No	(Deban *et al.*, 2020)
Ambystoma opacum	Terrestrial	(Baken et Adams, 2019; Ponssa *et al.*, 2022)	Biphasic	(Ponssa *et al.*, 2022)	No	(Deban *et al.*, 2020)
Ambystoma texanum	Terrestrial	(Ponssa *et al.*, 2022)	Biphasic	(Ponssa *et al.*, 2022)	No	(Deban *et al.*, 2020)
Amphiuma pholeter	Aquatic	(Baken and Adams, 2019)	Strict paedomorphic	(Vitt and Caldwell, 2013)	No	(Deban *et al.*, 2020)
Aneides aeneus	Terrestrial	(Raffaëlli, 2007)	Direct	(Petranka, 1998)	No	(Deban *et al.*, 2020)
Aneides ferreus	Arboreal	(Baken and Adams, 2019)	Direct	(Petranka, 1998)	No	(Deban *et al.*, 2020)
Aquiloeurycea cephalica	Terrestrial	(Baken and Adams, 2019)	Direct	(Petranka, 1998)	Yes	(Lombard and Wake, 1986)
Batrachoseps pacificus	Terrestrial	(Bird *et al.*, 2018)	Direct	(Stebbins, 2003)	Yes	(Lombard and Wake, 1986)
Batrachuperus pinchonii	Aquatic	(Raffaëlli, 2007)	Biphasic	(Raffaëlli, 2007)	No	(Deban *et al.*, 2020)
Batrachuperus tibetanus	Aquatic	(Baken and Adams, 2019)	Biphasic	(Fei and Ye, 2001)	No	(Deban *et al.*, 2020)
Bolitoglossa adspersa	Terrestrial	(Blankers *et al.*, 2012)	Direct	(Rovito *et al.*, 2015)	Yes	(Lombard and Wake, 1986)
Bolitoglossa altamazonica	Terrestrial	(Blankers *et al.*, 2012)	Direct	(Rovito *et al.*, 2015)	Yes	(Lombard and Wake, 1986)

Species	Microhabitat	Reference Microhabitat	Life cycle	Reference Life cycle	Ballistic tongue	Reference Ballistic tongue
Bolitoglossa chica	Arboreal	(McEntire, 2016)	Direct	(Rovito *et al.*, 2015)	Yes	(Lombard and Wake, 1986)
Bolitoglossa helmrichi	Arboreal	(Baken and Adams, 2019; Ponssa *et al.*, 2022)	Direct	(Ponssa *et al.*, 2022)	Yes	(Lombard and Wake, 1986)
Bolitoglossa rufescens	Arboreal	(Baken and Adams, 2019)	Direct	(IUCN, 2020)	Yes	(Lombard and Wake, 1986)
Bolitoglossa schizodactyla	Arboreal	(Baken and Adams, 2019)	Direct	(Solís *et al.*, 2008)	Yes	(Lombard and Wake, 1986)
Bolitoglossa sima	Arboreal	(Blankers *et al.*, 2012)	Direct	(Rovito *et al.*, 2015)	Yes	(Lombard and Wake, 1986)
Bolitoglossa subpalmata	Arboreal	(Baken and Adams, 2019)	Direct	(Rovito *et al.*, 2015)	Yes	(Lombard and Wake, 1986)
Chiropterotriton chiropterus	Arboreal	(Ponssa *et al.*, 2022)	Direct	(Ponssa *et al.*, 2022)	Yes	(Lombard and Wake, 1986)
Cryptobranchus alleganiensis	Aquatic	(Baken and Adams, 2019)	Strict paedomorphic	(Petranka, 1998)	No	(Deban *et al.*, 2020)
Cryptotriton veraepacis	Arboreal	(Baken and Adams, 2019)	Direct	(Rovito *et al.*, 2015)	Yes	(Lombard and Wake, 1986)
Cynops pyrrhogaster	Aquatic	(Stebbins, 2003)	Biphasic	(Raffaëlli, 2007)	No	(Deban *et al.*, 2020)
Dendrotriton bromeliacius	Arboreal	(Baken and Adams, 2019)	Direct	(Rovito *et al.*, 2015)	Yes	(Lombard and Wake, 1986)
Desmognathus monticola	Terrestrial	(Ponssa *et al.*, 2022)	Biphasic	(Ponssa *et al.*, 2022)	No	(Deban *et al.*, 2020)
Desmognathus ochrophaeus	Terrestrial	(Ponssa *et al.*, 2022)	Biphasic	(Ponssa *et al.*, 2022)	No	(Deban *et al.*, 2020)
Dicamptodon ensatus	Terrestrial	(Petranka, 1998)	Facultative paedomorphic	(Petranka, 1998)	No	(Deban *et al.*, 2020)
Ensatina eschscholtzii	Terrestrial	(Bird *et al.*, 2018)	Direct	(Duellman and Trueb, 1994)	Yes	(Lombard and Wake, 1986)
Eurycea bislineata	Semiaquatic	(Bonett and Blair, 2017; Fabre *et al.*, 2020)	Biphasic	(Ponssa *et al.*, 2022)	Yes	(Lombard and Wake, 1986)

Species	Microhabitat	Reference Microhabitat	Life cycle	Reference Life cycle	Ballistic tongue	Reference Ballistic tongue
Eurycea cirrigera	Aquatic	(Bonett and Blair, 2017; Fabre *et al.*, 2020)	Facultative paedomorphic	(Ponssa *et al.*, 2022)	Yes	(Lombard and Wake, 1986)
Eurycea lucifuga	Cave	(Baken and Adams, 2019)	Biphasic	(Ponssa *et al.*, 2022)	Yes	(Lombard and Wake, 1986)
Eurycea multiplicata	Semiaquatic	(Blankers *et al.*, 2012)	Facultative paedomorphic	(Powell *et al.*, 1998)	Yes	(Lombard and Wake, 1986)
Gyrinophilus porphyriticus	Semiaquatic	(Ponssa *et al.*, 2022)	Biphasic	(Ponssa *et al.*, 2022)	Yes	(Lombard and Wake, 1986)
Hydromantes genei	Cave	(Baken and Adams, 2019)	Direct	(Raffaëlli, 2007)	Yes	(Lombard and Wake, 1986)
Hydromantes platycephalus	Terrestrial	(Baken and Adams, 2019)	Direct	(Lannoo, 2005)	Yes	(Lombard and Wake, 1986)
Hynobius leechii	Semiaquatic	(Raffaëlli, 2007)	Biphasic	(Raffaëlli, 2007)	No	(Deban *et al.*, 2020)
Hynobius nebulosus	Terrestrial	(Raffaëlli, 2007)	Biphasic	(Raffaëlli, 2007)	No	(Deban *et al.*, 2020)
Hynobius sonani	Semiaquatic	(Raffaëlli, 2007)	Biphasic	(Raffaëlli, 2007)	No	(Deban *et al.*, 2020)
Hynobius tsuensis	Terrestrial	(Goris and Maeda, 2004)	Biphasic	(Goris and Maeda, 2004)	No	(Deban *et al.*, 2020)
Hynobius yiwuensis	Terrestrial	(Baken and Adams, 2019)	Biphasic	(Raffaëlli, 2007)	No	(Deban *et al.*, 2020)
Ichthyosaura alpestris	Semiaquatic	(Ćirović *et al.*, 2008)	Facultative paedomorphic	(Raffaëlli, 2007)	No	(Deban *et al.*, 2020)
Isthmura bellii	Terrestrial	(Hutchins *et al.*, 2003)	Direct	(Stuart, 2008)	Yes	(Lombard and Wake, 1986)
Lissotriton montandoni	Semiaquatic	(Kuzmin, 1999)	Complex	(Kuzmin, 1999)	No	(Deban *et al.*, 2020)
Lyciasalamandra luschani	Cave	(Baken and Adams, 2019)	Complex	(Sinsch *et al.*, 2017)	No	(Deban *et al.*, 2020)
Necturus maculosus	Aquatic	(Baken and Adams, 2019; Ponssa *et al.*, 2022)	Strict paedomorphic	(Ponssa *et al.*, 2022)	No	(Deban *et al.*, 2020)
Notophthalmus viridescens	Semiaquatic	(Ponssa *et al.*, 2022)	Facultative paedomorphic	(Ponssa *et al.*, 2022)	No	(Deban *et al.*, 2020)

Species	Microhabitat	Reference Microhabitat	Life cycle	Reference Life cycle	Ballistic tongue	Reference Ballistic tongue
Nototriton picadoi	Arboreal	(Baken and Adams, 2019)	Direct	(Rovito *et al.*, 2015)	Yes	(Lombard and Wake, 1986)
Oedipina complex	Terrestrial	(Blankers *et al.*, 2012)	Direct	(Rovito *et al.*, 2015)	Yes	(Lombard and Wake, 1986)
Oedipina cyclocauda	Terrestrial	(Blankers *et al.*, 2012)	Direct	(Rovito *et al.*, 2015)	Yes	(Lombard and Wake, 1986)
Onychodactylus japonicus	Terrestrial	(Ponssa *et al.*, 2022)	Biphasic	(Ponssa *et al.*, 2022)	No	(Deban *et al.*, 2020)
Pachytriton brevipes	Aquatic	(Baken and Adams, 2019; Ponssa *et al.*, 2022)	Biphasic	(Ponssa *et al.*, 2022)	No	(Deban *et al.*, 2020)
Plethodon dunni	Terrestrial	(Baken and Adams, 2019)	Direct	(Petranka, 1998)	No	(Deban *et al.*, 2020)
Plethodon elongatus	Terrestrial	(Baken and Adams, 2019)	Direct	(Petranka, 1998)	No	(Deban *et al.*, 2020)
Plethodon glutinosus	Terrestrial	(Ponssa *et al.*, 2022)	Direct	(Ponssa *et al.*, 2022)	No	(Deban *et al.*, 2020)
Plethodon hoffmani	Terrestrial	(Raffaëlli, 2007)	Direct	(Lannoo, 2005)	No	(Deban *et al.*, 2020)
Plethodon vandykei	Terrestrial	(Baken and Adams, 2019)	Direct	(Petranka, 1998)	No	(Deban *et al.*, 2020)
Plethodon vehiculum	Terrestrial	(Baken and Adams, 2019)	Direct	(Petranka, 1998)	No	(Deban *et al.*, 2020)
Pseudobranchus striatus	Aquatic	(Baken and Adams, 2019)	Strict paedomorphic	(Petranka, 1998)	No	(Deban *et al.*, 2020)
Pseudoeurycea leprosa	Terrestrial	(Ponssa *et al.*, 2022)	Direct	(Ponssa *et al.*, 2022)	Yes	(Lombard and Wake, 1986)
Pseudoeurycea rex	Terrestrial	(Elias, 1984)	Direct	(Rovito *et al.*, 2015)	Yes	(Lombard and Wake, 1986)
Pseudoeurycea saltator	Arboreal	(Baken and Adams, 2019)	Direct	(Rovito *et al.*, 2015)	Yes	(Lombard and Wake, 1986)
Rhyacotriton olympicus	Semiaquatic	(Ponssa *et al.*, 2022)	Biphasic	(Ponssa *et al.*, 2022)	No	(Deban *et al.*, 2020)
Salamandra salamandra	Terrestrial	(Baken and Adams, 2019)	Complex	(Buckley *et al.*, 2007)	No	(Deban *et al.*, 2020)
Salamandrella keyserlingii	Semiaquatic	(Vorobyeva and	Biphasic	(Vorobyeva and	No	(Deban *et al.*, 2020)

Species	Microhabitat	Reference Microhabitat	Life cycle	Reference Life cycle	Ballistic tongue	Reference Ballistic tongue
		Darevsky, 1994)		Darevsky, 1994)		
Siren intermedia	Aquatic	(Ponssa *et al.*, 2022)	Strict paedomorphic	(Ponssa *et al.*, 2022)	No	(Deban *et al.*, 2020)
Taricha granulosa	Terrestrial	(Stebbins, 2003)	Facultative paedomorphic	(Ponssa *et al.*, 2022)	No	(Deban *et al.*, 2020)
Thorius boreas	Terrestrial	(Baken and Adams, 2019)	Direct	(Rovito *et al.*, 2015)	Yes	(Lombard and Wake, 1986)
Thorius lunaris	Terrestrial	(Baken and Adams, 2019)	Direct	(Rovito *et al.*, 2015)	Yes	(Lombard and Wake, 1986)
Thorius macdougalli	Terrestrial	(Baken and Adams, 2019)	Direct	(Rovito *et al.*, 2015)	Yes	(Lombard and Wake, 1986)
Thorius pennatulus	Terrestrial	(Baken and Adams, 2019)	Direct	(Rovito *et al.*, 2015)	Yes	(Lombard and Wake, 1986)
Thorius spilogaster	Terrestrial	(Baken and Adams, 2019)	Direct	(Rovito *et al.*, 2015)	Yes	(Lombard and Wake, 1986)
Triturus cristatus	Semiaquatic	(Fabre *et al.*, 2020)	Biphasic	(Kuzmin, 1999)	No	(Deban *et al.*, 2020)
Triturus marmoratus	Terrestrial	(Baken and Adams, 2019)	Biphasic	(Gasc *et al.*, 2004)	No	(Deban *et al.*, 2020)
Tylototriton ziegleri	Terrestrial	(Nishikawa *et al.*, 2013)	Biphasic	(Hernandez, 2016)	No	(Deban *et al.*, 2020)

Table F2 PGLS results for each major brain region and their corresponding endocast area against life cycle categories. The centroid size (log transformation) was used as a covariate on all of these PGLS. Bold values represent significant results ($p < 0.05$). LC = Life cycle. CS = Centroid size. Df = total degree of freedom.

	Response	Predictor	Df	F	R^2	P-value
Brain	Olfactory bulb shape	Life cycle	3	1.312	0.050	0.206
		Interaction (LC:CS)	3	2.170	0.082	**0.021**
		Life cycle	3	5.638	0.072	**0.017**

	Telencephalon shape	Interaction (LC:CS)	3	0.994	0.038	0.366
	Hypothalamus shape	Life cycle	3	0.900	0.035	0.421
		Interaction (LC:CS)	3	0.750	0.030	0.533
	Thalamus shape	Life cycle	3	0.676	0.023	0.886
		Interaction (LC:CS)	3	1.318	0.045	0.167
	Mesencephalon shape	Life cycle	3	0.752	0.030	0.564
		Interaction (LC:CS)	3	0.916	0.037	0.308
	Rhombencephalon shape	Life cycle	3	0.901	0.035	0.393
		Interaction (LC:CS)	3	0.490	0.019	0.683
Endocast	Olfactory bulb shape	Life cycle	3	0.699	0.028	0.507
		Interaction (LC:CS)	3	0.304	0.012	0.813
	Telencephalon shape	Life cycle	3	0.741	0.030	0.507
		Interaction (LC:CS)	3	0.380	0.015	0.812
	Hypothalamus shape	Life cycle	3	0.910	0.034	0.524
		Interaction (LC:CS)	3	1.337	0.050	0.187
	Thalamus shape	Life cycle	3	0.832	0.035	0.646
		Interaction (LC:CS)	3	1.203	0.050	0.235
	Mesencephalon shape	Life cycle	3	1.039	0.040	0.287
		Interaction (LC:CS)	3	0.526	0.020	0.683
	Rhombencephalon shape	Life cycle	3	1.038	0.040	0.278
		Interaction (LC:CS)	3	0.660	0.025	0.536

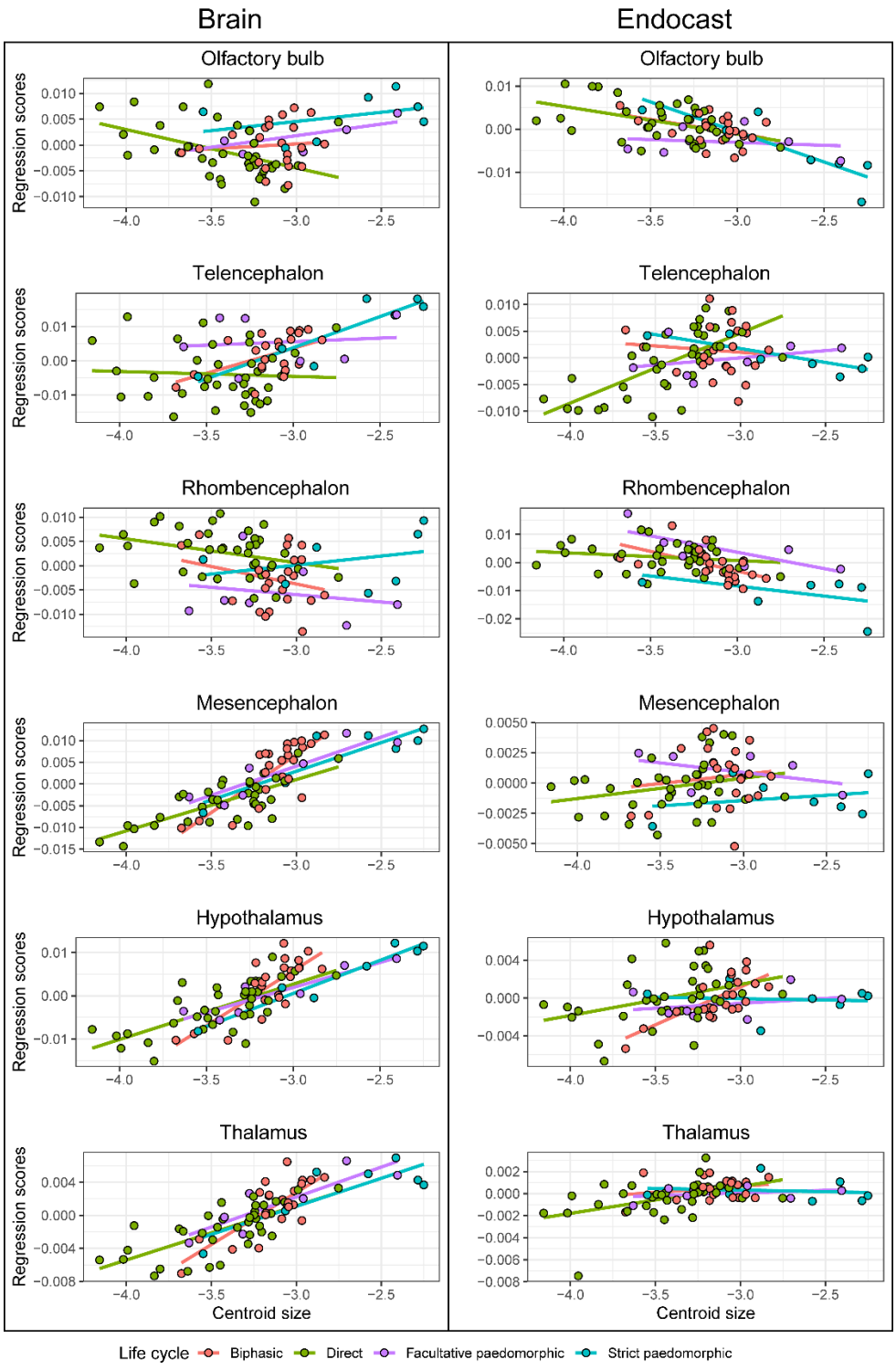

Figure F1 Shape regression scores of six major brain regions and corresponding areas of the endocast against the centroid size compared among species of different types of life cycle.

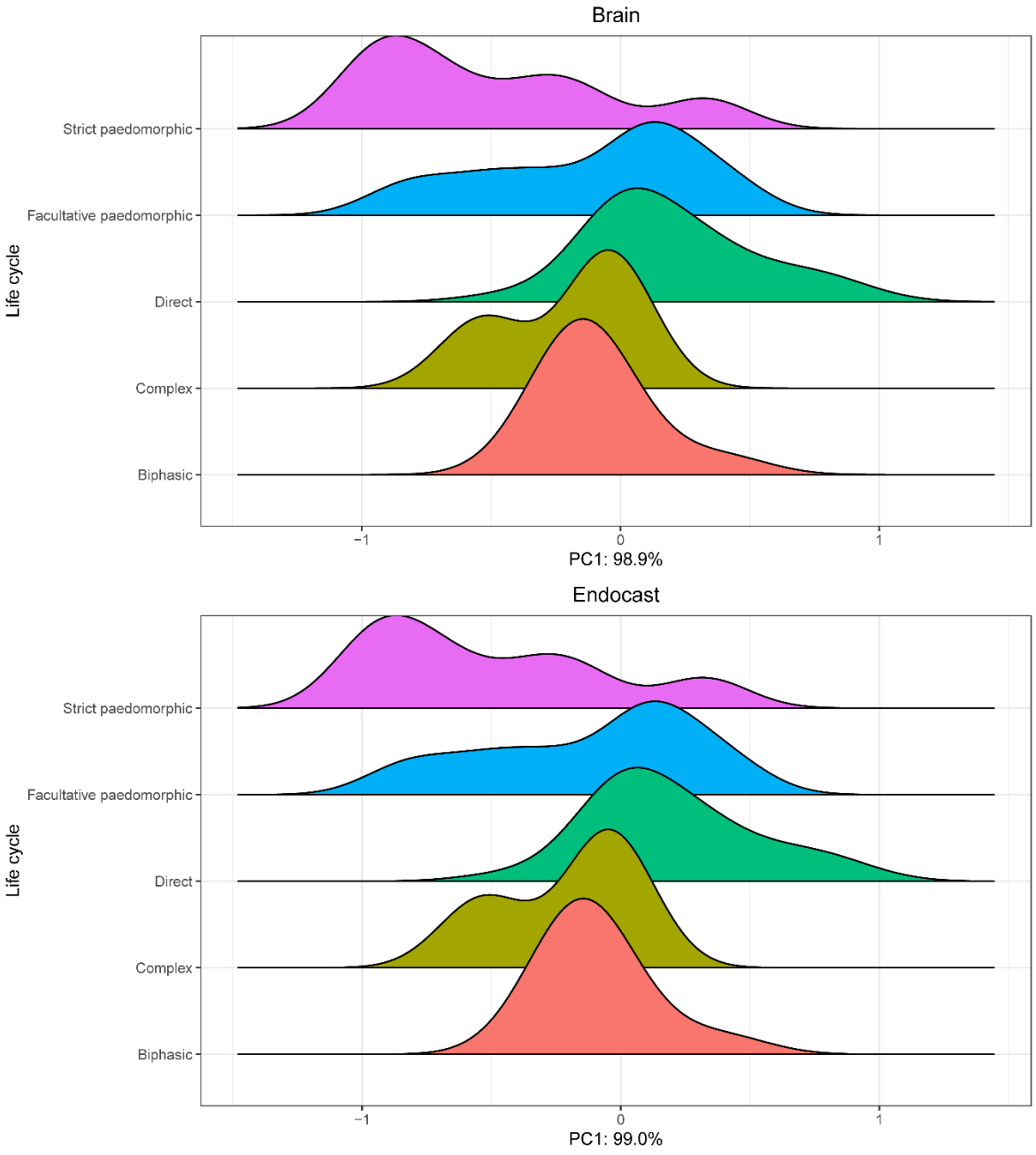

Figure F2 Density of PC1 values associated with different types of life cycle from size-shape principal component analyses of brain and endocast data.

Table F3 PGLS results for each major brain region and their corresponding endocast area against microhabitat categories. The centroid size (log transformation) was used as a covariate on all of these PGLS. Bold values represent significant results ($p < 0.05$). MH = Microhabitat. CS = Centroid size. Df = total degree of freedom.

	Response	Predictor	Df	F	R^2	P-value
Brain	Olfactory bulb shape	Microhabitat	3	2.520	0.092	**0.008**
		Interaction (MH:CS)	3	1.576	0.058	0.098
	Telencephalon shape	Microhabitat	3	1.067	0.042	0.279
		Interaction (MH:CS)	3	1.048	0.041	0.303
	Hypothalamus shape	Microhabitat	3	0.882	0.034	0.432
		Interaction (MH:CS)	3	1.063	0.041	0.289
	Thalamus shape	Microhabitat	3	0.968	0.034	0.487
		Interaction (MH:CS)	3	0.755	0.027	0.803
	Mesencephalon shape	Microhabitat	3	0.711	0.029	0.600
		Interaction (MH:CS)	3	1.004	0.040	0.308
	Rhombencephalon shape	Microhabitat	3	0.958	0.037	0.332
		Interaction (MH:CS)	3	0.795	0.031	0.457
Endocast	Olfactory bulb shape	Microhabitat	3	0.727	0.028	0.484
		Interaction (MH:CS)	3	0.722	0.028	0.484
	Telencephalon shape	Microhabitat	3	0.678	0.027	0.549
		Interaction (MH:CS)	3	0.886	0.035	0.397
	Hypothalamus shape	Microhabitat	3	1.204	0.044	0.237
		Interaction (MH:CS)	3	1.892	0.069	**0.028**
	Thalamus shape	Microhabitat	3	1.035	0.043	0.390
		Interaction (MH:CS)	3	0.879	0.037	0.559
	Mesencephalon shape	Microhabitat	3	0.899	0.034	0.376
		Interaction (MH:CS)	3	1.032	0.039	0.298
		Microhabitat	3	0.569	0.022	0.757

	Rhombencephalon shape	Interaction (MH:CS)	3	0.757	0.029	0.517

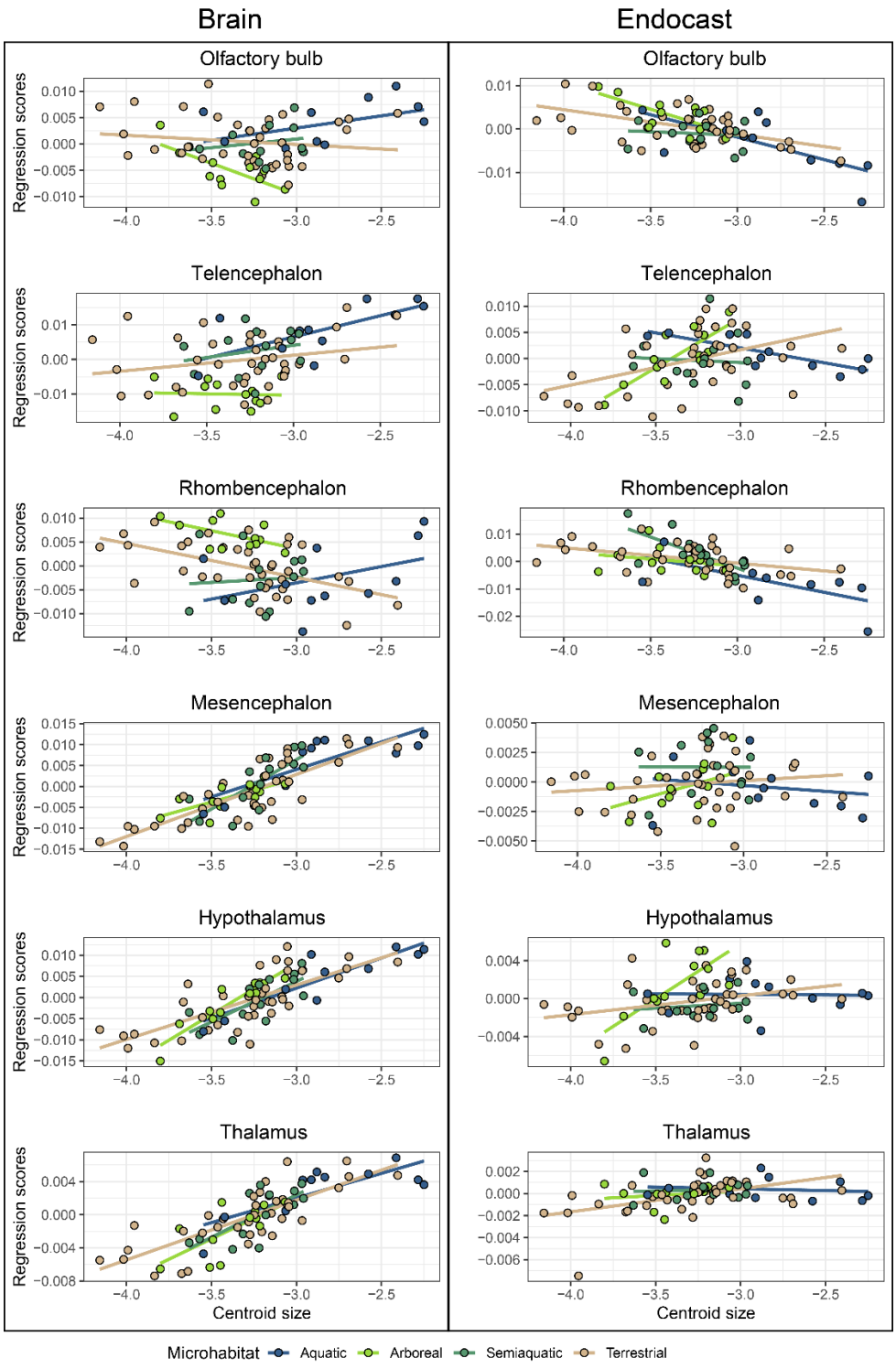

Figure F3 Shape regression scores of six major brain regions and corresponding areas of the endocast against the centroid size compared among species of different types of microhabitat.

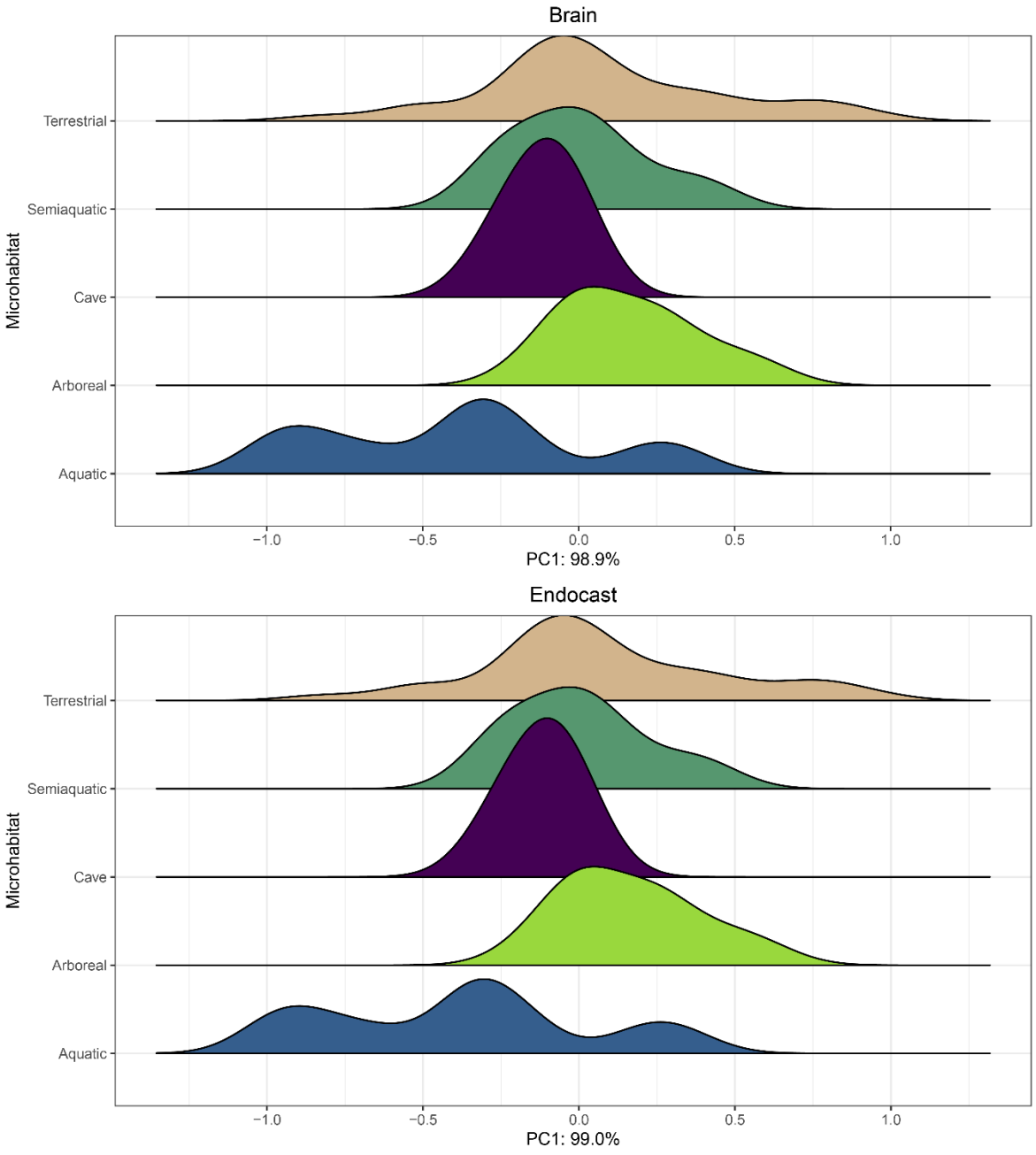

Figure F4 Density of PC1 values associated with different types of microhabitat from size-shape principal component analyses of brain and endocast data.

Table F4 PGLS results for each major brain region and their corresponding endocast area against the ballistic tongue factor. The centroid size (log transformation) was used as a covariate on all of these PGLS. BAL = Ballistic tongue. CS = Centroid size. Df = total degree of freedom.

	Response	Predictor	Df	F	R^2	P-value
Brain	Olfactory bulb shape	Ballistic tongue	1	1.273	0.016	0.252
		Interaction (BAL:CS)	1	2.087	0.026	0.085
	Telencephalon shape	Ballistic tongue	1	1.090	0.014	0.561
		Interaction (BAL:CS)	1	0.661	0.008	0.537
	Hypothalamus shape	Ballistic tongue	1	1.665	0.020	0.366
		Interaction (BAL:CS)	1	0.487	0.006	0.691
	Thalamus shape	Ballistic tongue	1	0.213	0.002	1.000
		Interaction (BAL:CS)	1	0.465	0.005	0.919
	Mesencephalon shape	Ballistic tongue	1	1.889	0.024	0.296
		Interaction (BAL:CS)	1	0.730	0.009	0.396
	Rhombencephalon shape	Ballistic tongue	1	3.036	0.037	0.158
		Interaction (BAL:CS)	1	0.324	0.004	0.743
Endocast	Olfactory bulb shape	Ballistic tongue	1	3.196	0.038	0.180
		Interaction (BAL:CS)	1	0.447	0.005	0.465
	Telencephalon shape	Ballistic tongue	1	2.583	0.032	0.241
		Interaction (BAL:CS)	1	0.686	0.009	0.371
	Hypothalamus shape	Ballistic tongue	1	0.641	0.008	0.686
		Interaction (BAL:CS)	1	1.325	0.016	0.212

Thalamus shape	Ballistic tongue	1	0.861	0.012	0.500
	Interaction (BAL:CS)	1	0.870	0.012	0.497
Mesencephalon shape	Ballistic tongue	1	1.899	0.023	0.366
	Interaction (BAL:CS)	1	0.402	0.005	0.668
Rhombencephalon shape	Ballistic tongue	1	2.640	0.032	0.192
	Interaction (BAL:CS)	1	0.374	0.005	0.762

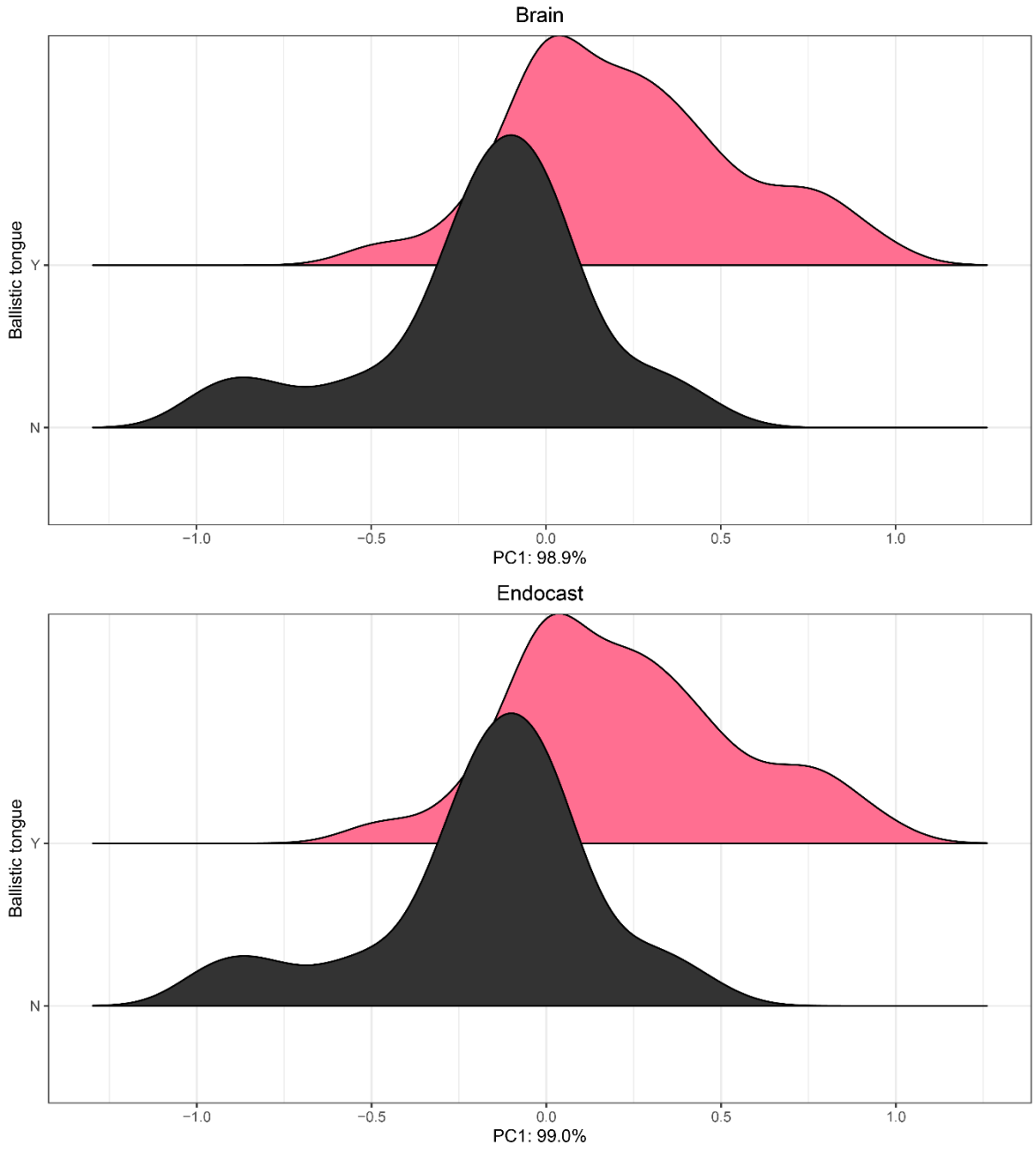

Figure F5 Density of PC1 values for species with or without a ballistic tongue from size-shape principal component analyses of brain and endocast data.

Table F5 Phylogenetic signal tests results for the brain and endocast shape for all species in the sample and among types of life cycle, microhabitat and between the presence or absence of a ballistic tongue. Bold values represent significant results ($p < 0.05$).

Shape dataset			K	Pagel's λ	Z	P-value
Brain	All species		0.996	0.100	11.338	**0.001**
	Life cycle	Strict paedomorphic	0.696	0.100	0.964	0.105
		Facultative paedomorphic	1.054	0.100	0.263	0.408
		Biphasic	0.815	0.441	7.193	**0.001**
		Direct	1.086	0.100	6.436	**0.001**
	Microhabitat	Aquatic	0.859	1.000	4.238	**0.001**
		Terrestrial	1.282	0.348	9.301	**0.001**
		Arboreal	0.901	0.100	0.345	0.289
		Semiaquatic	0.723	0.100	2.602	**0.004**
	Ballistic tongue	Absent	0.842	0.100	12.012	**0.001**
		Present	1.037	0.100	2.800	**0.001**
Endocast	All species		0.934	0.100	22.316	**0.001**
	Life cycle	Strict paedomorphic	0.923	0.100	1.200	0.118
		Facultative paedomorphic	0.834	0.100	1.022	0.135
		Biphasic	0.711	0.100	4.735	**0.001**
		Direct	1.309	0.100	4.070	**0.001**
	Microhabitat	Aquatic	0.900	0.100	2.239	**0.015**
		Terrestrial	1.224	0.100	6.720	**0.001**
		Arboreal	1.020	1.000	3.064	**0.001**
		Semiaquatic	0.772	0.100	2.353	**0.005**
	Ballistic tongue	Absent	0.874	0.100	8.402	**0.001**
		Present	1.353	0.100	2.823	**0.001**

Table F6 Comparison of the effect size of the phylogenetic signal among life cycle categories that exhibited a significant phylogenetic signal. The lower diagonal represents the P-value and the upper diagonal represents the effect size of the comparison. Bold values represent significant results ($p < 0.05$).

Shape dataset	Life cycle	Biphasic	Direct
Brain	Biphasic		6.819
	Direct	**0.000**	
	Life cycle	Biphasic	Direct
Endocast	Biphasic		4.610
	Direct	**0.000**	

Table F7 Pairwise comparison of the effect size of the phylogenetic signal among microhabitat categories that exhibited a significant phylogenetic signal. The lower diagonal represents the P-value and the upper diagonal represents the effect size of the comparison. Bold values represent significant results ($p < 0.05$).

Shape dataset	Microhabitat	Aquatic	Terrestrial	Semi-aquatic	
Brain	Aquatic		4.041	3.491	
	Terrestrial	**0.000**		2.547	
	Semi-aquatic	**0.000**	**0.011**		
	Microhabitat	Aquatic	Terrestrial	Arboreal	Semi-aquatic
Endocast	Aquatic		2.218	3.064	2.339
	Terrestrial	**0.027**		3.064	2.353
	Arboreal	**0.002**	**0.002**		3.064

	Semi-aquatic	**0.019**	**0.019**	**0.002**	

Table F8 Comparison of the effect size of the phylogenetic signal for the ballistic tongue factor. The lower diagonal represents the P-value and the upper diagonal represents the effect size of the comparison. Bold values represent significant results ($p < 0.05$).

Shape dataset	Ballistic tongue	Absent	Present
Brain	Absent		2.800
	Present	**0.005**	
	Ballistic tongue	Absent	Present
Endocast	Absent		2.195
	Present	**0.028**	

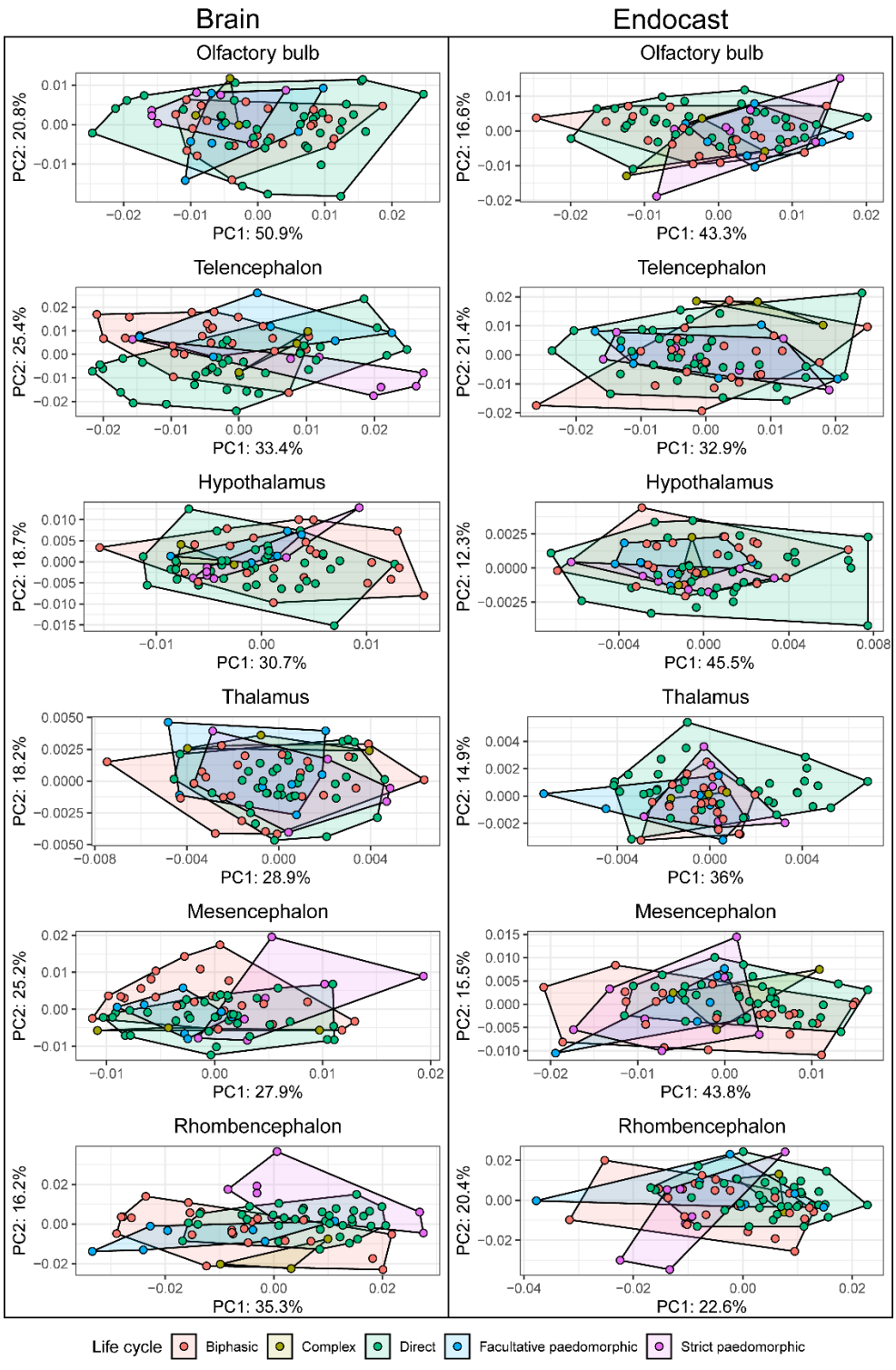

Figure F6 PCA plots for six major brain regions and their corresponding areas of the endocast with a comparison of different types of life cycle (polygons).

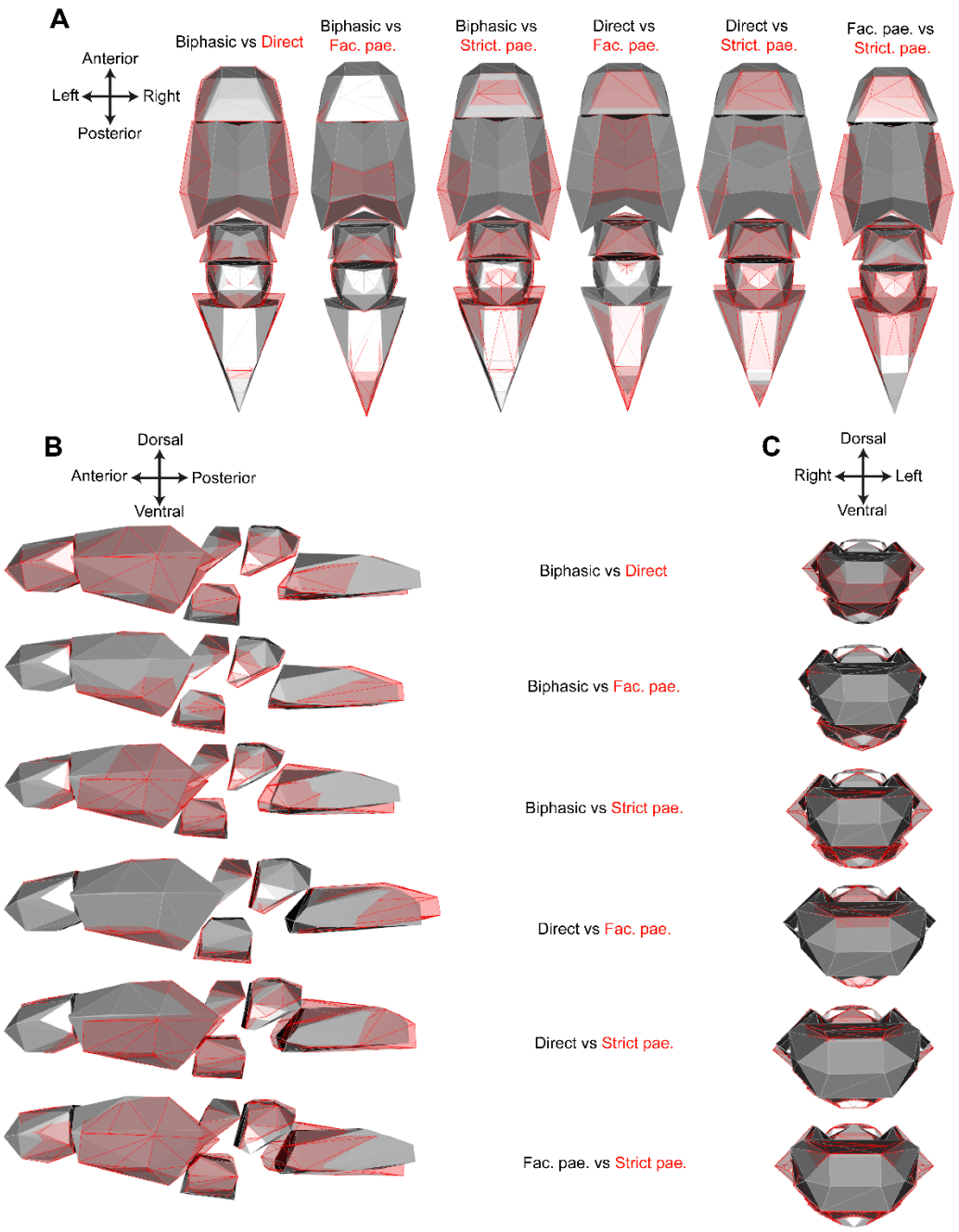

Figure F7 Mean brain shape differences among types of life cycle. The grey polygons represent the mean shape of a type of life cycles and the red semitransparent shapes represent the shape of another group. Shape differences are represented from three views, (A) dorsal, (B) lateral and (C) frontal. Fac. pae. = Facultative paedomorphic. Strict pae. = Strict paedomorphic.

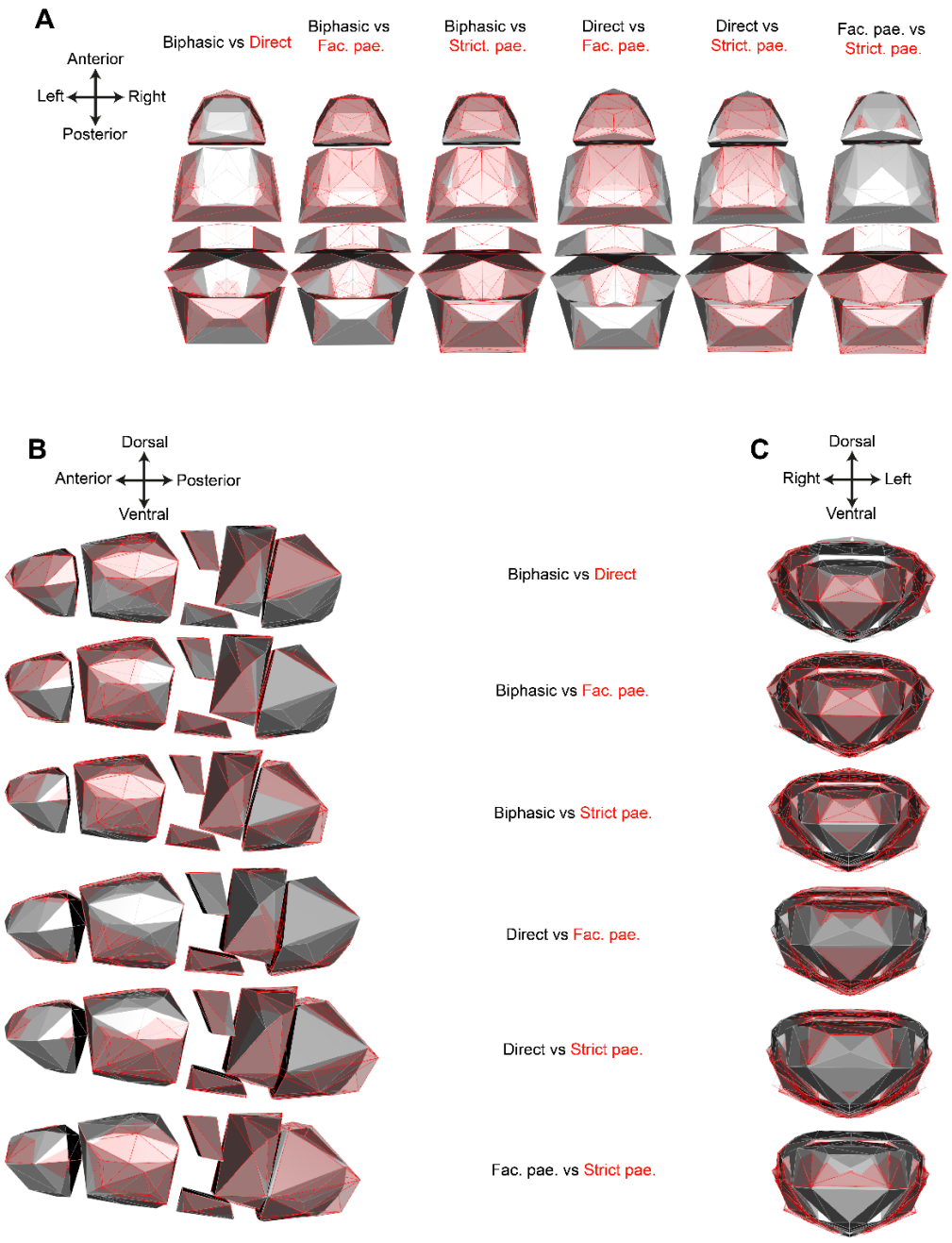

Figure F8 Mean endocast shape differences among types of life cycle. The grey polygons represent the mean shape of a type of life cycles and the red semitransparent shapes represent the shape of another group. Shape differences are represented from three views, (A) dorsal, (B) lateral and (C) frontal. Fac. pae. = Facultative paedomorphic. Strict pae. = Strict paedomorphic.

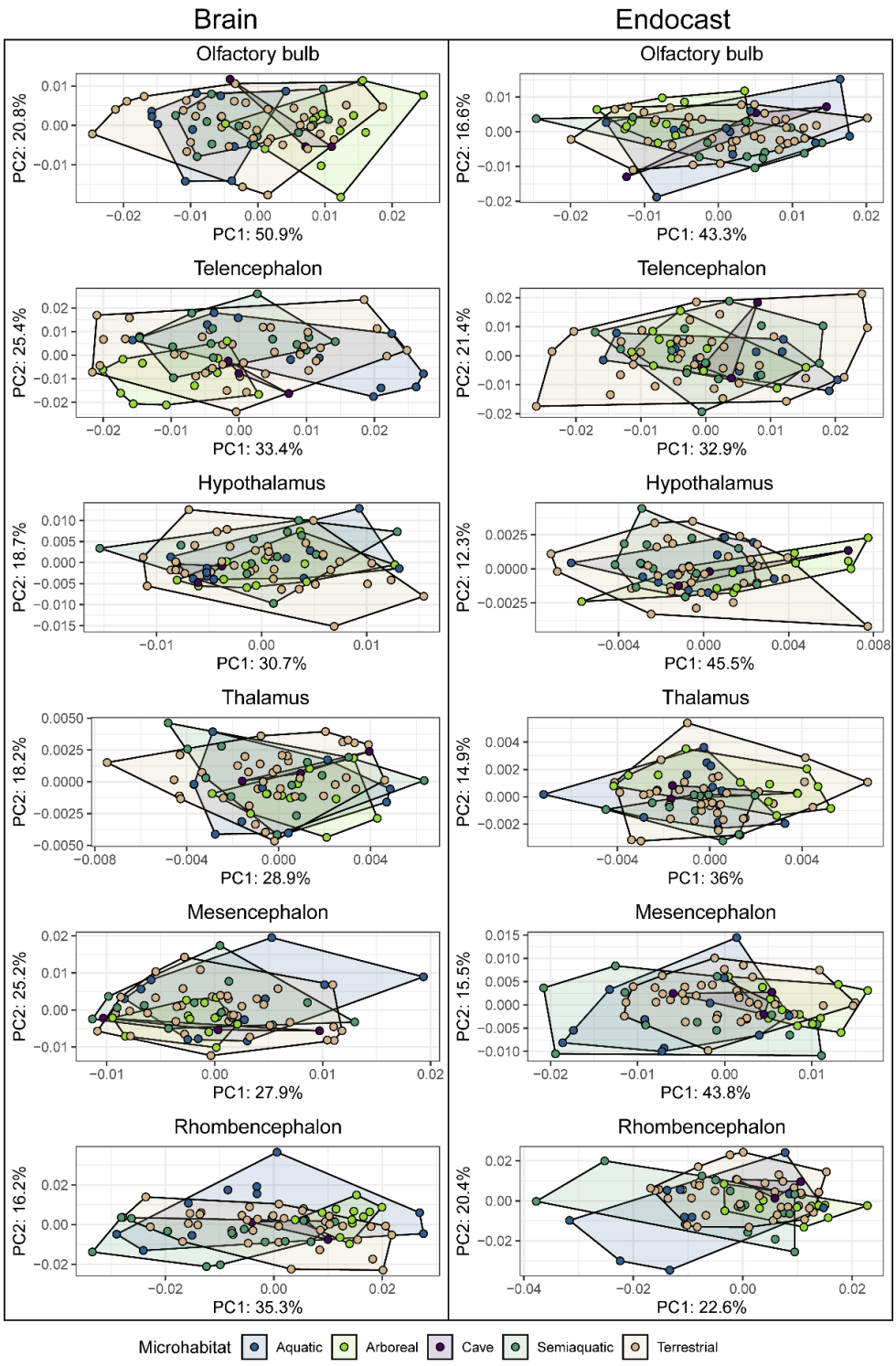

Figure F9 PCA plots for six major brain regions and their corresponding areas of the endocast with a comparison of different types of microhabitat (polygons).

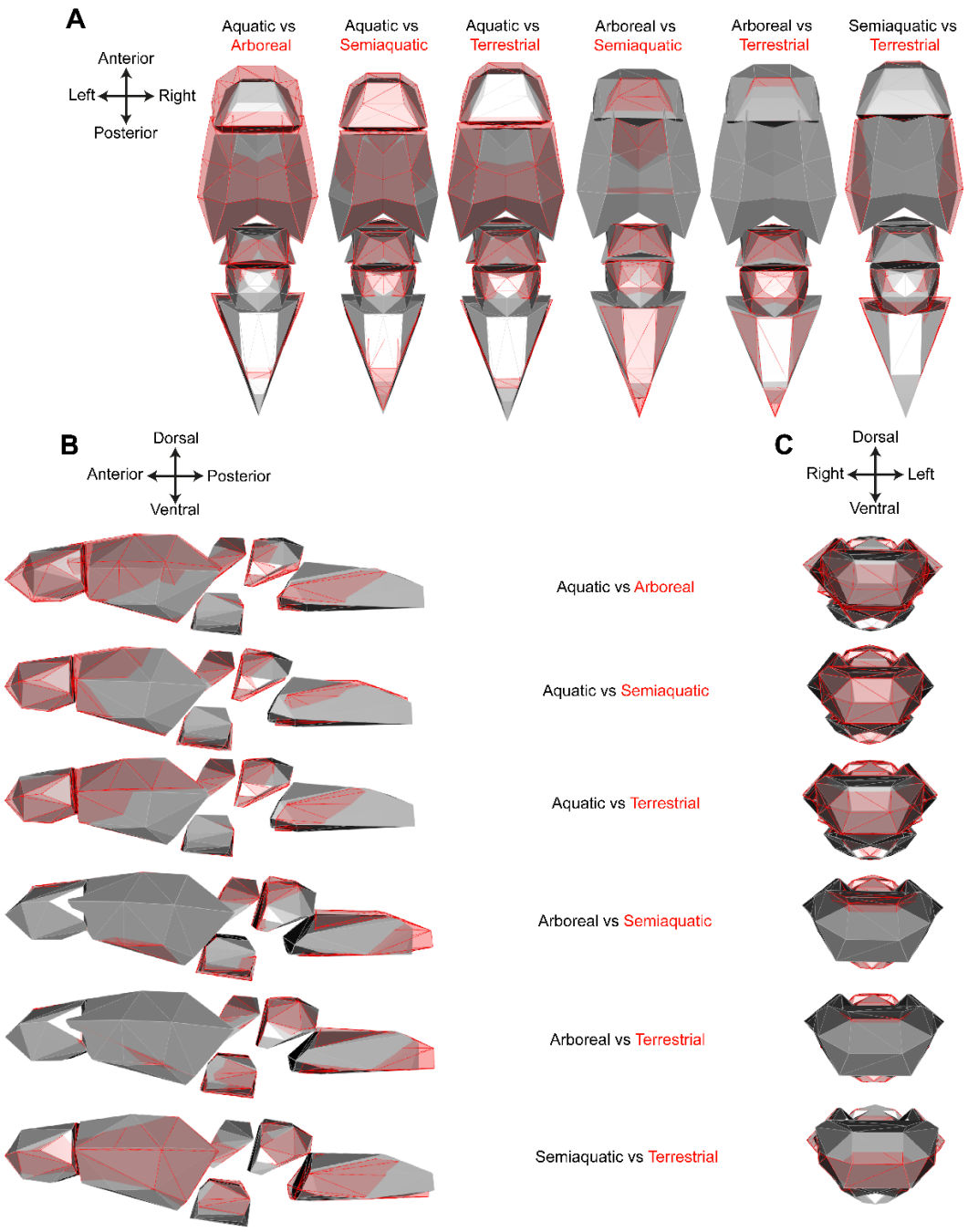

Figure F10 Mean brain shape differences among types of microhabitat. The grey polygons represent the mean shape of a type of microhabitats and the red semitransparent shapes represent the shape of another group. Shape differences are represented from three views, (A) dorsal, (B) lateral and (C) frontal.

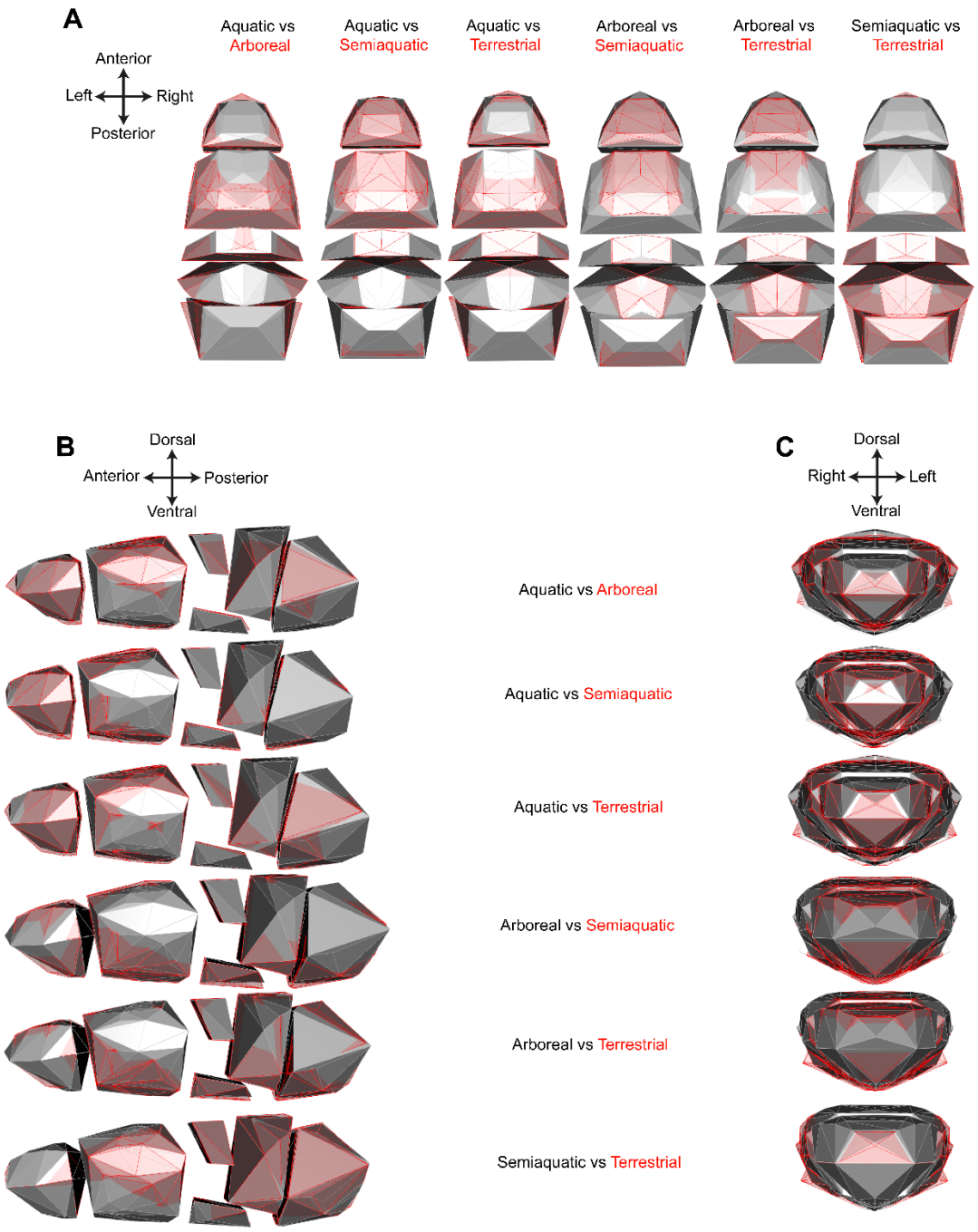

Figure F11 Mean endocast shape differences among types of microhabitat. The grey polygons represent the mean shape of a type of microhabitats and the red semitransparent shapes represent the shape of another group. Shape differences are represented from three views, (A) dorsal, (B) lateral and (C) frontal.

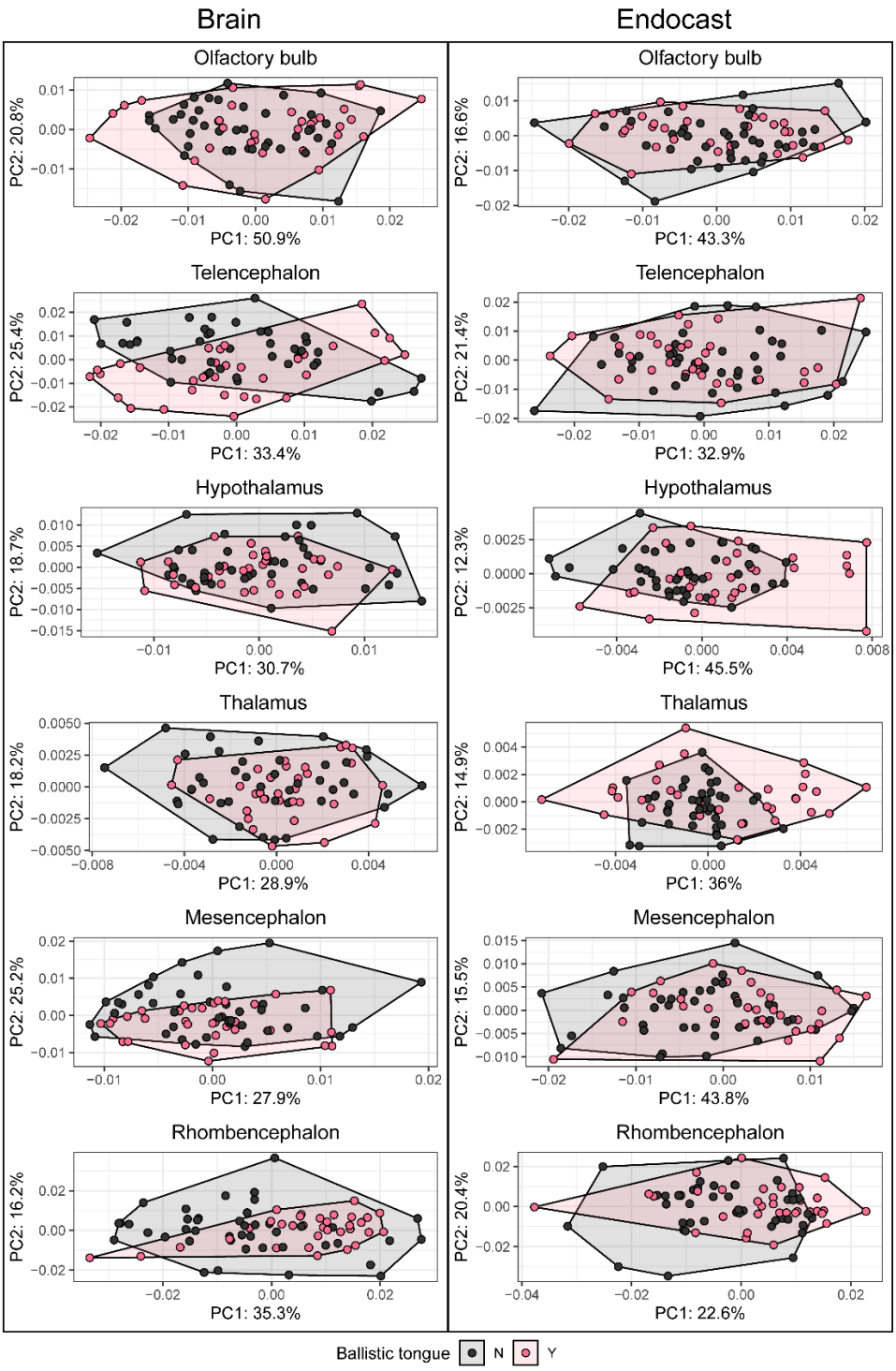

Figure F12 PCA plots for six major brain regions and their corresponding areas of the endocast with a comparison of species that possess a ballistic tongue (Y) and species that do not (N).

Table F9 Evaluation of evolutionary rate differences of centroid size, brain shape and endocast shape among life cycle, microhabitat and tongue-type categories.

	Centroid size		
	Observed rate ratio	Effect size	P-value
Life cycle	10.116	1.703	**0.044**
Microhabitat	11.590	2.603	**0.007**
Ballistic tongue	9.520	1.236	0.085
	Brain shape		
Life cycle	1.307	0.341	0.381
Microhabitat	1.225	-0.091	0.528
Ballistic tongue	1.760	0.136	0.494
	Endocast shape		
Life cycle	1.421	0.642	0.289
Microhabitat	1.405	0.881	0.191
Ballistic tongue	1.009	-1.324	0.920
	Major brain regions		
	13.519	4.901	0.001

Table F10 Centroid size evolutionary rate among types of life cycle. Bold values represent a significant result ($p < 0.05$).

Life cycle	Biphasic	Direct	Facultative paedomorphic	Strict paedomorphic
Rate	24.813	19.987	73.450	202.190

Life cycle	Direct	Facultative paedomorphic	Strict paedomorphic
Biphasic	0.732	0.261	**0.016**

Direct	-	0.162	**0.008**
Facultative paedomorphic		-	0.403

Table F11 Centroid size evolutionary rate among types of microhabitat. Bold values represent a significant result ($p < 0.05$).

Microhabitat	Aquatic	Arboreal	Semiaquatic	Terrestrial
Rate	130.164	11.230	31.669	34.345

Microhabitat	Arboreal	Semiaquatic	Terrestrial
Aquatic	**0.005**	0.112	0.066
Arboreal	-	0.222	0.120
Semiaquatic		-	0.916

Table F12 Disparity results among types of life cycle for the brain shape. The first two lines represent the Procrustes variance values for each type of life cycle. The four subsequent lines represent the P-value of pairwise comparison of the Procrustes variance. Bold values represent a significant result ($p < 0.05$).

Life cycle	Biphasic	Direct	Facultative paedomorphic	Strict paedomorphic
Procrustes variance	0.00159	0.00171	0.00125	0.00273

Life cycle	Direct	Facultative paedomorphic	Strict paedomorphic
Biphasic	0.649	0.384	**0.010**

Direct	-	0.237	**0.015**
Facultative paedomorphic		-	**0.004**

Table F13 Disparity results among types of life cycle for the endocast shape. The first two lines represent the Procrustes variance values for each type of life cycle. The four subsequent lines represent the P-value of pairwise comparison of the Procrustes variance. Bold values represent a significant result ($p < 0.05$).

Life cycle	Biphasic	Direct	Facultative paedomorphic	Strict paedomorphic
Procrustes variance	0.00144	0.00175	0.00161	0.00310

Life cycle	Direct	Facultative paedomorphic	Strict paedomorphic
Biphasic	0.235	0.645	**0.002**
Direct	-	0.743	**0.004**
Facultative paedomorphic		-	**0.007**

Table F14 Disparity results among types of microhabitat for the brain shape. The first two lines present the Procrustes variance values for each type of microhabitat and the subsequent four lines present P-values from pairwise comparisons of the Procrustes variance. Bold values represent a significant result ($p < 0.05$).

Microhabitat	Aquatic	Arboreal	Semiaquatic	Terrestrial
Procrustes variance	0.00292	0.00148	0.00240	0.00196

Microhabitat	Arboreal	Semiaquatic	Terrestrial
Aquatic	**0.003**	0.272	**0.019**
Arboreal	-	**0.035**	0.195
Semiaquatic		-	0.245

Table F15 Disparity results among types of microhabitat for the endocast shape. The first two lines present the Procrustes variance values for each type of microhabitat and the four subsequent lines present P-values from pairwise comparisons of the Procrustes variance. Bold values represent a significant result ($p < 0.05$).

Microhabitat	Aquatic	Arboreal	Semiaquatic	Terrestrial
Procrustes variance	0.00291	0.00206	0.00231	0.00213

Microhabitat	Arboreal	Semiaquatic	Terrestrial
Aquatic	0.113	0.255	0.082
Arboreal	-	0.575	0.842
Semiaquatic		-	0.673

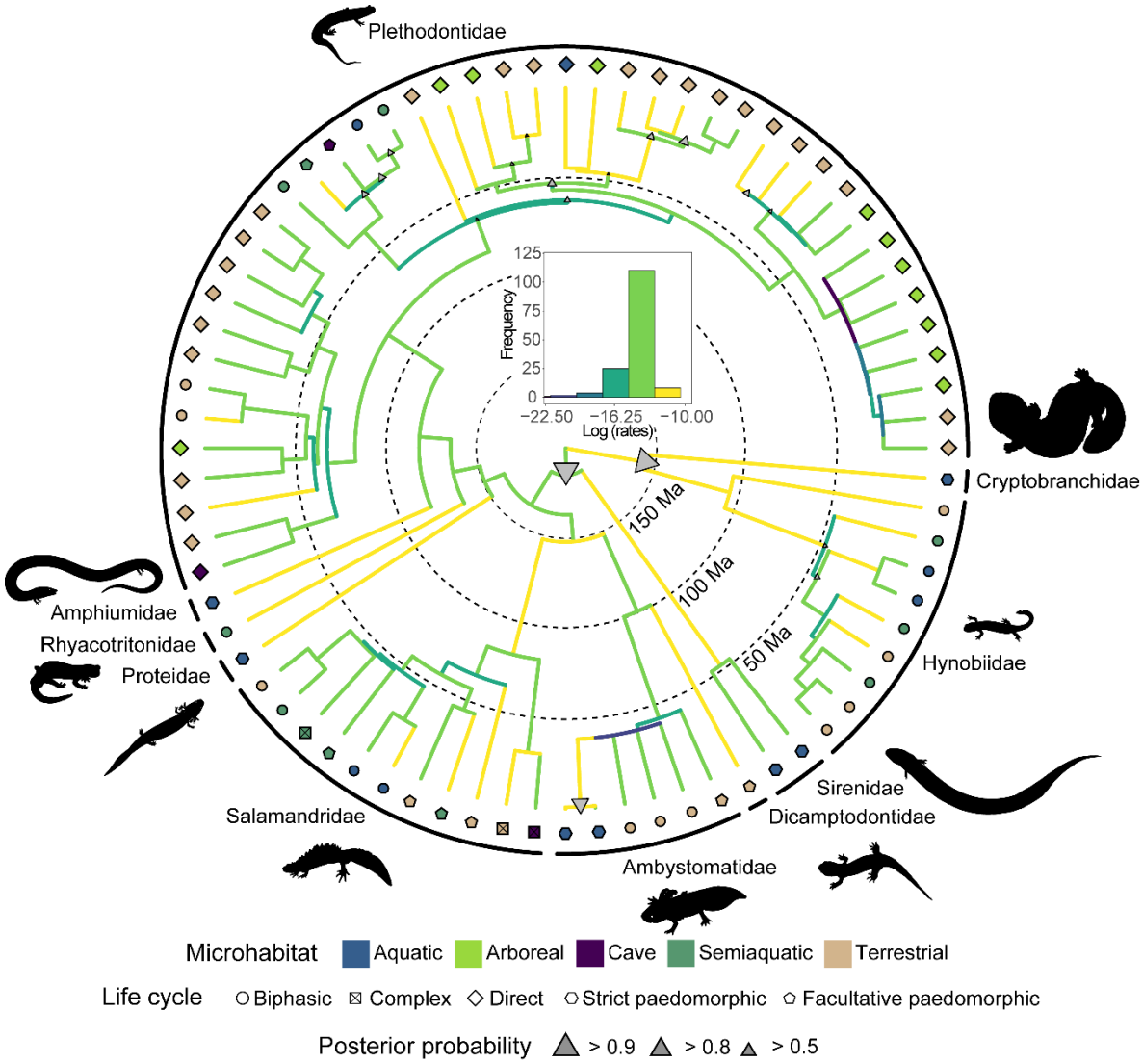

Figure F13 Evolutionary rates and rate shifts of the endocast shape of salamanders (PhyloPic silhouettes were used except for Proteidae, which was made by the first author). Branch colour gradients represent rates of endocast shape evolution, with yellow colours indicating higher rates and purple colours indicating lower ones. The distribution plot shows the frequencies of log-transformed evolutionary rates. Grey triangles mark the stem branches of clades for which whole-clade rate shifts are supported, with the size of each triangle reflecting the posterior probability of the shift. Time is expressed in millions of years (MA). PhyloPic credit: T. Michael Keesey (https://creativecommons.org/licenses/by/4.0/).

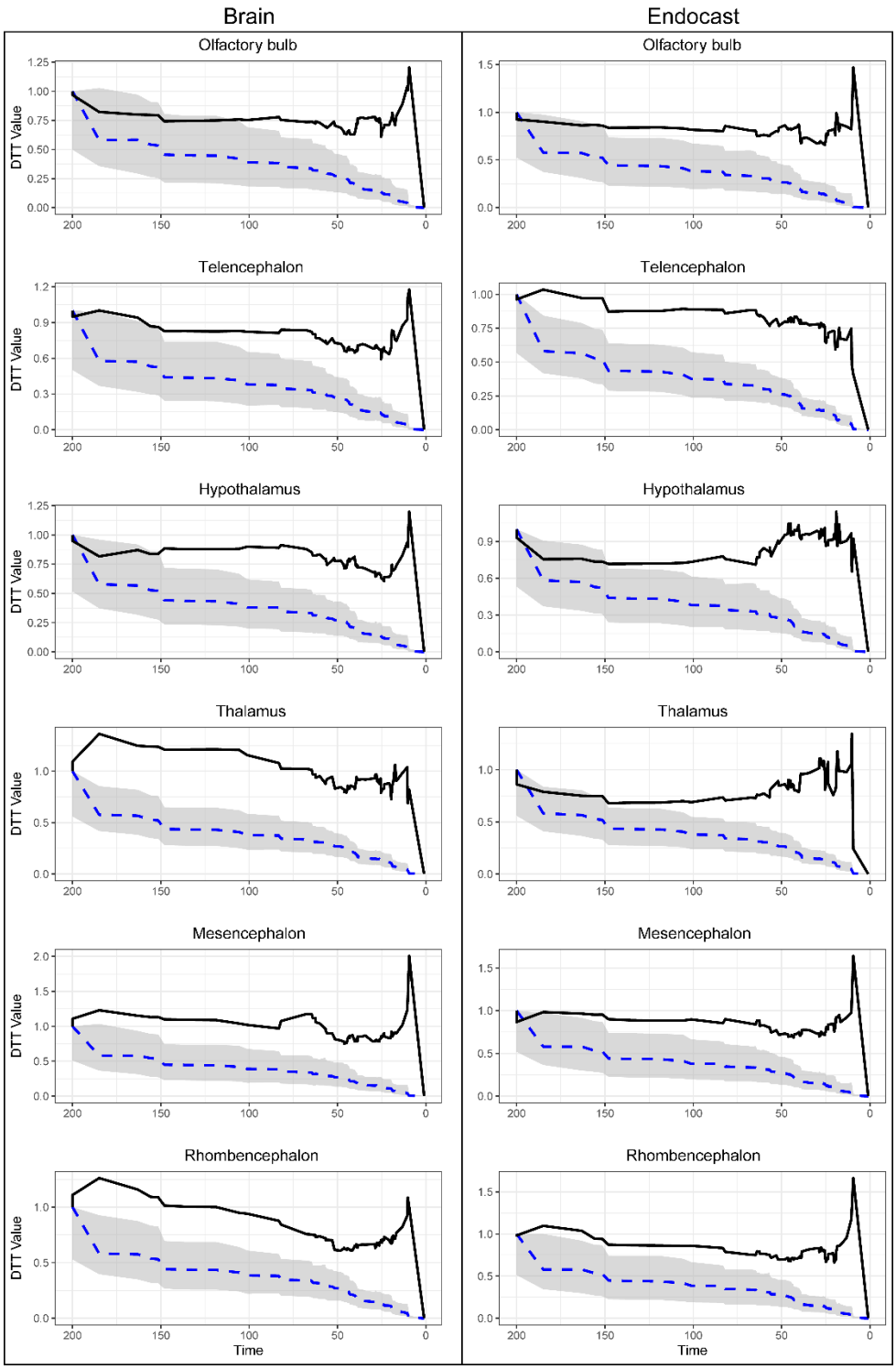

Figure F14 Disparity through time for each major brain regions and corresponding areas of the endocast. Time is expressed in millions of years (Ma).

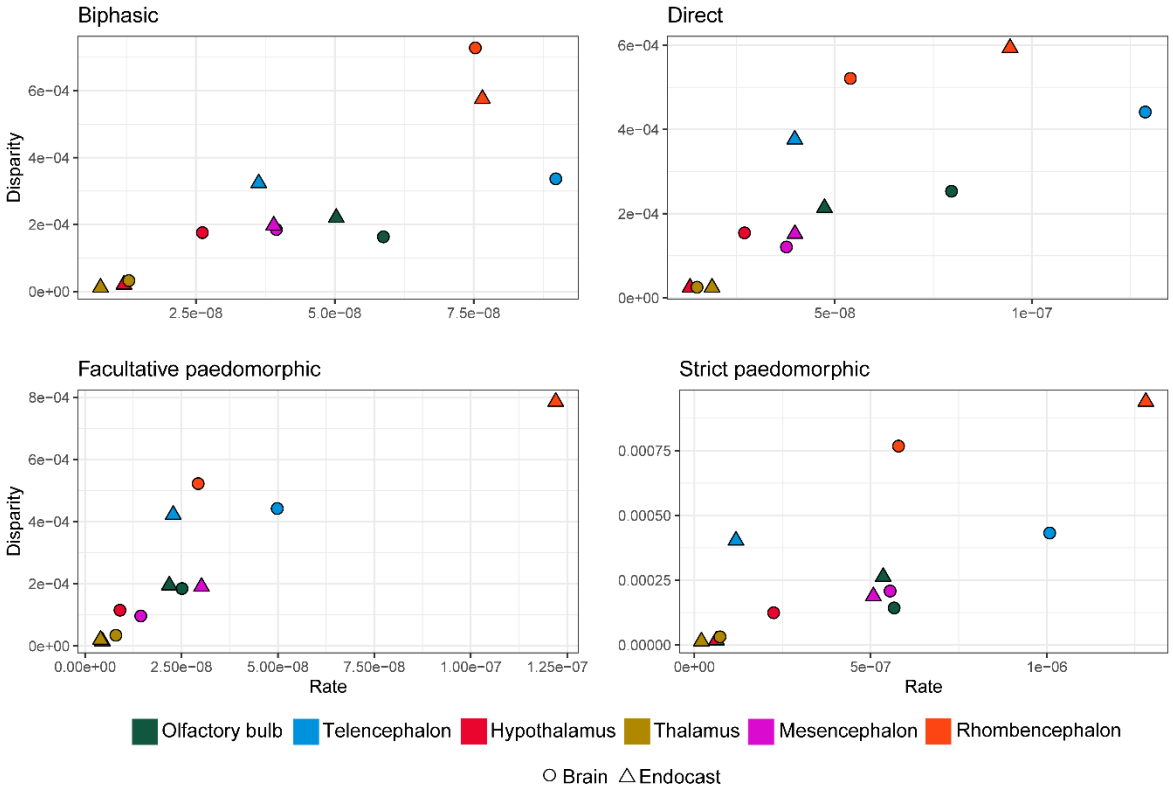

Figure F15 Relationship between disparity and evolutionary rate of major brain regions and corresponding areas of the endocast for four types of life cycle.

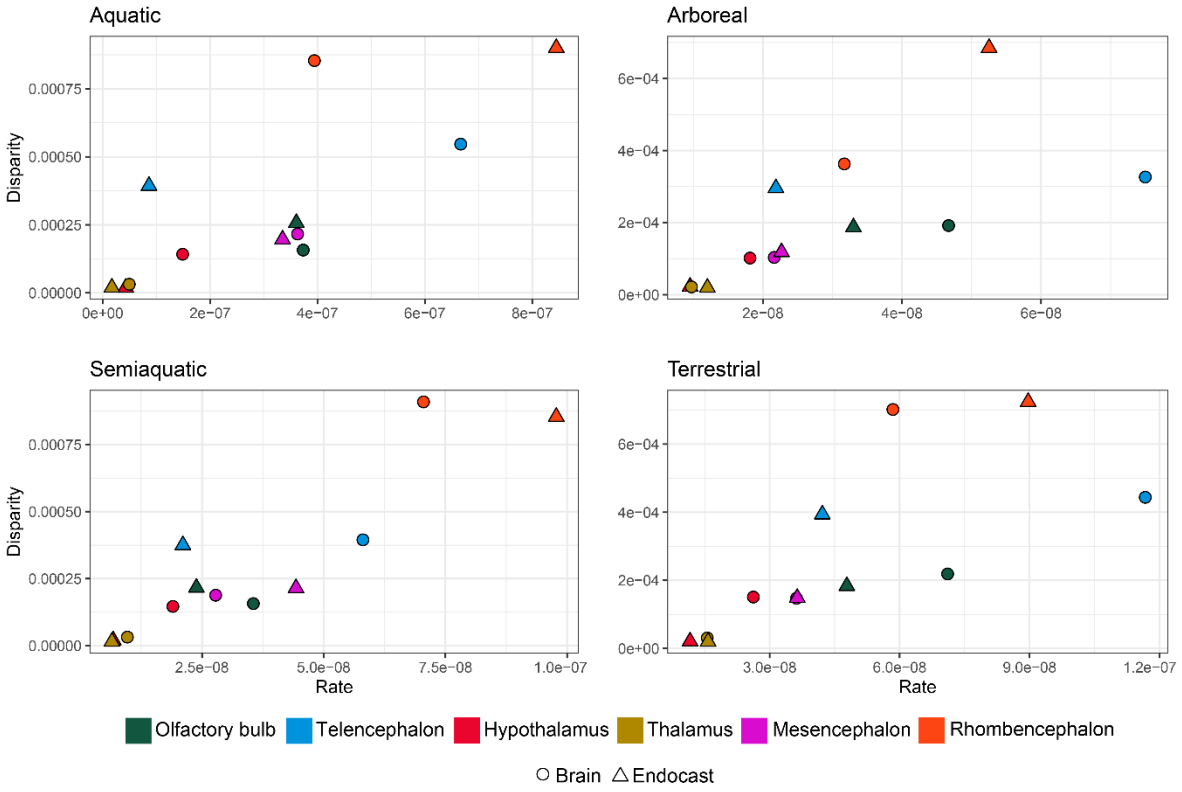

Figure F16 Relationship between disparity and evolutionary rate of major brain regions and corresponding areas of the endocast for four types of microhabitat.

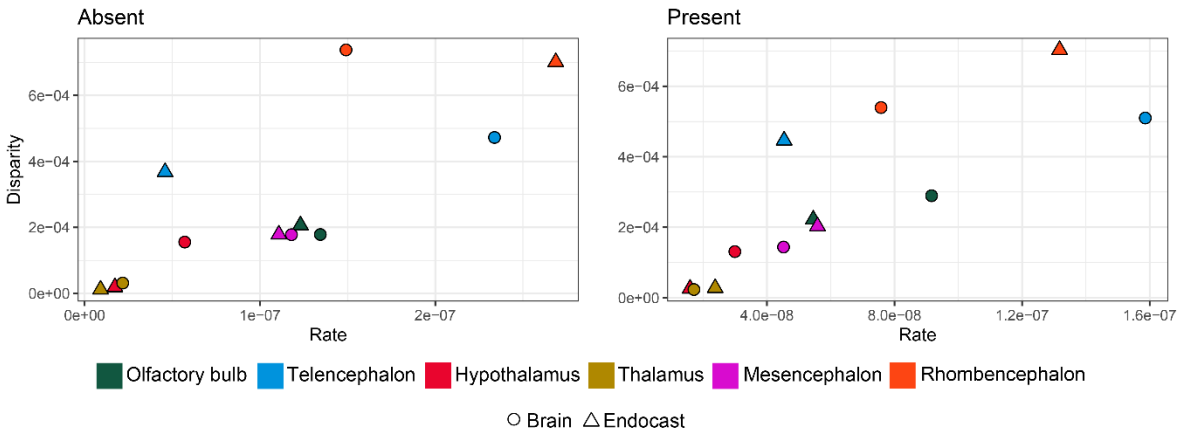

Figure F17 Relationship between disparity and evolutionary rate of major brain regions and corresponding areas of the endocast for species with (Present) or without (Absent) a ballistic tongue.

Table F16 Spearman correlation tests results between disparity levels and evolutionary rates of each major brain regions associated with each life cycle, microhabitat and ballistic tongue category. Bold values represent a significant result ($p < 0.05$).

	Life cycle			Microhabitat			Ballistic tongue		
		r	P-value		r	P-value		r	P-value
Brain	Biphasic	0.771	0.103	Aquatic	0.771	0.106	Present	0.829	0.057
	Direct	0.771	0.104	Arboreal	0.829	0.061			
	Facultative paedomorphic	0.886	**0.033**	Semiaquatic	0.943	**0.018**	Absent	0.943	**0.016**
	Strict paedomorphic	0.886	**0.035**	Terrestrial	0.771	0.102			
Endocast	Biphasic	0.829	0.059	Aquatic	0.829	0.060	Present	0.771	0.104
	Direct	0.829	0.058	Arboreal	0.771	0.105			
	Facultative paedomorphic	0.771	0.101	Semiaquatic	0.714	0.136	Absent	0.829	0.058
	Strict paedomorphic	0.829	0.061	Terrestrial	0.886	**0.034**			

RÉFÉRENCES

Adams, D., Collyer, M., Otarola-Castillo, E., et Sherratt, E. (2014). geomorph: Software for geometric morphometric analyses. *R package version 2.1.* Available at *http://cran.r-project.org/web/packages/geomorph/index.html*.

Adams, D., Rohlf, F. J., et Slice, D. (2013). A field comes of age: geometric morphometrics in the 21st century. *Hystrix, the Italian Journal of Mammalogy*, *24*(1), 7-14.

Adams, D. C. (2014a). A generalized K statistic for estimating phylogenetic signal from shape and other high-dimensional multivariate data. *Systematic Biology*, *63*(5), 685-697.

Adams, D. C. (2014b). A method for assessing phylogenetic least squares models for shape and other high-dimensional multivariate data. *Evolution*, *68*(9), 2675-2688.

Adams, D. C. (2014c). Quantifying and comparing phylogenetic evolutionary rates for shape and other high-dimensional phenotypic data. *Systematic Biology*, *63*(2), 166-177.

Adams, D. C. (2016). Evaluating modularity in morphometric data: challenges with the RV coefficient and a new test measure. *Methods in Ecology and Evolution*, *7*(5), 565-572. https://doi.org/https://doi.org/10.1111/2041-210X.12511

Adams, D. C., et Collyer, M. L. (2019). Comparing the strength of modular signal, and evaluating alternative modular hypotheses, using covariance ratio effect sizes with morphometric data. *Evolution*, *73*(12), 2352-2367. https://doi.org/https://doi.org/10.1111/evo.13867

Adams, D. C., et Felice, R. N. (2014). Assessing trait covariation and morphological integration on phylogenies using evolutionary covariance matrices. *PLoS One*, *9*(4), e94335.

Adams, D. C., et Nistri, A. (2010). Ontogenetic convergence and evolution of foot morphology in European cave salamanders (Family: Plethodontidae). *BMC Evolutionary Biology*, *10*(1), e216.

Adams, D. C., Rohlf, F. J., et Slice, D. E. (2004). Geometric morphometrics: ten years of progress following the 'revolution'. *Italian Journal of Zoology*, *71*(1), 5-16.

Allemand, R., Abdul-Sater, J., Macrì, S., Di-Poï, N., Daghfous, G., et Silcox, M. T. (2023). Endocast, brain, and bones: Correspondences and spatial relationships in squamates. *The Anatomical Record*, *306*(10), 2443-2465.

Amamoto, R., Huerta, V. G. L., Takahashi, E., Dai, G., Grant, A. K., Fu, Z., et Arlotta, P. (2016). Adult axolotls can regenerate original neuronal diversity in response to brain injury. *eLife*, *5*, e13998. https://doi.org/https://doi.org/10.7554/eLife.13998

AmphibiaWeb. (2025). *Information on amphibian biology and conservation*. University of California, [En ligne], Consulté le 15 décembre 2025.

Anelli, V., Bars-Closel, M., Herrel, A., et Kohlsdorf, T. (2024). Different selection regimes explain morphological evolution in fossorial lizards. *Functional Ecology*, *38*(5), 1250-1264.

Ashley-Ross, M. A. (1994). Hindlimb kinematics during terrestrial locomotion in a salamander (*Dicamptodon tenebrosus*). *Journal of Experimental Biology*, *193*(1), 255-283.

Atkins, J. B., Houle, L., Cantelon, A. S., et Maddin, H. C. (2020). Normal development in *Ambystoma mexicanum*: a complementary staging table for the skull based on Alizarin red S staining. *Developmental Dynamics*, *249*(5), 656-665. https://doi.org/https://doi.org/10.1002/dvdy.152

Avilés, J. M., et Amo, L. (2018). The evolution of olfactory capabilities in wild birds: a comparative study. *Evolutionary Biology*, *45*(1), 27-36.

Baken, E. K., et Adams, D. C. (2019). Macroevolution of arboreality in salamanders. *Ecology and Evolution*, *9*(12), 7005-7016.

Baken, E. K., Collyer, M. L., Kaliontzopoulou, A., et Adams, D. C. (2021). geomorph v4. 0 and gmShiny: Enhanced analytics and a new graphical interface for a comprehensive morphometric experience. *Methods in Ecology and Evolution*, *12*(12), 2355-2363. https://doi.org/https://doi.org/10.1111/2041-210X.13723

Baker, J., Barton, R. A., et Venditti, C. (2025). Macroevolutionary brain scaling is a microevolutionary metaphenomenon. *Nature Communications*, *17*, e136

Baker, J., Meade, A., Pagel, M., et Venditti, C. (2015). Adaptive evolution toward larger size in mammals. *Proceedings of the National Academy of Sciences*, *112*(16), 5093-5098.

Balanoff, A. M., Smaers, J. B., et Turner, A. H. (2016). Brain modularity across the theropod–bird transition: testing the influence of flight on neuroanatomical variation. *Journal of Anatomy*, *229*(2), 204-214. https://doi.org/https://doi.org/10.1111/joa.12403

Barclay, O. R. (1946). The mechanics of amphibian locomotion. *Journal of Experimental Biology*, *23*(2), 177-203.

Bardua, C., Fabre, A.-C., Bon, M., Das, K., Stanley, E. L., Blackburn, D. C., et Goswami, A. (2020). Evolutionary integration of the frog cranium. *Evolution*, *74*(6), 1200-1215.

Bardua, C., Fabre, A.-C., Clavel, J., Bon, M., Das, K., Stanley, E. L., Blackburn, D. C., et Goswami, A. (2021). Size, microhabitat, and loss of larval feeding drive cranial diversification in frogs. *Nature Communications*, *12*(1), e2503.

Bardua, C., Wilkinson, M., Gower, D. J., Sherratt, E., et Goswami, A. (2019). Morphological evolution and modularity of the caecilian skull. *BMC Evolutionary Biology*, *19*, 1-23.

Baron, G., et P. Jolicoeur (1980). Brain structure in Chiroptera: Some multivariate trends. *Evolution*, *34*, 386–393.

Barton, R., Purvis, A., et Harvey, P. (1995). Evolutionary radiation of visual and olfactory brain systems in primates, bats and insectivores. *Philosophical Transactions of the Royal Society of London. Series B: Biological Sciences*, *348*(1326), 381-392. https://doi.org/https://doi.org/10.1098/rstb.1995.0076

Barton, R. A., et Harvey, P. H. (2000). Mosaic evolution of brain structure in mammals. *Nature*, *405*(6790), 1055-1058. https://doi.org/https://doi.org/10.1038/35016580

Bertrand, O., San Martin-Flores, G., et Silcox, M. (2019). Endocranial shape variation in the squirrel-related clade and their fossil relatives using 3D geometric morphometrics: contributions of locomotion and phylogeny to brain shape. *Journal of Zoology*, *308*(3), 197-211.

Bird, A. K., Prado-Irwin, S. R., Vredenburg, V. T., et Zink, A. G. (2018). Skin microbiomes of California terrestrial salamanders are influenced by habitat more than host phylogeny. *Frontiers in Microbiology*, *9*, 442.

Blankers, T., Adams, D., et Wiens, J. (2012). Ecological radiation with limited morphological diversification in salamanders. *Journal of Evolutionary Biology*, *25*(4), 634-646.

Blomberg, S. P., Garland Jr, T., et Ives, A. R. (2003). Testing for phylogenetic signal in comparative data: behavioral traits are more labile. *Evolution*, *57*(4), 717-745.

Blümel, R., Zink, M., Klopocki, E., et Liedtke, D. (2019). On the traces of tcf12: Investigation of the gene expression pattern during development and cranial suture patterning in zebrafish (*Danio rerio*). *PLoS One*, *14*(6), e0218286.

Boerckel, J. D., Mason, D. E., McDermott, A. M., et Alsberg, E. (2014). Microcomputed tomography: approaches and applications in bioengineering. *Stem Cell Research & Therapy*, *5*, 1-12.

Böhme, M., Vasilyan, D., et Winklhofer, M. (2012). Habitat tracking, range dynamics and palaeoclimatic significance of Eurasian giant salamanders (Cryptobranchidae)—indications for elevated Central Asian humidity during Cenozoic global warm periods. *Palaeogeography, Palaeoclimatology, Palaeoecology*, *342*, 64-72.

Bölük, A., Yavuz, M., et Demircan, T. (2022). Axolotl: A resourceful vertebrate model for regeneration and beyond. *Developmental Dynamics*, *251*(12), 1914-1933. https://doi.org/https://doi.org/10.1002/dvdy.520

Bon, M., Bardua, C., Goswami, A., et Fabre, A.-C. (2020). Cranial integration in the fire salamander, *Salamandra salamandra* (Caudata: Salamandridae). *Biological Journal of the Linnean Society*, *130*(1), 178-194. https://doi.org/https://doi.org/10.1093/biolinnean/blaa020

Bonett, R. M., et Blair, A. L. (2017). Evidence for complex life cycle constraints on salamander body form diversification. *Proceedings of the National Academy of Sciences*, *114*(37), 9936-9941.

Bonett, R. M., Ledbetter, N. M., Hess, A. J., Herrboldt, M. A., et Denoël, M. (2022). Repeated ecological and life cycle transitions make salamanders an ideal model for evolution and development. *Developmental Dynamics*, *251*(6), 957-972. https://doi.org/https://doi.org/10.1002/dvdy.373

Bonett, R. M., Steffen, M. A., Lambert, S. M., Wiens, J. J., et Chippindale, P. T. (2014). Evolution of paedomorphosis in plethodontid salamanders: ecological correlates and re-evolution of metamorphosis. *Evolution*, *68*(2), 466-482.

Bonfili, N., Barbeito-Andrés, J., Bernal, V., Hallgrímsson, B., et Gonzalez, P. N. (2022). Morphological correspondence between brain and endocranial surfaces in mice exposed to undernutrition during development. *Journal of Anatomy*, *241*(1), 1-12.

Bookstein, F. L. (1996). Combining the tools of geometric morphometrics. In L. F. Marcus, M. Corti, A. Loy, G. J. P. Naylor, D. E. Slice (Eds.), *Advances in Morphometrics* (pp. 131-151). Springer.

Bookstein, F. L. (2015). Integration, disintegration, and self-similarity: characterizing the scales of shape variation in landmark data. *Evolutionary Biology*, *42*, 395-426. https://doi.org/https://doi.org/10.1007/s11692-015-9317-8

Bordzilovskaya, N., Dettlaff, T., Duhon, S. T., et Malacinski, G. M. (1989). Developmental-stage series of axolotl embryos. In J. Armstrong et G. Malacinski (Eds.), *Developmental Biology of the Axolotl*. Oxford University Press.

Boyd, S. K., Tyler, C. J., et de Vries, G. J. (1992). Sexual dimorphism in the vasotocin system of the bullfrog (*Rana catesbeiana*). *Journal of Comparative Neurology*, *325*(2), 313-325.

Brainerd, E. L., Baier, D. B., Gatesy, S. M., Hedrick, T. L., Metzger, K. A., Gilbert, S. L., et Crisco, J. J. (2010). X-ray reconstruction of moving morphology (XROMM): precision, accuracy and applications in comparative biomechanics research. *Journal of Experimental Zoology Part A: Ecological Genetics and Physiology*, *313*(5), 262-279.

Briscoe, S. D., et Ragsdale, C. W. (2019). Evolution of the chordate telencephalon. *Current Biology*, *29*(13), R647-R662.

Brossman, K., Carlson, B., Swierk, L., et Langkilde, T. (2013). Aquatic tail size carries over to the terrestrial phase without impairing locomotion in adult Eastern Red-spotted Newts (*Notophthalmus viridescens viridescens*). *Canadian Journal of Zoology*, *91*(1), 7-12.

Brown, D. D., et Cai, L. (2007). Amphibian metamorphosis. *Developmental Biology*, *306*(1), 20-33.

Browne, R. K., Li, H., Wang, Z., Hime, P., McMillan, A., Wu, M., Diaz, R., Hongxing, Z., McGinnity, D., et Briggler, J. T. (2012). The giant salamanders (Cryptobranchidae): Part A. Palaeontology, phylogeny, genetics, and morphology. *Amphibian and Reptile Conservation*, *5*(4), 17-29.

Bruce, R. C. (2000). Sexual size dimorphism in the Plethodontidae. In R. C. Bruce, R. G. Jaeger, L. D. Houck (Eds.), *The Biology of Plethodontid Salamanders* (pp. 243-260). Springer.

Bruce, R. C. (2003). Life histories. In D. M. Sever (Ed.), *Reproductive Biology and Phylogeny of Urodela* (Vol. 1, pp. 477-525).

Buckley, D., Alcobendas, M., García-París, M., et Wake, M. H. (2007). Heterochrony, cannibalism, and the evolution of viviparity in *Salamandra salamandra*. *Evolution & Development*, *9*(1), 105-115.

Butler, A. B., et Hodos, W. (2005). *Comparative Vertebrate Neuroanatomy: Evolution and Adaptation*. John Wiley & Sons.

Cardini, A., et Elton, S. (2008). Does the skull carry a phylogenetic signal? Evolution and modularity in the guenons. *Biological Journal of the Linnean Society*, *93*(4), 813-834.

Cardini, A., Polly, D., Dawson, R., et Milne, N. (2015). Why the long face? Kangaroos and wallabies follow the same 'rule' of cranial evolutionary allometry (CREA) as placentals. *Evolutionary Biology*, *42*, 169-176.

Cardini, A., et Polly, P. D. (2013). Larger mammals have longer faces because of size-related constraints on skull form. *Nature Communications*, *4*(1), e2458.

Challands, T., Pardo, J. D., et Clement, A. M. (2020). Mandibular musculature constrains brain–endocast disparity between sarcopterygians. *Royal Society Open Science*, *7*(9), e200933.

Chevallier, S., Ijspeert, A. J., Ryczko, D., Nagy, F., et Cabelguen, J.-M. (2008). Organisation of the spinal central pattern generators for locomotion in the salamander: biology and modelling. *Brain Research Reviews*, *57*(1), 147-161.

Chippindale, P. T., Bonett, R. M., Baldwin, A. S., et Wiens, J. J. (2004). Phylogenetic evidence for a major reversal of life-history evolution in plethodontid salamanders. *Evolution*, *58*(12), 2809-2822.

Ćirović, R., Radović, D., et Vukov, T. D. (2008). Breeding site traits of European newts (*Triturus macedonicus*, *Lissotriton vulgaris*, and *Mesotriton alpestris*: Salamandridae) in the Montenegrin karst region. *Archives of Biological Sciences*, *60*(3), 459-468.

Clack, J. A. (2016). Vertebrate diversity in a sensory system: the fossil record of otic evolution. In J. A. Clack, R. R Fay, A. N. Popper (Eds.), *Evolution of the Vertebrate Ear: Evidence from the Fossil Record* (pp. 1-16). Springer.

Claverie, T., et Patek, S. (2013). Modularity and rates of evolutionary change in a power-amplified prey capture system. *Evolution*, *67*(11), 3191-3207.

Clement, A. M., Mensforth, C. L., Challands, T., Collin, S. P., et Long, J. A. (2021). Brain reconstruction across the fish-tetrapod transition; insights from modern amphibians. *Frontiers in Ecology and Evolution*, *9*, e640345.

Clement, A. M., Nysjö, J., Strand, R., et Ahlberg, P. E. (2015). Brain–endocast relationship in the Australian lungfish, *Neoceratodus forsteri*, elucidated from tomographic data (Sarcopterygii: Dipnoi). *PLoS One*, *10*(10), e0141277.

Collyer, M., Sekora, D., et Adams, D. (2015). A method for analysis of phenotypic change for phenotypes described by high-dimensional data. *Heredity*, *115*(4), 357-365. https://doi.org/https://doi.org/10.1038/hdy.2014.75

Collyer, M. L., et Adams, D. C. (2019). RRPP: linear model evaluation with randomized residuals in a permutation procedure. *R package version 0.4. 0*.

Collyer, M. L., et Adams, D. C. (2024). Interrogating Random and Systematic Measurement Error in Morphometric Data. *Evolutionary Biology*, *51*(1), 179-207. https://doi.org/https://doi.org/10.1007/s11692-024-09627-6

Collyer, M. L., Baken, E. K., et Adams, D. C. (2022). A standardized effect size for evaluating and comparing the strength of phylogenetic signal. *Methods in Ecology and Evolution*, *13*(2), 367-382.

Conaway, M. A., et Adams, D. C. (2022). An effect size for comparing the strength of morphological integration across studies. *Evolution*, *76*(10), 2244-2259. https://doi.org/https://doi.org/10.1111/evo.14595

Conith, A. J., Hope, S. A., et Albertson, R. C. (2023). Covariation of brain and skull shapes as a model to understand the role of crosstalk in development and evolution. *Evolution & Development*, *25*(1), 85-102.

Corfield, J. R., Price, K., Iwaniuk, A. N., Gutiérrez-Ibáñez, C., Birkhead, T., et Wylie, D. R. (2015). Diversity in olfactory bulb size in birds reflects allometry, ecology, and phylogeny. *Frontiers in Neuroanatomy*, *9*, e102.

Croizier, S., Chometton, S., Fellmann, D., et Risold, P.-Y. (2015). Characterization of a mammalian prosencephalic functional plan. *Frontiers in Neuroanatomy*, *8*, 161.

Cuny, R., et Malacinski, G. M. (1986). Axolotl retina and lens development: mutual tissue stimulation and autonomous failure in the eyeless mutant retina. *Development*, *96*(1), 151-170. https://doi.org/https://doi.org/10.1242/dev.96.1.151

D'Aniello, B., Di Cosmo, A., Scandurra, A., et Pinelli, C. (2019). Mosaic and concerted brain evolution: the contribution of microscopic comparative neuroanatomy in lower vertebrates. *Frontiers in Neuroanatomy*, *13*, 86. https://doi.org/https://doi.org/10.3389/fnana.2019.00086

Dawley, E. M., Fingerlin, A., Hwang, D., John, S. S., et Stankiewicz, C. A. (2000). Seasonal cell proliferation in the chemosensory epithelium and brain of red-backed salamanders, *Plethodon cinereus*. *Brain Behavior and Evolution*, *56*(1), 1-13.

de Sousa, A. A., Beaudet, A., Calvey, T., Bardo, A., Benoit, J., Charvet, C. J., Dehay, C., Gómez-Robles, A., Gunz, P., et Heuer, K. (2023). From fossils to mind. *Communications Biology*, *6*(1), e636.

Deban, S. M., et Marks, S. B. (2002). Metamorphosis and evolution of feeding behaviour in salamanders of the family Plethodontidae. *Zoological Journal of the Linnean Society*, *134*(4), 375-400.

Deban, S. M., O'Reilly, J. C., Dicke, U., et Van Leeuwen, J. L. (2007). Extremely high-power tongue projection in plethodontid salamanders. *Journal of Experimental Biology*, *210*(4), 655-667.

Deban, S. M., et Richardson, J. C. (2011). Cold-blooded snipers: thermal independence of ballistic tongue projection in the salamander *Hydromantes platycephalus*. *Journal of Experimental Zoology Part A: Ecological Genetics and Physiology*, *315*(10), 618-630.

Deban, S. M., Scales, J. A., Bloom, S. V., Easterling, C. M., O'Donnell, M. K., et Olberding, J. P. (2020). Evolution of a high-performance and functionally robust musculoskeletal system in salamanders. *Proceedings of the National Academy of Sciences*, *117*(19), 10445-10454.

Deban, S. M., Wake, D. B., et Roth, G. (1997). Salamander with a ballistic tongue. *Nature*, *389*(6646), 27-28.

Deckelbaum, R. A., Holmes, G., Zhao, Z., Tong, C., Basilico, C., et Loomis, C. A. (2012). Regulation of cranial morphogenesis and cell fate at the neural crest-mesoderm boundary by engrailed 1. *Development*, *139*(7), 1346-1358.

Deeg, K. E., Sears, I. B., et Aizenman, C. D. (2009). Development of multisensory convergence in the *Xenopus* optic tectum. *Journal of Neurophysiology*, *102*(6), 3392-3404.

Dempster, W. T. (1935). The brain case and endocranial cast of *Eryops megacephalus* (Cope). *Journal of Comparative Neurology*, *62*, 171–196.

Denis, J.-F., Lévesque, M., Tran, S. D., Camarda, A.-J., et Roy, S. (2013). Axolotl as a model to study scarless wound healing in vertebrates: role of the transforming growth factor beta signaling pathway. *Advances in Wound Care*, *2*(5), 250-260. https://doi.org/https://doi.org/10.1089/wound.2012.0371

Denoël, M., et Joly, P. (2000). Neoteny and progenesis as two heterochronic processes involved in paedomorphosis in *Triturus alpestris* (Amphibia: Caudata). *Proceedings of the Royal Society of London. Series B: Biological Sciences*, *267*(1451), 1481-1485.

Denoël, M., Joly, P., et Whiteman, H. H. (2005). Evolutionary ecology of facultative paedomorphosis in newts and salamanders. *Biological Reviews*, *80*(4), 663-671.

Domínguez, L., González, A., et Moreno, N. (2010). Sonic hedgehog expression during *Xenopus laevis* forebrain development. *Brain Research*, *1347*, 19-32.

Domínguez, L., González, A., et Moreno, N. (2015). Patterns of hypothalamic regionalization in amphibians and reptiles: common traits revealed by a genoarchitectonic approach. *Frontiers in Neuroanatomy*, *9*, e3.

Dragonfly 2022.2, O. Comet Technologies Canada Inc. https://www.theobjects.com/dragonfly

Drake, A. G., et Klingenberg, C. P. (2008). The pace of morphological change: historical transformation of skull shape in St Bernard dogs. *Proceedings of the Royal Society B: Biological Sciences*, *275*(1630), 71-76.

Drummond, A. J., et Rambaut, A. (2007). BEAST: Bayesian evolutionary analysis by sampling trees. *BMC Evolutionary Biology*, *7*, 1-8.

Duellman, W., et Trueb, L. (1994). *Biology of Amphibians*. The Johns Hopkins University Press.

Dumitru, M. L., et Frugård Opdal, A. M. (2024). Beyond the mosaic model of brain evolution: Rearing environment defines local and global plasticity. *Annals of the New York Academy of Sciences*, *1542*(1), 58-66. https://doi.org/https://doi.org/10.1111/nyas.15267

Durand, J. P. (1976). Ocular development and involution in the European cave salamander, *Proteus anguinus laurenti*. *The Biological Bulletin*, *151*(3), 450-466.

Dutel, H., Galland, M., Tafforeau, P., Long, J. A., Fagan, M. J., Janvier, P., Herrel, A., Santin, M. D., Clément, G., et Herbin, M. (2019). Neurocranial development of the coelacanth and the evolution of the sarcopterygian head. *Nature*, *569*(7757), 556-559. https://doi.org/https://doi.org/10.1038/s41586-019-1117-3

Early, C. M., Iwaniuk, A. N., Ridgely, R. C., et Witmer, L. M. (2020). Endocast structures are reliable proxies for the sizes of corresponding regions of the brain in extant birds. *Journal of Anatomy*, *237*(6), 1162-1176.

Eatock, R. A., et Songer, J. E. (2011). Vestibular hair cells and afferents: two channels for head motion signals. *Annual Review of Neuroscience*, *34*(1), 501-534.

Eisthen, H. L. (2000). Presence of the vomeronasal system in aquatic salamanders. *Philosophical Transactions of the Royal Society of London. Series B: Biological Sciences*, *355*(1401), 1209-1213. https://doi.org/https://doi.org/10.1098/rstb.2000.0669

Eisthen, H. L., Sengelaub, D. R., Schroeder, D. M., et Alberts, J. R. (1994). Anatomy and Forebrain Projections of the Olfactory and Vomeronasal Organs in Axolotls (*Ambystoma mexicanum*)(Part 2 of 2). *Brain, Behavior and Evolution*, *44*(2), 117-124. https://doi.org/https://doi.org/10.1159/000316239

Elias, P. (1984). *Salamanders of the Northwestern Highlands of Guatemala*. Natural History Museum of Los Angeles County.

Epskamp, S., Cramer, A. O., Waldorp, L. J., Schmittmann, V. D., et Borsboom, D. (2012). qgraph: Network visualizations of relationships in psychometric data. *Journal of Statistical Software*, *48*, 1-18.

Esteve-Altava, B. (2017). In search of morphological modules: a systematic review. *Biological Reviews*, *92*(3), 1332-1347.

Fabbri, M., Mongiardino Koch, N., Pritchard, A. C., Hanson, M., Hoffman, E., Bever, G. S., Balanoff, A. M., Morris, Z. S., Field, D. J., et Camacho, J. (2017). The skull roof tracks the brain during the evolution and development of reptiles including birds. *Nature Ecology & Evolution*, *1*(10), 1543-1550.

Fabre, A.-C., Bardua, C., Bon, M., Clavel, J., Felice, R. N., Streicher, J. W., Bonnel, J., Stanley, E. L., Blackburn, D. C., et Goswami, A. (2020). Metamorphosis shapes cranial diversity and rate of evolution in salamanders. *Nature Ecology & Evolution*, *4*(8), 1129-1140. https://doi.org/https://doi.org/10.1038/s41559-020-1225-3

Fasola, S., Muggeo, V. M., et Küchenhoff, H. (2018). A heuristic, iterative algorithm for change-point detection in abrupt change models. *Computational Statistics*, *33*, 997-1015. https://doi.org/https://doi.org/10.1007/s00180-017-0740-4

Fei, L., et Ye, C.-y. (2001). *The Colour Handbook of the Amphibians of Sichuan*. China Forestry Publishing House.

Feng, W., Liu, S., Deng, Q., Fu, S., Yang, Y., Dai, X., Wang, S., Wang, Y., Liu, Y., et Lin, X. (2023). A scATAC-seq atlas of chromatin accessibility in axolotl brain regions. *Scientific Data*, *10*(1), e627. https://doi.org/https://doi.org/10.1038/s41597-023-02533-0

Ficetola, G. F., Bonardi, A., Colleoni, E., Padoa-Schioppa, E., et Scali, S. (2013). Evolution of sexual dimorphism in the number of tail vertebrae in salamanders: comparing multiple hypotheses. *Evolutionary Biology*, *40*(2), 220-227.

Finlay, B. L., et Darlington, R. B. (1995). Linked regularities in the development and evolution of mammalian brains. *Science*, *268*(5217), 1578-1584. https://doi.org/10.1126/science.7777856

Finlay, B. L., Darlington, R. B., et Nicastro, N. (2001). Developmental structure in brain evolution. *Behavioral and Brain Sciences*, *24*(2), 263-278. https://doi.org/https://doi.org/10.1017/S0140525X01003958

Fong, S., Rogell, B., Amcoff, M., Kotrschal, A., van der Bijl, W., Buechel, S. D., et Kolm, N. (2021). Rapid mosaic brain evolution under artificial selection for relative telencephalon size in the guppy (*Poecilia reticulata*). *Science Advances*, *7*(46), eabj4314.

Fortuny, J., Marce-Nogue, J., Heiss, E., Sanchez, M., Gil, L., et Galobart, À. (2015). 3D bite modeling and feeding mechanics of the largest living amphibian, the Chinese giant salamander *Andrias davidianus* (Amphibia: Urodela). *PLoS One*, *10*(4), e0121885.

Fritzsch, B., Gregory, D., et Rosa-Molinar, E. (2005). The development of the hindbrain afferent projections in the axolotl: evidence for timing as a specific mechanism of afferent fiber sorting. *Zoology*, *108*(4), 297-306. https://doi.org/https://doi.org/10.1016/j.zool.2005.08.003

Fritzsch, B., et Straka, H. (2014). Evolution of vertebrate mechanosensory hair cells and inner ears: toward identifying stimuli that select mutation driven altered morphologies. *Journal of Comparative Physiology A*, *200*(1), 5-18.

Gasc, J.-P., Cabela, A., Crnobrnja-Isailovic, J., Dolmen, D., Grossenbacher, K., Haffner, P., Lescure, J., Martens, H., Martinez Rica, J. P., et Maurin, H. (2004). *Atlas of Amphibians and Reptiles in Europe*. Muséum national d'histoire naturelle, Paris.

Gee, B. M. (2020). Size matters: the effects of ontogenetic disparity on the phylogeny of Trematopidae (Amphibia: Temnospondyli). *Zoological Journal of the Linnean Society*, *190*(1), 79-113.

Gignac, P. M., et Kley, N. J. (2014). Iodine-enhanced micro-CT imaging: Methodological refinements for the study of the soft-tissue anatomy of post-embryonic vertebrates. *Journal of Experimental Zoology Part B: Molecular and Developmental Evolution*, *322*(3), 166-176.

Gignac, P. M., Kley, N. J., Clarke, J. A., Colbert, M. W., Morhardt, A. C., Cerio, D., Cost, I. N., Cox, P. G., Daza, J. D., et Early, C. M. (2016). Diffusible iodine-based contrast-enhanced computed tomography (diceCT): an emerging tool for rapid, high-resolution, 3-D imaging of metazoan soft tissues. *Journal of Anatomy*, *228*(6), 889-909.

Gilland, E., et Baker, R. (2005). Evolutionary patterns of cranial nerve efferent nuclei in vertebrates. *Brain Behavior and Evolution*, *66*(4), 234-254.

Gittleman, J. L. (1991). Carnivore olfactory bulb size: allometry, phylogeny and ecology. *Journal of Zoology*, *225*(2), 253-272.

Gómez-Robles, A., Hopkins, W. D., et Sherwood, C. C. (2014). Modular structure facilitates mosaic evolution of the brain in chimpanzees and humans. *Nature Communications*, *5*(1), e4469. https://doi.org/https://doi.org/10.1038/ncomms5469

Gonda, A., Trokovic, N., Herczeg, G., Laurila, A., et Merilä, J. (2010). Predation-and competition-mediated brain plasticity in *Rana temporaria* tadpoles. *Journal of Evolutionary Biology*, *23*(11), 2300-2308.

González-Forero, M., et Gardner, A. (2018). Inference of ecological and social drivers of human brain-size evolution. *Nature*, *557*(7706), 554-557.

Gonzalez-Voyer, A., Gonzalez-Suarez, M., Vilà, C., et Revilla, E. (2016). Larger brain size indirectly increases vulnerability to extinction in mammals. *Evolution*, *70*(6), 1364-1375. https://doi.org/https://doi.org/10.1111/evo.12943

Gonzalez-Voyer, A., et Kolm, N. (2010). Sex, ecology and the brain: evolutionary correlates of brain structure volumes in Tanganyikan cichlids. *PLoS One*, *5*(12), e14355.

Gonzalez-Voyer, A., Winberg, S., et Kolm, N. (2009). Brain structure evolution in a basal vertebrate clade: evidence from phylogenetic comparative analysis of cichlid fishes. *BMC Evolutionary Biology*, *9*, 1-12. https://doi.org/https://doi.org/10.1186/1471-2148-9-238

González, A., López, J., Morona, R., et Moreno, N. (2020). The organization of the central nervous system of amphibians. In J.H. Kaas (Eds.), *Evolutionary Neuroscience* (pp. 125-157). Elsevier.

Goris, R. C., et Maeda, N. (2004). *Guide to the Amphibians and Reptiles of Japan*. Krieger Publishing Company.

Goswami, A., et Finarelli, J. A. (2016). EMMLi: a maximum likelihood approach to the analysis of modularity. *Evolution*, *70*(7), 1622-1637. https://doi.org/https://doi.org/10.1111/evo.12956

Goswami, A., et Polly, P. D. (2010). Methods for studying morphological integration and modularity. *The Paleontological Society Papers*, *16*, 213-243.

Goswami, A., Smaers, J. B., Soligo, C., et Polly, P. D. (2014). The macroevolutionary consequences of phenotypic integration: from development to deep time. *Philosophical Transactions of the Royal Society B: Biological Sciences*, *369*(1649), e20130254.

Gould, S. (1977). Ontogeny and Phylogeny. Cambridge. MA: Harvard University Press.

Gower, J. C. (1975). Generalized procrustes analysis. *Psychometrika*, *40*, 33-51.

Green, P. J. (1995). Reversible jump Markov chain Monte Carlo computation and Bayesian model determination. *Biometrika*, *82*(4), 711-732.

Gunz, P., Mitteroecker, P., Bookstein, F.L. (2005). Semilandmarks in Three Dimensions. In: Slice, D.E. (Eds.), *Modern Morphometrics in Physical Anthropology,* Springer, Boston, MA. https://doi.org/10.1007/0-387-27614-9_3

Gutiérrez-Ibáñez, C., Iwaniuk, A. N., Moore, B. A., Fernandez-Juricic, E., Corfield, J. R., Krilow, J. M., Kolominsky, J., et Wylie, D. R. (2014). Mosaic and concerted evolution in the visual system of birds. *PLoS One*, *9*(3), e90102. https://doi.org/https://doi.org/10.1371/journal.pone.0090102

Hager, R., Lu, L., Rosen, G. D., et Williams, R. W. (2012). Genetic architecture supports mosaic brain evolution and independent brain–body size regulation. *Nature Communications*, *3*(1), e1079. https://doi.org/https://doi.org/10.1038/ncomms2086

Hall, Z. J., et Tropepe, V. (2018). Visual experience facilitates BDNF-dependent adaptive recruitment of new neurons in the postembryonic optic tectum. *Journal of Neuroscience*, *38*(8), 2000-2014. https://doi.org/https://doi.org/10.1523/JNEUROSCI.1962-17.2018

Haller, A. (1762). *Elementa Physiologiae Corporis Humani*. Gleditsch.

Hanken, J., et Wake, D. B. (1993). Miniaturization of body size: organismal consequences and evolutionary significance. *Annual Review of Ecology and Systematics*, *24*, 501-519.

Hanna, C. S., Alihosseini, C., Fischer, H. M., Davoli, E. C., et Granatosky, M. C. (2022). Are they arboreal? Climbing abilities and mechanics in the red-backed salamander (*Plethodon cinereus*). *Journal of Experimental Zoology Part A: Ecological and Integrative Physiology*, *337*(3), 238-249.

Hawes, R. (1945). On the eyes and reactions to light of *Proteus anguinus*. *Journal of Cell Science*, *2*(341), 1-51.

Hedrick, B. P., Yohe, L., Vander Linden, A., Dávalos, L. M., Sears, K., Sadier, A., Rossiter, S. J., Davies, K. T., et Dumont, E. (2018). Assessing soft-tissue shrinkage estimates

in museum specimens imaged with diffusible iodine-based contrast-enhanced computed tomography (diceCT). *Microscopy and Microanalysis*, *24*(3), 284-291.
Heimel, P., Swiadek, N. V., Slezak, P., Kerbl, M., Schneider, C., Nürnberger, S., Redl, H., Teuschl, A. H., et Hercher, D. (2019). Iodine-enhanced micro-CT imaging of soft tissue on the example of peripheral nerve regeneration. *Contrast Media & Molecular Imaging*, *2019*(1), e7483745.
Heled, J., et Bouckaert, R. R. (2013). Looking for trees in the forest: summary tree from posterior samples. *BMC Evolutionary Biology*, *13*, 1-11.
Hernandez, A. (2016). *Crocodile Newts: The Primitive Salamandridae of Asia: Genera Echinotriton and Tylototriton*. Edition Chimaira.
Hincapie, M., Carbonell-Medina, B., Arenas-Gomez, C. M., et Delgado, J. P. (2022). *Ambystoma mexicanum*, a model organism in developmental biology and regeneration: a colombian experience. *Acta Biológica Colombiana*, *27*(1), 113-126. https://doi.org/https://doi.org/10.15446/abc.v27n1.88309
Hodge, J. R., Adams, D. S., Williams, K. L., Alencar, L. R., Camper, B., Larouche, O., Thurman, M. A., Zapfe, K., et Price, S. A. (2025). Unraveling the Effects of Ecology and Evolutionary History in the Phenotypic Convergence of Fishes. *Systematic Biology*, *74*(6), 881-896.
Hodos, W. (1988). Comparative neuroanatomy and the evolution of intelligence. In H. J. Jerison, I. Jerison (Eds.), *Intelligence and Evolutionary Biology* (pp. 93-107). Springer.
Hofman, M. A. (1982). Encephalization in mammals in relation to the size of the cerebral cortex. *Brain, Behavior and Evolution*, *20*(1-2), 84-96. https://doi.org/https://doi.org/10.1159/000121583
Hoops, D., Vidal-García, M., Ullmann, J. F., Janke, A. L., Stait-Gardner, T., Duchêne, D. A., Price, W. S., Whiting, M. J., et Keogh, J. S. (2017). Evidence for concerted and mosaic brain evolution in dragon lizards. *Brain Behavior and Evolution*, *90*(3), 211-223. https://doi.org/https://doi.org/10.1159/000478738
Hopkins, M. J., et Gerber, S. (2017). Morphological disparity. In B. K. Hall (Ed.), *Evolutionary Developmental Biology* (pp. 1-12). Springer.
Hopson, J. A. (1979). Paleoneurology. In C. Gans, R. G. Northcutt, et P. Ulinski (Eds.), *Biology of the Reptilia* (Vol. 9, pp. 39-146).
Hou, Y., Shu, X., Shi, S., Lin, X., Xiao, L., Jiang, J., Ran, J., et Xie, F. (2022). Endocast Morphological Variation and Its Driving Forces in *Scutiger boulengeri*. *Asian Herpetological Research*, *13*(4), 1-21.
Huie, J. M., Park, G., et Kawano, S. M. (2025). Salamander ecomorphology reveals a unique suite of climbing adaptations. *Proceedings of the Royal Society B: Biological Sciences*, *292*(2053), 20251295.
Hutchins, M., Duellman, W., et Schlager, N. (2003). Grzimek's Animal Life Encyclopedia. Amphibians. Farmington Hills, MI: Gale Group
Ijspeert, A. J., Crespi, A., Ryczko, D., et Cabelguen, J.-M. (2007). From swimming to walking with a salamander robot driven by a spinal cord model. *Science*, *315*(5817), 1416-1420.

Iordansky, N. (2005). Paedomorphosis, neoteny, and evolution. *Entomological Review*, *85*(2), S147-S156.
IUCN, S. A. S. G. (2020). *Bolitoglossa rufescens*. The IUCN Red List of Threatened Species 2020: e.T50928774A50928633. https://dx.doi.org/10.2305/IUCN.UK.2020-3.RLTS.T50928774A50928633.en
Jeffery, W. R. (2008). Emerging model systems in evo-devo: cavefish and microevolution of development. *Evolution & development*, *10*(3), 265-272.
Jerison, H. (2012). *Evolution of the Brain and Intelligence*. Elsevier.
Jerison, H. J. (1985). Animal intelligence as encephalization. *Philosophical Transactions of the Royal Society of London. B, Biological Sciences*, *308*(1135), 21-35.
Jessell, T. M. (2000). Neuronal specification in the spinal cord: inductive signals and transcriptional codes. *Nature Reviews Genetics*, *1*(1), 20-29.
Jetz, W., et Pyron, R. A. (2018). The interplay of past diversification and evolutionary isolation with present imperilment across the amphibian tree of life. *Nature Ecology & Evolution*, *2*(5), 850-858.
Jolicoeur, P., Pirlot, P., Baron, G., et Stephan, H. (1984). Brain structure and correlation patterns in Insectivora, Chiroptera, and Primates. *Systematic Biology*, *33*(1), 14-29.
Jones, M. E., Benson, R. B., Skutschas, P., Hill, L., Panciroli, E., Schmitt, A. D., Walsh, S. A., et Evans, S. E. (2022). Middle Jurassic fossils document an early stage in salamander evolution. *Proceedings of the National Academy of Sciences*, *119*(30), e2114100119.
Kappers, C. A., Huber, G. C., et Crosby, E. C. (1936). The comparative anatomy of the nervous system of vertebrates including man. *The Journal of Nervous and Mental Disease*, *84*(6), 709-711.
Karten, H. J. (2015). Vertebrate brains and evolutionary connectomics: on the origins of the mammalian 'neocortex'. *Philosophical Transactions of the Royal Society B: Biological Sciences*, *370*(1684), 20150060.
Kawano, S. M., et Blob, R. W. (2022). Terrestrial force production by the limbs of a semi-aquatic salamander provides insight into the evolution of terrestrial locomotor mechanics. *Journal of Experimental Biology*, *225*(7), jeb242795.
Kawano, S. M., Martin, J., Medina, J., Doherty, C., Zheng, G., Hsiao, E., Evans, M. J., de Queiroz, K., Pyron, R. A., et Huie, J. M. (2024). Applying 3D Models of Giant Salamanders to Explore Form–Function Relationships in Early Digit-Bearing Tetrapods. *Integrative and Comparative Biology*, *64*(3), 715-728. https://doi.org/https://doi.org/10.1093/icb/icae129
Keirnan, A. R., Cunha, F., Citron, S., Prideaux, G., Iwaniuk, A. N., et Weisbecker, V. (2025). Avian telencephalon and cerebellum volumes can be accurately estimated from digital brain endocasts. *Biology Letters*, *21*(1), e20240596.
Kerney, R. (2011). Embryonic staging table for a direct-developing salamander, *Plethodon cinereus* (Plethodontidae). *The Anatomical Record: Advances in Integrative Anatomy and Evolutionary Biology*, *294*(11), 1796-1808.
Kiecker, C., et Lumsden, A. (2005). Compartments and their boundaries in vertebrate brain development. *Nature Reviews Neuroscience*, *6*(7), 553-564.

Kilmer, J. T., et Rodríguez, R. L. (2017). Ordinary least squares regression is indicated for studies of allometry. *Journal of Evolutionary Biology*, *30*(1), 4-12. https://doi.org/https://doi.org/10.1111/jeb.12986

Klingenberg, C. P. (2008). Morphological integration and developmental modularity. *Annual Review of Ecology, Evolution, and Systematics*, *39*(1), 115-132.

Klingenberg, C. P. (2014). Studying morphological integration and modularity at multiple levels: concepts and analysis. *Philosophical Transactions of the Royal Society B: Biological Sciences*, *369*(1649), e20130249.

Klingenberg, C. P., Badyaev, A. V., Sowry, S. M., et Beckwith, N. J. (2001). Inferring developmental modularity from morphological integration: analysis of individual variation and asymmetry in bumblebee wings. *The American Naturalist*, *157*(1), 11-23.

Klingenberg, C. P., Barluenga, M., et Meyer, A. (2002). Shape analysis of symmetric structures: quantifying variation among individuals and asymmetry. *Evolution*, *56*(10), 1909-1920. https://doi.org/https://doi.org/10.1111/j.0014-3820.2002.tb00117.x

Klingenberg, C. P., et Marugán-Lobón, J. (2013). Evolutionary covariation in geometric morphometric data: analyzing integration, modularity, and allometry in a phylogenetic context. *Systematic Biology*, *62*(4), 591-610.

Kollros, J. J. (1981). Transitions in the nervous system during amphibian metamorphosis. In L. I. In: Gilbert et E. Frieden (Eds.), *Metamorphosis: a Problem in Developmental Biology* (pp. 445-459). Springer. https://doi.org/https://doi.org/10.1007/978-1-4613-3246-6_13

Kotrschal, A., et Kotrschal, K. (2020). Fish brains: anatomy, functionality, and evolutionary relationships. In T. S. Kristiansen, A. Fernö, M. A. Pavlidis, H. van de Vis *The Welfare of Fish* (pp. 129-148). Springer.

Kriwet, J., Kiessling, W., et Klug, S. (2009). Diversification trajectories and evolutionary life-history traits in early sharks and batoids. *Proceedings of the Royal Society B: Biological Sciences*, *276*(1658), 945-951.

Krumlauf, R. (1994). Hox genes in vertebrate development. *Cell*, *78*(2), 191-201.

Krumlauf, R., et Wilkinson, D. G. (2021). Segmentation and patterning of the vertebrate hindbrain. *Development*, *148*(15), dev186460.

Kupfer, A. (2007). Sexual size dimorphism in amphibians: an overview. In D. J. Fairbairn, W. U. Blanckenhorn, et T. Székely (Eds.), *Sex, Size and Gender Roles: Evolutionary Studies of Sexual Size Dimorphism* (Vol. 5, pp. 50-60). Oxford University Press.

Kuratani, S. (2005). Craniofacial development and the evolution of the vertebrates: the old problems on a new background. *Zoological Science*, *22*(1), 1-19.

Kuzmin, S. L. (1999). *The Amphibians of the Former Soviet Union*. Pensoft Publishers.

Lamanna, F., Hervas-Sotomayor, F., Oel, A. P., Jandzik, D., Sobrido-Cameán, D., Santos-Durán, G. N., Martik, M. L., Stundl, J., Green, S. A., et Brüning, T. (2023). A lamprey neural cell type atlas illuminates the origins of the vertebrate brain. *Nature Ecology & Evolution*, *7*(10), 1714-1728.

Lancaster, M. A. (2024). Unraveling mechanisms of human brain evolution. *Cell*, *187*(21), 5838-5857.

Lannoo, M. (2005). *Amphibian Declines: the Conservation Status of United States Species*. University of California Press.

Lauder, G. V., et Shaffer, H. B. (1985). Functional morphology of the feeding mechanism in aquatic ambystomatid salamanders. *Journal of Morphology*, *185*(3), 297-326.

Lauder, G. V., et Shaffer, H. B. (1988). Ontogeny of functional design in tiger salamanders (*Ambystoma tigrinum*): are motor patterns conserved during major morphological transformations? *Journal of Morphology*, *197*(3), 249-268.

Lázaro, J., Hertel, M., Sherwood, C. C., Muturi, M., et Dechmann, D. K. (2018). Profound seasonal changes in brain size and architecture in the common shrew. *Brain Structure and Function*, *223*, 2823-2840. https://doi.org/https://doi.org/10.1007/s00429-018-1666-5

Lazcano, I., Cisneros-Mejorado, A., Concha, L., Ortiz-Retana, J. J., Garza-Villarreal, E. A., et Orozco, A. (2021). MRI-and histologically derived neuroanatomical atlas of the *Ambystoma mexicanum* (axolotl). *Scientific Reports*, *11*(1), e9850. https://doi.org/https://doi.org/10.1038/s41598-021-89357-3

Lazić, M. M., Carretero, M. A., Crnobrnja-Isailović, J., et Kaliontzopoulou, A. (2015). Effects of environmental disturbance on phenotypic variation: an integrated assessment of canalization, developmental stability, modularity, and allometry in lizard head shape. *The American Naturalist*, *185*(1), 44-58.

Lazić, M. M., Carretero, M. A., Crnobrnja-Isailović, J., et Kaliontzopoulou, A. (2016). Postnatal dynamics of developmental stability and canalization of lizard head shape under different environmental conditions. *Evolutionary Biology*, *43*(3), 368-379.

Ledbetter, N. M., et Bonett, R. M. (2019). Terrestriality constrains salamander limb diversification: Implications for the evolution of pentadactyly. *Journal of Evolutionary Biology*, *32*(7), 642-652.

Leung, R. F., George, A. M., Roussel, E. M., Faux, M. C., Wigle, J. T., et Eisenstat, D. D. (2022). Genetic regulation of vertebrate forebrain development by homeobox genes. *Frontiers in Neuroscience*, *16*, e843794.

Liao, W.-B., Lou, S., Zeng, Y., et Merilä, J. (2015). Evolution of anuran brains: disentangling ecological and phylogenetic sources of variation. *Journal of Evolutionary Biology*, *28*(11), 1986-1996. https://doi.org/https://doi.org/10.1111/jeb.12714

Liedtke, H. C., Wiens, J. J., et Gomez-Mestre, I. (2022). The evolution of reproductive modes and life cycles in amphibians. *Nature Communications*, *13*(1), e7039.

Lisney, T. J., Wagner, H.-J., et Collin, S. P. (2018). Ontogenetic shifts in the number of axons in the olfactory tract and optic nerve in two species of deep-sea grenadier fish (Gadiformes: Macrouridae: Coryphaenoides). *Frontiers in Ecology and Evolution*, *6*, e168.

Lombard, R. E., et Wake, D. B. (1986). Tongue evolution in the lungless salamanders, family Plethodontidae IV. Phylogeny of plethodontid salamanders and the evolution of feeding dynamics. *Systematic Zoology*, *35*(4), 532-551.

Louppe, V., Le Verger, K., Clavel, J., Ferreira, G. S., Kyriakouli, C., Stanley, E. L., Watt, E. C., Bardua, C., Pérez-Ben, C., et Fröbisch, N. B. (2025). Complete metamorphosis promotes morphological and functional diversity in Caudata. *Functional Ecology*, *2025*(39), 1732–1747. https://doi.org/10.1111/1365-2435.70044

Lowe, W. H., et Addis, B. R. (2019). Matching habitat choice and plasticity contribute to phenotype–environment covariation in a stream salamander. *Ecology*, *100*(5), e02661.

Lüdecke, D., Ben-Shachar, M. S., Patil, I., Waggoner, P., et Makowski, D. (2021). performance: An R package for assessment, comparison and testing of statistical models. *Journal of Open Source Software*, *6*(60), e3139.

Luisetto, M., Naseer, A., Ghulam, R. M., Ahmed, Y. R., et Farhan, A. K. (2018). Endogenous Archeological Sciences: Anatomy, Physiology, Neuroscience, Biochemistry, Immunology, Pharmacology, Oncology, Genetics as Instrument for A New Field of Investigation? Modern Global Aspects for A New Discipline. *Open Access Journal of Addiction and Psychology*. *1*(3), OAJAP.MS.ID.000513.

MacIver, M. A., et Finlay, B. L. (2022). The neuroecology of the water-to-land transition and the evolution of the vertebrate brain. *Philosophical Transactions of the Royal Society B*, *377*(1844), e20200523.

MacIver, M. A., Schmitz, L., Mugan, U., Murphey, T. D., et Mobley, C. D. (2017). Massive increase in visual range preceded the origin of terrestrial vertebrates. *Proceedings of the National Academy of Sciences*, *114*(12), E2375-E2384.

Macrini, T. E. (2006). The evolution of endocranial space in mammals and non-mammalian cynodonts, [Ph.D. Thesis], University of Texas at Austin. Austin, Texas, USA.

Macrini, T. E., De Muizon, C., Cifelli, R. L., et Rowe, T. (2007). Digital cranial endocast of *Pucadelphys andinus*, a Paleocene metatherian. *Journal of Vertebrate Paleontology*, *27*(1), 99-107.

Maddin, H. C. (2011). Deciphering morphological variation in the braincase of caecilian amphibians (Gymnophiona). *Journal of Morphology*, *272*(7), 850-871.

Maddin, H. C., et Anderson, J. S. (2012). Evolution of the amphibian ear with implications for lissamphibian phylogeny: insight gained from the caecilian inner ear. *Fieldiana Life and Earth Sciences*, *2012*(5), 59-76.

Maddin, H. C., Piekarski, N., Sefton, E. M., et Hanken, J. (2016). Homology of the cranial vault in birds: new insights based on embryonic fate-mapping and character analysis. *Royal Society Open Science*, *3*(8), e160356. https://doi.org/https://doi.org/10.1098/rsos.160356

Mai, C. L., et Liao, W. B. (2019). Brain size evolution in anurans: a review. *Animal Biology*, *69*(3), 265-279.

Malacinski, G. M. (1978). The Mexican axolotl, *Ambystoma mexicanum*: its biology and developmental genetics, and its autonomous cell-lethal genes. *American Zoologist*, *18*(2), 195-206. http://www.jstor.org/stable/3882374

Manenti, R., Ficetola, G. F., et De Bernardi, F. (2009). Water, stream morphology and landscape: complex habitat determinants for the fire salamander *Salamandra salamandra*. *Amphibia-Reptilia*, *30*(1), 7-15.

Manzano, A. S., Herrel, A., Fabre, A. C., et Abdala, V. (2017). Variation in brain anatomy in frogs and its possible bearing on their locomotor ecology. *Journal of Anatomy*, *231*(1), 38-58.

Mardia, K. V., Bookstein, F. L., et Moreton, I. J. (2000). Statistical assessment of bilateral symmetry of shapes. *Biometrika*, *87*(2), 285-300.

Marjanović, D., et Laurin, M. (2007). Fossils, molecules, divergence times, and the origin of lissamphibians. *Systematic Biology*, *56*(3), 369-388.
Marjanović, D., et Laurin, M. (2014). An updated paleontological timetree of lissamphibians, with comments on the anatomy of Jurassic crown-group salamanders (Urodela). *Historical Biology*, *26*(4), 535-550.
Marks, S. B., et Collazo, A. (1998). Direct development in *Desmognathus aeneus* (Caudata: Plethodontidae): a staging table. *Copeia*, *1998*(3), 637-648.
Matsumoto, R., Fujiwara, S. i., et Evans, S. E. (2024). The anatomy and feeding mechanism of the Japanese giant salamander (*Andrias japonicus*). *Journal of Anatomy*, *244*(5), 679-707.
Maximino, C. (2008). Evolutionary changes in the complexity of the tectum of nontetrapods: A cladistic approach. *PLoS One*, *3*(10), e3582.
McEntire, K. D. (2016). Arboreal ecology of Plethodontidae: a review. *Copeia*, *104*(1), 124-131.
Metscher, B. D. (2009). MicroCT for comparative morphology: simple staining methods allow high-contrast 3D imaging of diverse non-mineralized animal tissues. *BMC Physiology*, *9*(1), 1-14. https://doi.org/https://doi.org/10.1186/1472-6793-9-11
Mitteroecker, P., et Bookstein, F. (2007). The conceptual and statistical relationship between modularity and morphological integration. *Systematic Biology*, *56*(5), 818-836.
Mitteroecker, P., et Bookstein, F. (2008). The evolutionary role of modularity and integration in the hominoid cranium. *Evolution*, *62*(4), 943-958. https://doi.org/https://doi.org/10.1111/j.1558-5646.2008.00321.x
Mitteroecker, P., et Gunz, P. (2009). Advances in geometric morphometrics. *Evolutionary Biology*, *36*, 235-247.
Mitteroecker, P., Gunz, P., Bernhard, M., Schaefer, K., et Bookstein, F. L. (2004). Comparison of cranial ontogenetic trajectories among great apes and humans. *Journal of Human Evolution*, *46*(6), 679-698.
Monaghan, J. R., Stier, A. C., Michonneau, F., Smith, M. D., Pasch, B., Maden, M., et Seifert, A. W. (2014). Experimentally induced metamorphosis in axolotls reduces regenerative rate and fidelity. *Regeneration*, *1*(1), 2-14.
Montgomery, S. H., Mundy, N. I., et Barton, R. A. (2016). Brain evolution and development: adaptation, allometry and constraint. *Proceedings of the Royal Society B: Biological Sciences*, *283*(1838), e20160433.
Moore, J. M., et DeVoogd, T. J. (2017). Concerted and mosaic evolution of functional modules in songbird brains. *Proceedings of the Royal Society B: Biological Sciences*, *284*(1854), e20170469. https://doi.org/https://doi.org/10.1098/rspb.2017.0469
Mosimann, J. E. (1970). Size allometry: size and shape variables with characterizations of the lognormal and generalized gamma distributions. *Journal of the American Statistical Association*, *65*(330), 930-945. https://doi.org/https://doi.org/10.1080/01621459.1970.10481136
Mourouzis, I., Lavecchia, A. M., et Xinaris, C. (2020). Thyroid hormone signalling: from the dawn of life to the bedside. *Journal of Molecular Evolution*, *88*(1), 88-103.
Mueller, R. L., Macey, J. R., Jaekel, M., Wake, D. B., et Boore, J. L. (2004). Morphological homoplasy, life history evolution, and historical biogeography of plethodontid

salamanders inferred from complete mitochondrial genomes. *Proceedings of the National Academy of Sciences*, *101*(38), 13820-13825.

Muggeo, V. M. (2003). Estimating regression models with unknown break-points. *Statistics in medicine*, *22*(19), 3055-3071. https://doi.org/https://doi.org/10.1002/sim.1545

Murakami, Y., Uchida, K., Rijli, F. M., et Kuratani, S. (2005). Evolution of the brain developmental plan: Insights from agnathans. *Developmental Biology*, *280*(2), 249-259.

Napoli, A. J., et Powers, A. S. (2020). Brain evolution and comparative neuroanatomy. In D. J. Perkel (Ed.), *Encyclopedia of Life Sciences* (pp. 1-14). John Wiley & Sons, Ltd: Chichester. https://doi.org/https://doi.org/10.1002/9780470015902.a0000088.pub4

Nie, X., Luukko, K., et Kettunen, P. (2006). BMP signalling in craniofacial development. *The International Journal of Developmental Biology*, *50*(6), 511-521.

Nieuwenhuys, R., Ten Donkelaar, H. J., et Nicholson, C. (2014). *The Central Nervous System of Vertebrates*. Springer.

Nishikawa, K., Matsui, M., et Nguyen, T. T. (2013). A new species of *Tylototriton* from northern Vietnam (Amphibia: Urodela: Salamandridae). *Current Herpetology*, *32*(1), 34-49.

Noreikiene, K., Herczeg, G., Gonda, A., Balázs, G., Husby, A., et Merilä, J. (2015). Quantitative genetic analysis of brain size variation in sticklebacks: support for the mosaic model of brain evolution. *Proceedings of the Royal Society B: Biological Sciences*, *282*(1810), 20151008. https://doi.org/https://doi.org/10.1098/rspb.2015.1008

Northcutt, R. G. (1986). Lungfish neural characters and their bearing on sarcopterygian phylogeny. *Journal of Morphology*, *190*(S1), 277-297. https://doi.org/https://doi.org/10.1002/jmor.1051900418

Northcutt, R. G. (2002). Understanding vertebrate brain evolution. *Integrative and Comparative Biology*, *42*(4), 743-756.

Nye, H. L., Cameron, J. A., Chernoff, E. A., et Stocum, D. L. (2003). Extending the table of stages of normal development of the axolotl: limb development. *Developmental Dynamics*, *226*(3), 555-560. https://doi.org/https://doi.org/10.1002/dvdy.10237

O'Reilly, J. C., Summers, A. P., et Ritter, D. A. (2000). The evolution of the functional role of trunk muscles during locomotion in adult amphibians. *American Zoologist*, *40*(1), 123-135.

O'Malley, M. A., Wideman, J. G., et Ruiz-Trillo, I. (2016). Losing complexity: the role of simplification in macroevolution. *Trends in Ecology & Evolution*, *31*(8), 608-621.

Oksanen, J. (2016). Design decisions and implementation details in vegan. *Vignette of the package vegan. R package version*, *2016*, 2-4.

Olivares, J., et Schmachtenberg, O. (2019). An update on anatomy and function of the teleost olfactory system. *PeerJ*, *7*, e7808.

Ollonen, J., Khannoon, E. R., Macrì, S., Vergilov, V., Kuurne, J., Saarikivi, J., Soukainen, A., Aalto, I.-M., Werneburg, I., et Diaz Jr, R. E. (2024). Dynamic evolutionary interplay between ontogenetic skull patterning and whole-head integration. *Nature Ecology & Evolution*, *8*(3), 536-551. https://doi.org/https://doi.org/10.1038/s41559-023-02295-3

Olson, E. C., et Miller, R. L. (1958). *Morphological Integration*. University of Chicago Press.
Ord, T. J., et Summers, T. C. (2015). Repeated evolution and the impact of evolutionary history on adaptation. *BMC Evolutionary Biology*, *15*(1), e137.
Pagel, M. (1999). Inferring the historical patterns of biological evolution. *Nature*, *401*(6756), 877-884.
Pagel, M., et Meade, A. (2006). Bayesian analysis of correlated evolution of discrete characters by reversible-jump Markov chain Monte Carlo. *The American Naturalist*, *167*(6), 808-825.
Pan, X.-Y., Zeng, Y.-Y., Liu, Y.-M., et Fei, J.-F. (2023). Resolving vertebrate brain evolution through salamander brain development and regeneration. *Zoological Research*, *44*(1), 219.
Parker, H. J., Bronner, M. E., et Krumlauf, R. (2016). The vertebrate *Hox* gene regulatory network for hindbrain segmentation: Evolution and diversification: Coupling of a *Hox* gene regulatory network to hindbrain segmentation is an ancient trait originating at the base of vertebrates. *Bioessays*, *38*(6), 526-538.
Pélabon, C., Firmat, C., Bolstad, G. H., Voje, K. L., Houle, D., Cassara, J., Rouzic, A. L., et Hansen, T. F. (2014). Evolution of morphological allometry. *Annals of the New York Academy of Sciences*, *1320*(1), 58-75.
Pennell, M. W., Eastman, J. M., Slater, G. J., Brown, J. W., Uyeda, J. C., FitzJohn, R. G., Alfaro, M. E., et Harmon, L. J. (2014). geiger v2. 0: an expanded suite of methods for fitting macroevolutionary models to phylogenetic trees. *Bioinformatics*, *30*(15), 2216-2218.
Perens, J., et Hecksher-Sørensen, J. (2022). Digital brain maps and virtual neuroscience: An emerging role for light-sheet fluorescence microscopy in drug development. *Frontiers in Neuroscience*, *16*, e866884.
Perens, J., Salinas, C. G., Skytte, J. L., Roostalu, U., Dahl, A. B., Dyrby, T. B., Wichern, F., Barkholt, P., Vrang, N., et Jelsing, J. (2021). An optimized mouse brain atlas for automated mapping and quantification of neuronal activity using iDISCO+ and light sheet fluorescence microscopy. *Neuroinformatics*, *19*(3), 433-446.
Petranka, J. W. (1998). *Salamanders of the United States and Canada*. Smithsonian Institution Press.
Piekarski, N., Gross, J. B., et Hanken, J. (2014). Evolutionary innovation and conservation in the embryonic derivation of the vertebrate skull. *Nature Communications*, *5*(1), e5661. https://doi.org/https://doi.org/10.1038/ncomms6661
Pierce, S. E., Clack, J. A., et Hutchinson, J. R. (2012). Three-dimensional limb joint mobility in the early tetrapod Ichthyostega. *Nature*, *486*(7404), 523-526.
Plummer, M., Best, N., Cowles, K., et Vines, K. (2006). CODA: convergence diagnosis and output analysis for MCMC. *R news*, *6*(1), 7-11.
Pogoda, P., et Kupfer, A. (2018). Flesh and bone: An integrative approach towards sexual size dimorphism of a terrestrial salamander (genus *Salamandrina*). *Journal of Morphology*, *279*(10), 1468-1479.
Pollen, A. A., Dobberfuhl, A. P., Scace, J., Igulu, M. M., Renn, S. C., Shumway, C. A., et Hofmann, H. A. (2007). Environmental complexity and social organization sculpt the

brain in Lake Tanganyikan cichlid fish. *Brain, Behavior and Evolution*, *70*(1), 21-39. https://doi.org/https://doi.org/10.1159/000101067
Ponssa, M. L., Fratani, J., et Barrionuevo, J. S. (2022). Phalanx morphology in salamanders: A reflection of microhabitat use, life cycle or evolutionary constraints? *Zoology*, *154*, e126040.
Powell, R., Collins, J. T., et Hooper, E. D. (1998). *A Key to Amphibians and Reptiles of the Continental United States and Canada*. Lawrence, Kansas: University Press of Kansas.
Prahlad, K., et DeLanney, L. E. (1965). A study of induced metamorphosis in the axolotl. *Journal of Experimental Zoology*, *160*(1), 137-145.
Pryor, G. S., German, D. P., et Bjorndal, K. A. (2006). Gastrointestinal fermentation in greater sirens (*Siren lacertina*). *Journal of Herpetology*, *40*(1), 112-117.
Puelles, L. (2013). Plan of the developing vertebrate nervous system. *Pattering and Cell Type Specification in the Developing CNS and PNS*, *1*, 187-209.
Puelles, L., et Rubenstein, J. L. (2003). Forebrain gene expression domains and the evolving prosomeric model. *Trends in Neurosciences*, *26*(9), 469-476.
R Core Team, C. (2024). *_R: A Language and Environment for Statistical Computing_*. R Foundation for Statistical Computing. https://www.R-project.org/
R Core Team, C. (2025). *R: A Language and Environment for Statistical Computing*. R Foundation for Statistical Computing. https://www.R-project.org/
Raffaëlli, J. (2007). *Les Urodèles du Monde*. Penclen édition.
Redies, C., et Puelles, L. (2001). Modularity in vertebrate brain development and evolution. *Bioessays*, *23*(12), 1100-1111. https://doi.org/https://doi.org/10.1002/bies.10014
Reilly, S. M., et Lauder, G. V. (1991). Experimental morphology of the feeding mechanism in salamanders. *Journal of Morphology*, *210*(1), 33-44.
Reinhard, S., et Kupfer, A. (2015). Sexual dimorphism in a French population of the marbled newt, *Triturus marmoratus* (Urodela: Salamandridae). *Salamandra*, *51*(2), 121-128.
Rensch, B. (1948). Histological changes correlated with evolutionary changes of body size. *Evolution*, *2*(3), 218-230.
Rhinn, M., et Brand, M. (2001). The midbrain–hindbrain boundary organizer. *Current Opinion in Neurobiology*, *11*(1), 34-42.
Richtsmeier, J. T., Burke Deleon, V., et Lele, S. R. (2002). The promise of geometric morphometrics. *American Journal of Physical Anthropology*, *119*(S35), 63-91.
Richtsmeier, J. T., et Flaherty, K. (2013). Hand in glove: brain and skull in development and dysmorphogenesis. *Acta Neuropathologica*, *125*(4), 469-489.
Robb, R. C. (1935). A study of mutations in evolution: I. Evolution in the equine skull. *Journal of Genetics*, *31*, 39-46.
Rodrigues, M. V., de Carvalho-e-Silva, S. P., Rödel, M.-O., et de Mello Bezerra, A. (2025). Exploring the relationship between environment and brain morphology in anurans: a comparative phylogenetic approach. *Zoological Journal of the Linnean Society*, *203*(1), zlae025.
Rogers, S. W. (1999). Allosaurus, crocodiles, and birds: evolutionary clues from spiral computed tomography of an endocast. *The Anatomical Record*, *257*(5), 162-173.

Rohlf, F. J., et Slice, D. (1990). Extensions of the Procrustes method for the optimal superimposition of landmarks. *Systematic Zoology*, *39*(1), 40-59. https://doi.org/https://doi.org/10.2307/2992207

Romano, A., et Ficetola, G. F. (2010). Ecogeographic variation of body size in the spectacled salamanders (*Salamandrina*): influence of genetic structure and local factors. *Journal of Biogeography*, *37*(12), 2358-2370.

Romer, A. S., et Edinger, T. (1942). Endocranial casts and brains of living and fossil Amphibia. *Journal of Comparative Neurology*, *77*(2), 355-389.

Rot-Nikcevic, I., Denver, R. J., et Wassersug, R. (2005). The influence of visual and tactile stimulation on growth and metamorphosis in anuran larvae. *Functional Ecology*, *19*(6), 1008-1016.

Roth, G., Naujoks Manteuffel, C., et Grunwald, W. (1990). Cytoarchitecture of the tectum mesencephali in salamanders: A Golgi and HRP study. *Journal of Comparative Neurology*, *291*(1), 27-42.

Roth, G., Nishikawa, K. C., Naujoks-Manteuffel, C., Schmidt, A., et Wake, D. B. (1993). Paedomorphosis and Simplification in the Nervous System of Salamanders. *Brain, Behavior and Evolution*, *42*(3), 137-152. https://doi.org/https://doi.org/10.1159/000114147

Roth, G., Nishikawa, K. C., et Wake, D. B. (1997). Genome size, secondary simplification, and the evolution of the brain in salamanders. *Brain, Behavior and Evolution*, *50*(1), 50-59. https://doi.org/https://doi.org/10.1159/000113321

Roth, G., Rottluff, B., Grunwald, W., Hanken, J., et Linke, R. (1990). Miniaturization in plethodontid salamanders (Caudata: Plethodontidae) and its consequences for the brain and visual system. *Biological Journal of the Linnean Society*, *40*(2), 165-190.

Roth, G., et Schmidt, A. (1993). The nervous system of plethodontid salamanders: insight into the interplay between genome, organism, behavior, and ecology. *Herpetologica*, *49*(2), 185-194.

Roth, G., et Walkowiak, W. (2015). The influence of genome and cell size on brain morphology in amphibians. *Cold Spring Harbor Perspectives in Biology*, *7*(9), a019075. https://doi.org/10.1101/cshperspect.a019075

Roux, J., et Robinson-Rechavi, M. (2008). Developmental constraints on vertebrate genome evolution. *PLoS genetics*, *4*(12), e1000311.

Rovito, S. M., Parra-Olea, G., Recuero, E., et Wake, D. B. (2015). Diversification and biogeographical history of Neotropical plethodontid salamanders. *Zoological Journal of the Linnean Society*, *175*(1), 167-188.

Rowe, L., et Ludwig, D. (1991). Size and timing of metamorphosis in complex life cycles: time constraints and variation. *Ecology*, *72*(2), 413-427.

Różański, J. J., et Żuwała, K. D. (2020). Macro and micromorphological remodeling of olfactory organs throughout the ontogeny of the fire salamander *Salamandra salamandra* (Linnaeus, 1758). *Journal of Morphology*, *281*(10), 1173-1190. https://doi.org/https://doi.org/10.1002/jmor.21239

Ruta, M., et Coates, M. I. (2007). Dates, nodes and character conflict: addressing the lissamphibian origin problem. *Journal of Systematic Palaeontology*, *5*(1), 69-122.

Salas, C., Broglio, C., et Rodríguez, F. (2003). Evolution of forebrain and spatial cognition in vertebrates: conservation across diversity. *Brain Behavior and Evolution*, *62*(2), 72-82.

San Mauro, D. (2010). A multilocus timescale for the origin of extant amphibians. *Molecular Phylogenetics and Evolution*, *56*(2), 554-561.

San Mauro, D., Vences, M., Alcobendas, M., Zardoya, R., et Meyer, A. (2005). Initial diversification of living amphibians predated the breakup of Pangaea. *The American Naturalist*, *165*(5), 590-599.

Sánchez-Vázquez, F. J., López-Olmeda, J. F., Vera, L. M., Migaud, H., López-Patiño, M. A., et Míguez, J. M. (2019). Environmental cycles, melatonin, and circadian control of stress response in fish. *Frontiers in Endocrinology*, *10*, 279.

Sansalone, G., Allen, K., Ledogar, J., Ledogar, S., Mitchell, D., Profico, A., Castiglione, S., Melchionna, M., Serio, C., et Mondanaro, A. (2020). Variation in the strength of allometry drives rates of evolution in primate brain shape. *Proceedings of the Royal Society B: Biological Sciences*, *287*(e1930), e20200807.

Sansalone, G., Profico, A., Wroe, S., Allen, K., Ledogar, J., Ledogar, S., Mitchell, D. R., Mondanaro, A., Melchionna, M., et Castiglione, S. (2023). *Homo sapiens* and Neanderthals share high cerebral cortex integration into adulthood. *Nature Ecology & Evolution*, *7*(1), 42-50.

Schlager, S. (2017). Morpho and Rvcg–shape analysis in R: R-packages for geometric morphometrics, shape analysis and surface manipulations. In G. Zheng, S. Li, G. Székely (Eds.), *Statistical Shape and Deformation Analysis* (pp. 217-256). Elsevier.

Schoch, R. R. (2013). How body size and development biased the direction of evolution in early amphibians. *Historical Biology*, *25*(2), 155-165.

Schoch, R. R., Werneburg, R., et Voigt, S. (2020). A Triassic stem-salamander from Kyrgyzstan and the origin of salamanders. *Proceedings of the National Academy of Sciences*, *117*(21), 11584-11588.

Schowing, P. J. (1968). Mise en évidence du rôle inducteur de l'encéphale dans l'ostéogenèse du crâne embryonnaire du poulet. *Development*, *19*(1), 83-94.

Schumacher, E. L., et Carlson, B. A. (2022). Convergent mosaic brain evolution is associated with the evolution of novel electrosensory systems in teleost fishes. *eLife*, *11*, e74159. https://doi.org/https://doi.org/10.7554/eLife.74159

Schwarz, D., Heiss, E., Pierson, T. W., Konow, N., et Schoch, R. R. (2023). Using salamanders as model taxa to understand vertebrate feeding constraints during the Late Devonian water-to-land transition. *Philosophical Transactions of the Royal Society B*, *378*(1891), e20220541. https://doi.org/https://doi.org/10.1098/rstb.2022.0541

Sears, K., Bianchi, C., Powers, L., et Beck, A. (2013). Integration of the mammalian shoulder girdle within populations and over evolutionary time. *Journal of Evolutionary Biology*, *26*(7), 1536-1548.

Semlitsch, R. D. (1987). Paedomorphosis in *Ambystoma talpoideum*: effects of density, food, and pond drying. *Ecology*, *68*(4), 994-1002.

Semlitsch, R. D., et Gibbons, J. W. (1985). Phenotypic variation in metamorphosis and paedomorphosis in the salamander *Ambystoma talpoideum*. *Ecology*, *66*(4), 1123-1130.

Semlitsch, R. D., Harris, R. N., et Wilbur, H. M. (1990). Paedomorphosis in *Ambystoma talpoideum*: maintenance of population variation and alternative life-history pathways. *Evolution*, *44*(6), 1604-1613.

Senovilla-Ganzo, R., et García-Moreno, F. (2024). The Phylotypic Brain of Vertebrates, from Neural Tube Closure to Brain Diversification. *Brain Behavior and Evolution*, *99*(1), 45-68.

Shaffer, H. B. (1993). Phylogenetics of model organisms: the laboratory axolotl, *Ambystoma mexicanum*. *Systematic Biology*, *42*(4), 508-522.

Shaffer, H. B., Flores-Villela, O., Parra-Olea, G., et Wake, D. (2004). *Ambystoma andersoni*. IUCN 2012: IUCN Red List of Threatened Species.

Sherratt, E., Gower, D. J., Klingenberg, C. P., et Wilkinson, M. (2014). Evolution of cranial shape in caecilians (Amphibia: Gymnophiona). *Evolutionary Biology*, *41*, 528-545.

Shimogori, T., Lee, D. A., Miranda-Angulo, A., Yang, Y., Wang, H., Jiang, L., Yoshida, A. C., Kataoka, A., Mashiko, H., et Avetisyan, M. (2010). A genomic atlas of mouse hypothalamic development. *Nature Neuroscience*, *13*(6), 767-775.

Sinsch, U., Böcking, H., Leskovar, C., Öz, M., et Veith, M. (2017). Demography and lifetime growth patterns in viviparous salamanders (genus *Lyciasalamandra*): Living underground attenuates interspecific variation. *Zoologischer Anzeiger*, *269*, 48-56.

Skelly, D. K., et Kiesecker, J. M. (2001). Venue and outcome in ecological experiments: manipulations of larval anurans. *Oikos*, *94*(1), 198-208.

Sket, B. (1997). Distribution of *Proteus* (Amphibia: Urodela: Proteidae) and its possible explanation. *Journal of Biogeography*, *24*(3), 263-280.

Slice, D. E. (2007). Geometric morphometrics. *Annual Review of Anthropology 36*(1), 261-281. https://doi.org/https://doi.org/10.1146/annurev.anthro.34.081804.120613

Smith, M. P., Sansom, I. J., et Cochrane, K. D. (2001). The Cambrian origin of vertebrates. *Systematics Association Special Volume*, *61*, 67-84.

Soares, D., Yamamoto, Y., Strickler, A. G., et Jeffery, W. R. (2005). The lens has a specific influence on optic nerve and tectum development in the blind cavefish *Astyanax*. *Developmental Neuroscience*, *26*(5-6), 308-317. https://doi.org/https://doi.org/10.1159/000082272

Sol, D., et Price, T. D. (2008). Brain size and the diversification of body size in birds. *The American Naturalist*, *172*(2), 170-177.

Solís, F., Ibáñez, R., Savage, J., Wake, D., Chaves, G., et Bolaños, F. (2008). *Bolitoglossa schizodactyla*. www.iucnredlist.org

Sood, N. B. (1980). *A Comparative Anatomical Study of the Pineal Gland in Mammals*. Western Michigan University.

Stearns, S. (2018). *The Evolution of Vertebrate Brain Architecture in Response to Divergent Natural Selection: Concerted Vs. Mosaic Evolution?* The University of Texas at Arlington.

Stebbins, R. C. (2003). *Western Reptiles and Amphibians*. Houghton Mifflin Company.

Stephan, H., Frahm, H., et Baron, G. (1981). New and revised data on volumes of brain structures in insectivores and primates. *Folia Primatologica*, *35*(1), 1-29.
Stephan, H., et Pirlot, P. (1970). Volumetric comparisons of brain structures in bats. *Zeitschrift für zoologische Systematik und Evolutionsforschung*, *8*, 200-236.
Striedter, G. F. (2005). *Principles of Brain Evolution*. Sinauer associates.
Stuart, S. N. (2008). *Threatened Amphibians of the World*. Lynx Edicions.
Sukhum, K. V., Shen, J., et Carlson, B. A. (2018). Extreme enlargement of the cerebellum in a clade of teleost fishes that evolved a novel active sensory system. *Current Biology*, *28*(23), 3857-3863.
Szostakiwskyj, M., et Anderson, J. S. (2022). Salamander braincase morphology as revealed by micro-computed tomography. *Journal of Morphology*, *283*(4), 462-501.
Tata, J. R. (2006). Amphibian metamorphosis as a model for the developmental actions of thyroid hormone. *Molecular and Cellular Endocrinology*, *246*(1-2), 10-20.
Taylor, G. M., Nol, E., et Boire, D. (1995). Brain regions and encephalization in anurans: adaptation or stability? *Brain, Behavior and Evolution*, *45*(2), 96-109.
Teng, C. S., Cavin, L., Maxson, R. E., Sánchez-Villagra, M. R., et Crump, J. G. (2019). Resolving homology in the face of shifting germ layer origins: Lessons from a major skull vault boundary. *eLife*, *8*, e52814. https://doi.org/https://doi.org/10.7554/eLife.52814
Thompson, A. W., Vanwalleghem, G. C., Heap, L. A., et Scott, E. K. (2016). Functional profiles of visual-, auditory-, and water flow-responsive neurons in the zebrafish tectum. *Current Biology*, *26*(6), 743-754.
Tomašević Kolarov, N., Cvijanović, M., Denoël, M., et Ivanović, A. (2017). Morphological integration and alternative life history strategies: a case study in a facultatively paedomorphic newt. *Journal of Experimental Zoology Part B: Molecular and Developmental Evolution*, *328*(8), 737-748.
Triki, Z., Fong, S., Amcoff, M., et Kolm, N. (2022). Artificial mosaic brain evolution of relative telencephalon size improves inhibitory control abilities in the guppy (*Poecilia reticulata*). *Evolution*, *76*(1), 128-138.
Trokovic, N., Gonda, A., Herczeg, G., Laurila, A., et Merilä, J. (2011). Brain plasticity over the metamorphic boundary: carry-over effect of larval environment on froglet brain development. *Journal of Evolutionary Biology*, *24*(6), 1380-1385.
Trueb, L., et Cloutier, R. (1991). A phylogenetic investigation of the inter-and intrarelationships of the Lissamphibia (Amphibia: Temnospondyli). In H.-P. Schultze et L. Trueb (Eds.), *Origins of the Higher Groups of Tetrapods: Controversy and Consensus* (pp. 223-313). Cornell University Press.
Tsuboi, M., van der Bijl, W., Kopperud, B. T., Erritzøe, J., Voje, K. L., Kotrschal, A., Yopak, K. E., Collin, S. P., Iwaniuk, A. N., et Kolm, N. (2018). Breakdown of brain–body allometry and the encephalization of birds and mammals. *Nature Ecology & Evolution*, *2*(9), 1492-1500.
Tytiuk, O., Stepanyuk, Y., et Yaryhin, O. (2018). The influence of fixatives on the validity of histological preparations of olfactory organ in Teleostei. *Vestnik Zoologii*, *52*(6), 521-528.

Ussing, A. P., et Rosenkilde, P. (1995). Effect of induced metamorphosis on the immune system of the axolotl, *Ambystoma mexicanum*. *General and Comparative Endocrinology*, *97*(3), 308-319.
Van Buskirk, J., et Smith, D. C. (1991). Density-dependent population regulation in a salamander. *Ecology*, *72*(5), 1747-1756.
van Rietbergen, B., Weinans, H., Huiskes, R., et Odgaard, A. (1995). A new method to determine trabecular bone elastic properties and loading using micromechanical finite-element models. *Journal of Biomechanics*, *28*(1), 69-81.
Venditti, C., Meade, A., et Pagel, M. (2011). Multiple routes to mammalian diversity. *Nature*, *479*(7373), 393-396.
Vieira, W. A., Wells, K. M., et McCusker, C. D. (2020). Advancements to the axolotl model for regeneration and aging. *Gerontology*, *66*(3), 212-222. https://doi.org/https://doi.org/10.1159/000504294
Vitt, L. J., et Caldwell, J. P. (2013). *Herpetology: an Introductory Biology of Amphibians and Reptiles*. Academic press.
Vonesh, J. R., et De la Cruz, O. (2002). Complex life cycles and density dependence: assessing the contribution of egg mortality to amphibian declines. *Oecologia*, *133*(3), 325-333.
Vorobyeva, E., et Darevsky, I. (1994). *The Siberian Newt (*Salamandrella keyserlingii *Dybowski, 1870): Zoogeography, Systematics, Morphology*. Nauka Moscow.
Voss, S. R., Epperlein, H. H., et Tanaka, E. M. (2009). *Ambystoma mexicanum*, the axolotl: a versatile amphibian model for regeneration, development, and evolution studies. *Cold Spring Harbor Protocols*, *2009*(8), pdb. emo128. https://doi.org/10.1101/pdb.emo128
Wagner, G. P. (1996). Homologues, natural kinds and the evolution of modularity. *American Zoologist*, *36*(1), 36-43.
Wagner, G. P., et Altenberg, L. (1996). Perspective: complex adaptations and the evolution of evolvability. *Evolution*, *50*(3), 967-976.
Wake, D., et Hanken, J. (1996). Direct development in the lungless salamanders: what are the consequences for developmental biology, evolution and phylogenesis? *The International Journal of Developmental Biology*, *40*(4), 859-869.
Wake, D. B. (1991). Homoplasy: the result of natural selection, or evidence of design limitations? *The American Naturalist*, *138*(3), 543-567.
Wake, D. B., Deban, S. M., et Schwenk, K. (2000). Terrestrial feeding in salamanders. In K. Schwenk (Ed.), *Feeding: Form, Function and Evolution in Tetrapod Vertebrates* (pp. 95-116).
Wake, D. B., et Dresner, I. G. (1967). Functional morphology and evolution of tail autotomy in salamanders. *Journal of Morphology*, *122*(4), 265-305.
Wake, D. B., et Vredenburg, V. T. (2008). Are we in the midst of the sixth mass extinction? A view from the world of amphibians. *Proceedings of the National Academy of Sciences*, *105*(supplement_1), 11466-11473.
Wake, M. H., et Dickie, R. (1998). Oviduct structure and function and reproductive modes in amphibians. *Journal of Experimental Zoology*, *282*(4-5), 477-506.

Wang, K., Brandon, T., McDonald, K.-A., et Pierson, T. (2023). An evaluation of sexual dimorphism in head size and shape of red salamanders (*Pseudotriton ruber*). *Reptiles & Amphibians*, *30*(1), e18211.

Wassersug, R. J. (1989). Locomotion in amphibian larvae (or" Why aren't tadpoles built like fishes?"). *American Zoologist*, *29*, 65-84.

Watanabe, A., Balanoff, A. M., Gignac, P. M., Gold, M. E. L., et Norell, M. A. (2021). Novel neuroanatomical integration and scaling define avian brain shape evolution and development. *eLife*, *10*, e68809. https://doi.org/https://doi.org/10.7554/eLife.68809

Watanabe, A., Fabre, A.-C., Felice, R. N., Maisano, J. A., Müller, J., Herrel, A., et Goswami, A. (2019). Ecomorphological diversification in squamates from conserved pattern of cranial integration. *Proceedings of the National Academy of Sciences*, *116*(29), 14688-14697.

Watanabe, A., Gignac, P. M., Balanoff, A. M., Green, T. L., Kley, N. J., et Norell, M. A. (2019). Are endocasts good proxies for brain size and shape in archosaurs throughout ontogeny? *Journal of Anatomy*, *234*(3), 291-305.

Weisbecker, V. (2012). Distortion in formalin-fixed brains: using geometric morphometrics to quantify the worst-case scenario in mice. *Brain Structure and Function*, *217*, 677-685.

Weisbecker, V., et Mitgutsch, C. (2010). A large-scale survey of heterochrony in anuran cranial ossification patterns. *Journal of Zoological Systematics and Evolutionary Research*, *48*(4), 332-347.

Weisbecker, V., Rowe, T., Wroe, S., Macrini, T. E., Garland, K. L., Travouillon, K. J., Black, K., Archer, M., Hand, S. J., et Berlin, J. C. (2021). Global elongation and high shape flexibility as an evolutionary hypothesis of accommodating mammalian brains into skulls. *Evolution*, *75*(3), 625-640.

Wells, K. D. (2019). *The Ecology and Behavior of Amphibians*. University of Chicago press.

Werner, E. (1988). Size, scaling, and the evolution of complex life cycles. In B. Ebenman et L. Persson (Eds.), *Size-structured Populations: Ecology and Evolution* (pp. 60-81). Springer.

Werner, E. E. (1986). Amphibian metamorphosis: growth rate, predation risk, and the optimal size at transformation. *The American Naturalist*, *128*(3), 319-341.

Whiteman, H. H. (1994). Evolution of facultative paedomorphosis in salamanders. *The Quarterly Review of Biology*, *69*(2), 205-221.

Wilbur, H. M., et Collins, J. P. (1973). Ecological Aspects of Amphibian Metamorphosis: Nonnormal distributions of competitive ability reflect selection for facultative metamorphosis. *Science*, *182*(4119), 1305-1314.

Willemet, R. (2013). Reconsidering the evolution of brain, cognition, and behavior in birds and mammals. *Frontiers in Psychology*, *4*, e396.

Willemet, R. (2020). Commentary: Mosaic and concerted brain evolution: the contribution of microscopic comparative neuroanatomy in lower vertebrates. *Frontiers in Neuroanatomy*, *14*, 6. https://doi.org/https://doi.org/10.3389/fnana.2020.00006

Wilson, S. W., et Houart, C. (2004). Early steps in the development of the forebrain. *Developmental Cell*, *6*(2), 167-181.

Winemiller, K. O., et Rose, K. A. (1992). Patterns of life-history diversification in North American fishes: implications for population regulation. *Canadian Journal of Fisheries and Aquatic Sciences*, *49*(10), 2196-2218.

Wong, M. D., Spring, S., et Henkelman, R. M. (2013). Structural stabilization of tissue for embryo phenotyping using micro-CT with iodine staining. *PLoS One*, *8*(12), e84321.

Woodley, S. (2015). Chemosignals, hormones, and amphibian reproduction. *Hormones and Behavior*, *68*, 3-13.

Yamamoto, Y., Espinasa, L., Stock, D. W., et Jeffery, W. R. (2003). Development and evolution of craniofacial patterning is mediated by eye-dependent and-independent processes in the cavefish *Astyanax*. *Evolution & Development*, *5*(5), 435-446.

Yaskin, V. (2011). Seasonal changes in hippocampus size and spatial behavior in mammals and birds. *Biology Bulletin Reviews*, *1*(3), 279-288. https://doi.org/https://doi.org/10.1134/S2079086411030108

Yopak, K. E., et Lisney, T. J. (2012). Allometric scaling of the optic tectum in cartilaginous fishes. *Brain, Behavior and Evolution*, *80*(2), 108-126. https://doi.org/https://doi.org/10.1159/000339875

Yopak, K. E., Lisney, T. J., et Collin, S. P. (2015). Not all sharks are "swimming noses": variation in olfactory bulb size in cartilaginous fishes. *Brain Structure and Function*, *220*(2), 1127-1143.

Yopak, K. E., Lisney, T. J., Darlington, R. B., Collin, S. P., Montgomery, J. C., et Finlay, B. L. (2010). A conserved pattern of brain scaling from sharks to primates. *Proceedings of the National Academy of Sciences*, *107*(29), 12946-12951. https://doi.org/https://doi.org/10.1073/pnas.1002195107

Zamora-Camacho, F. J. (2023). Evolution and ecology of locomotion in amphibians. In G. Moreno-Rueda, M. Comas (Eds.), *Evolutionary Ecology of Amphibians* (pp. 135-157). CRC Press.

Zelditch, M., Swiderski, D., et Sheets, H. D. (2012). *Geometric Morphometrics for Biologists: a primer*. Academic Press.

Zhao, E. (1998). China red data book of endangered animals: Amphibia and Reptilia. *Beijing: Science Press*, *120*, 121.